THE CIRCULATION OF THE ATMOSPHERE OF VENUS

by

EUGENIA E. KÁLNAY de RIVAS

Licenciada en Meteorología
Universidad Nacional de Buenos Aires
(1965)

SUBMITTED IN PARTIAL FULFILLMENT

OF THE REQUIREMENTS FOR THE

DEGREE OF DOCTOR OF PHILOSOPHY

at the

MASSACHUSETTS INSTITUTE OF TECHNOLOGY

July, 1971

Signature of Author..
Department of Meteorology, July   , 1971

Certified by....   ....
                                            Thesis Supervisor

Accepted by...
                        Chairman, Departmental Committee
                                on Graduate Students

THE CIRCULATION OF THE ATMOSPHERE OF VENUS

Eugenia E. Kálnay de Rivas

ABSTRACT

The circulation of the atmosphere of Venus is simulated by means of two-dimensional numerical models. Two extreme cases are considered: first, rotation is neglected and the subsolar point is assumed to be fixed; second (and probably more realistically), the solar heating is averaged over a Venus solar day and rotation is included. For each case a Boussinesq model, in which density variations are neglected except when coupled with gravity, and a quasi-Boussinesq model, which includes a basic stratification of density and a semi-grey treatment of radiation, are developed. The results obtained with the Boussinesq models are similar to those obtained by Goody and Robinson and by Stone. However, when the stratification of density is included and most of the solar radiation is absorbed near the top, the large-scale circulation is confined to the upper layers of the atmosphere and cannot maintain an adiabatic stratification in the interior. The thermal equilibrium in the interior is radiative-diffusive. When solar radiation is allowed to penetrate the atmosphere, so that at the equator 6% of the incoming solar radiation reaches the surface, then the combination of a more deeply

driven circulation and a partial greenhouse effect is able to maintain an adiabatic stratification.

The effect of symmetrical solar heating is to produce direct Hadley cells in each hemisphere with small reverse cells near the poles. Poleward angular momentum transport in the upper atmosphere produces a shear in the zonal motion with a maximum retrograde velocity of the order of 10 m/sec at the top of the atmosphere.

The numerical integrations were performed using non-uniform grids to allow adequate resolution of the boundary layers. A study of the truncation errors introduced by the use of non-uniform grids is included, and it is shown that the use of stretched coordinates has several advantages for flows with boundary layers.

A proposal for a simple three-dimensional model, capable in principle of explaining the observed rapid zonal velocities at cloud level as well as the deep circulation, is presented.

Thesis Supervisor: Jule G. Charney
Title: Sloan Professor of Meteorology

TO THE PEACE MOVEMENT

ACKNOWLEDGEMENTS

I am very grateful to my advisor, Professor J. G. Charney, whose enthusiasm, advice, help and encouragement allowed me to complete this work. I am also grateful to Professor N. A. Phillips for his patient guidance and advice during my first years at M.I.T.

I had some helpful discussions with Professors R. M. Goody, V. P. Starr, P. Rhines, and Doctors Sulochana Gadgil and G. Philander, for which I am most grateful.

Mrs. Karen MacQueen carefully and cheerfully, as usual, typed the thesis. Miss Diana Lees gave me invaluable programming help and advice, and drew many of the pictures. To them I would like to express my deep gratitude, for their help, encouragement, and especially, for their wonderful friendship.

Most of the computations were performed at the NASA Institute for Space Studies in New York. Thanks are due to Doctors Robert Jastrow and Milt Halem for making these facilities available and to Mr. Peter Aschenbrenner for his helpful cooperation in running the programs.

My deepest debt is to my husband, Alberto Rivas, whose encouragement and understanding were much greater than what I could fairly expect. His careful advice helped me to design most of the numerical methods used in this thesis. He also designed the new method for obtaining unusually smooth computer contours that was used in Chapter 5, and which can be used with non-uniform grids.

I would like to thank my family, my family-in-law and especially my mother and my sister Patricia for their love, help

and encouragement.

I have been very privileged to be able to continue my studies at the Department of Meteorology at M.I.T. I want to express my thanks to all the people who made it possible, and in particular to Professors Rolando V. García, Jule G. Charney and Norman A. Phillips. The National Science Foundation generously supported my work with a research assistantship under grant GA 402X.

TABLE OF CONTENTS

CHAPTER 1

Introduction

The atmospheres of our planet Earth and our neighboring planets Venus and Mars seem to have been designed with an experimental purpose in mind. While they are all subject to approximately the same driving, i.e., the incident minus the reflected solar radiation differs by less than a factor of 2, other parameters important to meteorologists are quite different (Table 1.1).

	Venus	Earth	Mars
Main constituent	CO_2	N_2	CO_2
Solar constant × (1-albedo) (erg $cm^{-2}sec^{-1}$)	6.3×10^5	9.0×10^5	5.1×10^5
Specific gravity (cm sec^{-2})	850	980	376
Rotation period (sec)	2×10^7	7×10^5	7×10^5
Inclination of Equator to ecliptic plane (degrees)	∿0	23	25
Surface pressure (atm)	∿ 100	1	6×10^{-3}

Table 1.1: Some physical data of the planets Venus, Earth, and Mars.

For example: (a) the inclination of the Equator with respect to the plane of the ecliptic is near zero in Venus, which means that very little seasonal variation is observed, and is about 25° for both Mars and the Earth, with correspondingly strong seasonal variations

of insolation; (b) the total mass of the atmosphere measured by the

surface pressure, which together with the length of a solar day gives

a measure of the importance of diurnal effects, also varies dramati-

cally: it is about one hundred atmospheres for Venus, one atmosphere

for the Earth and one hundredth of an atmosphere for Mars; (c) the

rate of rotation of the planet is rapid for Mars and the Earth, which

have a rotation period of about one earth day in the positive direc-

tion, and is very small for Venus, which has a rotation period of

about 243 earth days and (with the marginal exception of Uranus

whose equator is inclined 98° with respect to the plane of the eclip-

tic) . is the only planet known to rotate in a retrograde direction.

It can be expected that the general circulation of the at-

mospheres of Mars and Venus will be found to be widely and interest-

ingly different from the Earth's general circulation. This paper is

an attempt to study the general circulation of the atmosphere of Venus.

The recent history of the investigation of the atmosphere

of Venus contains some surprising discoveries. The emission temper-

ature of the top of the cloud deck which covers most of the atmosphere

is about 230°K, but at the beginning of the 1960's microwave emission

temperatures indicated the existence of surface temperatures of at

least 600°K (Roberts, 1963; Barath, 1964; and others). There were

three theories offered to try to explain this high temperature. Öpik

(1961) proposed an "aeolospheric" model of the atmosphere of Venus

between the planet's surface and the top of the clouds in which strong

winds driven by the differential heating at the top were responsible

both for grinding and raising dust from the surface, making the at-

mosphere opaque to radiation, and for the heating of the surface

layers due to frictional dissipation of kinetic energy.

In the more popular "greenhouse" model proposed by Sagan (1962) and others, most of the solar radiation is assumed to penetrate through the atmosphere to the planet's surface, but the atmosphere is very opaque in the infrared region, so that emission into space takes place in the colder regions near the top of the cloud layers. The main objection to this model is not the large opacity required in the long wave region, but the relative transparency in the short wave region necessary to heat up the lower layers of the atmosphere.

The first dynamical model offered to explain the high surface temperatures was that of Goody and Robinson (1966). They used a two-dimensional Boussinesq model on a flat surface with the subsolar and antisolar points represented by vertical planes. The atmosphere was considered to be completely opaque, so that radiation was absorbed and emitted at the top of the atmosphere (the top of the cloud deck). In the interior, radiative and turbulent transfer were parameterized as a diffusion process.

Using scale and boundary layer analysis, they developed a model for the circulation of the atmosphere of Venus with slow rising motion in most of the atmosphere and a narrow region of sinking motion, which they called mixing region, at the antisolar point. There was a thin horizontal upper boundary layer with strong horizontal motion towards the antisolar point, and a slow return motion towards the subsolar point in the interior (Figure 1.1). The narrowness of the region with downward motion could explain why most of Venus' disk seems to be covered by clouds, if these are of a condensation
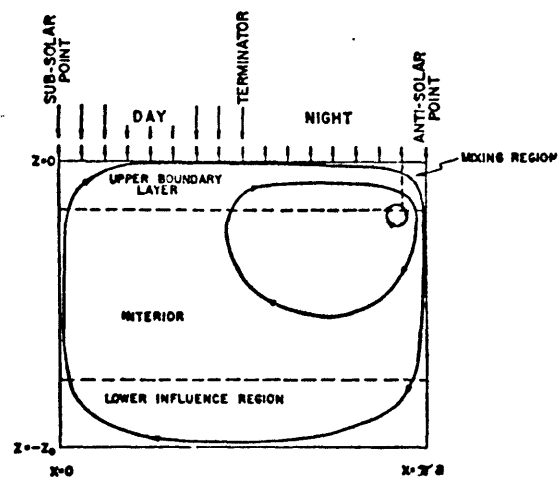
Figure 1.1: Schematic representation
of the deep circulation of Venus. After
Goody and Robinson (1966).

type. Goody and Robinson's analysis suggested that the large scale atmospheric motions were able to keep the lapse rate nearly adiabatic throughout the atmosphere. In this way the high temperatures at the surface could be explained even if the solar radiation were absorbed near the top of the atmosphere.

Stone (1968) developed a similar two-dimensional Boussinesq model on a flat surface with an improved scaling of the mixing region at the antisolar point. He did not deal with the problem of the maintenance of the adiabatic lapse rate in the interior. The main difference between Stone's and Goody and Robinson's results was the width of the mixing region. Goody and Robinson's scale analysis gave a width of 3 km while Stone's gave a width of 150 km. Furthermore, Stone pointed out the magnitude of the vertical velocity would decay slowly away from the mixing region so that downward motion would not be confined to the mixing region.

Both Goody and Robinson and Stone concluded that the Rossby number would be large due to the small rotation rate of the planet so that the effects of rotation would be minor.

Hess (1968) performed a numerical computation with a similar nonrotating, two-dimensional model in Cartesian geometry. He used pressure as the vertical coordinate so that the Boussinesq approximation was not made. The initial conditions were a state of no motion and a small static stability. A circulation was produced by the uneven heating at the top. Although after the equivalent of 160 earth days the model had not converged, the results were similar to Goody and Robinson's except that the motion was confined to the top third of the atmosphere, probably due to the increase of density

with depth. The width of the mixing region was much larger than in Goody and Robinson's or Stone's analyses, probably because the grid that Hess used was too coarse to resolve the boundary layers. The negligible value of the winds near the surface made Opik's "aeolospheric" model improbable (Figure 1.2).

In 1961 Boyer and Camichel published the results of their ultraviolet photographs of Venus. They found cloud patterns shaped like a horizontal Y which seemed to move in a zonal direction with a speed corresponding to a rotational period of about four days, as well as a tendency for certain cloud patterns to recur every four or five days. A rotation period of four days implies zonal velocities of the order of 100 m/s, i.e., about 50 times larger than the speed of rotation of the planet itself at the Equator. For a while it was generally felt that the "four-day rotation" was probably an observational error. More recent observations, reviewed by Smith (1967) and by Schubert and Young (1970) support the evidence for the existence of a retrograde rotation of the Venus atmosphere with a period of four to five days.

There have been a series of papers suggesting that the cause of these high velocities is the apparent rotation of the Sun during a Venusian solar day, implying that the Reynolds stresses that arise from the vertical circulation driven by a periodically-moving thermal forcing are able to sustain a mean horizontal flow. Fultz (1959) and Stern (1959) did moving flame experiments on a stationary annulus and found that a weak motion developed in a direction opposite to the motion of the flame. Schubert and Whitehead (1969) performed a similar experiment with a flame rotating under an annulus filled with
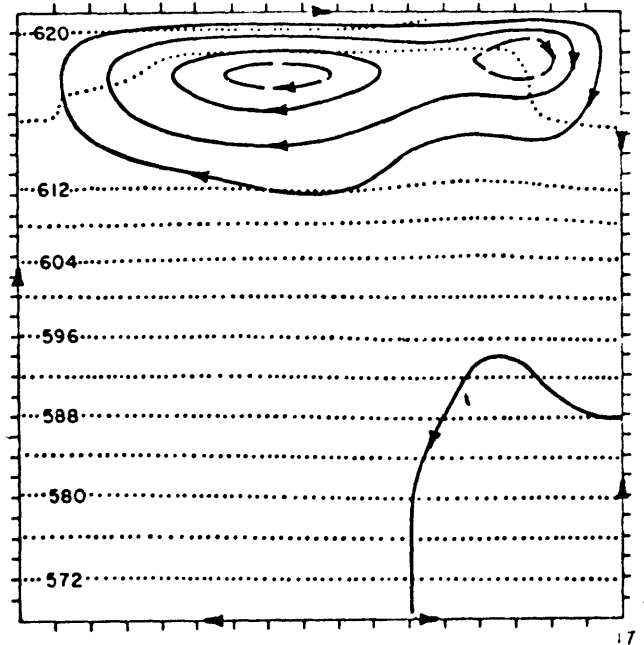
Figure 1.2: Stream function and potential
temperatures obtained by Hess after 160
earth days.

liquid mercury and found that the liquid rotated in an opposite direction with a speed about four times larger than the speed of the flame. They were the first to suggest that the rotation of the clouds of Venus was due to this mechanism.

Theoretical studies to explain the occurrence of a mean flow due to periodical thermal forcing were carried out by Stern (1959), Davey (1967), Schubert (1969), Schubert and Young (1970) and Malkus (1970). Schubert and Young showed that this effect is likely to play a significant role only in the dynamics of the atmosphere of Venus, mainly because of the favorably low overhead speed of the Sun, which is about 3 m/s. Malkus found zonal velocities of the right order of magnitude, even at a vanishingly small forcing speed, for a wide range of physical parameters, particularly the Prandtl number. Gierasch (1970) showed that the radiative time constants are of the correct magnitude to cause a strong zonal flow by the mechanism suggested by Schubert and Whitehead.

More recently Schubert, Young and Hinch (1970) have disputed Malkus' results. According to them the average motion of a fluid driven by a moving thermal source is either prograde (in the same direction of the thermal wave) or retrograde depending on the magnitude of the Prandtl number ν/κ . The downward diffusion of the thermal wave produces a tilt of the convection cells that tends to produce prograde motion, and viscous diffusion from the lower rigid surface tilts the convection cells in the opposite sense tending to produce retrograde motion. Only if the heat is well diffused $(\nu/\kappa \ll 1$) can retrograde motion occur. They conclude that the four-day retrograde circulation is a proof that the thermal balance at the cloud

top level is mainly radiative, with a correspondingly high radiative thermal diffusivity, since a turbulent diffusion would tend to have $\nu/\kappa \sim 1$.

Thompson (1970), like Malkus, suggested that while the zonal flow could be started by the Schubert-Whitehead mechanism, the interaction of a shearing flow with the tilted cells via the Reynolds stresses could intensify the shear and produce an upper zonal flow of the required magnitude. In both Thompson's and Malkus' models the moving Sun mechanism only provides the initial zonal flow. The final flow is much larger and is produced by what is essentially a finite-amplitude instability mechanism.

We should also mention a qualitative discussion by Mintz (1961) who concluded from the visible cloud observations of Dollfus, and from the zonal structure observed in the ultraviolet cloud pictures, that there might be a lower level circulation in the atmosphere of Venus with convection cells driven by the day-night heating contrast, together with a rapid zonal circulation aloft. Considering the large thermal inertia of the lower atmosphere of Venus (Chapters IV and V), his conjecture of a deep diurnal circulation is questionable.

Review papers on the circulation of Venus have been written by Goody (1969) and Hunten and Goody (1969).

The present thesis is an attempt to study the general circulation of the atmosphere of Venus from a dynamical point of view. The complexity of the processes that must be considered and the obvious importance of nonlinear effects that one deduces from simple analytical models and from the strong cloud motions, make imperative the use of numerical models. Although the observational data of the atmosphere is very scarce, we know enough to develop some simple

models. Until good "meteorological" observations become available, which will not happen in the near future, the results of analytical and numerical models are the best one can hope for to obtain some insight into what happens in the atmosphere of Venus.

The observational data that we now have available include:

(a) Astronomical data, which by this time are well established: Venus' gravity, mass, rotation period, length of year and solar day, albedo, solar constant, inclination of the equator with respect to the ecliptic plane.

(b) Atmospheric data: the Soviet spacecraft probes Venera 4, Venera 5 and Venera 6 penetrated the atmosphere of Venus on October 18, 1967, May 16 and May 17, 1969 respectively, but they ceased sending information before they reached the surface. On October 19, 1967, the American spacecraft Mariner 5 flew by the planet at less than one planetary radius. On December 15, 1970 the Soviet spacecraft Venera 7 was able to land softly on the surface of Venus and transmit information throughout the descent from an altitude of about 60 km to the surface.

From the observations made by these vehicles we now have some data on the atmospheric structure of Venus (Avduevsky et al, 1970; Avduevsky et al, 1970; see Figures 1.3 and 1.4). We also have the cloud observations mentioned before and the thermal maps made by Murray, Wildey and Westphal (1963).

Based on these data, a series of numerical models was developed. Two extreme cases were considered: first the case in which rotation is neglected and the subsolar point is fixed, and then the case in which rotation is included and diurnal effects are neglected,
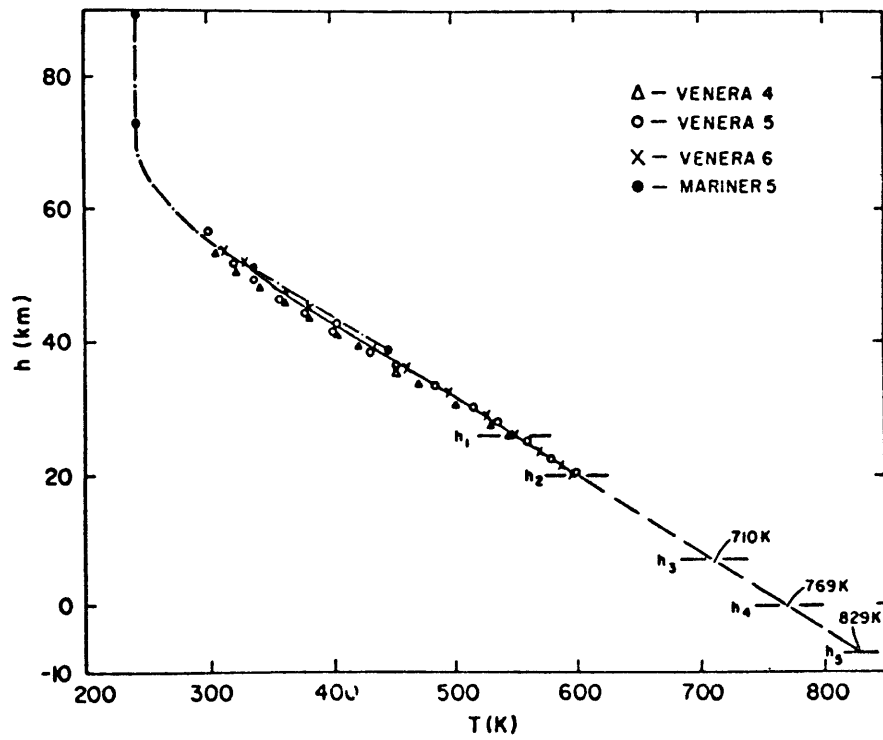
Figure 1.3: Temperature as a function of altitude in the
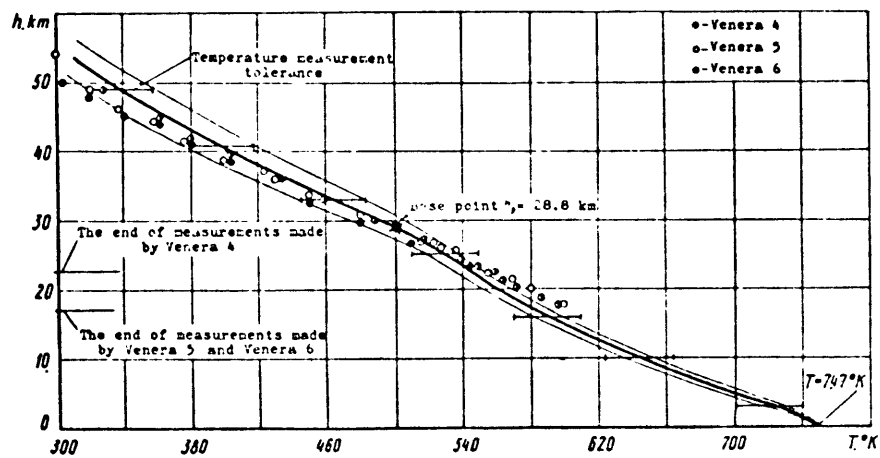' Venus atmosphere. After Advuevsky et al. (1970).

Figure 1.4: Altitude distribution of temperature based
on measured temperatures and calculations of distance de-
scended based on Doppler frequency-shift observations.
After Avduevsky, et al. (1970).

as if the heating were to come from a "toroidal sun". For each of these cases we used the Boussinesq approximation which neglects the variations of density except when theyproduce buoyancy forces, and the quasi-Boussinesq approximation,which implies mean density and temperature stratifications close to the adiabatic. All these models have been developed for flow on a sphere.

The main conclusions of this investigation are the following:

(a) The results of the Boussinesq numerical models agree qualitatively with the analyses by Goody and Robinson, except that downward motion occurs over almost half the surface of the planet. However, when a quasi-Boussinesq model is used with a near-adiabatic stratification, the circulation remains confined to the top of the atmosphere (as in Hess' model) and therefore is incapable of maintaining an adiabatic stratification in the interior. It is concluded that some penetration of the solar radiation in the atmosphere is necessary, both because it drives a deeper circulation and for the greenhouse effect.

(b) The planetary rotation, even though very slow, is not negligible. In the interior the relative velocities are very small so that the Rossby number is small. Near the top, even though the Rossby number is large, the relative zonal velocities generated because of the planetary rotation are important.

(c) A basic retrograde zonal shear is produced by the solar heating when diurnal effects are neglected. This shear may be combined with Thompson's mechanism to produce strong zonal shear near the cloud top level. The mechanism of Schubert and Whitehead requires a strong viscous effect from the ground; it is felt that the strong

density stratification (which is absent in their model) makes this
mechanism less probable.

In the course of this investigation a numerical method of
dealing with boundary layers was developed using variable grid inter-
vals defined through a stretched coordinate. It was shown that the
truncation errors are of second order <u>in the stretched coordinate</u>,
both for the first and second finite difference derivatives, and that
the particular choice of the stretched coordinate made in this paper
has very distinct advantages.

The organization of the thesis is as follows:

In Chapter 2 we discuss the characteristics and results of
a Boussinesq model without rotation, similar to the models of Goody
and Robinson and of Stone. A quasi-Boussinesq model without rotation
is described in Chapter 3. This allows an estimation of the nature
of the Boussinesq approximation for a deep atmosphere. In Chapter 4
a Boussinesq model with rotation and axi-symmetric heating is de-
scribed. A quasi-Boussinesq model with rotation and symmetric heating
is presented in Chapter 5. With this model the effects of varying
the value of the horizontal and vertical coefficients of eddy viscosity
and diffusivity, and of the solar optical depth, are tested. The
properties of a simple model of radiative equilibrium in a grey atmo-
sphere are also presented here. Both Chapters 2 and 5 contain some
discussion of conservative finite-difference convective models. A
summary and discussion of the results, and a proposal for future work
is given in Chapter 6. Appendix A contains a description of a simple
three-dimensional, quasi-Boussinesq model, and Appendix B a detailed
discussion of the truncation errors in the method of stretched

coordinates and a comparison of the results in a test case using both

the method proposed here and *that of* Sundquist and Veronis (1970).

CHAPTER 2

Non-rotating Boussinesq Model of the Atmosphere of Venus

2.1 Introduction

In this chapter we describe a non-rotating Boussinesq model
of the atmosphere of Venus which is similar to the analytical models
of Goody and Robinson and of Stone. The main difference is that we
have used the full spherical equations, and that the numerical model
gives a complete solution both at the boundaries and in the interior.

We consider that the point of maximum insolation (subsolar
point) is fixed so that both the rotation of Venus and its revolution
around the Sun are neglected. In this way there is symmetry about
the subsolar-antisolar axis, and no zonal motion arises.

The results obtained with this model, as well as those ob-
tained by Goody and Robinson, by Stone and by Hess, are interesting
from a theoretical point of view but cannot be applied directly to
the visible circulation of the atmosphere of Venus, which is undoubtedly
greatly influenced by rotation. The observations of high zonal vel-
ocities (Smith, 1967) as well as the zonal symmetry in the temperature
field shown by measurements at the cloud top level (Murray, Wildey
and Westphal, 1963) suggest that the rotation of the planet, however
small, plays a very significant role. Furthermore, the large thermal
inertia of the deep atmosphere would not allow a deep circulation to
follow the Sun.

We make use in this model of the Boussinesq approximation
in which variations of density are neglected except when they produce
buoyancy forces. Ogura and Phillips (1962) show that this approxi-
mation is justified if the dynamic processes are confined to a depth

smaller than the scale height RT/g. Since the height of the clouds in the Venus atmosphere is several scale heights, the use of the Boussinesq approximation is not really justified. On the other hand, it may give some insight into the balance of forces, and since it has been used by several authors, we present the results obtained with it in order to compare them in the next chapter with those obtained with the more realistic quasi-Boussinesq approximation.

One must be aware that in the Boussinesq approximation, the temperature T and the potential temperature θ are related by the equation

$$T = \theta - \Gamma z \tag{2.1.1}$$

and therefore that there is no dynamical difference between them except in the heat flux boundary condition. This is the only place where it makes a difference whether we assume that the heat transfer is brought about by turbulent diffusion, which tends to equalize potential temperature, or by radiation with the opaque approximation, which tends to equalize temperatures. In this respect the model presented here is more comparable to Stone's than to Goody and Robinson's model because the heat transfer is parameterized as a turbulent diffusion process, even at the boundaries.

In the numerical model we have used density (which can be interpreted as potential density) instead of temperature. They are related by

$$\delta\rho/\rho_0 = -\delta T/T_0 \tag{2.1.2}$$

T_o was taken as 230°, i.e., the mean temperature at the cloud top level, where the driving of the atmospheric model takes place. P_o however was interpreted as the mean density of the atmosphere, so that the large inertial mass of the atmosphere of Venus is represented by a relatively large value of P_o .

The characteristics and boundary conditions of the model are described in sections 2.2 and 2.3. To be able to resolve the boundary layers using a reasonably small number of grid points we used "stretched coordinates", which are described in section 2.4. In section 2.5 we discuss a conservative finite difference scheme that can be used with non-regular grids. The finite difference equations that were actually used are given in 2.6 and the computational procedure in 2.7. The numerical values that were used in the model are given in section 2.8, and the results are described and discussed in 2.9.

2.2 Basic description of the model

A numerical model of the atmosphere of Venus was developed for spherical coordinates with the following approximations:

(a) Boussinesq.

(b) Hydrostatic. This is based on the small aspect ratio H/a where H is the height of the cloud layer top (60 km) and a is the radius of Venus (6060 km). It is only in the mixing region that this approximation may not be very accurate.

(c) No rotation.

(d) The subsolar point remains fixed.

(e) The atmosphere is very opaque so that short and long wave radiation is absorbed and emitted only at the top of the cloud

layer. The heat flux is parameterized as a turbulent diffusion process.

(f) Constant horizontal and vertical coefficients of eddy viscosity and diffusivity. Unit Prandtl number.

The Boussinesq equations in spherical coordinates are:

$$\frac{\partial v}{\partial t} = - \frac{(v^2 \sin \alpha)_\alpha}{a \sin \alpha} - (v w)_z - \frac{p'_\alpha}{\rho_o}$$

$$+ \frac{\nu_H}{a^2} \left[\frac{(v_\alpha \sin \alpha)_\alpha}{\sin \alpha} - \frac{v}{\sin^2 \alpha} - 2 w_\alpha \right] + \nu_v \, v_{zz} , \qquad (2.2.1)$$

the meridional component of the equation of motion,

$$0 = - \frac{p'_z}{\rho_o} - \tilde{\rho} g \qquad (2.2.2)$$

the hydrostatic equation,

$$0 = - \frac{(v \sin \alpha)_\alpha}{a \sin \alpha} - w_z \qquad (2.2.3)$$

the continuity equation, and

$$\frac{\partial \tilde{\rho}}{\partial t} = - \frac{(\tilde{\rho} v \sin \alpha)_\alpha}{a \sin \alpha} - (\tilde{\rho} w)_z + \frac{K_H}{a^2} \frac{(\tilde{\rho}_\alpha \sin \alpha)_\alpha}{\sin \alpha} + K_v \, \tilde{\rho}_{zz} \qquad (2.2.4)$$

the thermal equation. In the above equations a is the radius of Venus, α is the colatitude measured from the antisolar point, ρ_o is the surface pressure, $\tilde{\rho}$ is the potential density departure divided by the mean density ρ_o , and ρ_o is given by $\rho_o/(g H)$, K_H and K_v are the horizontal and vertical coefficients of eddy diffusivity, and ν_H and ν_v are the corresponding coefficients of eddy viscosity. The other symbols have their usual meanings. (Note: the $2 w_\alpha$ component

of the horizontal viscosity term in the horizontal momentum equation should have been dropped because of the small aspect ratio H/a, but the term is so small that it made no difference.)

From (2.2.1) and (2.2.2) we can eliminate the pressure and obtain a forecast equation for υ_z . This equation contains nonlinear terms generated by the convergence of the meridians which can produce a weak numerical instability. It is preferable to work with the vortex strength which, for an inviscid, homogeneous fluid, is individually conserved over the whole sphere.

Consider a vortex tube (Figure 2.2.1). By Helmholtz' circulation theorem the vorticity times the cross section of the tube is constant if the fluid is homogeneous and inviscid. The cross section is given by $a\,\delta\alpha\,\delta z$ (we can neglect the variations of the radial distance due to the small aspect ratio). From the Boussinesq approximation the volume of the tube $\pi\,a^2\,\delta\alpha\,\delta z$ is constant, so that the cross section is inversely proportional to the sine of the colatitude. Therefore the vortex strength η is

$$\eta = \frac{\upsilon_z - \frac{w\alpha}{a}}{\sin\alpha} \approx \frac{\upsilon_z}{\sin\alpha} \tag{2.2.5}$$

because of the small aspect ratio, H/a.

From equations (2.2.1), (2.2.2), (2.2.3) and (2.2.5) we obtain

$$\frac{\partial\eta}{\partial t} = -\frac{(\upsilon\,\eta\,\sin\alpha)_\alpha}{a\,\sin\alpha} - (w\,\eta)_z + \frac{g}{a}\frac{\tilde{\rho}_\alpha}{\sin\alpha}$$

$$+ \frac{\nu_H}{a^2}\left[\frac{((\eta\,\sin\alpha)_\alpha\,\sin\alpha)_\alpha}{\sin^2\alpha} - \frac{\eta}{\sin^2\alpha} - \frac{2\,w_{\alpha z}}{\sin\alpha}\right] + \nu_v\,\eta_{zz} \tag{2.2.6}$$
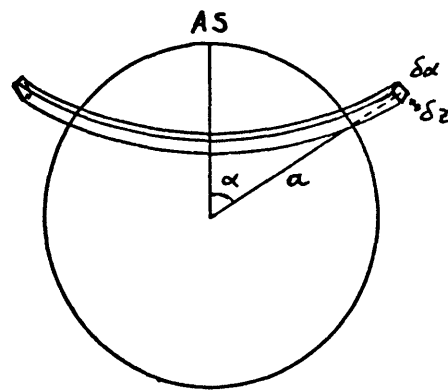
Figure 2.2.1: Vortex tube.

We define a mass stream function Ψ :

$$\eta \sin^2 \alpha = \Psi_{zz} + \frac{2}{a} \Psi_z + \frac{\Psi_{\alpha\alpha}}{a^2} + \frac{\cot\alpha}{a^2} \Psi_\alpha \approx \Psi_{zz} \qquad (2.2.7)$$

so that

$$v \sin \alpha = \Psi_z \qquad (2.2.8)$$

$$w \sin \alpha = - \frac{\Psi_\alpha}{a} \qquad (2.2.9)$$

Equations (2.2.4) and (2.2.6) to (2.2.9) are the ones used in the model. To complete the problem we need the boundary conditions.

2.3 Boundary conditions

We assume a no-stress rigid top at the cloud top level and a non-slip rigid bottom at the surface. From the geometry of the model the horizontal velocity is zero at the subsolar and antisolar points. We have then the following boundary conditions for the mass stream function:

$$\Psi = \Psi_{zz} = 0 \qquad \text{at} \quad z = H \qquad \text{(a)}$$

$$\Psi = \Psi_z = 0 \qquad \text{at} \quad z = 0 \qquad \text{(b)} \qquad (2.3.1)$$

$$\Psi = 0 \qquad \text{at} \quad \alpha = 0 \text{ and } \alpha = \pi \qquad \text{(c)}$$

We assume that all the absorption and emission of radiation takes place at the top. The short wave radiative flux is

$$\downarrow F_{sw} = \begin{cases} 0 & \text{if } 0 \le \alpha \le \frac{\pi}{2} \\ -(1-A) \, S_0 \, \cos\alpha & \text{if } \frac{\pi}{2} < \alpha \le \pi \end{cases}$$

where S_0 is the Venusian solar constant and A the planetary albedo taken as constant.

If we assume that the temperature departures from the mean value at the top are small, i.e., $\delta T/T_0 \ll 1$, we can approximate the long wave radiation as

$$\uparrow F_{LW} = \sigma T_0^4 \left(1 + 4 \, \delta T/T_0 \right)$$

where T_0 is the mean emission temperature at the top. From the overall balance between incoming shortwave and outgoing long wave radiation we have

$$\sigma T_0^4 = \frac{(1-A) \, S_0}{4}$$

At the fixed height of the cloud top we have

$$\frac{\delta P}{P_0} = \tilde{P} = -\frac{\delta T}{T_0}$$

so that the heat flux F is given by

$$F = K_v \, P_0 \, C_p \, T_z = - K_v \, P_0 \, C_p \, T_0 \, \tilde{P}_z$$

From the previous relationships we get as upper boundary condition for $\tilde{P}$:

$$\tilde{P}_z = \frac{\sigma T_0^3}{K_v C_p P_0} \left[(1 - 4\tilde{P}) + \begin{cases} 0 & \text{for } 0 \leq \alpha \leq \frac{\pi}{2} \\ 4\cos\alpha & \text{for } \frac{\pi}{2} < \alpha \leq \pi \end{cases} \right]$$

$$\text{at } z = H$$

(2.3.2a)

At the bottom we assume that the heat flux is negligible:

$$\tilde{P}_z = 0 \qquad\qquad \text{at } z = 0 \qquad\qquad (2.3.2b)$$

2.4 Stretched coordinates

From the previous studies by Stommel (1962), Goody and Robinson, and Stone, we expect the appearance of horizontal boundary layers at the top and possibly at the bottom of the atmosphere, and a vertical boundary layer at the antisolar point.

In these narrow regions we need a fine grid (at least two or three points within the boundary layers) to be able to resolve them but in the interior much less resolution is necessary. The solution of the problem with a regularly spaced grid that is fine enough to resolve the boundary layer was not possible because it would have consumed too much computer time. But if we use a coarse grid that doesn't resolve the boundary layers, for example as Hess (1968) did, large truncation errors will arise and we can expect that, even in the interior, the numerical solution will be quite different from the exact solution.

Barcilon and Veronis (1965) and Sommerville (1966) obtained numerical solutions for simple models of a fluid driven by differential heating at a horizontal boundary. They were obliged to weaken the

intensity of the driving until the boundary layers were wide enough

to be resolved by a regular grid with a reasonable number of points.

This procedure would not be satisfactory in our problem because it

would not correspond to realistic values of the parameters.

Another possibility is to use an irregular net with smaller

spacing in the boundary layer regions. Some computations have been

performed in which the grid size was divided by two in the region of

interest. This method however has two disadvantages: first, it is

necessary to interpolate values of the variables or their derivatives

at intermediate points, and weak numerical instabilities may arise in

the boundary between the small and large grids; second, this method

does not permit really small grid sizes without greatly increasing

the number of intermediate interpolations.

In our numerical model we have avoided these problems by

varying the gris size continuously. This is done by defining a func-

tion $\xi = g(x)$ which maps the physical space x into a "stretched"

space ξ , where we use a regularly spaced grid.

In Appendix B we show that this procedure, together with the

use of a finite difference equivalent of

$$\frac{\partial f}{\partial x} = \frac{d\xi}{dx} \frac{\partial f}{\partial \xi} \tag{2.4.1}$$

$$\frac{\partial^2 f}{\partial x^2} = \frac{d\xi}{dx} \frac{\partial}{\partial \xi} \left[\frac{d\xi}{dx} \frac{\partial f}{\partial \xi} \right] \tag{2.4.2}$$

gives the following approximations for the first and second derivatives

$$\frac{f_{i+1} - f_{i-1}}{2\Delta\xi \left(\frac{dx}{d\xi}\right)_i} = f'_i \left[1 + \frac{(\Delta\xi)^2}{6} \left(\frac{d^3x}{d\xi^3}\right)_i \Big/ \left(\frac{dx}{d\xi}\right)_i \right]$$

$$+ f''_i \frac{(\Delta\xi)^2}{2} \left[\left(\frac{d^2x}{d\xi^2}\right)_i + \frac{(\Delta\xi)^2}{6} \left\langle \frac{1}{4}\left(\frac{d^4x}{d\xi^4}\right)_i + \left(\frac{d^3x}{d\xi^3}\right)_i \Big/ \left(\frac{dx}{d\xi}\right)_i \right\rangle \right]$$

$$+ f'''_i \frac{(\Delta\xi)^2}{6} \left[\left(\frac{dx}{d\xi}\right)_i + \frac{(\Delta\xi)^2}{2} \left\langle \left(\frac{d^3x}{d\xi^3}\right)_i \left(\frac{dx}{d\xi}\right)_i + \frac{3}{2}\left(\frac{d^2x}{d\xi^2}\right)\right\rangle \right]$$

$$+ O\left(\Delta\xi\right)^3 \tag{2.4.3}$$

and similarly

$$\frac{\dfrac{f_{i+1} - f_i}{\left(\frac{dx}{d\xi}\right)_{i+\frac{1}{2}}} - \dfrac{f_i - f_{i-1}}{\left(\frac{dx}{d\xi}\right)_{i-\frac{1}{2}}}}{(\Delta\xi)^2 \left(\frac{dx}{d\xi}\right)_i} = f''_i \left[1 + \frac{5}{24}(\Delta\xi)^2 \left(\frac{d^3x}{d\xi^3}\right)_i \Big/ \left(\frac{dx}{d\xi}\right)_i \right]$$

$$+ f'''_i \frac{(\Delta\xi)^2}{3} \left[\left(\frac{d^2x}{d\xi^2}\right)_i + \frac{(\Delta\xi)^2}{12} \left\langle \left(\frac{d^4x}{d\xi^4}\right)_i + \frac{5}{2}\left(\frac{d^3x}{d\xi^3}\right)_i \Big/ \left(\frac{dx}{d\xi}\right)_i \right\rangle \right]$$

$$+ f^{IV}_i \frac{(\Delta\xi)^2}{12} \left[\left(\frac{dx}{d\xi}\right)_i + \frac{(\Delta\xi)^2}{4} \left\langle \left(\frac{13}{6}\right)\left(\frac{d^3x}{d\xi^3}\right)_i \left(\frac{dx}{d\xi}\right)_i + 3\left(\frac{d^2x}{d\xi^2}\right)^2 \right\rangle \right]$$

$$+ O\left(\Delta\xi\right)^3 \tag{2.4.4}$$

Therefore the truncation errors due to the non-uniformity

of the grid sizes are of second order with respect to the stretched

variable ξ . Furthermore we show that the choice

$$x = \xi^2 \tag{2.4.5}$$

for a problem with a boundary layer at x = 0 has three distinct

advantages:

(a) The extra truncation error introduced by the use of

a non-uniform grid is independent of x (except for the variations of

f itself).

(b) The density of points near x = 0 grows with the square

of the total number of grid points.

(c) The resolution at the worst point is equal to one half

of the resolution obtained with a regular grid if the same number of

points is used.

In our model we expect a vertical boundary layer in the re-

gion of the antisolar point, i.e., where the colatitude α is zero.

We therefore define a new horizontal "stretched" coordinate (Figure

2.4.1):

$$y = \sqrt{\alpha} \quad ; \quad \frac{dy}{d\alpha} = \frac{1}{2y} \tag{2.4.6}$$

In the vertical we expect boundary layers at the top, where

the driving takes place, and probably at the bottom also, due to the

presence of the solid surface. We must choose a coordinate which

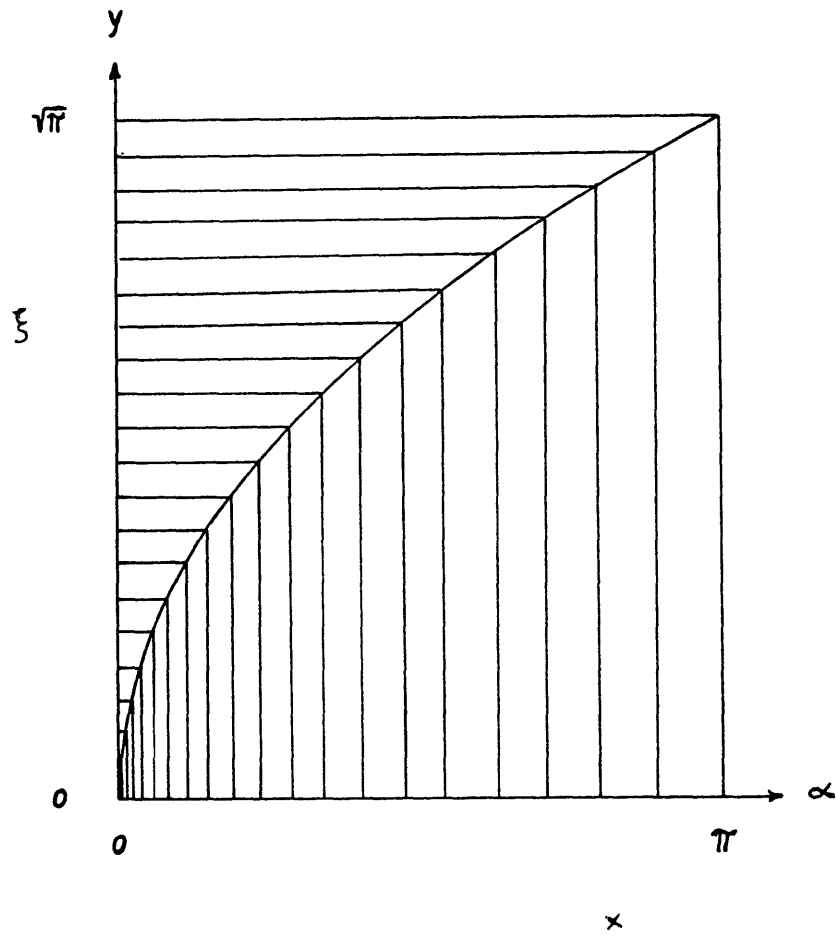is stretched at the top and bottom and quasi-linear in the interior.

Figure 2.4.1: Distribution of grid points in the horizontal direction obtained through the use of the stretched coordinate $y = \sqrt{\alpha}$.

In particular, we take a coordinate whose derivative is proportional

to $\dfrac{1}{\sqrt{z\,(H-z)}}$, i.e., (Figure 2.4.2)

$$\lambda = \frac{2}{\pi}\ \text{arc}\ \tan\sqrt{\frac{z}{H-z}}\quad ; \quad \frac{d\lambda}{dz} = \frac{1}{HS} \qquad (2.4.7)$$

where $S = \pi\sqrt{\tfrac{z}{H}\left(1-\tfrac{z}{H}\right)}$.

This coordinate seems to be very well suited to numerical

problems with boundary layers at both boundaries of a region, as in

the Rayleigh problem, the turbulent flow in a channel, etc.

It should be noted that when stretched variables are intro-

duced, the geometric factor $\dfrac{d\xi}{dx}$ needs to be computed at each grid

point only once, so that very little extra computer time is involved.

When the computational stability criteria are applied, the smallest

grid size in physical space has to be used in general.

In this model we used 20 grid intervals in both the hori-

zontal and vertical directions, i.e.,

$$\Delta\eta = \frac{\sqrt{\pi}}{20}\quad ; \quad \Delta\lambda = \frac{1}{20}$$

Even with this sparse grid the first interior point was at

only 47 km from the antisolar point and 340 m from top and bottom.

The equations corresponding to (2.2.4) and (2.2.6) to (2.2.9)

in the new coordinates are:

$$\frac{\partial\tilde{P}}{\partial t} = -\frac{(\tilde{P}\sigma\sin\alpha)_y}{2a\eta\sin\alpha} - \frac{(w\tilde{P})_\lambda}{HS} + \frac{K_H}{a^2}\ \frac{\left(\tilde{P}_y\ \frac{\sin\alpha}{\eta}\right)_y}{4\eta\sin\alpha} + \frac{K_v}{H^2}\ \frac{\left(\tilde{P}_\lambda\ \frac{1}{S}\right)_\lambda}{S}\ ,$$
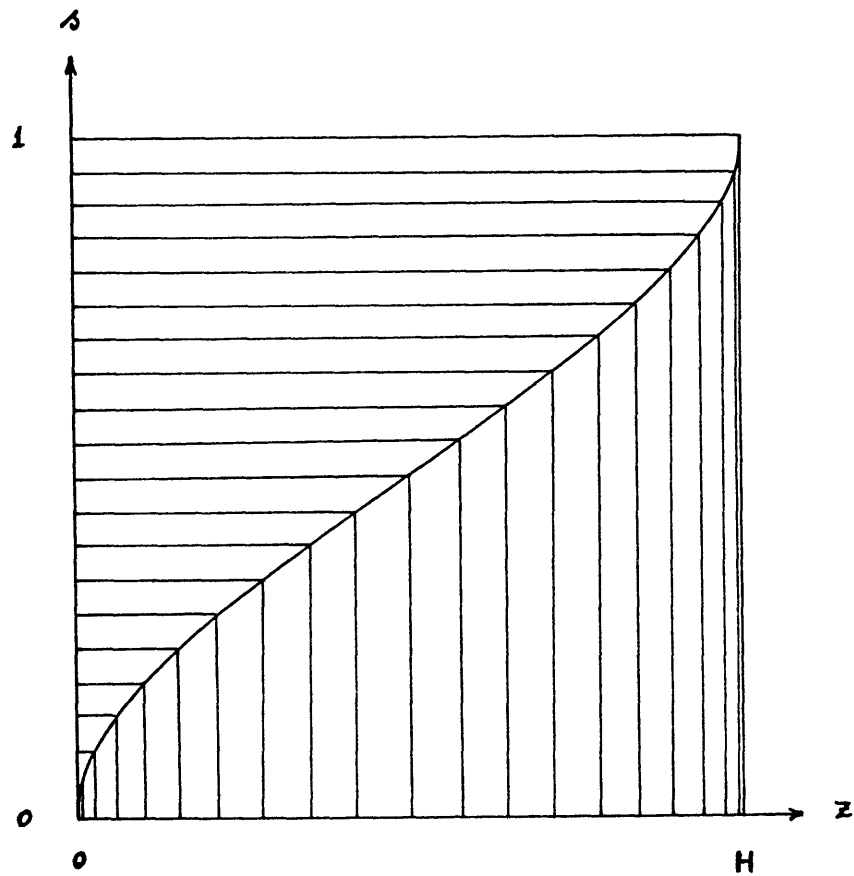
$$(2.4.8)$$

Figure 2.4.2: Distribution of grid points in the vertical direction obtained through the use of the stretched coordinate $s = \dfrac{2}{\pi} \, arc \, tan \sqrt{\dfrac{z}{H-z}}$

$$\frac{\partial \eta}{\partial t} = -\frac{(\eta v \sin \alpha)_y}{2 a y \sin \alpha} - \frac{(w \eta)_s}{H S} + \frac{g}{2 a y \sin \alpha}\tilde{P}_y$$

$$+ \frac{\nu_H}{a^2}\left[\frac{((\eta \sin \alpha)_y \frac{\sin \alpha}{y})_y}{4 y \sin \alpha} - \frac{\eta}{\sin^2 \alpha} - \frac{w_{ys}}{H S y \sin \alpha}\right] + \frac{\nu_v}{H^2}\frac{1}{S}\left(\frac{\eta_s}{S}\right)_s \qquad (2.4.9)$$

$$\frac{1}{H^2 S}\left(\frac{\Psi_s}{S}\right)_s = \eta \sin^2 \alpha \qquad (2.4.10)$$

$$v = \frac{\Psi_s}{H S \sin \alpha} \qquad (2.4.11)$$

$$w = -\frac{\Psi_y}{2 a y \sin \alpha} \qquad (2.4.12)$$

The boundary conditions corresponding to (2.3.1) and (2.3.2) are

$$\Psi = 0 \qquad \text{at} \quad s = 1 \qquad \text{(a)}$$

$$\Psi = 0 \qquad \text{at} \quad s = 0 \qquad \text{(b)}$$

$$\Psi = 0 \qquad \text{at} \quad y = 0, \sqrt{\pi} \qquad \text{(c)} \qquad\qquad (2.4.13)$$

$$\left(\frac{\Psi_s}{S}\right)_s = 0 \qquad \text{at} \quad s = 1 \qquad \text{(d)}$$

$$\Psi_s = 0 \qquad \text{at} \quad s = 0 \qquad \text{(e)}$$

$$P_\lambda = \frac{\sigma T_o^3 H S}{K_v} \left[(1 - 4\tilde{P}) + \begin{cases} 0 & \text{if } 0 \le y < \sqrt{\pi/2} \\ 4\cos\alpha & \text{if } \sqrt{\pi/2} \le y \le \sqrt{\pi} \end{cases} \right] \quad \text{at } \lambda = 1$$

(2.4.14a)

$$P_\lambda = 0 \qquad \text{at } \lambda = 0$$

(2.4.14b)

2.5 Conservative finite-difference formulation of the non-linear terms of the hydrodynamic equations in a nonregular grid

Lilly (1965) and Bryan (1966) have proposed a finite-difference scheme for the advective terms which can be used with nonregular grids and which conserves the average value and the mean square value of the quantity being advected (except for time truncation errors). As was shown by Arakawa (1966), the conservation of these integral properties eliminates non-linear instability.

Bryan's scheme is as follows. Consider the equation

$$\frac{\partial \alpha}{\partial t} = - \mathbf{v} \cdot \nabla \alpha$$

(2.5.1)

If the continuity equation is

$$\nabla \cdot \mathbf{v} = 0$$

(2.5.2)

then (2.5.1) can be written in a "flux" form:

$$\frac{\partial \alpha}{\partial t} = -\nabla \cdot (\alpha \, \vec{v}) \qquad (2.5.3)$$

The finite differences scheme corresponding to (2.5.2) and (2.5.3) are

$$\sum_{k=1}^{K_j} V_{kj} \, A_{kj} = 0 \qquad (2.5.4)$$

$$r_j \, \frac{\partial \alpha_j}{\partial t} = -\sum_{k=1}^{K_j} V_{kj} \, A_{kj} \, \frac{(\alpha_j + \alpha_k)}{2} \qquad (2.5.5)$$

where the volume R is divided in J subvolumes r_j each of which is bounded by K_j plane interfaces of area A_{kj} and average normal velocity V_{kj}, α_j is the average value of α in the subvolume r_j and α_k the average of α in the adjacent subvolume r_k.

If the normal velocities vanish on the boundaries of R the following finite-difference integrals are conserved except for truncation errors in time:

$$I_1 = \sum_{j=1}^{J} \alpha_j \, r_j \qquad (2.5.6)$$

$$I_2 = \sum_{j=1}^{J} \alpha_j^2 \, r_j \qquad (2.5.7)$$

The following remarks may be made about Bryan's algorithm:

(a) It can be used in any quasi-incompressible model, i.e., whenever the continuity equation doesn't contain time derivatives.

For example, in the quasi-Boussinesq approximation, the continuity equation is

$$\nabla \cdot (\rho_a \, v) = 0,$$

(2.5.8)

where $\rho_a = \rho_a(z)$.

Then the equations corresponding to (2.5.3) to (2.5.7) are

$$\rho_a \, \frac{\partial \alpha}{\partial t} = - \, \nabla \cdot (\rho_a \, \alpha \, v)$$

(2.5.9)

$$\sum_{k=1}^{K_j} V_{kj} \, \rho_{a_{kj}} \, A_{kj} = 0$$

(2.5.10)

$$\rho_{a_j} \, \Gamma_j \, \frac{\partial \alpha_j}{\partial t} = - \sum_{k=1}^{K_j} V_{kj} \, A_{kj} \, \rho_{kj} \, \frac{(\alpha_j + \alpha_k)}{2}$$

(2.5.11)

$$I_1 = \sum_{j=1}^{J} \Gamma_j \, \rho_{a_j} \, \alpha_j$$

(2.5.12)

$$I_2 = \sum_{j=1}^{J} \Gamma_j \, \rho_{a_j} \, \alpha_j^2$$

(2.5.13)

where $\rho_{a_{kj}}$ is the average of ρ_a on the interface A_{kj} , and I_1, I_2 are conserved except for time truncation errors.

(b) The staggered scheme can be simplified to

$$\Gamma_j \, \frac{\partial \alpha_j}{\partial t} = - \sum_{k=1}^{K_j} V_{kj} \, A_{kj} \, \frac{\alpha_k}{2}$$

(2.5.14)

since the term $\Gamma_j \, \frac{\alpha_j}{2} \sum_{k=1}^{K_j} V_{kj} \, A_{kj}$ that has been dropped is identically

zero by (2.5.4). This simpler scheme will have the same conservation properties as (2.5.5) with some saving of computer time.

Another scheme which by (2.5.4) will also give the same results as Bryan's scheme is

$$\Gamma_j \frac{\partial \alpha_j}{\partial t} = - \sum_{k=1}^{K_j} \frac{1}{2} [V_{kj} A_{kj} (\alpha_k - \alpha_j)] \qquad (2.5.15)$$

This shows that Bryan's "flux scheme" is really equivalent to an average of the finite-difference advection at the boundaries. In this way, when there is a flow towards a region with strong gradient of α we expect large truncation errors in the finite difference approximation of the advective terms.

These two schemes were found independently by Piacsek and Williams (1970). They point out that in the numerical models which use the primitive momentum equations the divergence is not strictly zero due to limited accuracy in the solution of the associated Poisson equation for the pressure. Even in this case, the simplified scheme (2.5.14) will conserve the integral I_2 (but not I_1) preventing nonlinear instability.

(c) The method can be generalized to the compressible case:

$$\frac{\partial \rho}{\partial t} = - \nabla \cdot (\rho v) \qquad (2.5.16)$$

$$\frac{\partial \rho \alpha}{\partial t} = - \nabla \cdot (\rho \alpha v) \qquad (2.5.17)$$

Then the finite-difference scheme

$$\Gamma_j \left(\frac{\partial \rho}{\partial t}\right)_j = - \sum_{k=1}^{K_j} V_{kj}\, A_{kj}\, \frac{\rho_j + \rho_k}{2} \qquad (2.5.18)$$

$$\Gamma_j \left(\frac{\partial \rho \alpha}{\partial t}\right)_j = - \sum_{k=1}^{K_j} V_{kj}\, A_{kj}\, \left(\frac{\rho_j + \rho_k}{2}\right)\left(\frac{\alpha_j + \alpha_k}{2}\right) \qquad (2.5.19)$$

will conserve the quantities

$$M = \sum_{j=1}^{J} \Gamma_j\, \rho_j \qquad (2.5.20)$$

$$I_1 = \sum_{j=1}^{J} \Gamma_j\, \rho_j\, \alpha_j \qquad (2.5.21)$$

$$I_2 = \sum_{j=1}^{J} \Gamma_j\, \rho_j\, \alpha_j^2 \qquad (2.5.22)$$

except for time truncation errors.

In this case the simplification corresponding to (2.5.14) cannot be made. This scheme is similar to the one used by Lilly (1965) for the shallow water equations.

2.6 Finite-difference equations

We use a staggered mesh so that in each grid rectangle the variables with the same subindex (i,j) are placed as in Figure 2.6.1. This placement has several advantages: it allows the use of conservative finite-differences for the density $\tilde{\rho}$, decreases the truncation error, effectively dividing by two the distance over which many

of the derivatives are computed, and finally it is the placement of variables which allows the simplest computation of the boundary conditions.

The complete grid is shown in Figure 2.6.2. The left and right vertical boundaries correspond to the antisolar and subsolar points respectively. The lower and upper horizontal boundaries correspond to the surface of the planet and top of the cloud level respectively.

Whenever it was necessary to fulfil a boundary condition on the normal derivative of a function, an extra value was placed at half a mesh length outside the boundaries.

The corresponding grid in the physical coordinates α and Z is shown in Figure 2.6.3, corresponding to IM = 20, JM = 20.

I used the simplest spatially-centered finite-difference scheme for the nonlinear terms written in a flux form, which conserved the mean density, the mean squared density and the mean vorticity, but not the mean squared vorticity (see section 2.5). The lack of conservation of the mean-squared vorticity was accompanied by a nonlinear numerical instability that ruined the computations after 7.5×10^5 secs. This instability was overcome when the horizontal coefficient of eddy viscosity was increased from $\nu_H = 10^{10} cm^2/sec$ to the perhaps unrealistically large value $\nu_H = 10^{11} cm^2/sec$.

The "leap-frog" method (centered differences in time) was used except that the viscosity and conductivity terms were evaluated at the time $t-\Delta t$, so that, with respect to these terms, the time differencing was forward. In this way one avoids the unconditional instability which occurs when centered time differences are used with
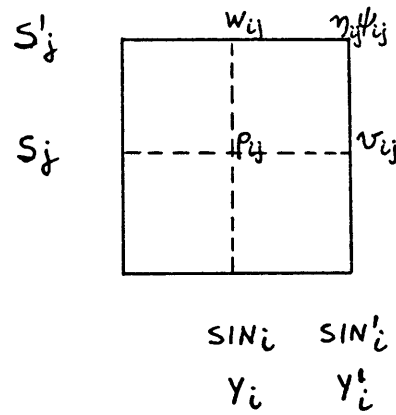
Figure 2.6.1: Typical cell with the placement of the variables and functions with the same subindices i,j. $SIN_i = \sin(\alpha_i)$.
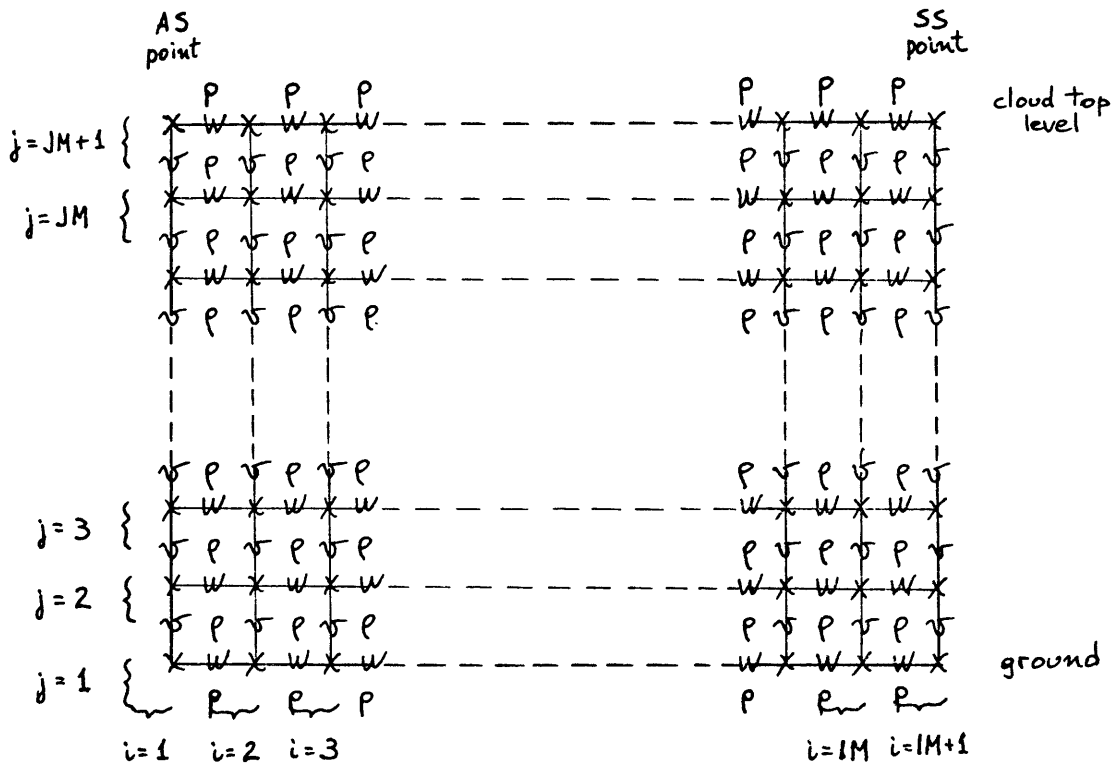
Figure 2.6.2: Complete grid as it appears in the stretched coordinates y,s. There are IM intervals in the horizontal direction and JM intervals in the vertical direction. ψ and η are defined at the x points.

Figure 2.6.3: Position of the grid points in the physical coordinates. Here, as in the following diagrams, the abscissa represents the colatitude α (degrees) and the ordinate height z (km).

diffusion. The leap-frog method is the most accurate of the second order time methods (Orszag, 1970), but it has the disadvantage that a numerical instability arises because the solutions at even and odd time steps tend to uncouple. This problem was easily avoided by averaging two successive solutions after forecasting 20 double time steps.
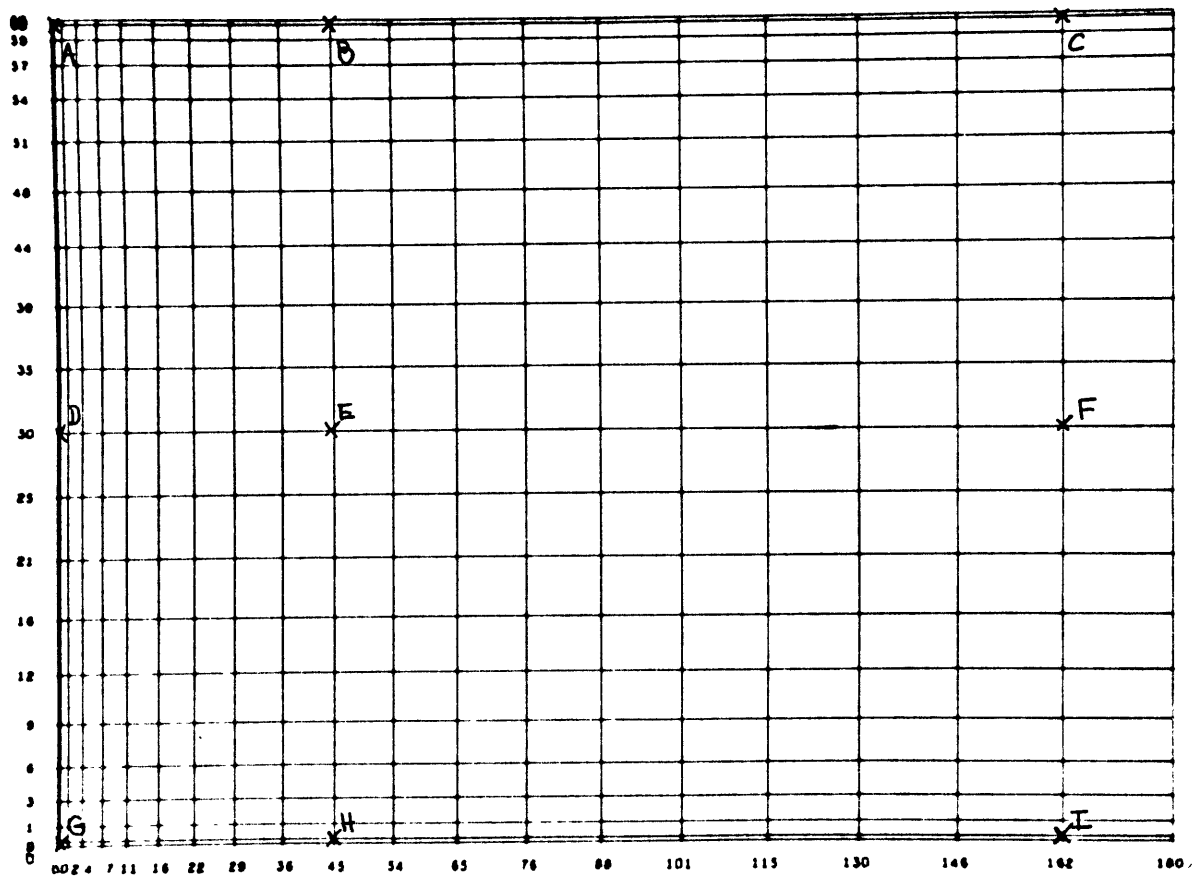
In the following finite-difference equations which were used in the model, the superindex n indicates the value of a variable at time $t = m \Delta t$; when it is omitted it is assumed to be n. (See Figure (2.6.1) for the position in a grid cell of the variables with subindices (i,j) and for the definition of SIN_i .)

$$
\tilde{\rho}_{ij}^{m+1} = \tilde{\rho}_{ij}^{m-1} + 2\Delta t \left\{ - \frac{v_{ij}(\tilde{\rho}_{ij} + \tilde{\rho}_{i+1j}) SIN_i' - v_{i-1j}(\tilde{\rho}_{ij} + \tilde{\rho}_{i-1j}) SIN_{i-1}'}{4 \Delta \eta \, a \, Y_i \, SIN_i} \right.
$$

$$
- \frac{w_{ij}(\tilde{\rho}_{ij} + \tilde{\rho}_{ij+1}) - w_{ij-1}(\tilde{\rho}_{ij} + \tilde{\rho}_{ij-1})}{2 \Delta H \, S_j}
$$

$$
+ \frac{K_H}{a^2} \left[\frac{(\tilde{\rho}_{i+1j}^{m-1} - \tilde{\rho}_{ij}^{m-1}) SIN_i'/Y_i' - (\tilde{\rho}_{ij}^{m-1} - \tilde{\rho}_{i-1j}^{m-1}) SIN_{i-1}'/Y_{i-1}'}{4 \Delta y^2 \, Y_i \, SIN_i} \right]
$$

$$
+ \frac{K_v}{H^2} \frac{1}{\Delta_h^2 S_j} \left[\frac{\tilde{\rho}_{ij+1}^{m-1} - \tilde{\rho}_{ij}^{m-1}}{S_j'} - \frac{\tilde{\rho}_{ij}^{m-1} - \tilde{\rho}_{ij-1}^{m-1}}{S_{j-1}'} \right] \right\}
$$

where

$i = 2, \ldots, IM+1$

$j = 2, \ldots, JM+1$

(2.6.1)

$$\eta_{ij}^{n+1} = \eta_{ij}^{n-1} + 2\Delta t \left\{ - \frac{(v_{i+1j} + v_{i+1j+1})\eta_{i+1j}\,SIN'_{i+1} - (v_{i-1j} + v_{i-1j+1})\eta_{i-1j}\,SIN'_{i-1}}{8\Delta\eta\,a\,Y'_i\,SIN'_i} \right.$$

$$- \frac{(w_{ij+1} + w_{i+1j+1})\eta_{ij+1} - (w_{ij-1} + w_{i+1j-1})\eta_{ij-1}}{4\Delta s\,H\,S'_j} + g\,\frac{\tilde{P}_{i+1j} + \tilde{P}_{i+1j+1} - \tilde{P}_{ij} - \tilde{P}_{ij-1}}{4\Delta y\,a\,Y'_i\,SIN'_i}$$

$$+ \frac{\nu_H}{a^2}\left[\frac{(\eta_{i+1j}^{n-1}\,SIN'_{i+1} - \eta_{ij}^{n-1}\,SIN'_i)\,SIN_{i+1}/Y_{i+1} - (\eta_{ij}^{n-1}\,SIN'_i - \eta_{i-1j}^{n-1}\,SIN'_{i-1})\,SIN_i/Y_i}{4\Delta y^2\,Y'_i\,SIN'^2_i} \right.$$

$$\left. - \frac{\eta_{ij}^{n-1}}{SIN'^2_i} - \frac{w_{i+1j+1}^{n-1} - w_{ij+1}^{n-1} - w_{i+1j-1}^{n-1} + w_{ij-1}^{n-1}}{2\Delta s\,H\,\Delta y\,Y'_i\,SIN'_i\,S'_j} \right.$$

$$\left. + \frac{\nu_v}{H^2}\,\frac{1}{\Delta s^2 S'_j}\left[\frac{\eta_{ij+1}^{n-1} - \eta_{ij}^{n-1}}{S_{j+1}} - \frac{\eta_{ij}^{n-1} - \eta_{ij-1}^{n-1}}{S_j} \right] \right\}$$

where $\quad i = 2, \cdots, IM$
$\qquad\quad j = 2, \cdots, JM$ $\hspace{4cm}$ (2.6.2)

$$\frac{\psi_{ij+1}^{n+1} - \psi_{ij}^{n+1}}{S_{j+1}} - \frac{\psi_{ij}^{n+1} - \psi_{ij-1}^{n+1}}{S_j} = \eta_{ij}^{n+1}\,SIN'^2_i\,S'_j\,\Delta s^2\,H^2 \hspace{2cm} (2.6.3)$$

where $i = 2, \cdots, IM;\ j = 2, \cdots, JM$

$$v_{ij}^{n+1} = \frac{\psi_{ij}^{n+1} - \psi_{ij-1}^{n+1}}{\Delta s\,H\,S_j\,SIN'_i} \qquad \text{where}\ i = 2, \cdots, IM;\ j = 2, \cdots, JM+1 \hspace{1.5cm} (2.6.4)$$

$$w_{ij}^{n+1} = \frac{\psi_{ij}^{n+1} - \psi_{i-1j}^{n+1}}{2\Delta y\,a\,Y_i\,SIN_i} \qquad \text{where}\ i = 2, \cdots, IM+1;\ j = 2, \cdots, JM \hspace{1.5cm} (2.6.5)$$

Due to the hydrostatic approximation the equations (2.6.3) are un-coupled in i (the index corresponding to the colatitude α).

Equation (2.6.3) can be written as the matrix equation

$$Q \ \Psi = M \ H$$

where the elements of Q do not depend on i (colatitude) or on n (time); Ψ has the elements ψ_{ij} and H has the elements η_{ij} . Q needs to be inverted only once. This was done in the model using a Guassian elimination method. Equation (2.6.3) was thus replaced by

$$\Psi^{m+1} = Q^{-1} M \ H^{m+1} \tag{2.6.6}$$

which permits a rapid and accurate evaluation of the mass stream function at the new time $t = (m+1)\Delta t$ from the predicted values of the vorticity.

The boundary conditions in finite-differences are

$$\psi_{i1}^{m+1} = \psi_{i\,JM+1}^{m+1} = 0 \qquad \text{for} \quad i = 2,\ldots, IM \tag{2.6.7a}$$

$$\psi_{1j}^{m+1} = \psi_{IM+1\,j}^{m+1} = 0 \qquad \text{for} \quad j = 2,\ldots, JM \tag{2.6.7b}$$

$$\eta_{1j}^{m+1} = \eta_{IM+1\,j}^{m+1} = 0 \qquad \text{for} \quad j = 2,\ldots, JM \tag{2.6.7c}$$

$$\eta_{i\,JM+1}^{m+1} = 0 \qquad \text{for} \quad i = 2,\ldots, IM$$

$$\tilde{\rho}_{i1}^{m+1} = \tilde{\rho}_{i2}^{m+1} \qquad \text{for} \quad i = 2,\ldots, IM+1 \tag{2.6.7d}$$

$$\tilde{\rho}_{i\,JM+2}^{m+1} = \left(\frac{1-2m}{1+2m}\right) + \frac{m}{1+2m}\left(1 + 4 C_i\right) \qquad \text{for} \quad i = 2,\ldots, JM+1 \tag{2.6.7e}$$

$$\text{where} \quad m = \frac{\sigma T_0^3 \, \Delta_4 H \, S'_{JM+1}}{K_v \, C_p \, P_0}$$

$$C_i = \begin{cases} 0 & \text{if} \quad 0 \leq \alpha_i \leq \pi/2 \\ \cos(\alpha_i) & \text{if} \quad \pi/2 < \alpha_i \leq \pi \end{cases}$$

The non-slip boundary condition at the bottom was imposed by the following procedure, which is similar to the one used by Pearson (1965) and by Williams (1967). We express ψ at the first two interior points using a Taylor expansion about the lower boundary

$$\psi_{i2} = \psi_{i1} + \left(\frac{\partial \psi}{\partial z}\right)_{i1} z_1 + \left(\frac{\partial^2 \psi}{\partial z^2}\right)_{i1} \frac{z_1^2}{2} + \left(\frac{\partial^3 \psi}{\partial z^3}\right)_{i1} \frac{z_1^3}{6} + O(\Delta z)^4$$

$$\psi_{i3} = \psi_{i1} + \left(\frac{\partial \psi}{\partial z}\right)_{i1} z_2 + \left(\frac{\partial^2 \psi}{\partial z^2}\right)_{i1} \frac{z_2^2}{2} + \left(\frac{\partial^3 \psi}{\partial z^3}\right)_{i1} \frac{z_2^3}{6} + O(\Delta z)^4$$

But at the lower boundary ψ_{i1} and $\partial \psi_{i1}/\partial z = 0$. We next eliminate $\left(\frac{\partial^3 \psi}{\partial z^3}\right)_{i1}$ from these equations and obtain

$$\left(\frac{\partial^2 \psi}{\partial z^2}\right)_{i1} = \frac{2 z_2}{z_1^2 (z_2 - z_1)} \psi_{i2} - \frac{2 z_1}{z_2^2 (z_2 - z_1)} \psi_{i3} + O(\Delta z^2)$$

Then from (2.2.7) the boundary condition for η at the bottom of the atmosphere becomes

$$\eta_{i1}^{n+1} = \left[\frac{2 z_2}{z_1^2(z_2 - z_1)} \psi_{i2}^{n+1} - \frac{2 z_1}{z_2^2(z_2 - z_1)} \psi_{i3}^{n+1}\right] \frac{1}{SIN_i'^2} \qquad (2.6.7f)$$

$$\text{for } i = 2, \ldots, IM$$

2.7 Initial conditions and computational procedure

The initial condition is taken as a state of no motion (v = w = 0) and constant potential density ($\tilde{\rho} = 0$).

After that at each time step the field values are advanced as follows:

(a) The new interior values of the vorticity and density

fields corresponding to time $t = (m+1)\Delta t$ are obtained using for-mulas (2.6.1) and (2.6.2).

(b) The new stream function is obtained from the vorticity field by (2.6.6).

(c) The new boundary values of the vorticity and density fields are deduced from (2.6.7).

(d) The new velocity fields are obtained from the stream function field from (2.6.5) and (2.6.5).

The diffusivity computational stability criterion

$$\Delta t \leq \frac{1}{4} \left\{ \frac{1}{\frac{\nu_H}{a^2 \Delta\lambda^2}_{min} + \frac{\nu_v}{\Delta z^2}_{min}} \right\}$$

imposes the rather small value of 200 sec for the time step, because of the large value of the horizontal coefficient of eddy viscosity and the small spacing at the boundaries.

The differential heating by the sun was allowed to build up a circulation for 133×10^5 secs (about 154 earth days).

2.8 Numerical values of the physical parameters

The numerical values that follow are those used by Goody and Robinson (1966) with the following exceptions: H was taken as 60 km instead of 40 km as being closer to the actual height of the top of the clouds, the surface pressure was taken into account to obtain the value of ρ_o , and the horizontal coefficients of eddy viscosity and conductivity were taken as $10^{11} cm^2/sec$ instead of $10^{10} cm^2/sec$ to prevent a numerical instability which developed at the antisolar point for smaller values. We have

$$a = 6.06 \times 10^{8} \, cm$$

$$H = 6 \times 10^{6} \, cm$$

$$g = 870 \, cm^{2}/sec$$

$$C_{p} = 1.01 \times 10^{7} \, cm^{2}/(sec^{2} \, {}^{\circ}K)$$

$$P_{o} = 100 \, atm$$

$$T_{o} = 230 \, {}^{\circ}K$$

$$\rho_{o} = \frac{P_{o}}{gH} = 1.94 \times 10^{-2} \, g/cm^{3}$$

$$K_{H} = \nu_{H} = 10^{11} \, cm^{2}/sec$$

$$K_{v} = \nu_{v} = 10^{4} \, cm^{2}/sec$$

2.9 Results

Figure 2.9.1 shows the meridional mass stream function. Although the velocity vector is parallel to the isolines, the speed is proportional to the gradient of the mass stream function divided by the sine of the colatitude, i.e., much stronger near the anti-solar and subsolar points. There is a single strongly asymmetric Hadley cell with its center near 75° from the antisolar point and slightly below the central level. The existence and strength of the boundary layers is more apparent in the following figures:

Figure 2.9.2 is a cross section of the vortex strength $\eta = \frac{v_{z}}{sind}$. It shows that there is very little shear in the interior. Large values of the vertical shear of the horizontal velocity are confined to the top and bottom boundary layers, the latter due to the non-slip condition at the rigid bottom.
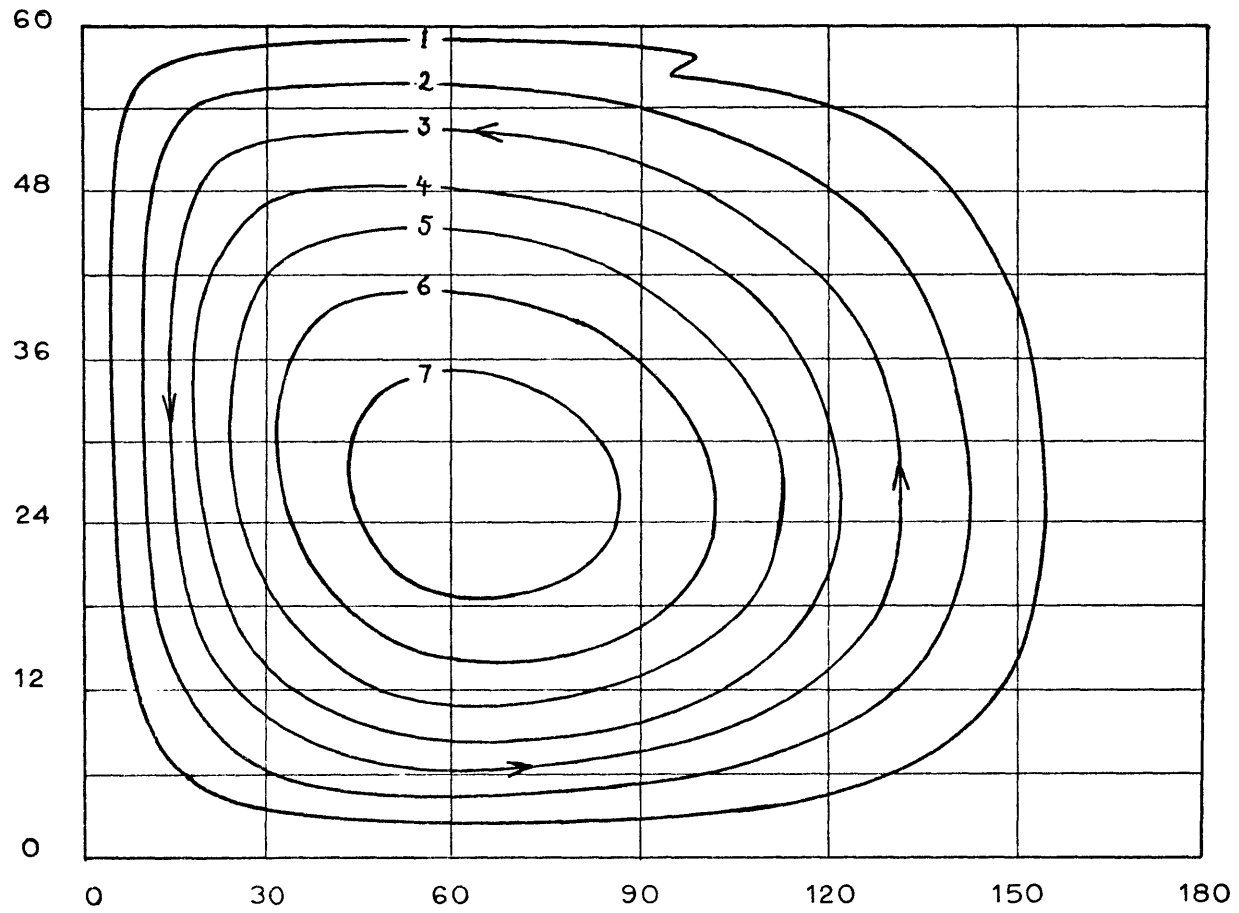
Figures 2.9.3 and 2.9.4 show the horizontal and vertical

Figure 2.9.1: Meridional mass stream function ψ in units of $10^8 \text{cm}^2/\text{sec}$ after running $1.33 \times 10^7 \text{sec}$.
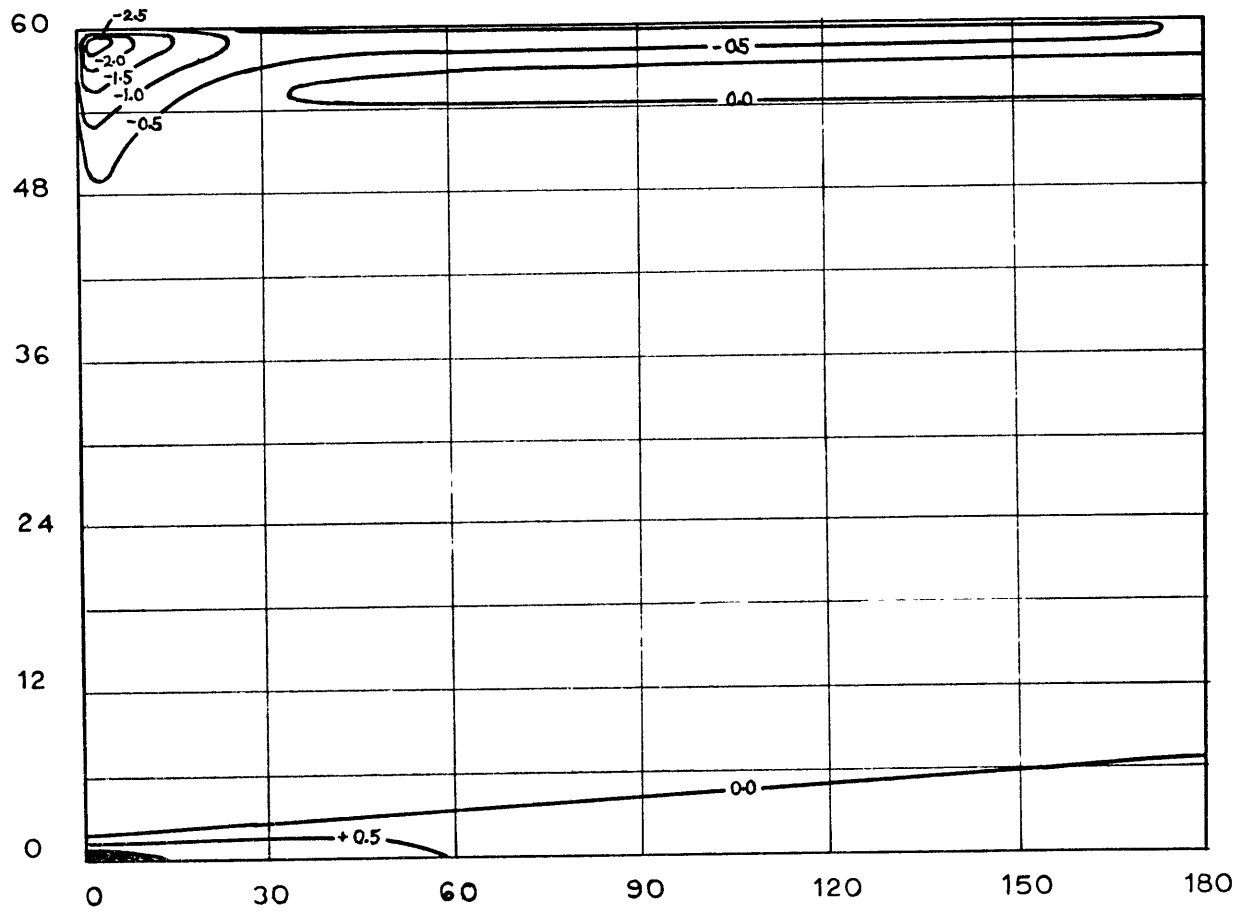
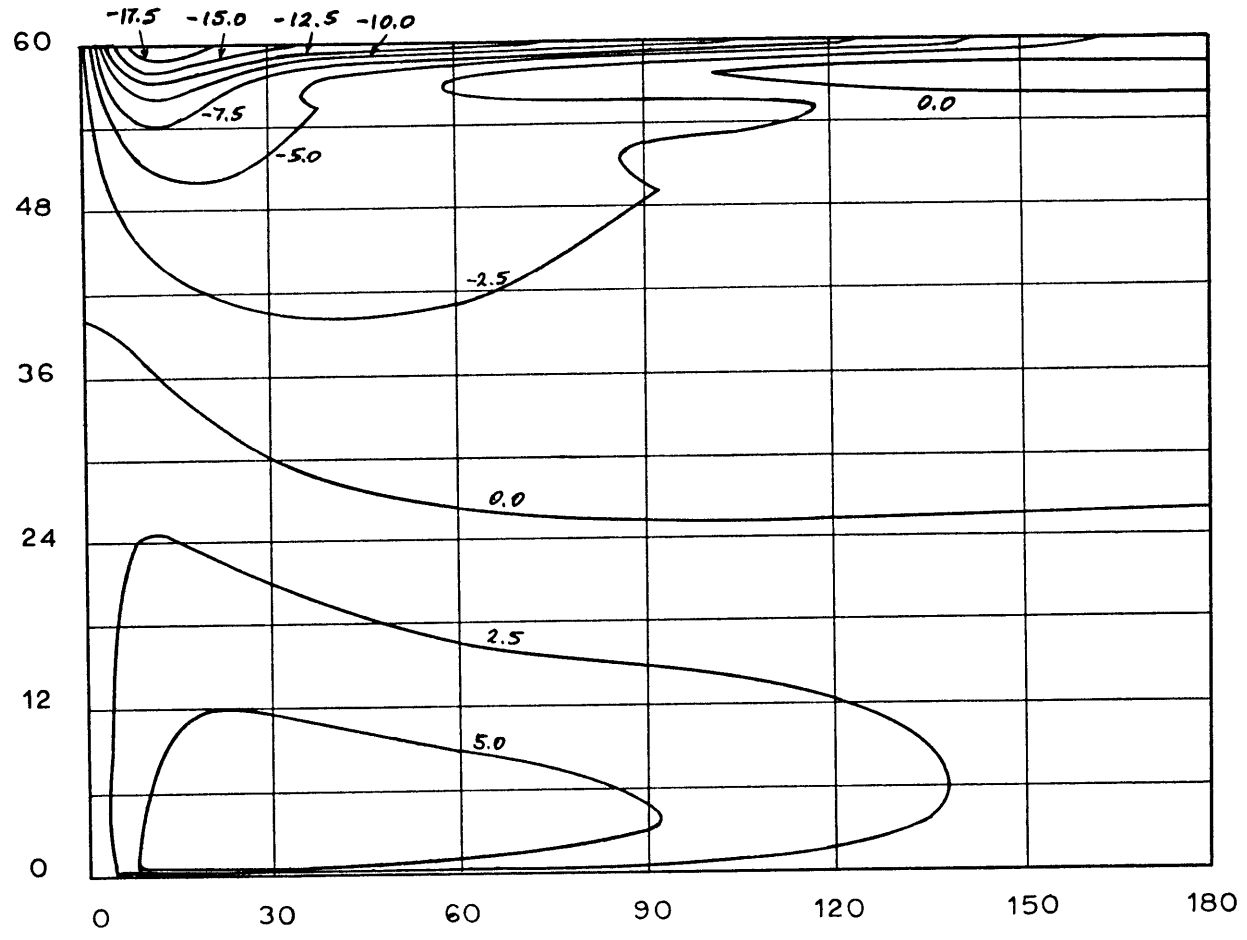Figure 2.9.2: Vortex strength in units of 10^{-2}sec^{-1}.
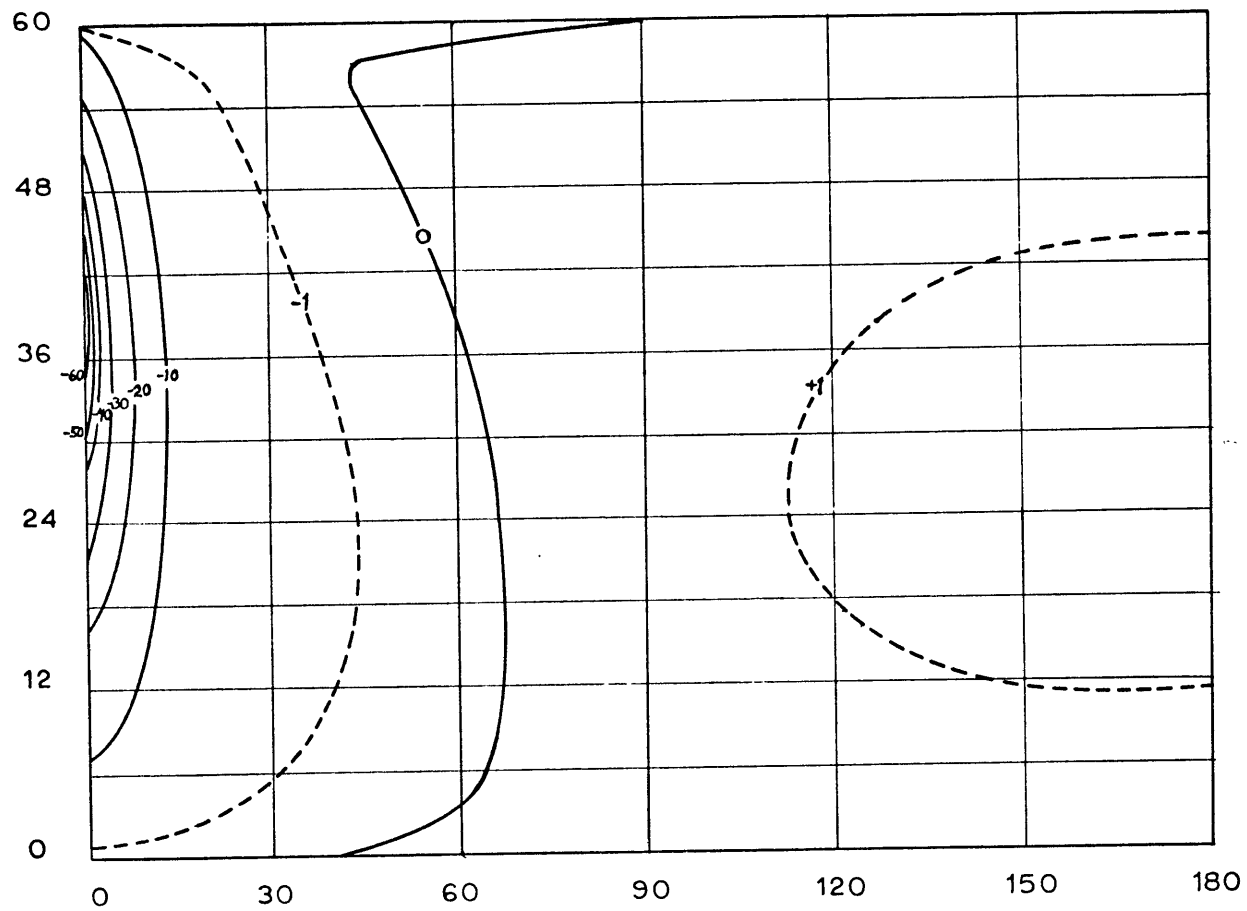
Figure 2.9.3: Meridional velocity v in m/sec.

Figure 2.9.4:   Vertical velocity w in cm/sec.

components of the velocity.

In the upper boundary layer, the typical meridional velocity is about 10 m/s with a maximum of 18 m/s; in the interior, the meridional velocities are of the order of 2 m/s and vary slowly. Although the flow towards the antisolar point is very strong in the narrow boundary layer at the top, it is not confined to it. Essentially it is the upper half of the atmosphere that moves towards the antisolar point, and the return flow towards the subsolar point occurs in the lower half of the atmosphere.

The vertical boundary layer at the antisolar point (or "mixing region" as Goody and Robinson called it) is characterized by a strong and concentrated downward flow with a maximum velocity of 60 cm/sec. In the interior the vertical velocity is of the order of 1 cm/sec. The width of the "mixing region" is about 15° latitude, or 1500 km.

It is interesting to note that, as Stone showed in his scale analysis, there is downward motion in large parts of the interior. Probably the spherical geometry also contributes to the extension of the downward motion far from the antisolar point. Sinking motion in the interior occurs up to 75° from the antisolar point and even more at the top. This is an important point because one of the most attractive features of Goody and Robinson's results was that downward motion was confined to a very narrow mixing region at the antisolar point; this would explain the almost complete cloud coverage of Venus' sky if the clouds were of condensational origin. However our numerical results are different in this respect, showing upward motion confined mainly to the illuminated hemisphere.

Figure 2.9.5 shows the relative density departure $\tilde{\rho} = \dfrac{\rho - \rho_0}{\rho_0}$

It is clear that the interior is almost completely adiabatic, or more

precisely, neutrally stable. The departures of density from the mean

value are very small, less than 0.1%, and this agrees well with the

adiabatic interior obtained by Goody and Robinson. However this

result may be due to the fact that in our model, as in Stone's, radi-

ation is not included, and therefore there is nothing to counteract

the tendency for turbulent diffusion to bring about an adiabatic

lapse-rate. Our Boussinesq model thus has a built-in tendency to

produce an adiabatic lapse-rate and therefore high surface temper-

atures. It is unrealistic in this respect. The strong density

gradients are confined to the top boundary layer with a thickness

of about 1 km. The density difference between the antisolar and sub-

solar points is about 10% corresponding to a temperature difference

of about 23°. This is rather large compared to the few degrees ob-

served temperature difference between the equator and the poles, and

almost no difference along longitude between the illuminated and

the dark hemispheres. However these temperatures are measured at

the cloud top level, and if the clouds are formed by condensation their

tops may correspond roughly to an isothermal surface. There is a

small region near the antisolar point with a gravitationally unstable

stratification.

Tables 2.9.1 and 2.9.2 show the numerical balance of the

terms in vorticity and density equations at different points in

the boundaries and interior. The position of the points is indicated

in Figure 2.6.3: A is in the mixing region; B and C in the upper

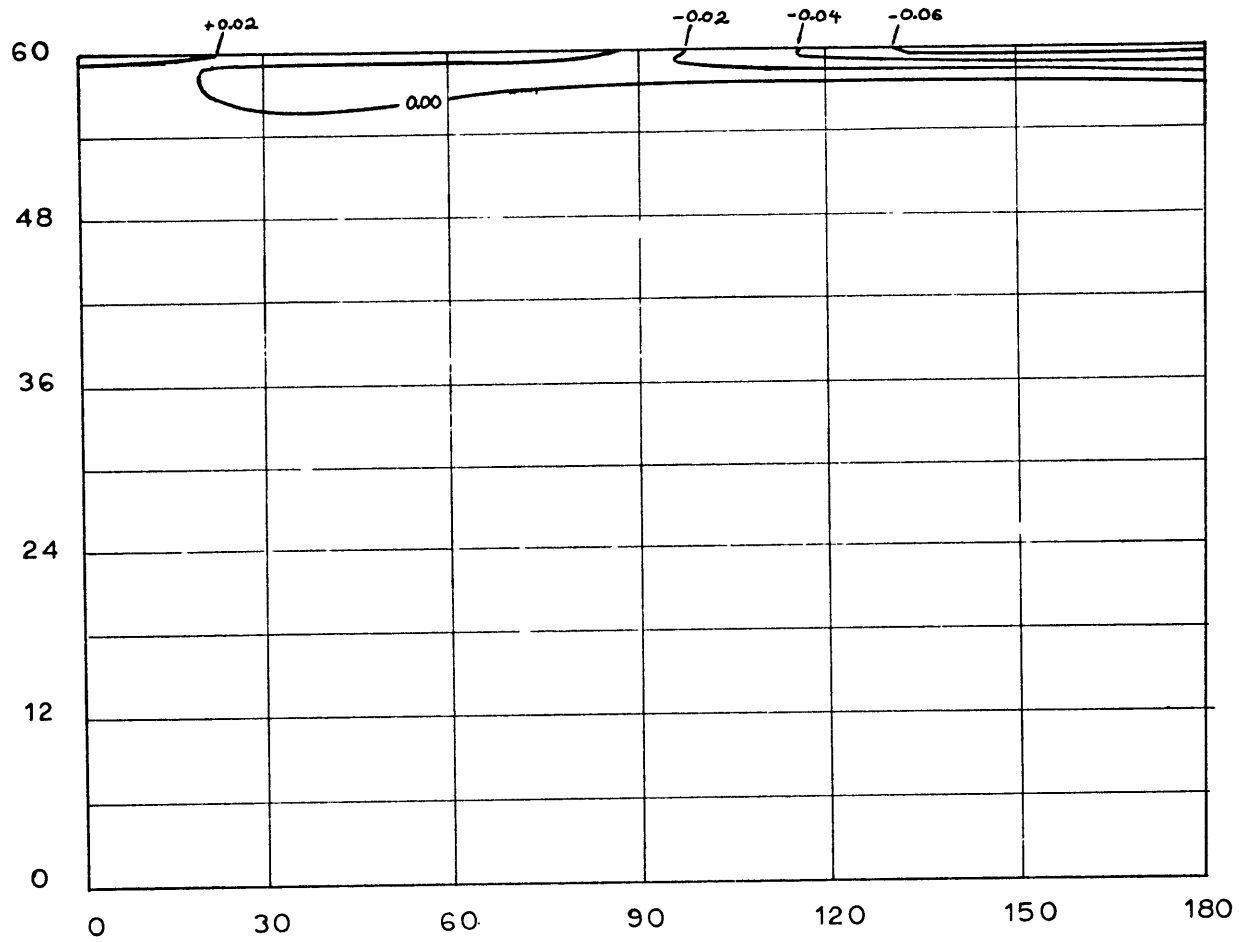boundary layer; D is within the sinking region below the mixing region;

Figure 2.9.5: Relative density departure from the initial value $\tilde{\rho}$.

E is a typical interior point; F is an interior point near the sub-solar point; F, H, and G show the effect of the lower boundary. Equations (2.2.6) and (2.2.4) are reproduced here for clarity.

$$\frac{\partial \eta}{\partial t} = - \frac{(v\eta \sin\alpha)_\alpha}{a \sin\alpha} - (w\eta)_z + \frac{g}{a \sin\alpha}\frac{\partial \tilde{\rho}}{\partial \alpha}$$

(Time Der.)   (Hor. Adv.)   (Vert. Adv.)   (Driving)

$$+ \frac{\nu_H}{a^2}\left[\frac{((\eta \sin\alpha)_\alpha \sin\alpha)_\alpha}{\sin^2\alpha} - \frac{\eta}{\sin^2\alpha} - \frac{2 w_{\alpha z}}{\sin\alpha}\right] + \nu_v\, \eta_{zz}$$

(HOR. Visc.)   (Vert. Visc.)

$$\frac{\partial \tilde{\rho}}{\partial t} = - \frac{(\tilde{\rho} v \sin\alpha)_\alpha}{a \sin\alpha} - (w\tilde{\rho})_z + \frac{\kappa_H}{a^2}\frac{(\tilde{\rho}_\alpha \sin\alpha)_\alpha}{\sin\alpha} + \kappa_v\, \tilde{\rho}_{zz}$$

(Time Der.)   (Hor. Adv.)   (Vert. Adv.)   (Hor. Diff.)   (Vert. Diff.)

In Tables 2.9.1 and 2.9.2 the principal balancing terms are underlined. In some interior points there is not a complete balance so that the numerical value of the local time derivative term is of the same order as the advective terms, especially in the density equation. Near the bottom, away from the antisolar point, the balance of forces is advective-vertically diffusive, and since the velocities are very small and the vertical coefficient of diffusion not large the relaxation times both for advection and diffusion are large and the system has not reached equilibrium. Nevertheless the density gradients are so small that the numerical value of the density only undergoes very small changes.

POINT	A	B	C	D	E	F	G	H	I
Hor. Adv.	-23706.	- 42.86	115.64	138.81	-0.58	0.24	-4632.1	54.87	1.88
Vert. Adv.	25368.	42.15	- 35.12	-356.70	1.50	-1.18	141.3	2.72	-2.30
Hor. Visc.	15924.	24.72	33.29	- 82.62	2.04	0.89	- 765.9	-74.99	2.02
Vert. Visc.	684.	282.92	310.75	- 0.04	0.00	0.00	4346.9	20.32	-1.09
Driving	-13880.	-306.86	-424.56	-123.12	-2.98	0.04	- 4.3	- 1.47	-0.79
Time Der.	4390.	0.06	0.00	-423.67	-0.02	-0.01	- 913.4	1.45	-0.28

Table 2.9.1: Balance of terms in the vorticity equation at 9 points in units of $10^{-10}\mathrm{sec}^{-2}$. Underlined are the terms that are numerically larger. See Figure 2.9.6 for the position of the points A through I.

POINT	A	B	C	D	E	F	G	H	I
Hor. Adv.	15324.3	-198.1	163.6	-139.1	2.40	-0.63	-131.6	0.213	0.434
Vert. Adv.	-6127.6	48.0	196.5	213.4	-2.91	1.10	133.4	-0.072	-0.431
Hor. Diff.	-9394.3	- 20.6	41.3	- 74.0	0.90	-0.02	- 2.2	-0.295	0.262
Vert. Diff.	197.8	171.1	-401.0	0.0	-0.00	-0.02	0.9	0.573	0.087
Time Der.	0.3	0.4	0.4	0.4	0.38	0.43	0.4	0.419	0.352

Table 2.9.2: Balance of terms in the density equation at 9 points in units of 10^{-10}sec^{-1}. The terms that are numerically larger are underlined. See Figure 2.9.6 for the position of the points A through I.

The results show that the nonlinear advective terms are important everywhere. There is a good agreement in the overall balance of terms between the results of our numerical model and the scale analyses of Goody and Robinson and of Stone. In the mixing region (point A) the balance in the vorticity equation is between the advective terms, the horizontal viscosity (due to the large horizontal gradients), the vertical viscosity (due to the proximity of the upper boundary) and the driving. Similarly the balance in the energy equation is between the advective terms and the horizontal and vertical eddy diffusivity terms.

In the upper boundary layer, away from the antisolar point (points B and C), as in Goody and Robinson's and in Stone's results, the horizontal viscosity (or diffusivity) ceases to be important and the balance is between advection and vertical diffusivity in the energy equation and between advection, vertical viscosity and the driving term in the vorticity equation.

Point D is directly below the mixing region. As could be expected, the horizontal viscosity is still important and the vertical viscosity term is negligible. At this point the time derivative of the vorticity is as large as the other terms, but it still represents a very small variation of the actual value of the vorticity over several days.

In the interior point E, as in Goody and Robinson's analysis, there is a balance between the driving and the advective terms. In our results, however, the horizontal viscosity and diffusivity terms are not negligible because of the excessively large values of ν_H and K_H . The situation is similar at point F, under the subsolar

point, except that the horizontal gradient of the density is smaller
so that the driving term is very small.

Points G, H, and I are very close to the lower boundary.
Point G, near the antisolar point, is in the region where most of
the dissipation of the vorticity occurs. In the vorticity equation
there is a balance between horizontal advection of vorticity and ver-
tical viscosity. As was pointed out before, in the bottom, away
from the antisolar point (points H and I) the balance in the energy
equation is advective-diffusive with very slow velocities.

In Table 2.9.3 we compare the orders of magnitude of the
velocity components, the density departures, and the width of the
boundary layers in our numerical model with those in Stone's scale
analysis. The subindex "mr" represents the value of the magnitude
at the mixing region, and "bl" at the upper boundary layer. We have
replaced Stone's expression αG , where α is the expansion coef-
ficient and G the magnitude of the boundary condition on T_z , by
$[\rho_z] = F_0 /(\kappa_v C_p \rho_0 T_0)$, the magnitude of the flux boundary condition
applied to ρ_z , where $F_0 = \sigma T_0^4$. We include also the results
obtained by Goody and Robinson, although the comparison is more dif-
ficult because of their use of radiative diffusive boundary conditions,
whereas ours are diffusive only, and because we use a larger value
of ρ_0 corresponding to the mean density of the atmosphere. In
the mixing region the agreement with Stone's results is good except
for the vertical velocity which is much larger in our results. This
is probably due to the convergence of the meridians in the spherical
geometry. It is probably also this effect that makes the downward
jet penetrate most of the interior of the atmosphere. In the upper

MAGNITUDE	STONE'S ANALYSIS	NUMERICAL MODEL	GOODY AND ROBINSON
z_{mr}	$\left(\dfrac{K_v\,K_H}{g\,[\rho_z]}\right)^{1/4} = 430$ m	~ 5 km	800 m
y_{mr}	$\left(\dfrac{K_H^3}{K_v\,g\,[\rho_z]}\right)^{1/4} = 1350$ km	~ 1500 km	3 km
w_{mr}	$\left(\dfrac{K_v^3\,g\,[\rho_z]}{K_H}\right)^{1/4} = 0.23\ \dfrac{cm}{sec}$	~ 20 cm/sec	$1000\ \dfrac{cm}{sec}$
v_{mr}	$\left(K_H\,K_v\,g\,[\rho_z]\right)^{1/4} = 7.4$ m/s	~ 10 m/sec	34 m/sec
ρ_{mr}	$\left(\dfrac{K_H\,K_v\,[\rho_z]^3}{g}\right)^{1/4} = 1.5\times10^{-2}$	$\sim 2\times10^{-2}$	1.7×10^{-1}
$z_{b\ell}$	$\left(\dfrac{K_v^2\,L^2}{g\,[\rho_z]}\right)^{1/6} = 1$ km	~ 1 km	1.2 km
$w_{b\ell}$	$\left(\dfrac{K_v^4\,g\,[\rho_z]}{L^2}\right)^{1/6} = 0.1\ \dfrac{cm}{sec}$	~ 1 cm/sec	$0.12\ \dfrac{cm}{sec}$
$v_{b\ell}$	$\left(g\,[\rho_z]\,K_v\,L\right)^{1/6} = 0.43\ \dfrac{m}{sec}$	~ 5 m/sec	34 m/sec
$\rho_{b\ell}$	$\left(\dfrac{K_v^2\,L^2\,[\rho_z]^5}{g}\right)^{1/6} = 3.7\times10^{-2}$	$\sim 6\times10^{-2}$	1.7×10^{-1}

Table 2.9.3: Comparison of the width and velocity magnitudes at the upper boundary layer and the mixing region obtained by Stone, by Goody and Robinson, and by using the numerical Boussinesq model.

boundary layer there is a discrepancy in the scale of the velocity

components which are ten times larger in our results. But in this

region Stone's analysis is not completely valid because he assumes

$\frac{H^2}{L^2} \ll \frac{K_v}{K_H}$ which is not true even with $K_H = 10^{10} \text{cm}^2/\text{sec}$.

As was anticipated in section 2.5 the truncation errors

due to the "flux form" of the finite-difference equations are most

apparent in the region below the subsolar point where the errors associ-

ated with flow towards a zone with strong gradients produce irregu-

larities in the density and vorticity patterns. This is apparent

in the density field (Figure 2.9.5) where we find small positive

density values imbedded in a region of large negative values, and

especially in the vorticity field (Figure 2.9.2) where we find

a similar but stronger effect. It is also the cause of the kink

in the upper right of the mass stream function field (Figure 2.9.1),

and the small countercurrent in the upper right of the horizontal

velocity field (Figure 2.9.3).

The time taken by the integration to converge was the

equivalent of about 100 earth days and was probably given by the ad-

vective time $\tau \sim L/v_{int} \sim H/w_{int} \sim 10^7 sec$ where L is the distance be-

tween the antisolar and subsolar points (20,000 km), H the height of

the atmosphere (60 km) and v_{int} and w_{int} the interior horizontal

and vertical velocity scales ($\sim$ 2 m/s and $\sim$ 1 cm/s respectively).

However, near the bottom the velocities are smaller and the larger

diffusive relaxation time $H^2/2v_v \sim 10^9 sec$ is probably required be-

fore the system converges. But the rotation period of Venus is 243

earth days and the length of a solar day is only 117 earth days so

that it is clearly impossible to obtain a realistic result with a

model in which rotation is neglected.

CHAPTER 3

Non-rotating Quasi-Boussinesq Model of the Atmosphere of Venus

3.1 Introduction

The atmosphere of Venus is much deeper than the Earth's at-
mosphere: the cloud top level is located at about 60 km from the
solid surface; the ratio of the density at the surface level to the
density at the cloud top level is of the order of 100, the temperature
ratio is of the order of 3 and the pressure ratio about 400. A
Boussinesq model neglects density variations except when coupled with
gravity, so that the basic density stratification is not taken into
account, even for a compressible fluid (Spiegel and Veronis, 1959;
Ogura and Phillips, 1962). The Boussinesq approximation applied to
a compressible fluid can be strictly justified only if the vertical
dimension is smaller than any scale height, which is not the case in
Venus' atmosphere. For this relatively deep atmosphere, a better
approximation is the use of local mean values of temperature, pres-
sure and density which vary with height, rather than constant mean
values.

The observations made by the space probes Venera 4 to Venera
7 (Avduevsky et al.,1970; Avduevsky et al., 1971) showed that the
stratification of the atmosphere of Venus is nearly adiabatic. This
allows us to use the "anelastic" or "quasi-Boussinesq" model (Ogura
and Phillips, 1962; Charney and Ogura, 1960). In this approximation,
the distribution of pressure and density is assumed to be always
close to the distribution of pressure and density in an adiabatically
stratified atmosphere. Here it is the variations of potential temperature

that are neglected except when coupled with gravity. The quasi-Boussinesq approximation, as well as the Boussinesq approximation, eliminates the sound waves from the original hydrodynamic equations.

In this chapter we describe a quasi-Boussinesq numerical model for the atmosphere of Venus, in which rotation is neglected and which includes a simple, semi-grey treatment of radiation.

Section 3.2 contains the basic equations of the model; the modeling of radiation is described in section 3.3; the boundary conditions are stated in section 3.4; sections 3.5 through 3.8 describe the numerical algorithms; and the results are given and discussed in section 3.9.

3.2 Quasi-Boussinesq model: hydrodynamic equations

A numerical model of the atmosphere of Venus with spherical geometry, which takes into account the basic density stratification, was developed with the following approximations:

(a) quasi-Boussinesq

(b) hydrostatic

(c) no rotation

(d) the subsolar point is fixed

(e) "semi-grey" approximation, i.e., the atmosphere has two different constant absorption coefficients for short and long wave radiation.

(f) constant horizontal and vertical coefficients of eddy viscosity and diffusivity. Prandtl number equal to unity.

Following Ogura and Phillips (1962) we define a non-dimensional vertical coordinate

$$\zeta = z / D \tag{3.2.1}$$

where $D = \dfrac{C_p \, \theta_a}{g}$ is the adiabatic height of the atmosphere, is the temperature at the surface level. The potential temperature is defined by

$$\theta = T \left(\frac{p}{p_o} \right)^{-\kappa} \tag{3.2.2}$$

where p_o is the surface pressure and $\kappa = R/c_p$.

It is convenient to define a new variable to replace the pressure:

$$\pi = \left(p / p_o \right)^{\kappa} \tag{3.2.3}$$

We expand all variables as

$$\pi = \pi_a (\zeta) + \pi' (x, y, \zeta, t) \tag{3.2.4}$$

where π_a is the value of π in an adiabatic stratification and π', the departure from the adiabatic value, is assumed to be small everywhere.

Assuming that the mean stratification is approximately that of an adiabatic atmosphere, we have

$$\theta_a = T_o$$

$$\Pi_a = 1 - \varsigma$$

$$T_a = T_o (1-\varsigma)$$

$$p_a = p_o (1-\varsigma)^{1/\kappa}$$

$$\rho_a = \frac{p_o}{RT_o} (1-\varsigma)^{1/\kappa - 1} = \rho_o (1-\varsigma)^{1/\kappa - 1}$$

(3.2.5)

As in the Boussinesq model, we assume a slippery rigid top at a height H, which is assumed to be near the cloud top level, at which

$$\varsigma_H = H/D < 1$$

(3.2.6)

Then the quasi-Boussinesq hydrodynamic equations in spherical coordinates are as follows: the meridional component of the equation of motion is

$$\frac{\partial v}{\partial t} = - \frac{(v^2 \sin\alpha)_\alpha}{a \sin\alpha} - \frac{(w v \rho_a)_z}{\rho_a} - \frac{c_p \theta_a}{a} \frac{\partial \Pi'}{\partial \alpha}$$

$$\cdot + \frac{\nu_H}{a^2} \left[\frac{(v_a \sin\alpha)_\alpha}{\sin\alpha} - \frac{v}{\sin^2\alpha} \right] + \nu_v \, v_{zz}$$

(3.2.7)

We have dropped the term $2 w_\alpha$ from the expression in square brackets for the horizontal eddy viscosity because of the smallness of the aspect ratio. In the Boussinesq model (chapter 2) this term came out

to be numerically less than 1% of the other two terms or their sum.

The hydrostatic equation is

$$0 = -C_p \, \theta_\alpha \, \frac{\partial \pi'}{\partial z} + g \, \frac{\theta'}{\theta_\alpha} \; ; \qquad (3.2.8)$$

the continuity equation is

$$0 = -\frac{(v \sin \alpha)_\alpha}{a \sin \alpha} - \frac{(w \, \rho_\alpha)_z}{\rho_\alpha} \qquad (3.2.9)$$

and the first law of thermodynamics for a perfect gas may be written

$$\frac{\partial \theta'}{\partial t} = -\frac{(v \theta'_\alpha \sin \alpha)_\alpha}{a \sin \alpha} - \frac{(w \, \theta' \rho_\alpha)_z}{\rho_\alpha} + \frac{K_H}{a^2} \frac{(\theta'_\alpha \sin \alpha)_\alpha}{\sin \alpha} + K_v \, \theta'_{zz} + \frac{q_v}{C_p \rho_\alpha \pi_\alpha} \qquad (3.2.10)$$

where q_v is the radiative energy absorbed per unit volume and per

unit time.

The small aspect ratio allows us to define the vorticity

as N_z , neglecting the term $-\frac{w_\alpha}{a}$. As before, it is conven-

ient to employ the vortex strength instead of the vorticity for its

conservation properties: if the atmosphere were isentropic and

inviscid, then by Bjerknes or Kelvin's theorem, the circulation of

an infinitesimal ring of fluid symmetric around the subsolar-anti-

solar axis would be individually conserved. Applying Stokes' theorem,

we have

$$N_z \, d\sigma = \text{constant}$$

where $d\sigma$ is the cross-section of the ring. Since the mass of

the ring is also conserved,

$$\rho_a \, 2\pi a \, \sin\alpha \, d\sigma = \text{constant}$$

Thus, in an isentropic inviscid atmosphere, the vortex strength

$$\eta = \frac{v_z}{\rho_a \sin\alpha} \qquad\qquad (3.2.11)$$

is individually conserved.

  As before, the use of the variable η instead of the vorticity avoids a non-linear numerical instability near the subsolar and antisolar points that appears because of the sudden convergence of the meridians.

  From equations (3.2.7) to (3.2.9) we obtain an equation for the vortex strength η :

$$\frac{\partial\eta}{\partial t} = -\frac{(v\eta\sin\alpha)_\alpha}{a\sin\alpha} - \frac{(w\,\eta\,\rho_a)_z}{\rho_a} - \frac{g}{a\,\rho_a\sin\alpha\,\theta_a}\,\frac{\partial\theta'}{\partial\alpha}$$

$$+ \frac{\nu_H}{a^2}\left[\frac{((\eta\sin\alpha)_\alpha\sin\alpha)_\alpha}{\sin^2\alpha} - \frac{\eta}{\sin^2\alpha}\right] + \frac{\nu_v}{\rho_a}\,\frac{\partial^2(\rho_a\eta)}{\partial z^2} \qquad (3.2.12)$$

We define the mass stream function ψ by

$$\left(\frac{\psi_z}{\rho_a}\right)_z = \eta\,\rho_a\,\sin^2\alpha \qquad\qquad (3.2.13)$$

Then

$$v\sin\alpha\,\rho_a = \psi_z \qquad\qquad (3.2.14)$$

$$w\sin\alpha\,\rho_a = -\frac{\psi_\alpha}{a} \qquad\qquad\qquad (3.2.15)$$

Equations (3.2.10), (3.2.12) to (3.2.15), the boundary

conditions, and the formulation of the radiative heating q_v define

the model.

We note that an alternative method of integration could

have been used instead of the "vorticity method" used here. In the

"pressure method" equation (3.2.7) is used directly to forecast v,

instead of the vorticity equation, and π' is obtained by the fol-

lowing procedure:

From equation (3.2.9) and the boundary condition of no

meridional velocity at the subsolar and antisolar points, we obtain

$$\int_0^H v \rho_a \, dz = 0 ,$$ (3.2.16)

i.e., the mean meridional transport of mass (as well as its time

derivative) is zero. We define $\bar{\rho}_a = \frac{1}{H} \int_0^H \rho_a \, dz$ and $\overline{\pi'(\alpha)} = \frac{1}{\bar{\rho}_a H} \int_0^H \pi' \rho_a \, dz$

Then multiplying equation (3.2.7) by ρ_a , integrating it from bot-

tom to top, and using equation (3.2.16) we obtain an equation for

from which $\frac{\partial \overline{\pi'}}{\partial \alpha}$ can be determined except for a constant. From

equation (3.2.8) we obtain

$$\overline{\pi'(\alpha)} = \pi'(\alpha, H) - \frac{1}{\bar{\rho}_a D H} \int_0^H \left[\int_0^z \frac{\theta'(\alpha, z')}{\theta_a} dz \right] \rho_a \, dz$$ (3.2.17)

Eliminating $\overline{\pi'(\alpha)}$ from the previous two equations,

$\pi'(\alpha, H)$ can be determined except for a constant. Then from

equation (3.2.8)

$$\pi'(\alpha, z) = \pi'(\alpha, H) - \frac{1}{D} \int_z^H \frac{\theta'(\alpha, z')}{\theta_a} \, dz'$$ (3.2.18)

This procedure has the advantage that it is not necessary to solve an elliptic equation equivalent to (3.2.13) at each step, and the disadvantage that the vertical velocity, computed by integration of the continuity equation (3.2.9), may not be exactly zero at a horizontal rigid boundary due to truncation errors, and this might cause numerical instability problems.

3.3 Radiative transfer

We assume that the atmosphere is semi-grey, so that it has constant absorption coefficients different for solar and thermal radiation. In what follows the subindices "T" and "S" refer to thermal and solar radiation respectively, a star indicates the value of a variable at the surface level and a subindex H its value at the cloud top level.

(a) Long wave radiative transfer

The upward energy flux by thermal radiation is given by (Gierasch and Goody, 1970)

$$\uparrow F_T(\tau_T) = \int_{\tau_T}^{\tau_T^*} \sigma T^4(t)\, e^{-r(t-\tau_T)}\, r\, dt + \sigma T^{*4} e^{-r(\tau_T^*-\tau_T)}$$
$$- \int_0^{\tau_T} \sigma T^4(t)\, e^{r(t-\tau_T)}\, r\, dt \tag{3.3.1}$$

where σ is the Stefan-Boltzmann constant, $r = 1.66$ is a diffusivity factor that compensates for the neglect of the angular dependence of the radiation field, and τ_T is the thermal optical depth given by

$$\tau_T = \int_z^\infty k_T\, dz \tag{3.3.2}$$

We assume that k_r, the volume absorption coefficient, is given by

$$k_T = \begin{cases} c_T \rho_a & \text{if } 0 \leq z \leq H \\ 0 & \text{if } z > H \end{cases} \qquad (3.3.3)$$

that is, there is no absorption above the top of the atmospheric model and below this level the volume absorption coefficient is proportional to the mean density.

Then

$$\zeta_T = \int_S^{S_H} \rho_o D (1-S)^{1/\kappa - 1} dS = \zeta_{T_o} \left(\pi_a^{1/\kappa} - \pi_{a_H}^{1/\kappa} \right), \qquad (3.3.4)$$

where ζ_{T_o} is the total optical depth of an adiabatic atmosphere if $H = D$. The optical depth between two points in the vertical is proportional to the pressure difference.

We now separate the radiation of thermal energy into two parts: one due to the mean adiabatic stratification, which needs to be computed only once, and the other due to the small departures of the temperature from its mean adiabatic value, which should be computed along with the other variables as the time integration goes on.

The temperature is

$$T = T_a + T' = \left(\pi_a + \pi' \right)\left(\theta_a + \theta' \right) \simeq \pi_a \theta_a + \pi_a \theta' + \pi' \theta_a \qquad (3.3.5)$$

In the radiation computations we approximated

$$T' \simeq \Pi_a \; \theta' \tag{3.3.6}$$

which is not totally consistent with the quasi-Boussinesq approximation (3.3.5) (Ogura and Phillips, 1962), but which allows a great simplification of the computations. In section 3.9 we give an "a posteriori" justification for this approximation.

Then, since $\theta' \ll \theta_a$

$$\sigma T^4 \simeq \sigma T_a^4 \left(1 + 4\frac{T'}{T_a} \right) \simeq \sigma \theta_a^4 \Pi_a^4 \left(1 + \frac{4\theta'}{\theta_a} \right) \tag{3.3.7}$$

From (3.3.4)

$$\Pi_a = \left(\frac{z_T + z_{TH}}{z_{T_0}} \right)^K \tag{3.3.8}$$

where $z_{T_H} = z_{T_0} \, \Pi_{a_H}^{1/K}$

The "adiabatic" component of the thermal radiative flux is computed as

$$\uparrow F_{T_a} (z_T) = \sigma T_a^4 \left\{ \int_{z_T}^{z_T^*} \left(\frac{t + z_{TH}}{z_{T_0}} \right)^{4K} e^{-r(t - z_T)} \, r \, dt \right.$$

$$\left. - \int_0^{z_T} \left(\frac{t + z_{TH}}{z_{T_0}} \right)^{4K} e^{r(t - z_T)} r \, dt + e^{-r(z_T^* - z_T)} \right\} \tag{3.3.9}$$

The thermal flux corresponding to the nonadiabatic temperature component is

$$\uparrow F_T'(\tau_T) = 4\sigma\theta_a^3 \left\{ \int_{\tau_T}^{\tau_T^*} \left(\frac{t+\tau_{TH}}{\tau_{To}}\right)^{4K} \theta'(t)\, e^{-r(t-\tau_T)}\, r\, dt \right.$$

$$\left. - \int_0^{\tau_T} \left(\frac{t+\tau_{TH}}{\tau_{To}}\right)^{4K} \theta'(t)\, e^{r(t-\tau_T)}\, r\, dt + \theta'^* e^{-r(\tau_T^*-\tau_T)} \right\} \tag{3.3.10}$$

We assume that the atmosphere of Venus has a large optical depth (Gierasch and Goody, 1970), so that the exponentials in (3.3.10) will go to zero very fast, and only layers that are very near to the level τ_T will give a significant contribution to (3.3.10). We can then evaluate the integrals with sufficient accuracy if we make the linear expansion:

$$f(t) \approx f(\tau_T) + (t-\tau_T)\frac{df}{d\tau_T}, \tag{3.3.11}$$

where $\quad f(t) = \left(\frac{t+\tau_{TH}}{\tau_{To}}\right)^{4K} \theta'(t)$

We can neglect the last term of (3.3.10) except near the ground. The integrals

$$\int_{\tau_T}^{\tau_T^*} f(t)\, e^{-r(t-\tau_T)}\, r\, dt - \int_0^{\tau_T} f(t)\, e^{r(t-\tau_T)}\, r\, dt \approx$$

$$\approx f(\tau_T)\left[\int_{\tau_T}^{\tau_T^*} e^{-r(t-\tau_T)}\, r\, dt - \int_0^{\tau_T} e^{r(t-\tau_T)}\, r\, dt \right] + \frac{df(\tau_T)}{d\tau_T}\left[\int_{\tau_T}^{\tau_T^*} (t-\tau_T)e^{-r(t-\tau_T)}\, r\, dt \right.$$

$$\left. - \int_0^{\tau_T} (t-\tau_T)\, e^{r(t-\tau_T)}\, r\, dt \right] \approx f(\tau_T)\left[\int_0^{\infty} e^{-ru}\, r\, du - \int_{-\infty}^0 e^{ru}\, r\, du \right]$$

$$+ \frac{df(\tau_T)}{d\tau_T}\left[\int_0^{\infty} u\, e^{-ru}\, r\, du - \int_{-\infty}^0 u\, e^{ru}\, r\, du \right] = \frac{2}{r}\frac{df}{d\tau_T} \tag{3.3.12}$$

At the interior points we compute the upwards flux departure from the mean "adiabatic" value by means of the explicit formula

$$\uparrow F_T'(\tau_r) = 4\sigma\theta_a^3 \left\{ \frac{2}{r} \left[\frac{4\kappa}{\tau_{T_0}} \left(\frac{\tau_r + \tau_{TH}}{\tau_{T_0}} \right)^{4\kappa-1} \theta'(\tau_r) + \left(\frac{\tau_r + \tau_{TH}}{\tau_{T_0}} \right)^{4\kappa} \frac{d\theta'(\tau_r)}{d\tau_r} \right] + \theta'^* e^{-r(\tau_T^* - \tau_r)} \right\}$$

(3.3.13)

At the top we assume that there is no turbulent transfer of heat so that $\left(\frac{d\theta'}{d\tau_T} \right)_{\tau = \tau_{TH}} = 0$. From (3.3.10) and the same linear approximation we obtain

$$\uparrow F_T'(\tau_{TH}) = 4\sigma\theta_a^3 \left\{ \left(\frac{\tau_{TH}}{\tau_{T_0}} \right)^{4\kappa} + \frac{4\kappa}{r\tau_{T_0}} \left(\frac{\tau_{TH}}{\tau_{T_0}} \right)^{4\kappa-1} \right\} \theta'_H$$

(3.3.14)

At the bottom we get from (3.3.9)

$$\uparrow F_T'(\tau_T^*) = 4\sigma\theta_a^3 \left\{ \frac{4\kappa}{r\tau_{T_0}} \theta'^* + \left(\frac{d\theta'}{d\tau_T} \right)^* \right\}$$

(3.3.15)

The last term on the right hand side of (3.13) was included only at the first point next to the ground.

Professor Goody has pointed out that this approximation may not be accurate near the top of the atmospheric model where the mean

molecular free path becomes larger than the distance to the top, but this is not important unless convection is negligible near the top, which is not true in our model.

(b)   Short wave radiation

We assume that the volume extinction coefficient in the short wave region of the spectrum is also proportional to the mean adiabatic density and is zero above z = H.

If

$$\tau_s = \int_z^\infty k_s \, dz \tag{3.3.16}$$

then

$$\tau_s = \tau_{s_0} \left[\pi_a^{1/\kappa} - \pi_{a_H}^{1/\kappa} \right] \tag{3.3.17}$$

We further assume that diffuse radiation is absorbed at the same level at which it is generated. The downgoing flux of solar radiation is then given by

$$\downarrow F_s (\tau_s) = \begin{cases} - S_0 (1-A) \cos\alpha \; e^{\tau_s / \cos\alpha} & \text{if } \frac{\pi}{2} \leq \alpha \leq \pi \\ 0 & \text{if } 0 \leq \alpha \leq \frac{\pi}{2} \end{cases} \tag{3.3.18}$$

(c)   Heating rate

The radiative energy q_v absorbed per unit volume, per unit time in equation (3.2.10) is

$$q_v = \frac{\partial (F_s - F_T)}{\partial z} \tag{3.3.19}$$

3.4 Boundary conditions

The mechanical boundary conditions are similar to those used in the Boussinesq model: non-stress rigid top, non-slip rigid bottom. We have then:

$$\Psi = \left(\frac{\Psi_z}{\rho_\alpha}\right)_z = 0 \qquad\qquad at \quad z = H \qquad\qquad a$$

$$\Psi = \Psi_z = 0 \qquad\qquad at \quad z = 0 \qquad\qquad b \qquad\qquad (3.4.1)$$

$$\Psi = 0 \qquad\qquad at \quad \alpha = 0, \pi \qquad\qquad c$$

For the energy equation we assume that there is no turbulent transfer of heat at the top, since radiation is considered as a separate term.

$$\theta_z = 0 \qquad\qquad at \quad z = H \qquad\qquad (3.4.2)$$

At the bottom we assume a state of equilibrium such that there is no net flux of heat,[*] i.e., there is an instantaneous energy balance between the downgoing thermal radiation and the upgoing thermal radiation plus convective heat transfer:

$$\downarrow F_s\left(z_s^*\right) = \uparrow F_T\left(z_T^*\right) + \uparrow C^* \qquad\qquad (3.4.3)$$

$\downarrow F_s\left(z_s^*\right)$ is obtained from (3.3.18). $\uparrow F_T\left(z_T^*\right)$ is formed

---

[*] Unlike Jupiter, there is no evidence that there is any appreciable flux of heat from the Venus surface.

by the "adiabatic" component $\uparrow F_{T_a}\left(\tau_T^*\right)$, which doesn't vary with

time (evaluated from equation (3.3.9)), and the perturbation part

$\uparrow F_T'(\tau_r^*)$ evaluated from (3.3.15).

The turbulent transfer of heat at the ground is parame-

terized as

$$\rho c^* = -K_v \, \rho_* \, C_p \, \theta_z'$$

by consistency with the assumption of a constant coefficient of ver-

tical eddy viscosity. In the finite difference model this coincides

numerically with the parameterization developed by Leovy (1968)

and adopted by Leovy and Mintz (1969) of the turbulent transfer of

heat in a stable atmosphere:

$$\uparrow c^* = \rho \, C_p \, C_M^2 \, |V_s| \, \Delta T$$

where $C_M^2 \approx 0.9 \times 10^{-3}$ is the momentum drag coefficient for stable

conditions and ΔT is the temperature change across the boundary

layer, if V_s , the wind speed a few meters above the surface, is

of the order of 2.5 m/s. This was the order of the wind speed near

the ground in the Boussinesq model, but in the quasi-Boussinesq

model the mean wind speed near the ground was much smaller.

Equation (3.4.3) can be written as

$$-K_v \, \rho_a^* \, C_p \, \theta_z'^* + 4\sigma\theta_a^3 \left\{ \frac{4k}{r z_{T_0}} \, \theta'^* + \frac{1}{r} \left(\frac{d\theta'}{d\tau_r}\right)^* \right\} = F_s - F_{T_a} \qquad (3.4.4)$$

$$at \quad z = 0$$

3.5 Equations in stretched coordinates

As in the Boussinesq model, we used stretched coordinates giving a finer resolution near the antisolar point and near the top and bottom of the atmosphere, although the resolution near the ground turned out to be unnecessary since the density stratification causes the presence of the ground to have a negligible effect upon the circulation.

The horizontal stretched coordinate is, as before

$$y = \sqrt{\alpha} \quad ; \quad \frac{dy}{d\alpha} = \frac{1}{2y} \tag{3.5.1}$$

and the vertical coordinate

$$\lambda = \frac{2}{\pi} \arctan\sqrt{\frac{z}{H-z}} \quad ; \quad \frac{d\lambda}{dz} = \frac{1}{HS} \tag{3.5.2}$$

where $\quad S = \pi \sqrt{z/H \, (1- z/H)}$

If we write $\tilde{\theta} = \frac{\theta'}{\theta_a}$, the relative potential temperature departure, equations (3.2.10a) and (3.2.12) to (3.2.15) become

$$\frac{\partial \tilde{\theta}}{\partial t} = - \frac{(v\,\tilde{\theta} \sin\alpha)_y}{2y\,a\sin\alpha} - \frac{(w\,\tilde{\theta}\,\rho_a)_\lambda}{HS\rho_a} + \frac{K_H}{a^2}\left[\frac{(\tilde{\theta}_y \sin\alpha/y)_y}{4y\sin\alpha} \right]$$

$$+ \frac{K_V}{H^2}\,\frac{1}{S}\left(\frac{\theta_\lambda}{S}\right)_\lambda + \frac{q_V}{c_p\theta_a\,\pi_a\,\rho_a} \tag{3.5.3}$$

$$\frac{\partial \eta}{\partial t} = - \frac{(v\eta \sin\alpha)_y}{2y\,a\,\sin\alpha} - \frac{(w\eta\,\rho_a)_\lambda}{HS\rho_a} - \frac{g}{2y\,a\,\rho_a\sin\alpha}\,\frac{\partial\tilde{\theta}}{\partial y}$$

$$\tag{3.5.4}$$

$$+ \frac{\nu_H}{a^2}\left[\frac{((\eta\sin\alpha)_y \sin\alpha/y)_y}{4\,y\,\sin^2\alpha} - \frac{\eta}{\sin^2\alpha}\right] + \frac{\nu_V}{H^2}\,\frac{1}{\rho_a S}\left(\frac{(\rho_a\,\eta)_\lambda}{S}\right)_\lambda$$

$$\left(\frac{\Psi_s}{S\rho_a}\right)_s = \eta \, \rho_a \, S \sin^2\alpha \, H^2 \tag{3.5.5}$$

$$\nu = \frac{\Psi_s}{H \, S \, \rho_a \, \sin\alpha} \tag{3.5.6}$$

$$w = -\frac{\Psi_y}{2 y a \, \rho_a \sin\alpha} \tag{3.5.7}$$

The boundary conditions are

$$\Psi = \left(\frac{\Psi_s}{S\rho_a}\right)_s = 0 \qquad at \; s = 1 \qquad \text{a}$$

$$\Psi = \Psi_s = 0 \qquad at \; s = 0 \qquad \text{b} \qquad \Bigg\} \tag{3.5.8}$$

$$\Psi = 0 \qquad at \; y = 0, \sqrt{\pi} \qquad \text{c}$$

$$\tilde{\theta}_s = 0 \qquad at \; s = 1 \qquad \text{a}$$

$$-\frac{k\nu \, \rho_a C_p \theta_a}{HS} \tilde{\theta}_s + 4\sigma\theta_a^3 \left\{\frac{4\kappa}{r c_{T_0}} \tilde{\theta} + \frac{1}{r}\frac{\partial\tilde{\theta}}{\partial c_T}\right\} = F_s - F_{Ta} \qquad \Bigg\} \tag{3.5.9}$$

$$\text{b}$$

$$at \; s = 0$$

3.6 Finite difference equations

We used a staggered mesh similar to the one used in the Boussinesq model. Figure 3.6.1 shows a typical cell with the position of the variables having the same subindices i,j. The complete grid is similar to Figure 2.6.2, with $\tilde{\theta}_{ij}$ instead of $\tilde{\rho}_{ij}$.
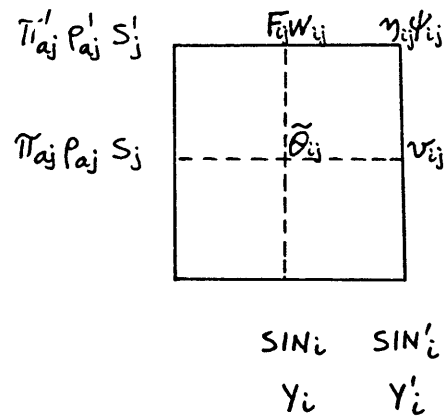
Figure 3.6.1: Typical cell with the position of the variables and functions having the subindices i j.
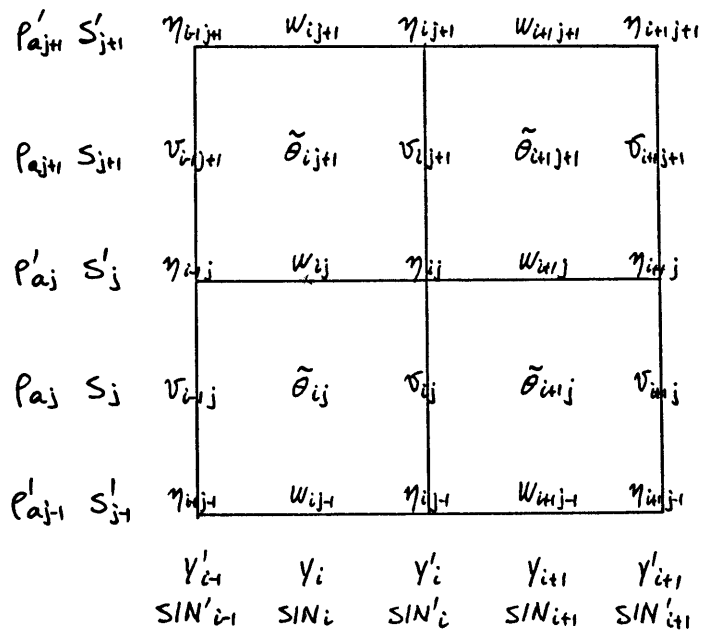

Figure 3.6.2: Cell centered at an " η_{ij} -point".

Equation (3.5.3) is straightforwardly written in finite

differences; we drop the superindex n.

$$\tilde{\Theta}_{ij}^{m+1} = \tilde{\Theta}_{ij}^{m-1} + 2\Delta t \left\{ -\frac{v_{ij}(\tilde{\Theta}_{ij} + \tilde{\Theta}_{i+ij})\,SIN_i' - v_{i-ij}(\tilde{\Theta}_{ij} + \tilde{\Theta}_{i-ij})\,SIN_{i-1}'}{4\,\Delta y\,a\,Y_i\,SIN_i} \right.$$

$$- \frac{w_{ij}(\tilde{\Theta}_{ij} + \tilde{\Theta}_{ij+1})\,P_{a\,j}' - w_{ij-1}(\tilde{\Theta}_{ij} + \tilde{\Theta}_{ij-1})\,P_{a\,j-1}'}{2\,\Delta s\,H\,S_j\,P_{a\,j}}$$

$$+ \frac{K_H}{a^2}\left[\frac{(\tilde{\Theta}_{i+ij}^{m-1} - \tilde{\Theta}_{ij}^m)\,SIN_i'/Y_i' - (\tilde{\Theta}_{ij}^{m-1} - \tilde{\Theta}_{i-ij}^{m-1})\,SIN_{i-1}'/Y_{i-1}'}{4\,Y_i\,SIN_i\,\Delta y^2}\right]$$

$$+ \frac{K_V}{H^2}\left[\frac{(\tilde{\Theta}_{ij+1}^{m-1} - \tilde{\Theta}_{ij}^{m-1})/S_j' - (\tilde{\Theta}_{ij}^{m-1} - \tilde{\Theta}_{ij-1}^{m-1})/S_{j-1}'}{\Delta s^2\,S_j}\right]$$

$$+ \left.\frac{F_{ij} - F_{ij-1}}{\Delta s\,H\,S_j\,P_{a\,j}\,C_p\,\Theta_a\,\pi_{a\,j}} \right\}$$

$$(3.6.1)$$

where $i = 2, ..., IM+1$

$j = 2, ..., JM+1$

and $F_{ij} = (F_s - F_{T_a} - F_T')_{ij}$ is the radiative flux. The "nonadiabatic"

component of the thermal radiative flux $F_{T_{ij}}'$ was updated every 20

steps.

The finite difference scheme for the nonlinear terms con-

serves both the mean value and the root mean square of $\tilde{\Theta}$, as

can be proved in a manner similar to Bryan's for an incompressible

model (section 2.5).

A simple finite difference vorticity equation similar to

equation (2.6.2) in the Boussinesq model was tried but nonlinear

instability ruined the computations after the equivalent of about thirty days. The problem was solved in the following way:

The continuity equation in stretched coordinates is

$$\frac{(v \sin \alpha)_y}{2y a \sin \alpha} + \frac{(w P_a)_s}{H S P_a} = 0$$

The simple finite-difference equivalent of the continuity equation,

$$\frac{(v_{ij} \sin'_i - v_{i-1j} \sin'_{i-1})}{2\Delta y\, a\, Y_i \sin_i} + \frac{(W_{ij}\, P'_{aj} - W_{ij-1}\, P'_{aj-1})}{\Delta s\, H\, S_j\, P_{aj}} = 0, \qquad (3.6.2)$$

is valid at the center of a grid cell (Figure 3.6.1), where $\tilde{\theta}_{ij}$ is, and not at the corners, where η_{ij} is. To obtain the finite-difference continuity equation valid at an " η_{ij}-point" (Figure 3.6.1) we have to average the finite difference continuity equations similar to (3.6.2) valid at the center of the four adjacent cells, where $\tilde{\theta}_{ij}$, $\tilde{\theta}_{i+1j}$, $\tilde{\theta}_{ij+1}$ and $\tilde{\theta}_{i+1j+1}$ are located (Figure 3.6.2).

The resulting continuity equation in finite differences valid at an " η_{ij} - point" is

$$\frac{\left(v_{i+1j}\, S_j\, P_{aj} + v_{i+1j+1}\, S_{j+1}\, P_{aj+1}\right) \sin'_{i+1} - \left(v_{i-1j}\, S_j\, P_{aj} + v_{i-1j+1}\, S_{j+1}\, P_{aj+1}\right)\sin'_{i-1}}{8\Delta y\, a\, Y'_i\, \sin'_i\, S'_j\, P'_{aj}}$$

$$+ \frac{\left(w_{ij+1}\, Y_i\, \sin_i + w_{i+1j+1}\, Y_{i+1}\, \sin_{i+1}\right) P'_{aj+1} - \left(w_{ij-1}\, Y_i\, \sin_i + w_{i+1j-1}\, Y_{i+1}\, \sin_{i+1}\right) P'_{aj-1}}{4\Delta s\, H\, Y'_i\, \sin'_i\, S'_j\, P'_{aj}} = 0$$

$$(3.6.3)$$

According to Bryan's scheme (section 2.5) the flux terms in

the vorticity equation should be written in a form consistent with this finite difference continuity equation. Therefore the finite difference vorticity equation equivalent to (3.5.4) was written as follows:

$$\eta_{ij}^{m+1} = \eta_{ij}^{m-1} + 2\Delta t \left\{ - \left[(\varpi_{i+1j}\, S_j\, P_{a_j} + \varpi_{i+1j+1}\, S_{j+1}\, P_{a_{j+1}}) SIN'_{i+1}\, (\eta_{ij} + \eta_{i+2j}) \right. \right.$$

$$- (\varpi_{i-1j}\, S_j\, P_{a_j} + \varpi_{i-1j+1}\, S_{j+1}\, P_{a_{j+1}}) SIN'_{i-1}\, (\eta_{ij} + \eta_{i-2j})] / (16\, \Delta y\, a\, Y'_i\, SIN'_i\, S'_j\, P'_{a_j})$$

$$- [(w_{ij+1}\, Y_i\, SIN_i + w_{i+1j+1}\, Y_{i+1}\, SIN_{i+1})\, P'_{a_{j+1}}\, (\eta_{ij} + \eta_{ij+2}) -$$

$$- (w_{ij-1}\, Y_i\, SIN_i + w_{i+1j-1}\, Y_{i+1}\, SIN_{i+1})\, P'_{a_{j-1}} (\eta_{ij} + \eta_{ij-2})] / (8\, \Delta s\, H\, Y'_i\, SIN'_i\, S'_j\, P'_{a_j})$$

$$- g\, / (4\, \Delta y\, a\, Y'_i\, SIN'_i\, P'_{a_j})\, \left[\tilde{\theta}_{i+1j} + \tilde{\theta}_{i+1j+1} - \tilde{\theta}_{ij} - \tilde{\theta}_{ij+1} \right]$$

$$+ \frac{\nu_H}{a^2} \left\langle \left[(\eta_{i+1j}^{m-1}\, SIN'_{i+1} - \eta_{ij}^{m-1}\, SIN'_i)\, SIN_{i+1}/Y_{i+1} - (\eta_{ij}^{m-1}\, SIN'_i - \eta_{i-1j}^{m-1}\, SIN'_{i-1}) \times \right. \right.$$

$$\times SIN_i/Y_i] / (4\, \Delta y^2\, Y'_i\, SIN'^2_i) - \eta_{ij}^{m-1}/SIN'^2_i \Big\rangle + \frac{\nu_V}{H^2} \left[(\eta_{ij+1}^{m-1}\, P'_{a_{j+1}} - \eta_{ij}^{m-1}\, P'_{a_j})/S_{j+1} \right.$$

$$- (\eta_{ij}^{m-1}\, P'_{a_j} - \eta_{ij-1}^{m-1}\, P'_{a_{j-1}})/S_j] / (\Delta s^2\, S'_j\, P'_{a_j}) \Big\}$$

where $i = 2, \ldots, IM$

$j = 2, \ldots, JM$

<div align="right">(3.6.4)</div>

The scheme is conservative if we define the vorticity at the center of a cell as the weighted average of the vorticity at the four corners, (Figure 3.6.1) and if we assume that there is symmetry at the boundaries. Then it can be shown that the contribution of the nonlinear terms to the integral:

$$I_1 = \frac{1}{H} \int_0^\pi \int_0^H \overline{\frac{\partial \eta}{\partial t} \sin \alpha \, P_a} \, d\alpha \, dz \approx$$

$$\approx \frac{1}{4} \sum_{i=2}^{IM+1} \sum_{j=2}^{JM+1} \left\{ \frac{(\eta_{ij}^{m+1} - \eta_{ij}^{m-1})}{2\Delta t} \, 2 \gamma_i' \, SIN_i' \, P_{a_j}' \, S_j' + \right.$$

$$\frac{(\eta_{ij-1}^{m+1} - \eta_{ij-1}^{m-1})}{2\Delta t} \, 2 \gamma_i' \, SIN_i' \, P_{a_{j-1}}' \, S_{j-1}' + \frac{(\eta_{i-1j}^{m+1} - \eta_{i-1j}^{m-1})}{2\Delta t} \, 2 \gamma_{i-1}' \, SIN_{i-1}' \, P_{a_j}' \, S_j'$$

$$\left. + \frac{(\eta_{i-1j-1}^{m+1} - \eta_{i-1j-1}^{m-1})}{2\Delta t} \, 2 \gamma_{i-1}' \, SIN_{i-1}' \, P_{a_{j-1}}' \, S_{j-1}' \right\}$$

is zero, as well as their contribution to the similar finite difference equivalent of

$$I_2 = \frac{1}{H} \int_0^\pi \int_0^H \overline{\frac{\partial \eta^2}{\partial t} \sin \alpha \, P_a} \, d\alpha \, dz$$

This conservative finite-difference scheme succeeded in eliminating the problem of catastrophic nonlinear instability. It had the disadvantage that truncation errors were increased by roughly four times over the simpler scheme, since it used values of η situated at a distance of 2Δ from the centerpoint instead of Δ. This disadvantage was overcome in an improved version of the scheme used for the rotating case (Chapter 5).

Equations (3.5.5) to (3.5.7) are now written simply as

$$\psi_{ij+1}^{n+1} - \psi_{ij}^{n+1}\left(1 + \frac{\rho_{aj+1} S_{j+1}}{\rho_{aj} S_j}\right) + \frac{\rho_{aj+1} S_{j+1}}{\rho_{aj} S_j}\, \psi_{ij-1}^{n+1} = \left(\Delta s^2 H^2 \rho_{aj}' S_j'\, \rho_{aj+1} S_{j+1} SIN_i'\right)\eta_{ij}^{n+1}$$

(3.6.6)

$$\text{where } j = 2, \ldots, JM$$

$$v_{ij}^{n+1} = \frac{\psi_{ij}^{n+1} - \psi_{ij-1}^{n+1}}{\Delta s\, H\, S_j\, \rho_{aj}\, SIN_i'}$$

(3.6.7)

$$\text{where } \quad i = 2, \ldots, IM$$
$$\qquad\qquad j = 2, \ldots, JM+1$$

$$w_{ij}^{n+1} = -\frac{\psi_{ij}^{n+1} - \psi_{i-1j}^{n+1}}{2\Delta y\, a Y_i\, SIN_i\, \rho_{aj}'} \qquad \text{where } \quad i = 2, \ldots, IM+1$$
$$\qquad\qquad\qquad\qquad\qquad\qquad\qquad j = 2, \ldots, JM$$

(3.6.8)

Equation (3.6.6) can be written as a matrix equation

$$Q\, \underline{\Psi}^{n+1} = M\, \underline{H}^{n+1}$$

where Q needs to be inverted only once so that (3.6.6) is replaced

by

$$\underline{\Psi}^{n+1} = Q^{-1}\, M\, \underline{H}^{n+1}$$

(3.6.9)

The boundary conditions in finite differences are the

following:

$$\psi_{i1}^{n+1} = \psi_{iJM+1}^{n+1} = 0 \qquad \text{for} \quad i = 2, \ldots, IM \quad \Big\}$$

(3.6.10)

$$\psi_{1j}^{n+1} = \psi_{IM+1j}^{n+1} = 0 \qquad \text{for} \quad j = 2, \ldots, JM$$

$$\eta_{ij}^{n+1} = \eta_{IM+1j}^{n+1} = 0 \qquad \text{for} \quad j = 2, \ldots, JM$$

(3.6.11)

$$\eta_{i,JM+1}^{n+1} = 0 \qquad \text{for } i = 2, \ldots, IM \qquad (3.6.12a)$$

The non-slip boundary condition at the bottom is introduced in the model as follows: from (3.2.13) we have

$$\eta = \frac{(\psi_z / \rho_a)_z}{\rho_a \sin^2 \alpha} = \frac{\psi_{zz}}{\rho_a^2 \sin^2 \alpha} - \frac{\rho_{az}}{\rho_a^3} \frac{\psi_z}{\sin^2 \alpha}$$

At $\quad z = 0$, $\quad \psi = \psi_z = 0$

Then

$$\left(\eta \right)_{z=0} = \left(\frac{\psi_{zz}}{\rho_a^2 \sin^2 \alpha} \right)_{z=0} \quad ,$$

Making a Taylor expansion of ψ about $z = 0$ as we did in section 2.6, and solving for ψ_{zz} at $z = 0$, we get

$$\left(\psi_{zz} \right)_{i1} = \frac{2 z_2}{z_1^2 (z_2 - z_1)} \psi_{i2} - \frac{2 z_1}{z_2^2 (z_2 - z_1)} \psi_{i3} + O(\Delta z)^2$$

Then

$$\eta_{i1}^{n+1} = \left[\frac{2 z_2}{z_1^2 (z_2 - z_1)} \psi_{i2}^{n+1} - \frac{2 z_1}{z_1^2 (z_2 - z_1)} \psi_{i3}^{n+1} \right] \frac{1}{\rho_{a_1}^{'2} \sin_i^{'2}} \qquad (3.6.12b)$$

$$\text{for } i = 2, \ldots, IM$$

From equations (3.5.9) the boundary conditions on the potential temperature are

$$\tilde{\theta}_{i\,JM+2}^{m+1} = \tilde{\theta}_{i\,JM+1}^{m+1} \qquad \text{where} \quad i = 2, ..., IM+1 \qquad\qquad (3.6.13a)$$

(no turbulent transfer of heat at the top)

and

$$C_1\,\tilde{\theta}_{i1}^{m+1} = C_2\,\tilde{\theta}_{i2}^{m+1} + \left(F_s - F_{T_a}\right)_{i1} \qquad\qquad (3.6.13b)$$

(zero net flux of heat at the bottom)

where $i = 2, ..., IM+1$,

$$C_1 = \frac{K_v\,C_p\,\rho'_{a_1}\,\theta_a}{\Delta_A H\,S'_1} + \frac{4\sigma\theta_a^4}{r\,\Delta z_{T_1}} + \frac{8\,\sigma\,\theta_a^4\,K_v}{r\,z_{T_0}}$$

and

$$C_2 = \frac{K_v\,C_p\,\rho'_{a_1}\,\theta_a}{\Delta_A H\,S'_1} + \frac{4\sigma\theta_a^4}{r\,\Delta z_{T_1}} - \frac{8\,\sigma\,\theta_a^4\,K_v}{r\,z_{t_0}}$$

3.7 Numerical values of the physical data

In this model we used the following numerical values:

$$a = 6.05 \times 10^8 \text{ cm}$$

$$H = 5.3 \times 10^6 \text{ cm}$$

$$g = 8.5 \times 10^2 \text{ cm}/\text{sec}^2$$

$$C_p = 8.5 \times 10^6 \text{ cm}^2/(\text{sec}^2\,{}^\circ K)$$

$$\Gamma = g/C_p = 10^{-4}\ {}^\circ K/\text{cm}$$

$$R = 1.9 \times 10^6 \text{ cm}^2/(\text{sec}^2\,{}^\circ K)$$

$$\sigma = 5.67 \times 10^{-5} \; g \; / (sec^3 \, ^\circ K^4)$$

$$\kappa = R/C_p = 0.224$$

$$T_{eff} = 230^\circ K \quad (effective \; emission \; temperature)$$

$$\sigma T_{eff}^4 = S_0 \frac{(1-A)}{4} = 1.586 \; g \, / sec^3$$

$$\theta_a = T(z=0) = 730^\circ K$$

$$p_o = 100 \, atm = 1.013 \times 10^8 \, dyne \, / cm^2$$

$$\zeta_s^* = 13.76$$

$$\zeta_T^* = 222.0$$

$$\nu_H = \chi_H = 10^{11} \; cm^2/sec$$

$$\nu_V = K_V = 10^4 \; cm^2/sec$$

Although C_p depends on the temperature, it was taken as a con-
stant, with a value corresponding roughly to 300°K. This introduces
an error of the order of ten percent. The values of the pressure
and temperature at the surface are similar to those reported by the
Venera 7 (Avduevsky et al., 1971), 90 ± 15 atm and 748 ± 20 °K respec-
tively.

The temperature at the top of the model was taken as 200°K
and by trial and error a value for the optical thickness of the at-
mosphere in the long wave range was found such that under an adia-
batic stratification the effective radiative temperature was 230°K,
thus balancing the shortwave incoming radiation. The value obtained,
$\zeta_T^* = 222.0$ is rather high but not unreasonably so or large enough,
with the assumed transmission of solar radiation, to allow a green-
house effect to maintain the observed high surface temperature

(Gierasch and Goody, 1970).

We used a high value for the effective optical thickness of the atmosphere in the short wave region so that most of the solar radiation was assumed to be absorbed in the upper third of the atmosphere. This allowed a better comparison of the results with those of the Boussinesq model, but more cases should be run, corresponding to absorption mainly in the lower atmosphere, or even much of the solar radiation reaching the surface.

Unrealistically large values for the horizontal coefficients of eddy viscosity and diffusivity have been used for two reasons: (1) except near the antisolar point, the horizontal scale is very large, so that even these high values of ν_H and κ_H will affect the results only quantitatively, but not qualitatively; (2) it allows a better comparison with the Boussinesq model in which we used the same numbers.

Figure (3.7.1) shows the intensity of the solar radiation as a function of latitude and height computed with $\zeta_s^* = 13.76$.

Figure (3.7.2) shows the sum of solar and thermal radiation in an adiabatic atmosphere and Figure (3.7.3) the corresponding heating rate. Note that long wave radiation tends to cool the atmosphere at all levels, as shown in Figure (3.7.3) for the dark hemisphere. This result follows from the grey atmosphere approximation which was used: Gierasch and Goody (1970) have shown that in a deep adiabatic atmosphere, the thermal radiative flux can be approximated by

$$F_T \simeq \frac{8 \sigma T^4 \kappa}{r z_T} \qquad (3.7.1)$$
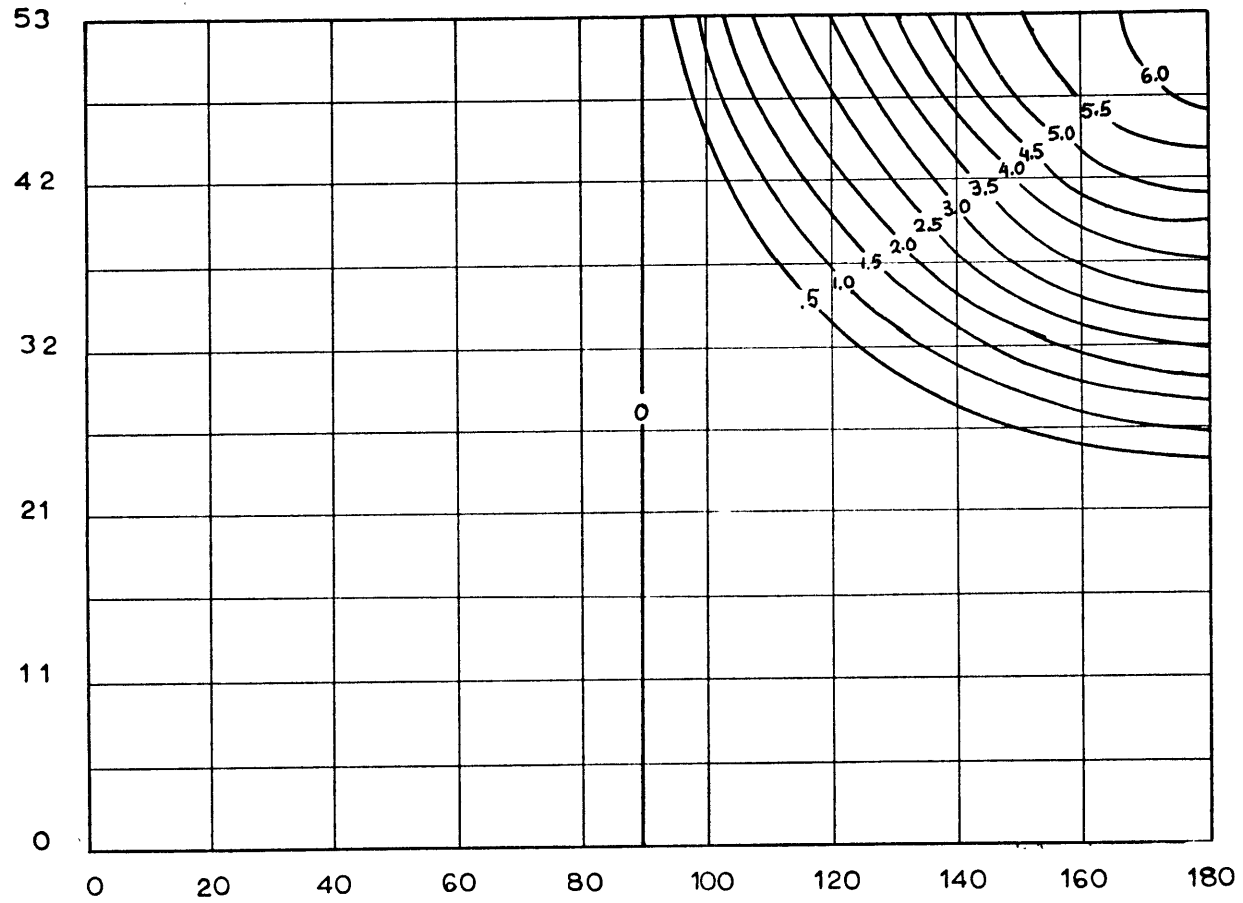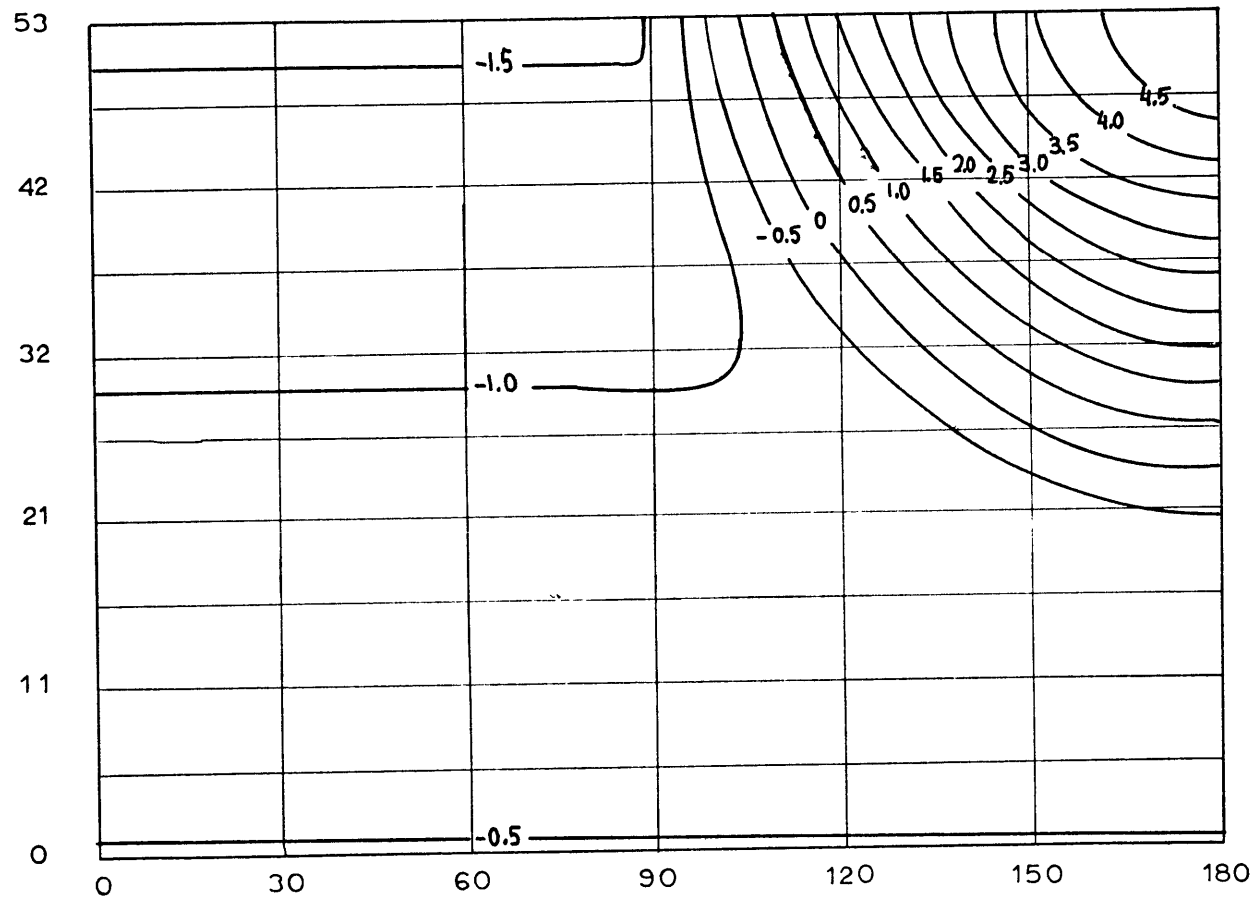
Figure 3.7.1: Solar radiation flux in 10^5 g/sec^3.

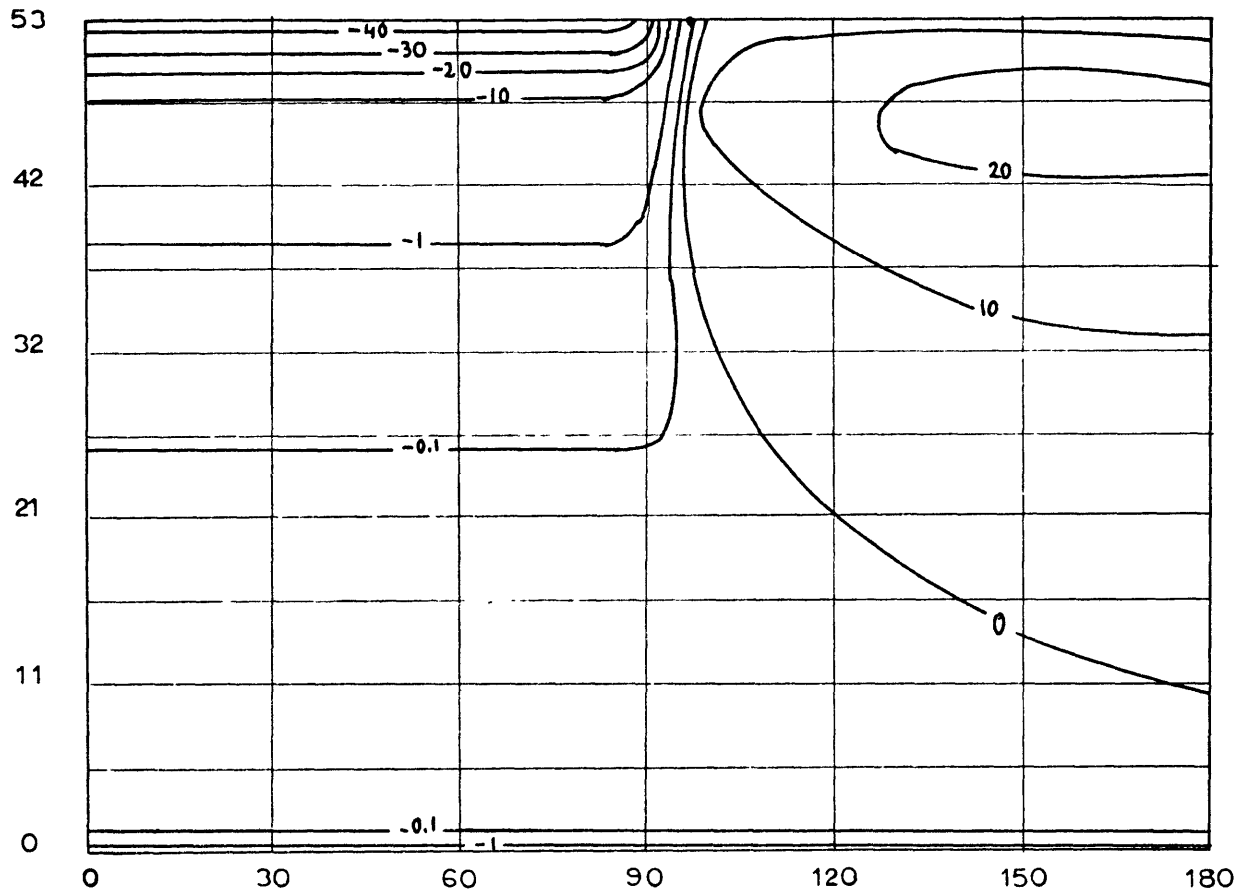Figure 3.7.2: Flux of solar plus thermal radiation in an adiabatic
stratification.

Figure 3.7.3: Heating rate $\dfrac{q_{v\alpha}}{C_p \, \rho_\alpha \, \theta_\alpha \, \overline{\Pi}_\alpha}$ in an adiabatic stratification. Units of 10^{-9}sec^{-1}.

which can also be obtained from our equation (3.3.9) by allowing

$\tau_T \longrightarrow \infty$. From equations (3.2.5), (3.3.4) and (3.7.1)

$$F_T \approx \frac{8\sigma \theta_a^4 \kappa}{r \, \tau_{T_0}} \left(1 - s\right)^{4 - 1/\kappa} \tag{3.7.2}$$

The heating rate corresponding to this thermal flux is

$$H_T = -\frac{1}{C_p \pi_a \rho_a} \frac{\partial F_T}{\partial z} = -\frac{g}{C_p^2 \theta_a \pi_a \rho_a} \frac{\partial F_T}{\partial s} \tag{3.7.3}$$

and from equations (3.2.5), (3.7.2) and (3.7.3)

$$H_T = (4\kappa - 1) \frac{8 g \sigma \theta_a^3}{C_p^2 \rho_a \, r \tau_{T_0}} \left(1 - s\right)^{3 - 2/\kappa} \tag{3.7.4}$$

In our computations we used a value of C_p corresponding to CO_2 at 300°K, which gives $(4\kappa - 1) = -0.104$. In Table 1 of Gierasch and Goody (1970) it may be seen that for any temperature higher than $\sim 210°K$ the factor $(4\kappa - 1) < 0$ so that thermal radiation will cool the atmosphere at all levels. The cooling rate in units of relative potential temperature increase per unit time varies from $4 \times 10^{-8} sec^{-1}$ at the top to less than $1 \times 10^{-10} sec^{-1}$ in the interior, giving thermal relaxation time constants of the order of several Venus solar days at the top to about 10^3 Venus solar days in the interior (Figure 3.7.3).

3.8 Initial conditions and computational procedure

Initially the atmosphere was adiabatically stratified and in a state of no motion.

The computational procedure was similar to the one used for the Boussinesq model (section 2.7) except that the new field of F_T' , the thermal radiation flux corresponding to the departure of the atmosphere from the initial adiabatic stratification, was computed every 20 double time steps.

The model was run for 1.5×10^7 secs of simulated time, (about 1.5 Venus solar days). At that time the system had approximately converged to an equilibrium state except near the bottom.

3.9   Results

The results obtained with the non-rotating quasi-Boussinesq model are rather similar to those of the nonrotating Boussinesq model. The main difference is that the inclusion of a basic stratification and a more realistic treatment of radiation confine the circulation mostly to the upper third of the atmosphere. This result was also obtained by Hess (1968) in a model in which he used pressure as vertical coordinate.

Figure 3.9.1 shows the meridional mass stream function. The strength of the velocity at any point is proportional to the inverse of the spacing divided by the density and by the sine of the colatitude. There is one strong Hadley cell in the upper third of the atmosphere. The smaller and weaker cells below are probably frictionally driven and correspond to horizontal velocities of the order of 1 cm/s in the lower atmosphere and less than 1 m/s at middle levels. The asymmetry of the circulation is more apparent in Figure 3.9.2 where the vortex strength $\eta = \dfrac{U_\lambda}{\rho_a \, a \sin \theta}$ is shown. In this model we see that the presence of the lower boundary has very little
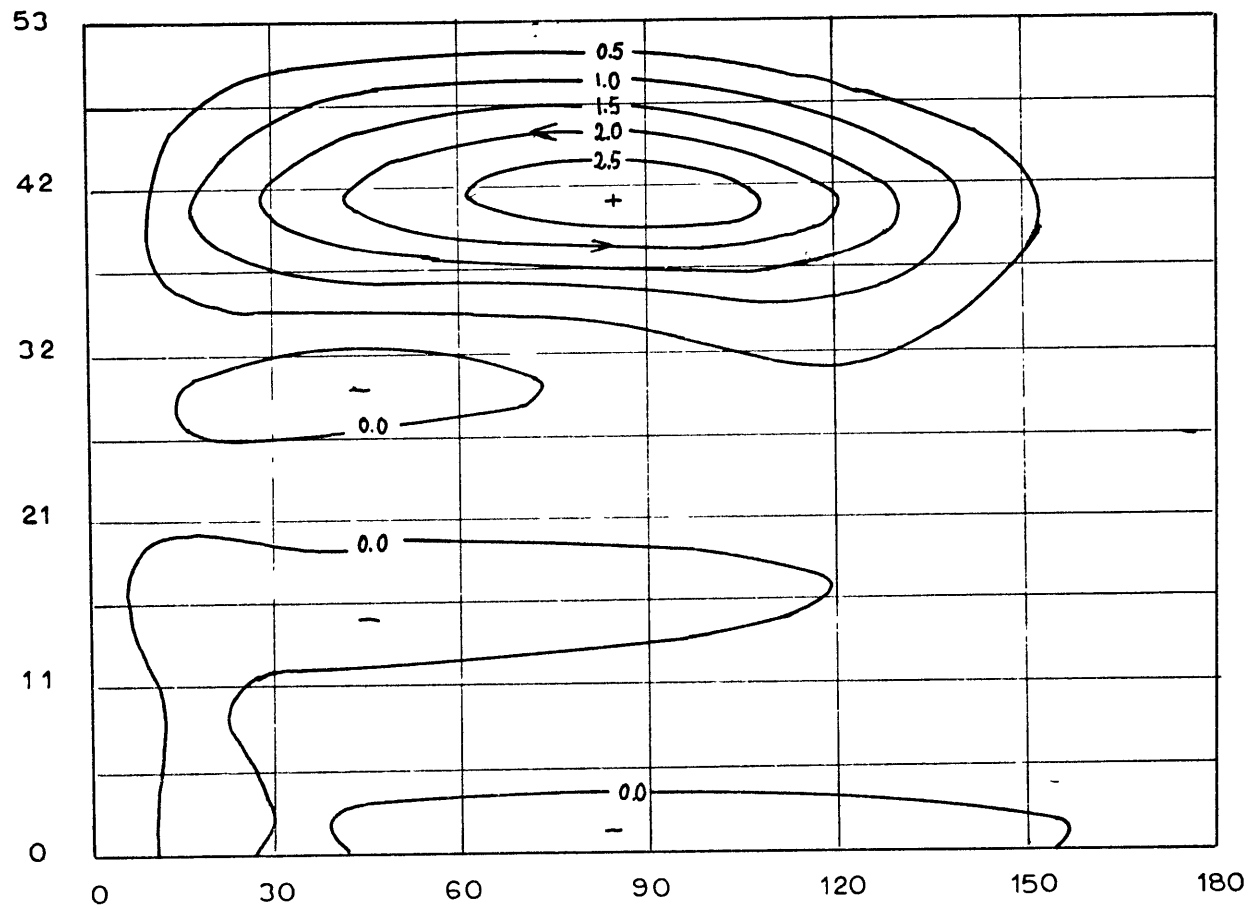
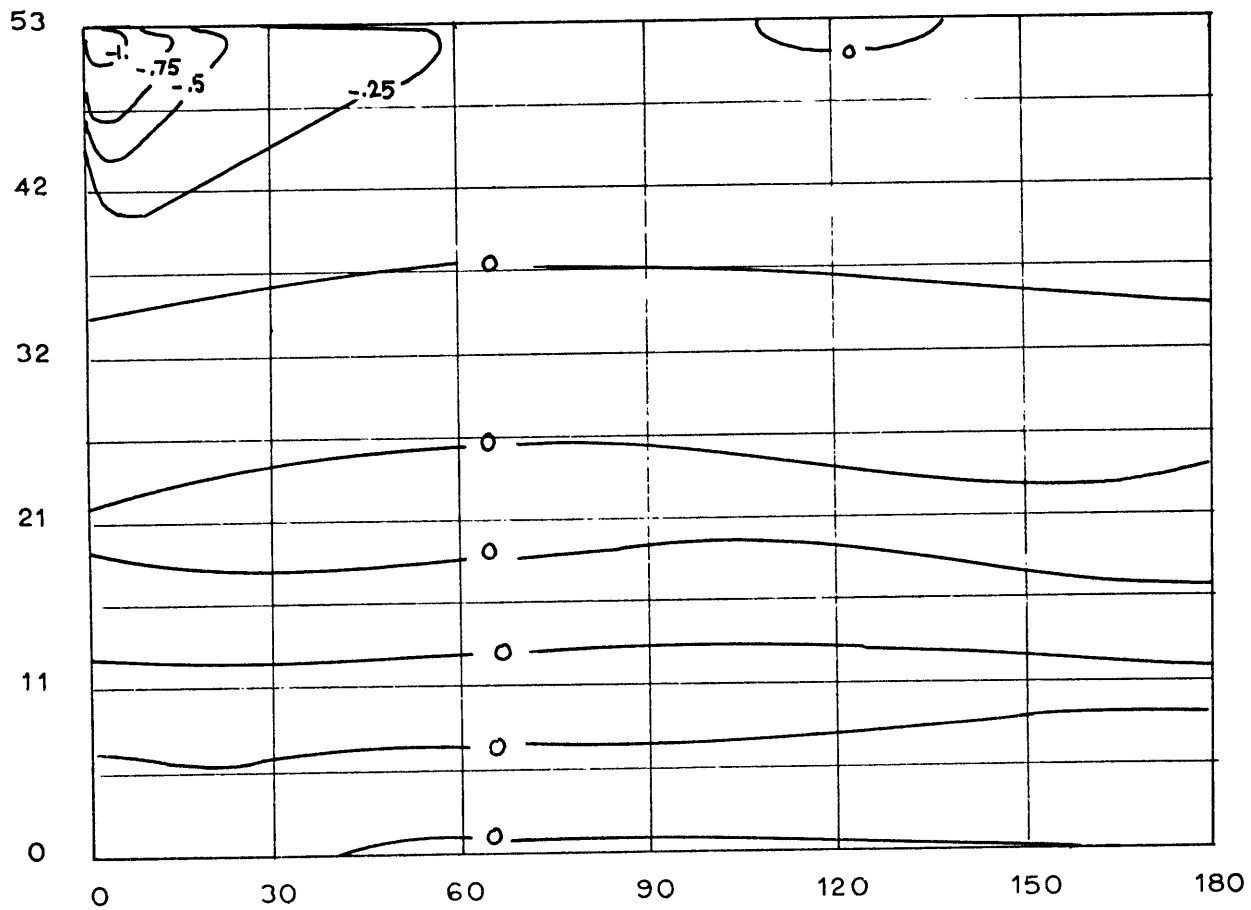Figure 3.9.1: Meridional mass stream function after running 1.5×10^7 sec.

Figure 3.9.2: Vortex strength $\eta = \dfrac{v_z}{\rho_a \sin\alpha}$ in $cm^3 g^{-1} sec^{-1}$.

effect on the circulation as compared to the Boussinesq model, in which the return flow tends to be strongest very near the lower boundary.

Figures 3.9.3 and 3.9.4 show the horizontal and vertical velocity components corresponding to Figure 3.9.1 The maximum velocity in the top boundary layer is about 30 m/s, about twice as much as in the Boussinesq model. However, owing to the basic adiabatic stratification of the density the return flow occupies a much narrower layer than the direct flow from the SS to the AS point, and has a maximum of only 6.6 m/s. This return flow in turn produces a small region of flow from SS to AS with a maximum speed of 1 m/s, at a height of 32 km, and below that velocities are of the order of a few cm/s.

The picture of the vertical velocity is very similar to the one obtained with the Boussinesq model except in its confinement to the upper part of the atmosphere. The maximum speed of the down-going jet at the AS point is about 44 cm/s, compared to about 60 cm/s in the Boussinesq case. Again we find that although the downward current at the AS point is very strong, much stronger than the upward motion at the SS point, there is nevertheless upward motion in only slightly more than half of the atmosphere, and downward motion is not confined to the "mixing region" near the AS point, but occurs in slightly less than half of the atmosphere. This kind of model apparently would not be able to explain an almost complete cloud coverage of the atmosphere of Venus, as proposed by Goody and Robinson (1966).
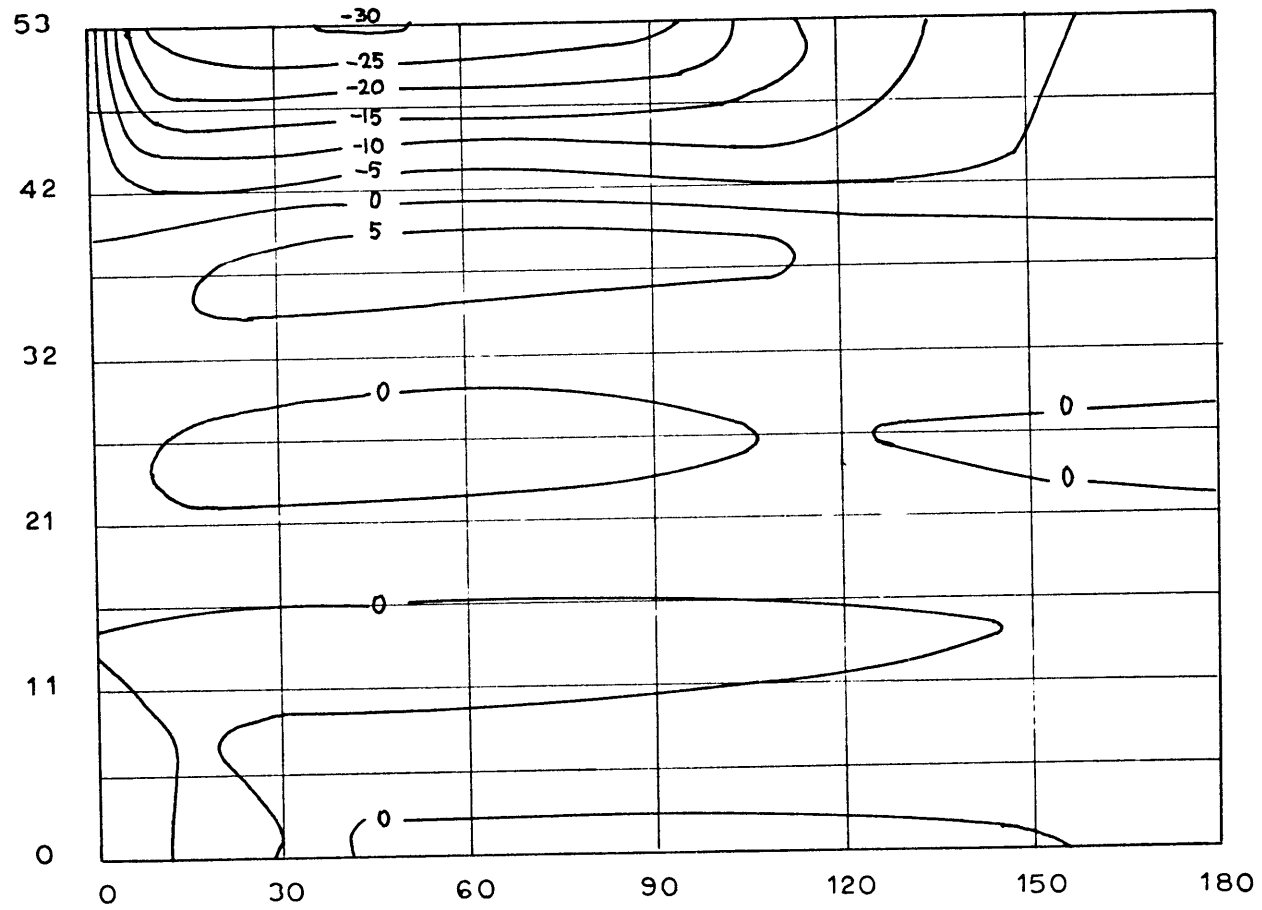
Figure 3.9.5 shows a cross section of the relative
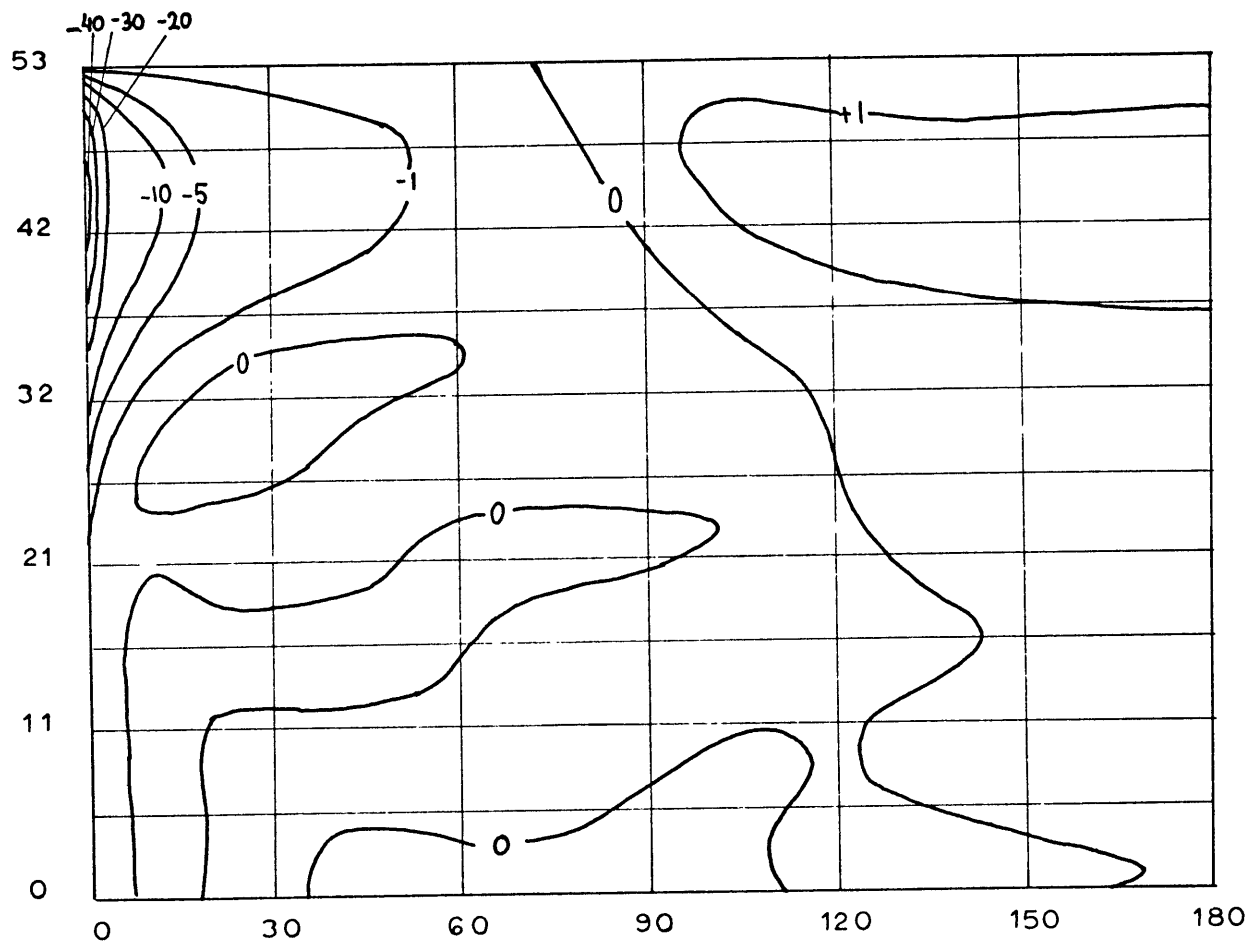
Figure 3.9.3: Horizontal velocity v in m/sec.
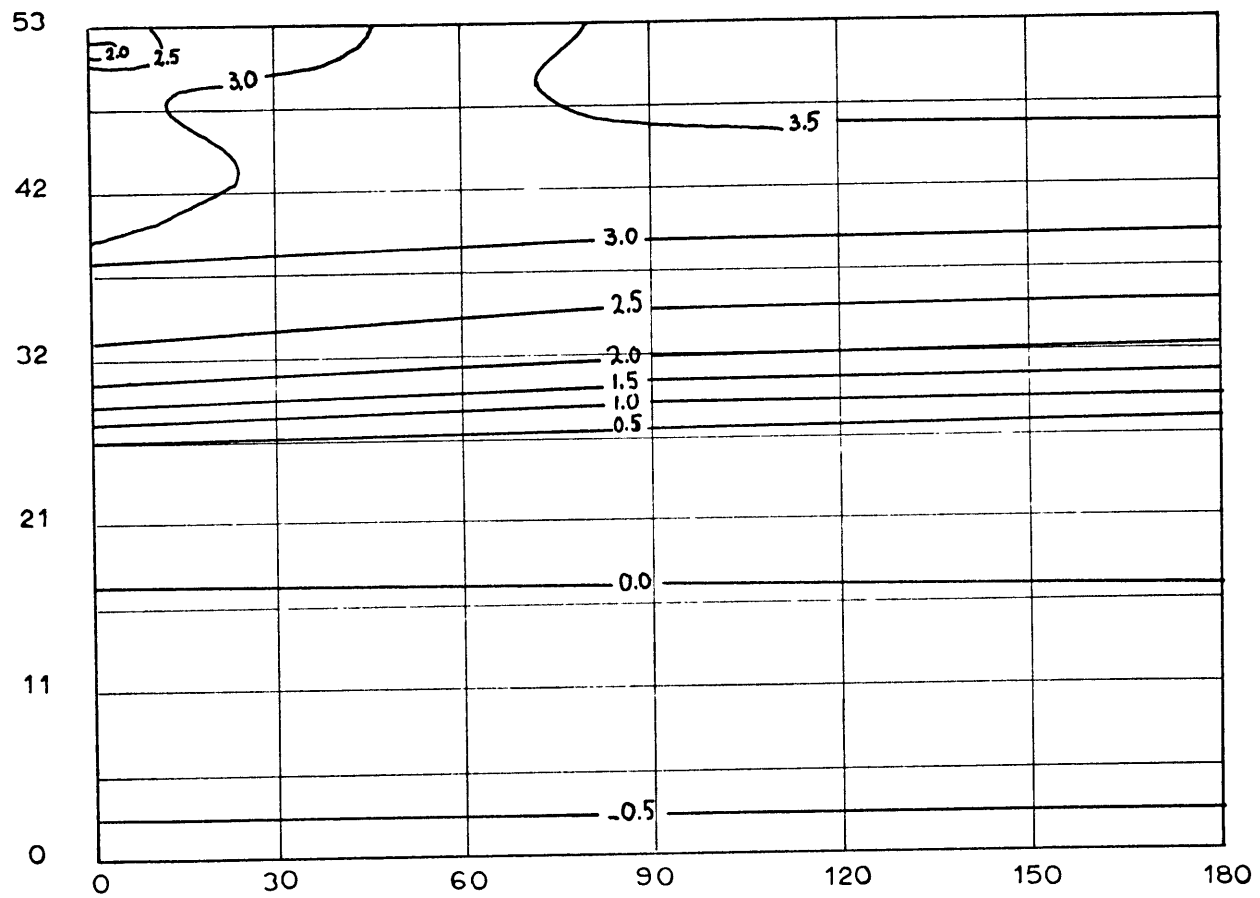
Figure 3.9.4: Vertical velocity w in cm/sec.

Figure 3.9.5: Relative potential temperature departure $\tilde{\theta}$ in units of 10^{-2}.

potential temperature $\tilde{\theta}$. The shaded regions near the top corres-
pond to a weakly unstable stratification ($\partial\tilde{\theta}/\partial z \sim -0.5°K/km$). The
top 20 km of the atmosphere is almost neutrally stable or slightly
unstable. This is true even in the day hemisphere because the maxi-
mum heating due to solar radiation occurs not at the top but at about
6 km below the top. Between 26 and 32 km there is a region with a
stronger static stability, with $\partial\theta/\partial z \sim 1.5°K/km$. The beginning of
this stable layer gives the lower limit of penetration of the direct
Hadley cell. The indirect cell occurs within the very stable region.
This circulation is similar to the roll vortices observed in a fluid
contained between two cylinders rotating in opposite directions. The
rolls produced by the inertially unstable centrifugal field near the
inner cylinder, frictionally drive indirect rolls in the stable region
near the outer cylinder (G.I. Taylor, 1923). In the lower half
of the atmosphere the stratification of $\tilde{\theta}$ is slightly stable, with
a vertical gradient of about 0.3°K/km. As discussed later on, this
is probably due to the fact that radiative processes have not acted
long enough to produce a more isothermal stratification.

We compute the corresponding field of temperature:

$$T = \pi_a \theta_a + \pi_a \theta' + \pi'\theta_a \tag{3.9.1}$$

Strictly speaking, the value of π' at the top of the at-
mosphere is different from zero, since a horizontal gradient of pres-
sure is required to balance the horizontal advection of momentum at
the top (Equation 3.2.7). π' should have been computed as
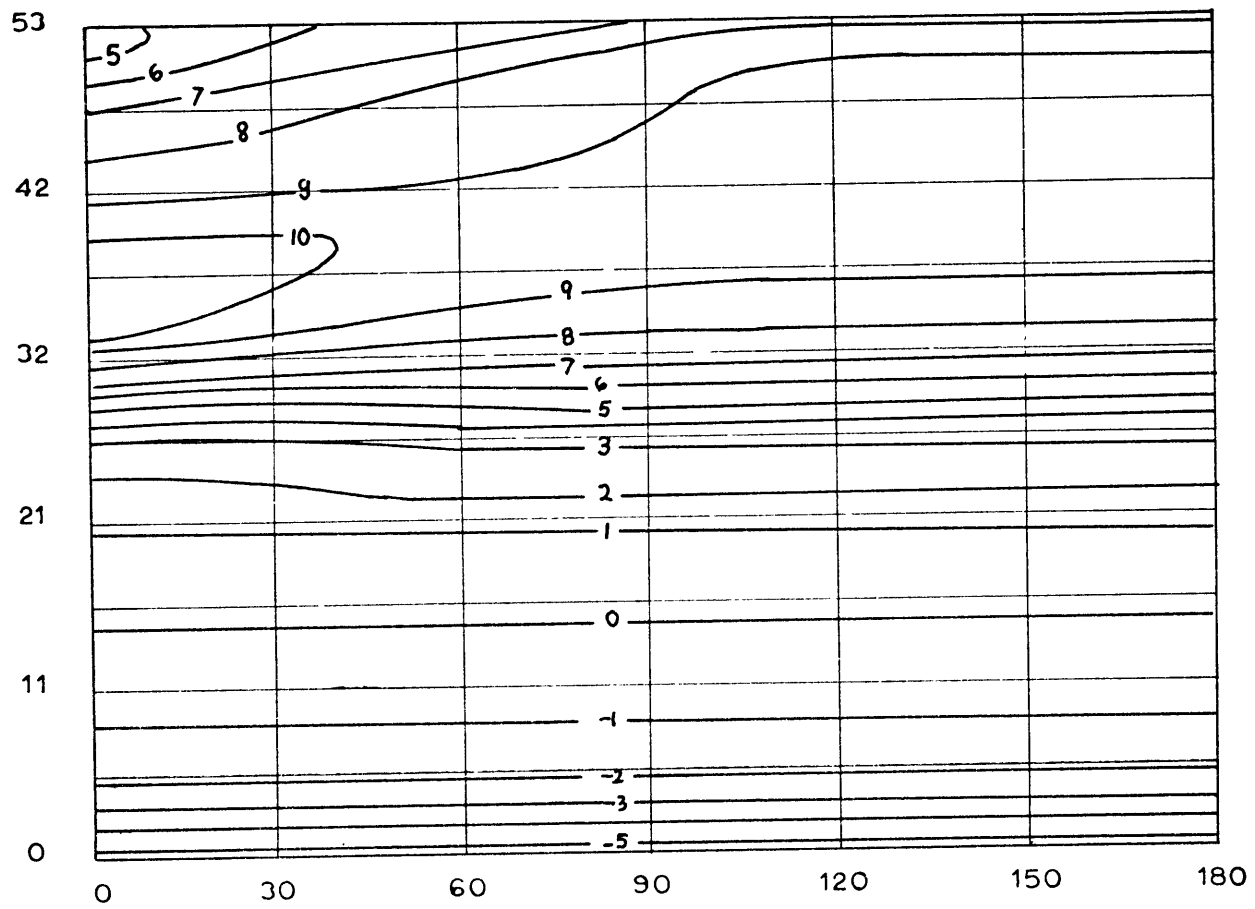described at the end of section 3.2. However we can estimate the

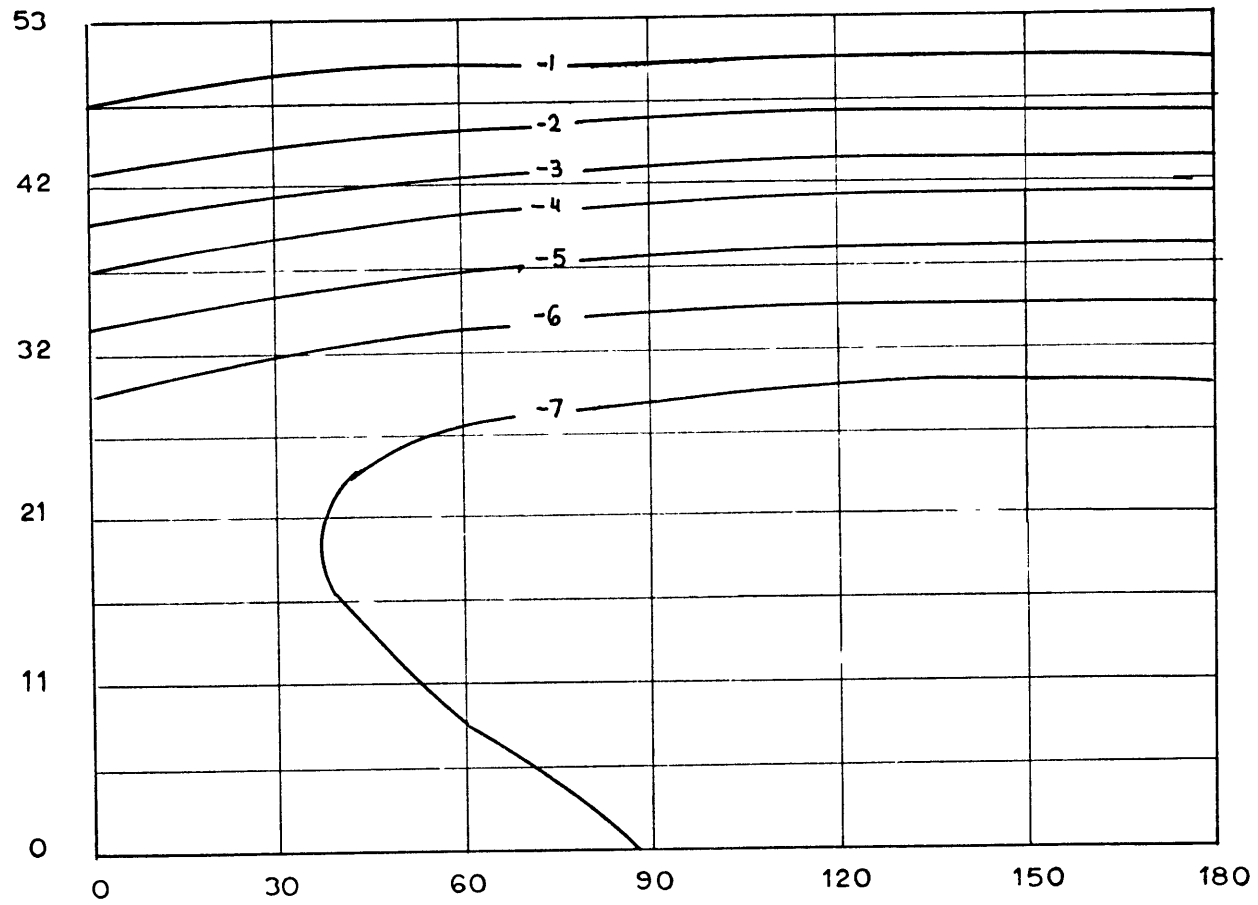Figure 3.9.6: $\pi_a \theta'$ in °K.

Figure 3.9.7: $\Pi' \theta_a$ in °K.

maximum amplitude of π' at the top from equation (3.2.7), and from this we find that it can be neglected in the computation of the temperature (see Appendix C). π' is computed from equation (3.2.8) written in stretched coordinates:

$$\pi' = \frac{H}{D} \int_\lambda^1 \tilde{\theta}\, S\, d\lambda \tag{3.9.3}$$

or in finite differences

$$\pi'_{ij} = \pi'_{ij+1} - \frac{H\, \Delta\lambda}{2D}\, S'_j \left(\hat{\theta}_{ij} + \tilde{\theta}_{ij+1} \right) \tag{3.9.4}$$

Figures (3.9.6) and (3.9.7) are the second and third components of the temperature in equation (3.9.1). If we compare them we see that they are of the same order of magnitude, except very near the top. Therefore the use of the approximation

$$T \simeq \pi_a \left(\theta_a + \theta' \right) \tag{3.9.5}$$

instead of (3.9.1) is inconsistent with the quasi-Boussinesq approximation, as shown by Ogura and Phillips (1962). Nevertheless there is some justification "a posteriori" for the use that was made of equation (3.9.5) instead of (3.9.1) in the computation of long wave radiation. First, it allowed the use of a simple method of computation of the thermal radiative flux, without which the computation time would have been prohibitive; second, the correction of the radiative flux due to departures from adiabatic stratification is negligible compared to the basic radiation field except near the top of the

atmosphere (Table 3.9.2), and in that region the third term in equation (3.9.1) is negligible. However, if the computations had been continued long enough, the lower atmosphere would probably have been in a state close to radiative-diffusive equilibrium. In that case the stratification in the lower atmosphere would have been much further from adiabatic. Thus the whole quasi-Boussinesq approximation is less accurate than appears at the present stage of the calculation for the lower atmosphere. Also, if a still smaller value of K_v had been used to simulate conditions in a stable region, the temperature stratification would have been still further from the adiabatic and the quasi-Boussinesq approximation still less accurate. (See discussion in Chapter 5.)

The temperature contrast between the subsolar and antisolar points is about 2%, or roughly 4°K, much smaller than the 23°K obtained with the Boussinesq model.

In Tables (3.9.1) and (3.9.2) we display the numerical values of the terms in the vorticity and potential temperature equation at nine different points, whose position is shown in Figure (3.9.8). The vorticity and energy equations (3.2.12) and (3.2.10) are reproduced here for the sake of clarity.

$$\frac{\partial \eta}{\partial t} = - \frac{(v\,\eta\,\sin\alpha)_\alpha}{a\sin\alpha} - \frac{(w\,\eta\,\rho_a)_z}{\rho_a} - \frac{g}{a\,\rho_a\sin\alpha}\frac{\partial\tilde{\theta}}{\partial\alpha}$$

Time Der.   Hor. Adv.   Vert. Adv.   Driving

$$+ \frac{\nu_H}{a^2}\left[\frac{((\eta\sin\alpha)_\alpha\sin\alpha)_\alpha}{\sin^2\alpha} - \frac{\eta}{\sin^2\alpha}\right] + \frac{\nu_v}{\rho_a}\frac{\partial^2\rho_a\eta}{\partial z^2}$$
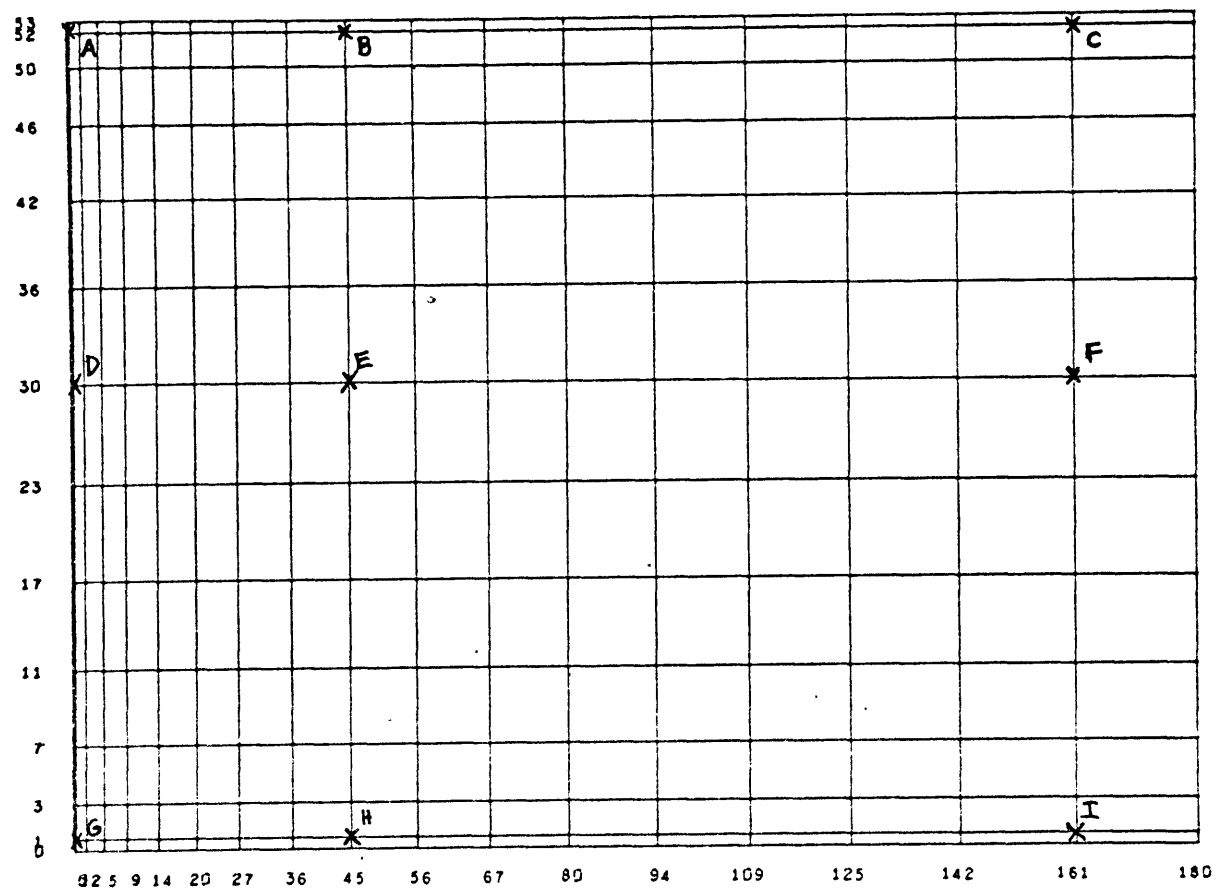
Hor. Visc.   Vert. Visc.

Figure 3.9.8: Position of the 9 points at which the balance of terms in the vorticity and energy equation is shown.

$$\frac{\partial \tilde{\theta}}{\partial t} = - \frac{(v\,\tilde{\theta}\,\sin\alpha)_{\alpha}}{a\,\sin\alpha} - \frac{(w\,\tilde{\theta}\,\rho_{a})_{z}}{\rho_{a}} + \frac{K_{H}}{a^{2}}\frac{(\tilde{\theta}_{\alpha}\,\sin\alpha)_{\alpha}}{\sin\alpha} + K_{V}\,\tilde{\theta}_{zz}$$

Time Der.   Hor. Adv.   Vert. Adv.   Hor. Diff   Vert. Diff

$$+ \frac{1}{C_{p}\,\Pi_{a}\,\rho_{a}\,\theta_{a}}\frac{\partial (F_{s} - F_{Ta})}{\partial z} - \frac{1}{C_{p}\,\Pi_{a}\,\rho_{a}\,\theta_{a}}\frac{\partial F_{T}'}{\partial z}$$

Basic Rad. Heating   Pert. Rad. Heating

The balance of terms in the vorticity and energy equations (Tables 3.9.1 and 3.9.2) is essentially similar to that in the Boussinesq model (section 2.9) except that the circulation remains confined to the upper regions of the atmosphere, and as velocities tend to zero in the deep atmosphere, nonlinear terms cease to be important, except perhaps at the antisolar point.

We expect therefore that in the lower atmosphere the thermal balance will be radiative-diffusive. In this case, as we discuss in Chapter 5, the stratification will be very stable, and the use of the large coefficients of eddy diffusivity is not really justified.

Point	HOR. ADV.	VERT. ADV.	HOR. VISC.	VERT. VISC.	DRIVING	TIME DERIV.
A	-154.12×10^{-5}	133.46×10^{-5}	49.98×10^{-5}	0.85×10^{-5}	$- 30.18 \times 10^{-5}$	0.02×10^{-5}
B	$- 12.16 \times 10^{-7}$	117.71×10^{-7}	35.56×10^{-7}	23.62×10^{-7}	-164.81×10^{-7}	$- 0.01 \times 10^{-7}$
C	16.23×10^{-8}	$- 92.73 \times 10^{-8}$	122.44×10^{-8}	10.36×10^{-8}	$- 57.48 \times 10^{-8}$	$- 1.19 \times 10^{-8}$
D	$- 20.0 \times 10^{-7}$	-170.8×10^{-7}	70.9×10^{-7}	$- 0.2 \times 10^{-7}$	120.2×10^{-7}	0.1×10^{-7}
E	12.76×10^{-9}	$- 2.38 \times 10^{-9}$	$- 63.44 \times 10^{-9}$	$- 2.65 \times 10^{-9}$	54.75×10^{-9}	$- 9.65 \times 10^{-9}$
F	3.01×10^{-9}	76.96×10^{-9}	$- 25.13 \times 10^{-9}$	1.02×10^{-9}	$- 54.86 \times 10^{-9}$	1.04×10^{-9}
G	$- 0.18 \times 10^{-10}$	0.12×10^{-10}	-187.77×10^{-10}	124.48×10^{-10}	63.27×10^{-10}	$- 0.08 \times 10^{-10}$
H	0.0004×10^{-12}	$- 0.0007 \times 10^{-12}$	$- 14.31 \times 10^{-12}$	$- 8.12 \times 10^{-12}$	18.07×10^{-12}	$- 4.36 \times 10^{-12}$
I	0.001×10^{-12}	$- 0.011 \times 10^{-12}$	-147.07×10^{-12}	14.73×10^{-12}	114.49×10^{-12}	-17.87×10^{-12}

Table 3.9.1: Balance of terms in the vorticity equation at 9 points (see Figure 3.9.10). The numerically larger terms are underlined.

	HOR. ADV.	VERT. ADV.	HOR. DIFF.	VERT. DIFF.	BASIC RAD. H.	VERT. RAD.H.	TIME DERIV.
A	23936.	-30376.	6262.	29.	-271.	432.	12.
B	1991.8	- 1710.8	14.3	- 0.9	-271.0	- 9.0	14.3
C	-1526.1	1512.5	- 2.8	- 4.9	128.7	-92.7	14.5
D	- 138.1	776.3	- 636.1	3.4	- 1.5	1.1	5.1
E	12.74	- 7.76	- 0.76	2.26	- 1.46	0.49	5.51
F	- 1.61	- 16.62	- 0.83	1.84	22.50	- 0.19	5.47
G	15.15	- 12.99	- 2.17	6.74	- 11.15	1.76	- 2.64
H	- 0.043	0.037	- 0.001	6.731	- 11.148	1.757	- 2.664
I	0.031	- 0.027	0.004	6.723	- 11.148	1.756	- 2.660

Table 3.9.2: Balance of terms in the energy equation in units of 10^{-10} sec^{-1} at 9 points (see Figure 3.9.10). The numerically larger terms are underlined.

CHAPTER 4

Boussinesq Model of the Atmosphere of Venus

Including Rotation and Axi-Symmetric Heating

4.1 Introduction

It was first suggested by Thaddeus (1968) that the atmosphere

of Venus has such a large heat capacity that it cannot respond to

diurnal heating changes even for the long Venusian day. Gierasch,

Goody and Stone (1969) estimated the value of $\frac{\Delta\theta_{day}}{\theta_b}$, where $\Delta\theta_{day}$

is the magnitude of the diurnal temperature variation and θ_e the

average emission temperature at several planets. They found that

$\Delta\theta_{day}/\theta_o \lesssim 10^{-2}$ in Venus, the same value as in the Earth where diur-

nal (tidal) effects are known to have a negligible effect on the gen-

eral circulation of the atmosphere. The smallness of diurnal effects

has been confirmed by observations both at the cloud top level and

at the ground. The brightness-temperature maps made by Murray, Wildey

and Westphal (1963) show no clear-cut night-to-day variation at the

cloud top level. They do however, show an appreciable temperature

contrast between equator and poles (see Figure 4.1). There have been

contradictory reports about the existence of a "phase effect" at the

ground, that is, a day-to-night temperature variation. (Pollack and

Sagan, 1965; Morrison, 1969.) Ultraviolet cloud pictures show a

marked zonal structure, and an absence of the radial structure that

would be expected if rotation were negligible (see Boyer and Newell,

1967 and Dollfus, 1968). Dollfus (1955) reported that the result of

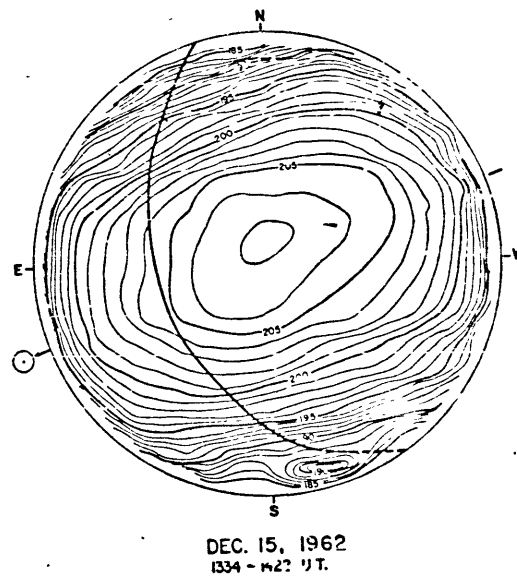superposing several images of Venus photographed through a yellow

DEC. 15, 1962
1334 - 1427 U.T.

Figure 4.1: Eight to fourteen micron brightness-
temperature map of Venus for the morning of Dec-
ember 15, 1962. After Murray, et al. (1963).

filter showed some kind of radial structure, but this has not been confirmed since then.

It is felt that there is enough motivation to explore a model that represents another limiting case of the possible circulation of the atmosphere of Venus, in which rotation is included and the daily variations are neglected, so that the solar heating is assumed to be symmetrical about the axis of rotation.

A symmetric model was developed using both the Boussinesq and the quasi-Boussinesq approximations. The Boussinesq model is briefly described in this chapter, and the quasi-Boussinesq symmetric model is described in next chapter.

4.2 Description of the model

This model is similar to the Boussinesq model described in Chapter 2 except that rotation is included and the solar radiation is averaged over a Venusian day. Since we assume that there is no orography, the flow is now symmetric about the rotation axis rather than the antisolar-subsolar axis.

We use the Boussinesq equations in rotating coordinates. The velocity components are defined as in Figure 4.2.1: u is the zonal velocity, positive in the retrograde direction (direction of rotation of Venus), v is the meridional velocity, positive from North to South, and w is the upward velocity. Ω is negative because of the retrograde rotation of Venus:

$$f = 2\Omega \cos \alpha$$

where $\Omega = -2\pi/\tau = -2.99 \times 10^{-7} \, sec^{-1}$
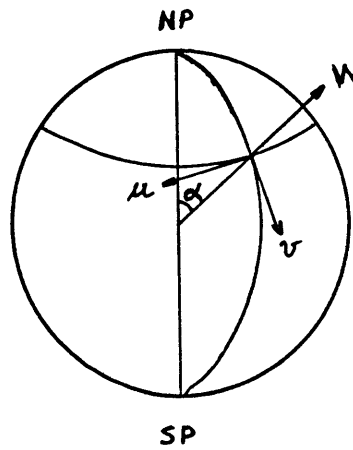
Figure 4.2.1: Velocities and coordinate system.

and $\tau = 243 \text{ days} = 2.1 \times 10^{-7} \text{ sec}$

In this system the Boussinesq equations are:

$$\frac{\partial u}{\partial t} = -\frac{(uv \sin \alpha)_\alpha}{a \sin \alpha} - (uw)_z + fv - \frac{\cot \alpha}{a} uv +$$

$$+ \frac{\nu_H}{a^2} \left[\frac{(u_\alpha \sin \alpha)_\alpha}{\sin \alpha} - \frac{u}{\sin^2 \alpha} \right] + \nu_v u_{zz} , \qquad (4.2.1)$$

the zonal momentum equation;

$$\frac{\partial v}{\partial t} = -\frac{(v^2 \sin \alpha)_\alpha}{a \sin \alpha} - (wv)_z - fu + \frac{\cot \alpha}{a} u^2 - \frac{p_\alpha}{\rho_o a}$$

$$+ \frac{\nu_H}{a^2} \left[\frac{(v_\alpha \sin \alpha)_\alpha}{\sin \alpha} - \frac{v}{\sin^2 \alpha} \right] + \nu_v v_{zz} , \qquad (4.2.2)$$

the meridional momentum equation;

$$0 = -\frac{1}{\rho_o} p_z - \tilde{\rho} g , \qquad (4.2.3)$$

the hydrostatic equation;

$$0 = -\frac{(v \sin \alpha)_\alpha}{a \sin \alpha} - w_z , \qquad (4.2.4)$$

the continuity equation; and

$$\frac{\partial \rho}{\partial t} = - \frac{(\rho v \sin \alpha)_\alpha}{a \sin \alpha} - (\rho w)_z + \frac{K_H}{a^2} \frac{(\rho_\alpha \sin \alpha)_\alpha}{\sin \alpha} + K_v \rho_{zz} \qquad (4.2.5)$$

the energy equation.

We have dropped the terms $\frac{uw}{a}$, $2\Omega \sin \alpha \, u \, w$, $\frac{vw}{a}$ and

$2\Omega \sin \alpha \, v \, w$ from the first two equations for consistency with

the "shallow approximation", in which r is replaced by a when it is

not differentiated (Phillips, 1966), and with the hydrostatic approx-

imation. For the same reason $\frac{2 w_\alpha}{a^2}$ was dropped in the horizontal

viscosity term of (4.2.2). The above approximations are all conse-

quences of the small aspect ratio H/a.

The terms proportional to f and to $\frac{\cot \alpha}{a} u$ in equations

(4.2.1) and (4.2.2) have different signs because f is now negative.

As in the non-rotating model, we define $\eta = \frac{v_z}{\sin \alpha}$, the

zonal component of the vortex strength. From equations (4.2.2) to

(4.2.4) we obtain the vorticity equation

$$\frac{\partial \eta}{\partial t} = - \frac{(v \eta \sin \alpha)_\alpha}{a \sin \alpha} - (w \eta)_z - \frac{f \, u_z}{\sin \alpha} + \frac{\cot \alpha}{a \sin \alpha} (u^2)_z$$

$$+ \frac{g}{a \sin \alpha} \tilde{\rho}_\alpha + \frac{v_H}{a^2} \left[\frac{((\eta \sin \alpha)_\alpha \sin \alpha)_\alpha}{\sin^2 \alpha} - \frac{\eta}{\sin^2 \alpha} \right] + v_v \eta_{zz} \qquad (4.2.6)$$

Again we define the mass stream function ψ :

$$\psi_{zz} = \eta \sin^2 \alpha \qquad (4.2.7)$$

so that

$$v \sin \alpha = \Psi_z \qquad \qquad (4.2.8)$$

and

$$w \sin \alpha = - \frac{\Psi_\alpha}{a} \qquad \qquad (4.2.9)$$

Equations (4.2.1) and (4.2.5) to (4.2.9) and the boundary conditions define the model.

4.3 Boundary conditions

The boundary conditions are similar to those described in section 2.3. We assume for both horizontal velocity components a zero stress rigid top at the cloud top level and a nonslip rigid bottom at the surface. Since the driving is symmetric with respect to the equator we need to consider only the northern hemisphere. At the equator symmetry considerations impose a zero meridional velocity and zero latitudinal gradient of the zonal velocity component.

We have then

$$
\begin{aligned}
\Psi &= \Psi_{zz} = 0 \quad \text{at } z = H &\qquad a \\
\Psi &= \Psi_z = 0 \quad \text{at } z = 0 &\qquad b \\
\Psi &= 0 \quad \text{at } \alpha = 0, \frac{\pi}{2} &\qquad c
\end{aligned}
\qquad (4.3.1)
$$

$$u_z = 0 \quad \text{at } z = H \qquad\qquad \text{a}$$

$$u = 0 \quad \text{at } z = 0 \qquad\qquad \text{b} \qquad\qquad (4.3.2)$$

$$u = 0 \quad \text{at } \alpha = 0 \qquad\qquad \text{c}$$

$$u_\alpha = 0 \quad \text{at } \alpha = \frac{\pi}{2} \qquad\qquad \text{d}$$

The flux of radiation at the upper boundary is treated as in Chapter 2. Solar radiation is averaged over one Venusian day:

$$\downarrow F_{SW} = \frac{(1-A) S_0 \, |\sin \alpha|}{\pi}$$

so that the heating contrast is π times smaller than in the non-rotating case. The long-wave outgoing radiation is calculated from the linearized relation

$$\uparrow F_{LW} = \sigma T_*^4 \left(1 + \frac{4 \, \delta T}{T_0} \right)$$

From these equations we get the upper boundary condition for $\tilde{\rho}$:

$$\tilde{\rho}_z = \frac{\sigma T_0^3}{k_v C_p \rho_0} \left[(1 - 4\tilde{\rho}) + \frac{4 \, |\sin \alpha|}{\pi} \right] \quad \text{at } z = H \qquad\qquad (4.3.3a)$$

At the bottom we assume that the heat flux is negligible:

$$\rho_z = 0 \quad \text{at} \quad z = 0 \qquad\qquad (4.3.3b)$$

Finally

$$\widetilde{\rho}_{\alpha} = 0 \qquad\qquad at \quad \alpha = \frac{\pi}{2}$$

4.4 Equations in stretched coordinates

We use the stretched coordinates defined in section 2.4, so as to give better resolution near the pole and near the upper and lower boundaries.

The new horizontal coordinate is

$$y = \sqrt{\alpha} \ ; \quad \frac{dy}{d\alpha} = \frac{1}{2y} \qquad\qquad (4.4.1)$$

and the vertical coordinate

$$\Delta = \frac{2}{\pi} \arctan \sqrt{\frac{z}{H-z}} \ ; \quad \frac{d\Delta}{dz} = \frac{1}{H\,S} \qquad\qquad (4.4.2)$$

where $S = \pi \sqrt{z/H(1-z/H)}$

In the present model 13 grid intervals are used, both in the horizontal and in the vertical directions $(IM = 13, \ JM = 13)$. This number of intervals gives approximately the same resolution in the northern hemsiphere as 20 intervals gave in the antisolar hemisphere in the nonrotating case, and it was felt that 13 grid intervals gives enough resolution in the vertical direction.

Equations (4.2.1) and (4.2.5) to (4.2.9) in the stretched coordinates are:

$$\frac{\partial u}{\partial t} = -\frac{(uv\sin\alpha)_y}{2a\sin\alpha\,y} - \frac{(uw)_s}{HS} + fv - \frac{\cot\alpha}{a}uv$$

$$+ \frac{\nu_H}{a^2}\left[\frac{(u_y\sin\alpha/y)_y}{4y\sin\alpha} - \frac{u}{\sin^2\alpha}\right] + \frac{\nu_v}{H^2}\frac{1}{S}\left(\frac{u_s}{S}\right)_s$$

$$\tag{4.4.3}$$

$$\frac{\partial\tilde{\rho}}{\partial t} = -\frac{(\tilde{\rho}v\sin\alpha)_y}{2a\sin\alpha\,y} - \frac{(\tilde{\rho}w)_s}{HS} + \frac{K_H}{a^2}\left[\frac{(\tilde{\rho}_y\sin\alpha/y)_y}{4y\sin\alpha}\right] + \frac{K_v}{H^2}\frac{1}{S}\left(\frac{\tilde{\rho}_s}{S}\right)_s \tag{4.4.4}$$

$$\frac{\partial\eta}{\partial t} = -\frac{(v\eta\sin\alpha)_\alpha}{2a\sin\alpha\,y} - \frac{(\eta w)_s}{HS} - \frac{fu_s}{HS\sin\alpha} + \frac{\cot\alpha}{HSa\sin\alpha}(u^2)_s + \frac{g}{a\sin\alpha\,2y}\tilde{\rho}_y$$

$$+ \frac{\nu_H}{a^2}\left[\frac{1}{\sin^2\alpha\,4y}\left((\eta\sin\alpha)_y\frac{\sin\alpha}{y}\right)_y - \frac{\eta}{\sin^2\alpha}\right] + \frac{\nu_v}{H^2}\frac{1}{S}\left(\frac{\eta_s}{S}\right)_s \tag{4.4.5}$$

$$\frac{1}{H^2S}\left(\frac{\psi_s}{S}\right)_s = \eta\sin^2\alpha \tag{4.4.6}$$

$$v = \frac{\psi_s}{HS\sin\alpha} \tag{4.4.7}$$

$$w = -\frac{\psi_y}{2ay\sin\alpha} \tag{4.4.8}$$

The boundary conditions (4.3.1) to (4.3.3) in the new coor-

dinates are

$$\psi = 0 \quad at \; s = 0 \qquad\qquad a$$

$$\psi = 0 \quad at \; s = 1 \qquad\qquad b$$

$$\Psi_s = 0 \qquad at \ s = 0 \qquad\qquad\qquad c$$

$$\left(\frac{\Psi_s}{S}\right)_s = 0 \qquad at \ s = 1 \qquad\qquad d$$

$$\Psi = 0 \qquad at \ y = 0, \ \sqrt{\pi}/2 \qquad\qquad e$$

$$(4.4.9)$$

$$u = 0 \qquad at \ s = 0 \qquad\qquad\qquad a$$

$$u_s = 0 \qquad at \ s = 1 \qquad\qquad\qquad b$$

$$u = 0 \qquad at \ y = 0 \qquad\qquad\qquad c$$

$$u_y = 0 \qquad at \ y = \sqrt{\pi}/2 \qquad\qquad d$$

$$(4.4.10)$$

$$\tilde{\rho}_s = 0 \qquad at \ s = 0 \qquad\qquad\qquad a$$

$$\tilde{\rho}_s = \frac{\sigma \theta_\oplus^3 \ HS}{K_v \ C_p \ \rho_0} \left[(1 - 4\tilde{\rho}) + \frac{4 \ |\sin \alpha|}{\pi} \right] \quad at \ s = 1 \qquad b$$

$$\tilde{\rho}_y = 0 \qquad at \ y = 0, \ \sqrt{\pi}/2 \qquad\qquad c$$

$$(4.4.11)$$

4.5 Finite-difference equations

The finite-difference scheme was similar to the one used

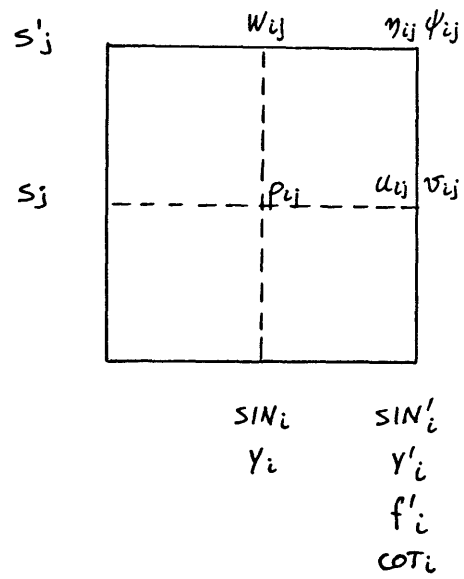in Chapter 2. Figure 4.5.1 shows a typical grid cell. The new

Figure 4.5.1: Typical cell with the position of the variables and functions having the sub-indices i,j.

variable μ_{ij} was placed at the same location as v_{ij} to improve the accuracy of the computation of the third and fourth terms in the right hand side of equation (4.4.3).

The finite-difference equations corresponding to equations (4.4.3) to (4.4.8) used in the model are the following (we have dropped the superscript n):

$$
u_{ij}^{n+1} = u_{ij}^{n-1} + 2\Delta t \Bigg\{ - \frac{\mu_{i+1j}\, v_{i+1j}\, SIN_{i+1}' - \mu_{i-1j}\, v_{i-1j}\, SIN_{i-1}'}{4 \Delta y\, a\, Y_i'\, SIN_i'}
$$

$$
- \frac{1}{4\Delta s H\, S_j} \Big[(\mu_{ij} + \mu_{ij+1})(w_{ij} + w_{i+1j}) - (\mu_{ij} + \mu_{ij-1})(w_{ij-1} + w_{i+1j-1}) \Big]
$$

$$
+ \frac{\nu_H}{a^2} \Bigg[\frac{(\mu_{i+1j}^{n-1} - \mu_{ij}^{n-1})\, SIN_{i+1}/y_{i+1} - (u_{ij}^{n-1} - u_{i-1j}^{n-1})\, SIN_i/y_i}{4\Delta y^2\, Y_i'\, SIN_i'} - \frac{\mu_{ij}}{SIN_i'^2} \Bigg]
$$

$$
+ \frac{\nu_v}{H^2} \Bigg[\frac{1}{\Delta s^2 S_j} \Big(\frac{\mu_{ij+1}^{n+1} - \mu_{ij}^{n-1}}{S_j'} - \frac{\mu_{ij}^{n-1} - u_{ij-1}^{n-1}}{S_{j-1}'} \Big) \Bigg] + f_i' v_{ij} - \frac{\cot_i}{a} \mu_{ij} v_{ij} \Bigg\}
$$

$$(4.5.1)$$

where $i = 2, \ldots, IM$; $j = 2, \ldots, JM+1$

$$
\tilde{\rho}_{ij}^{n+1} = \tilde{\rho}_{ij}^{n-1} + 2\Delta t \Bigg\{ - \frac{v_{ij}(\tilde{\rho}_{ij} + \tilde{\rho}_{i+1j})\, SIN_i' - v_{i-1j}(\tilde{\rho}_{ij} + \tilde{\rho}_{i-1j})\, SIN_{i-1}'}{4\Delta y\, a\, Y_i\, SIN_i}
$$

$$
- \frac{w_{ij}(\tilde{\rho}_{ij} + \tilde{\rho}_{ij+1}) - w_{ij-1}(\tilde{\rho}_{ij} + \tilde{\rho}_{ij-1})}{2\Delta s\, H\, S_j}
$$

$$
+ \frac{K_H}{a^2} \Bigg[\frac{(\tilde{\rho}_{i+1j}^{n-1} - \tilde{\rho}_{ij}^{n-1})\, SIN_i'/y_i' - (\rho_{ij}^{n-1} - \rho_{i-1j}^{n-1})\, SIN_{i-1}'/y_{i-1}'}{4\Delta y^2\, Y_i\, SIN_j} \Bigg]
$$

$$
+ \frac{K_v}{H^2}\, \frac{1}{\Delta s^2 S_j} \Big(\frac{\tilde{\rho}_{ij+1}^{n-1} - \tilde{\rho}_{ij}^{n-1}}{S_j'} - \frac{\tilde{\rho}_{ij}^{n-1} - \tilde{\rho}_{ij-1}^{n-1}}{S_{j-1}'} \Big) \Bigg\}
$$

$$(4.5.2)$$

where $i = 2, \ldots, IM+1$; $j = 2, \ldots, JM+1$

$$\eta_{ij}^{n+1} = \eta_{ij}^{n-1} + 2\Delta t \left\{ -\frac{(v_{i+1j} + v_{i+1j+1})\eta_{i+1j} SIN'_{i+1} - (v_{i-1j} + v_{i-1j+1})\eta_{i-1j} SIN'_{i-1}}{8 \Delta y\, a\, Y'_i\, SIN'_i} \right.$$

$$-\frac{(w_{ij+1} + w_{i+1j+1})\eta_{ij+1} - (w_{ij-1} + w_{i+1j-1})\eta_{ij-1}}{4\Delta_\lambda H S'_j} - \frac{f'_i(u_{ij+1} - u_{ij})}{\Delta_\lambda H\, SIN'_i}$$

$$+ \frac{COT_i}{SIN'_i} \frac{u_{ij+1}^2 - u_{ij}^2}{\Delta_\lambda H\, a\, S'_j} + g\frac{(\tilde{P}_{i+1j} + \tilde{P}_{i+1j+1} - \tilde{P}_{ij} - \tilde{P}_{ij+1})}{4\Delta y\, a\, Y'_i\, SIN'_i}$$

$$+ \frac{\gamma_H}{a^2}\left[\frac{(\eta_{i+1j}^{n-1} SIN'_{i+1} - \eta_{ij}^{n-1} SIN'_i) SIN_{i+1}/Y_{i+1} - (\eta_{ij}^{n-1} SIN'_i - \eta_{i-1j}^{n-1} SIN'_{i-1}) SIN_i/Y_i}{4\Delta y^2\, Y'_i\, SIN'_i}\right.$$

$$\left.\left. - \frac{\eta_{ij}^{n-1}}{SIN'^2_i}\right] + \frac{\gamma_v}{H^2}\frac{1}{\Delta_\lambda^2 S'_i}\left[\frac{\eta_{ij+1}^{n-1} - \eta_{ij}^{n-1}}{S_{j+1}} - \frac{\eta_{ij}^{n-1} - \eta_{ij-1}^{n-1}}{S_j}\right]\right\} \tag{4.5.3}$$

where $i = 2, \ldots, IM$; $j = 2, \ldots, JM$

$$\frac{\psi_{ij+1}^{n+1} - \psi_{ij}^{n+1}}{S_{j+1}} - \frac{\psi_{ij}^{n+1} - \psi_{ij-1}^{n+1}}{S_j} = \eta_{ij}^{n+1} \cdot SIN'^2_i S'_j \Delta_\lambda^2 H \tag{4.5.4}$$

where $i = 2, \ldots, IM$; $j = 2, \ldots, JM$

$$v_{ij}^{n+1} = \frac{\psi_{ij}^{n+1} - \psi_{ij-1}^{n+1}}{\Delta_\lambda H\, S_j\, SIN'_i} \tag{4.5.5}$$

where $i = 2, \ldots, IM$; $j = 2, \ldots, JM+1$

$$w_{ij}^{n+1} = \frac{\psi_{ij}^{n+1} - \psi_{i-1j}^{n+1}}{2\Delta y\, a\, Y_i\, SIN_i} \tag{4.5.6}$$

where $i = 2, \ldots, IM+1 \, ; \, j = 2, \ldots, JM$

Equation (4.5.4) was solved as in the nonrotating case (see Equation 2.6.6).

The boundary conditions in finite differences are:

$$\psi_{i,1}^{n+1} = \psi_{i,JM+1}^{n+1} = 0 \qquad \text{where } i = 2, \ldots, IM$$

$$\psi_{1,j}^{n+1} = \psi_{IM+1,j}^{n+1} = 0 \qquad \text{where } j = 2, \ldots, JM \qquad \Bigg\} \quad (4.5.7)$$

$$\eta_{i,JM+1}^{n+1} = 0 \qquad \text{where } i = 2, \ldots, IM$$

$$\eta_{i,1}^{n+1} = \left[\frac{2 z_2}{z_1^2 (z_2 - z_1)} \psi_{i,2}^{n+1} \right.$$

$$\left. - \frac{2 z_1}{z_2^2 (z_2 - z_1)} \psi_{i,3}^{n+1} \right] \frac{1}{SIN_i'^2} \qquad \Bigg\} \quad (4.5.8)$$

$$\text{where} \quad i = 2, \ldots, IM \, ,$$

$$\eta_{1,j}^{n+1} = \eta_{IM+1,j}^{n+1} = 0 \qquad \text{where } j = 2, \ldots, JM$$

$$\mu_{i,1}^{n+1} = - \mu_{i,2}^{n+1} \qquad \text{where } i = 2, \ldots, IM$$

$$\mu_{i,JM+2}^{n+1} = \mu_{i,JM+1}^{n+1} \qquad \text{where } i = 2, \ldots, IM \qquad$$

$$\mu_{1,j}^{n+1} = 0 \qquad \text{where } j = 2, \ldots, JM+1 \qquad \Bigg\} \quad (4.5.9)$$

$$\mu_{IM+1,j}^{n+1} = \mu_{IM,j}^{n+1} \qquad \text{where } j = 2, \ldots, JM+1$$

$$\check{\rho}_{i2}^{n+1} = \tilde{\rho}_{i1}^{n+1}$$

$$\tilde{\rho}_{i,JM+2}^{n+1} = \tilde{\rho}_{i,JM+1}^{n+1} \left(\frac{1-2m}{1+2m} \right) \tilde{\rho}_{i,JM+1}^{n+1} + \frac{m}{1+2m} \left(1 + \frac{4 C_i}{\pi} \right)$$

$$\text{where} \quad m = \frac{\sigma \theta_0^3 \, \Delta_A H \, S'_{JM+1}}{K_v C_p \, \rho_0}$$

$$C_i = \cos(\alpha_i)$$

$$i = 2, \cdots, IM+1$$

$$\tilde{\rho}_{IM+2,j}^{n+1} = \tilde{\rho}_{IM+1,j}^{n+1} \quad \text{where} \quad j = 2, \cdots, JM+1$$

(4.5.10)

4.6 Initial conditions and physical data

As initial conditions we assume a state of solid rotation ($u = v = w = 0$) and of neutral stability ($\tilde{\rho} = 0$).

The computational procedure is the same as described in section (2.7) except that at each step new interior values of the zonal velocity are computed.

The physical data were the same as in the nonrotating case (section 2.8) except that

$$K_H = 10^{10} \text{ cm}^2/\text{sec}$$

$$\nu_H = 10^{10} \text{ cm}^2/\text{sec}$$

Also, we set $2\Omega = -5.385 \times 10^{-7} \text{sec}^{-1}$ (corresponding to a rotation period of 243 earth days).

The horizontal eddy viscosity and eddy diffusivity coefficients now have the values suggested by Goody and Robinson (1966).

The differential heating between equator and pole of the sun was allowed to act for about 2×10^7 secs (approximately 2 solar

Venus days) at which time the model had converged.

4.7 Results

Figure 4.7.1 shows a cross-section of the meridional mass
stream function. As might be expected it consists mainly of a direct
Hadley cell similar to that in the nonrotating case. The main dif-
ference is that the region of downward motion (similar to the mixing
region in the nonrotating case) is not at the pole where the maximum
cooling occurs, but between 5 and 8 degrees from the pole. There is
a narrow reverse cell within the first 5 degrees in the polar region.
This is because the conservation of angular momentum (except for tur-
bulent viscosity) would create infinite zonal velocities and gradients
of velocities if the parcels at the top of the atmosphere coming from
the equator were to reduce their radius of rotation to zero at the
pole. The circulation resembles the vortex formed when a bath tub
is being emptied. The center of the positive cell is lower than in
the nonrotating case.

Figures 4.7.2, 4.7.3, and 4.7.4 are the corresponding cross-
sections of the vortex strength and the horizontal, meridional, and
vertical components of the velocity.

As in the nonrotating case there is a narrow meridional jet
directed towards the colder regions, except near the pole where the
indirect cell is located, but here the return flow occupies only the
lower third of the atmosphere. The region of downward motion occupies
a narrow band between 5 and 10 degrees of colatitude at middle levels,
but it extends more towards the equator at the top and bottom of the
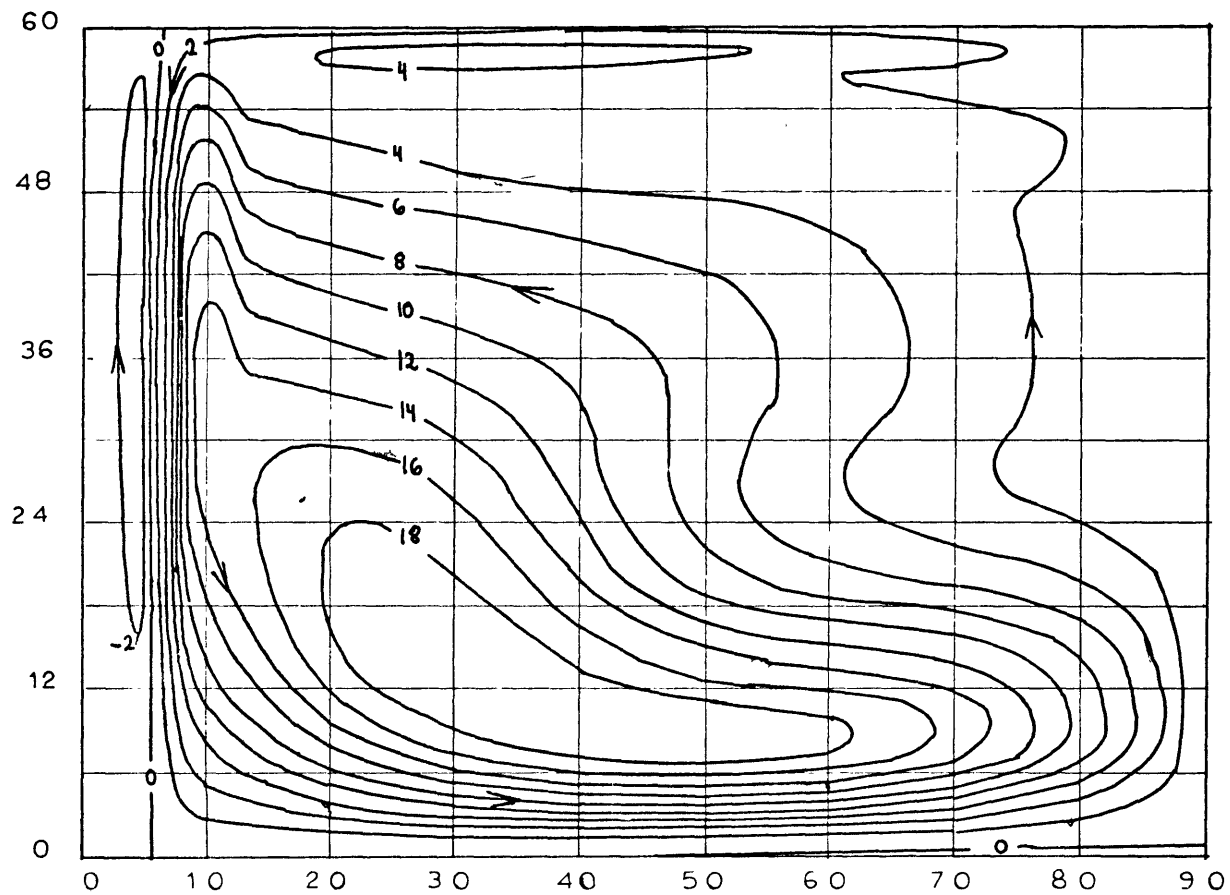atmosphere, up to 40° colatitude.

Figure 4.7.1: Meridional mass stream function after running 2.0×10^7 sec. Units of $10^8 \mathrm{cm}^2/\mathrm{sec}$.
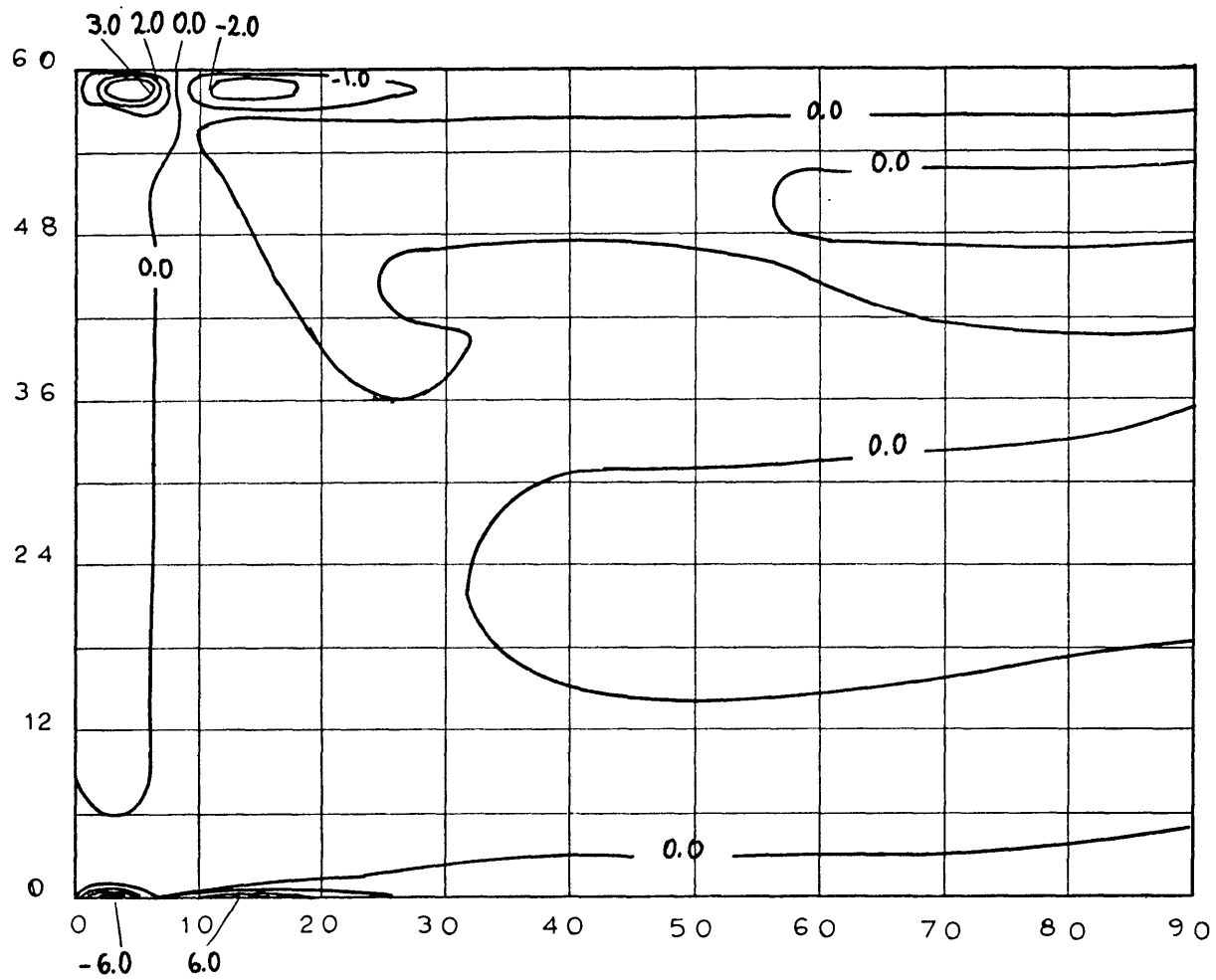
Figure 4.7.2: Zonal vortex strength $\eta = \dfrac{v_z}{\sin \alpha}$ in $10^{-2}\sec^{-1}$.
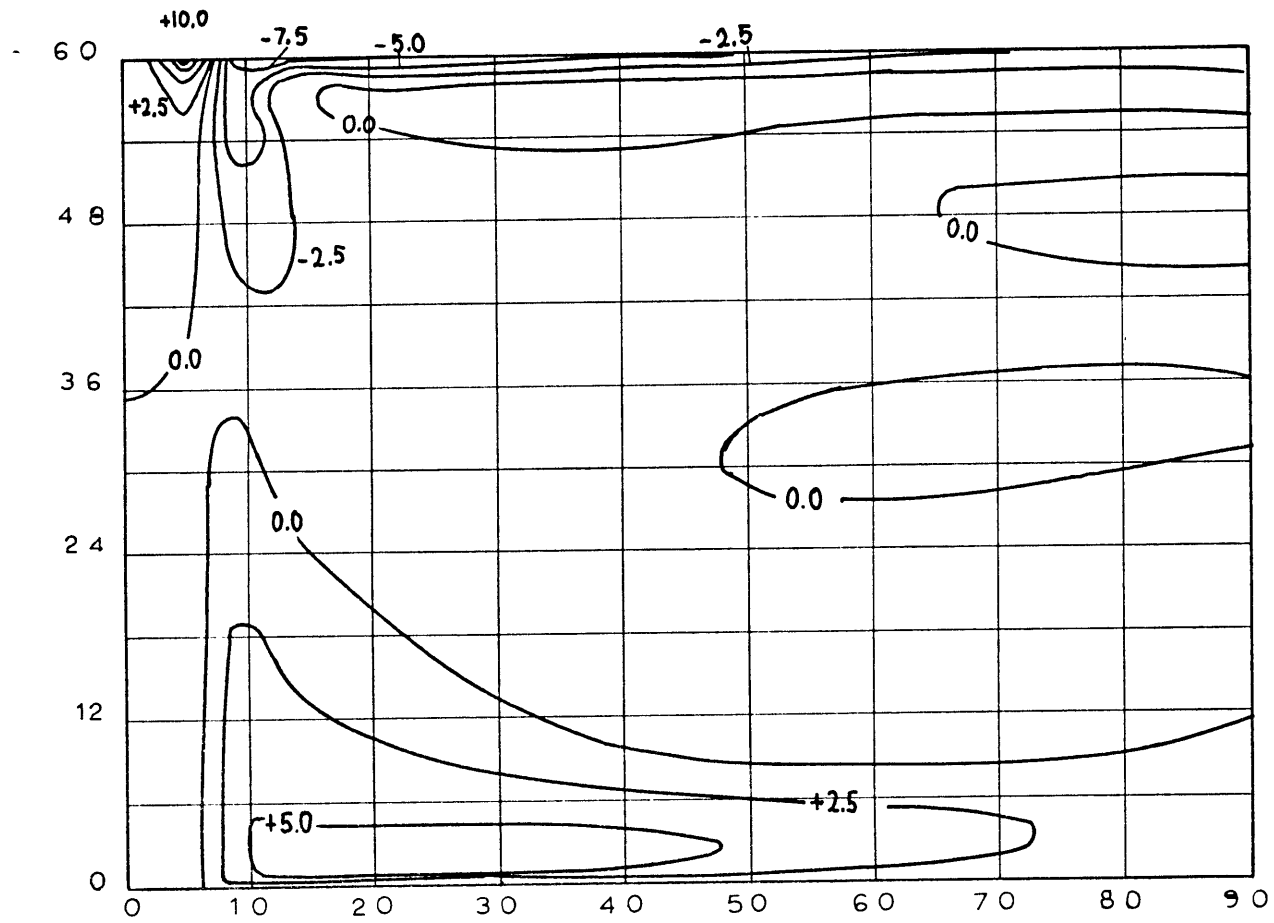
Figure 4.7.3: Meridional velocity v in m/sec.
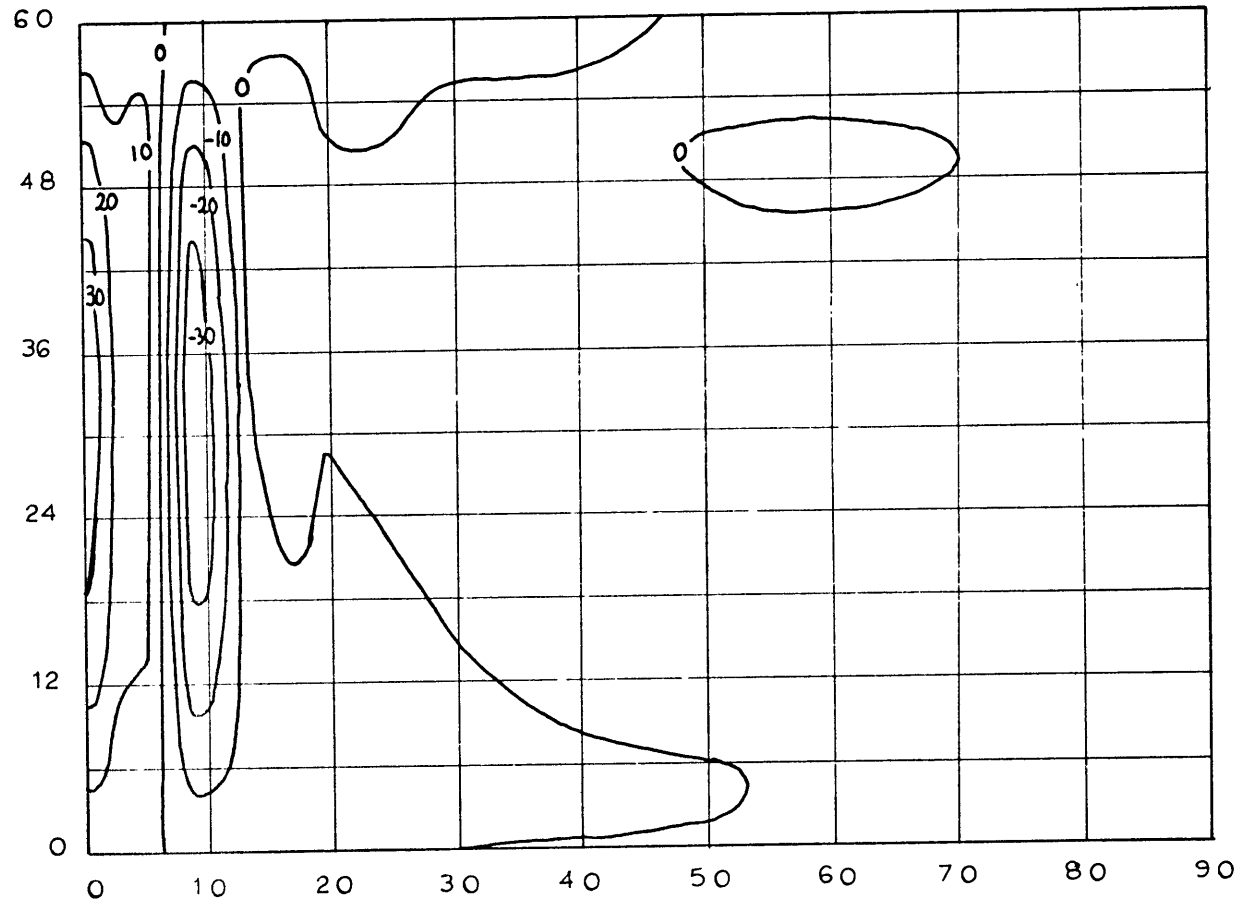
Figure 4.7.4: Vertical velocity w in cm/sec.

The meridional jet has a maximum of about 8 m/sec towards

the pole in the upper boundary layer and 11 m/sec in the narrow re-

verse cell at the pole. In the interior the direct meridional velo-

cities are of the order of 2 m/sec, the return flow having a maximum

of more than 5 m/sec near the surface of the planet. The vertical

velocity in the interior is still of the order of 1 cm/sec and has

a maximum of about 30 cm/sec both at the downward jet near the pole

and at the pole in the upward branch of the reverse cell.

Figure 4.7.5 shows the field of relative density departure

$\tilde{\rho}$. Again we find that the interior is neutrally stable. The

density difference between the equator and the pole is only 2.5×10^{-2}

at the top of the atmosphere, corresponding to about $6°K$ which is

of the order of the observed temperature contrast. Again the strong

density gradients are confined to a top boundary layer of less than

5 km thickness.

Figure 4.7.6 is the cross-section of the zonal component of

the velocity. As might be expected the zonal velocity is positive

(retrograde) in most of the atmosphere and attains rather large val-

ues near the pole where the maximum speed of the jet is 14 m/sec.

The indirect cell at the pole produces a negative zonal velocity at

the top of the atmosphere in a narrow band between $0°$ and $3°$ colati-

tude. Except in this small region there is a positive shear of the

zonal momentum everywhere in the atmosphere with a maximum near the

pole and a minimum at the equator.

Figure 4.7.7 shows a cross-section of the field of $AM =$

$= \left(-\Omega a \sin \alpha + u \right) \sin \alpha$, a quantity proportional to the angular momentum,
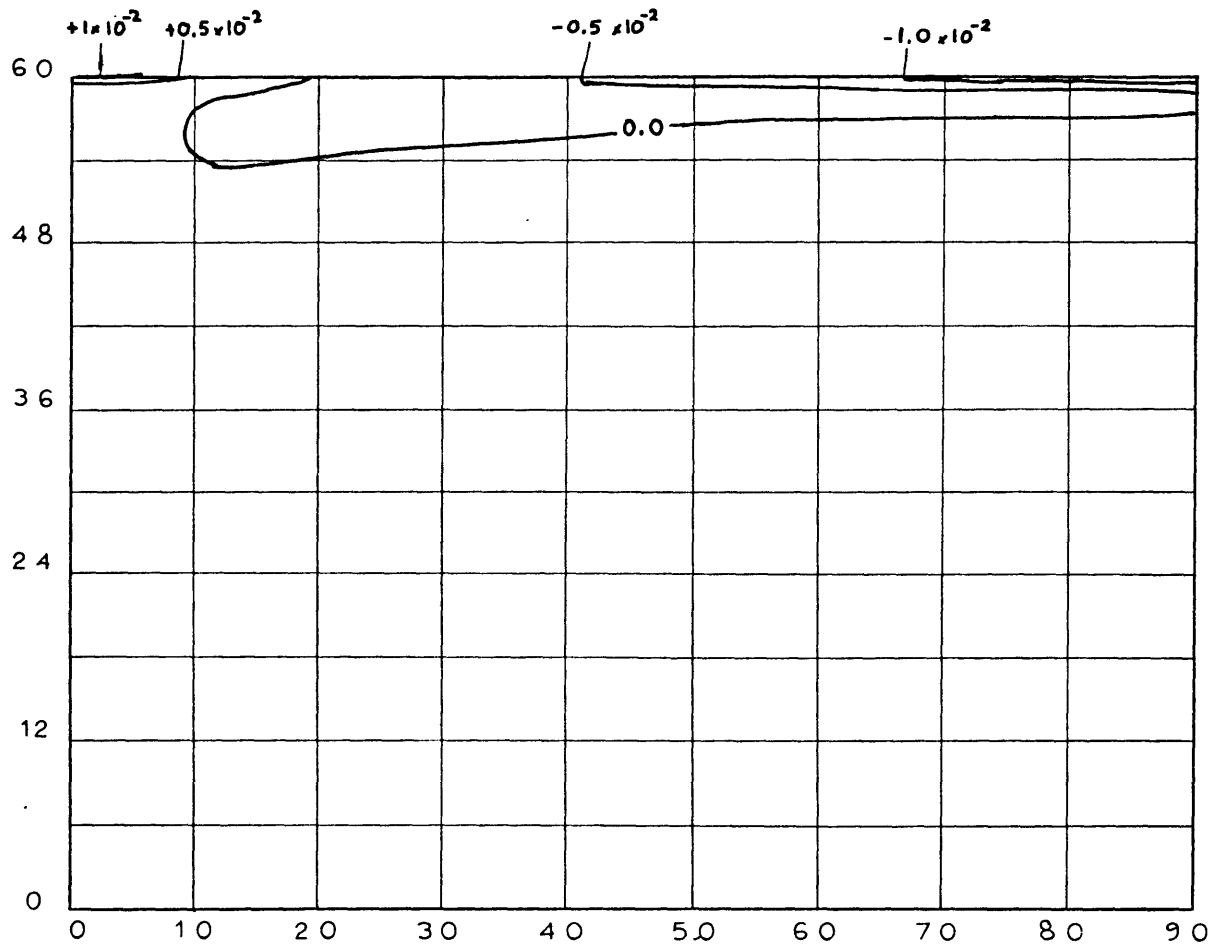
Figure 4.7.5: Relative density departure $\tilde{\rho}$.
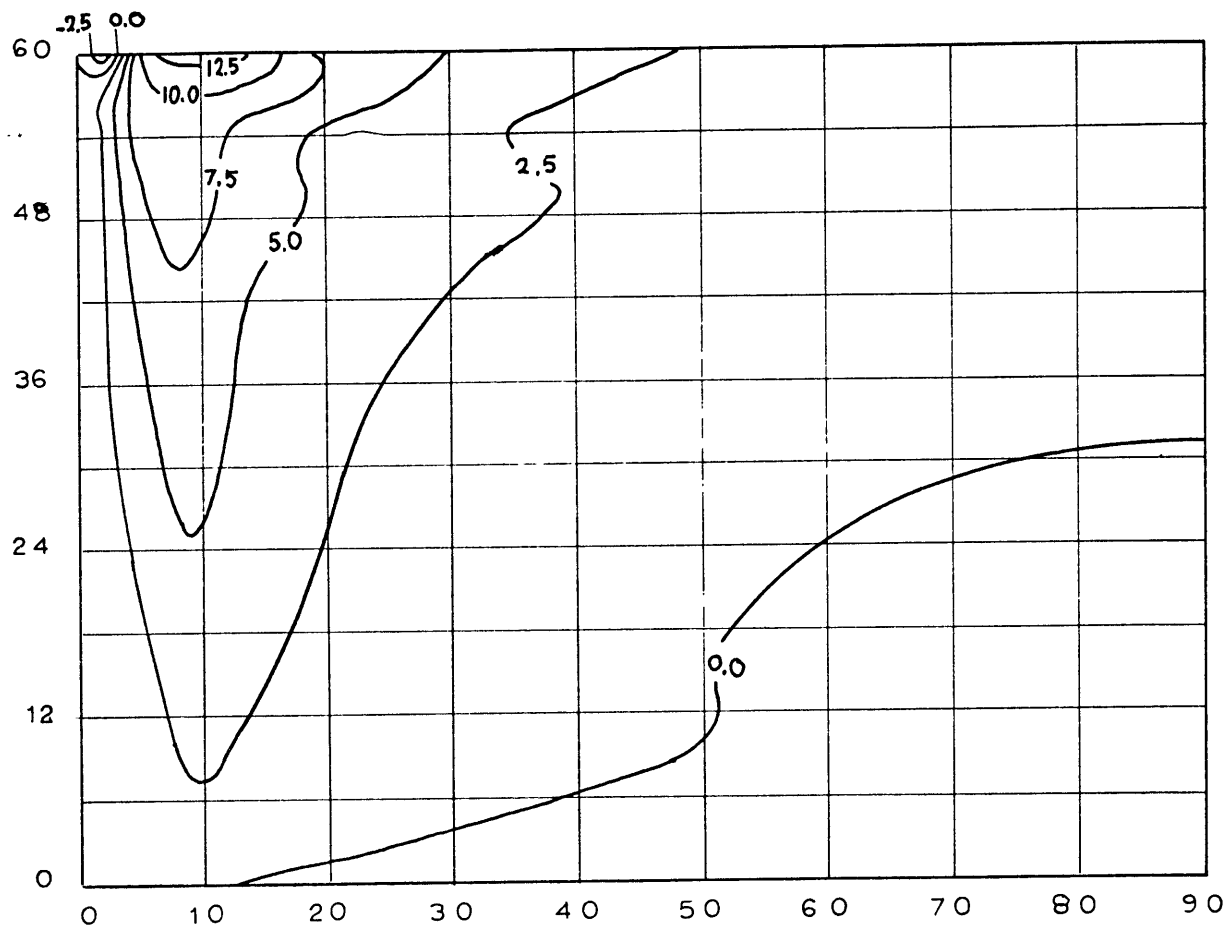
Figure 4.7.6: Zonal velocity u in m/sec.
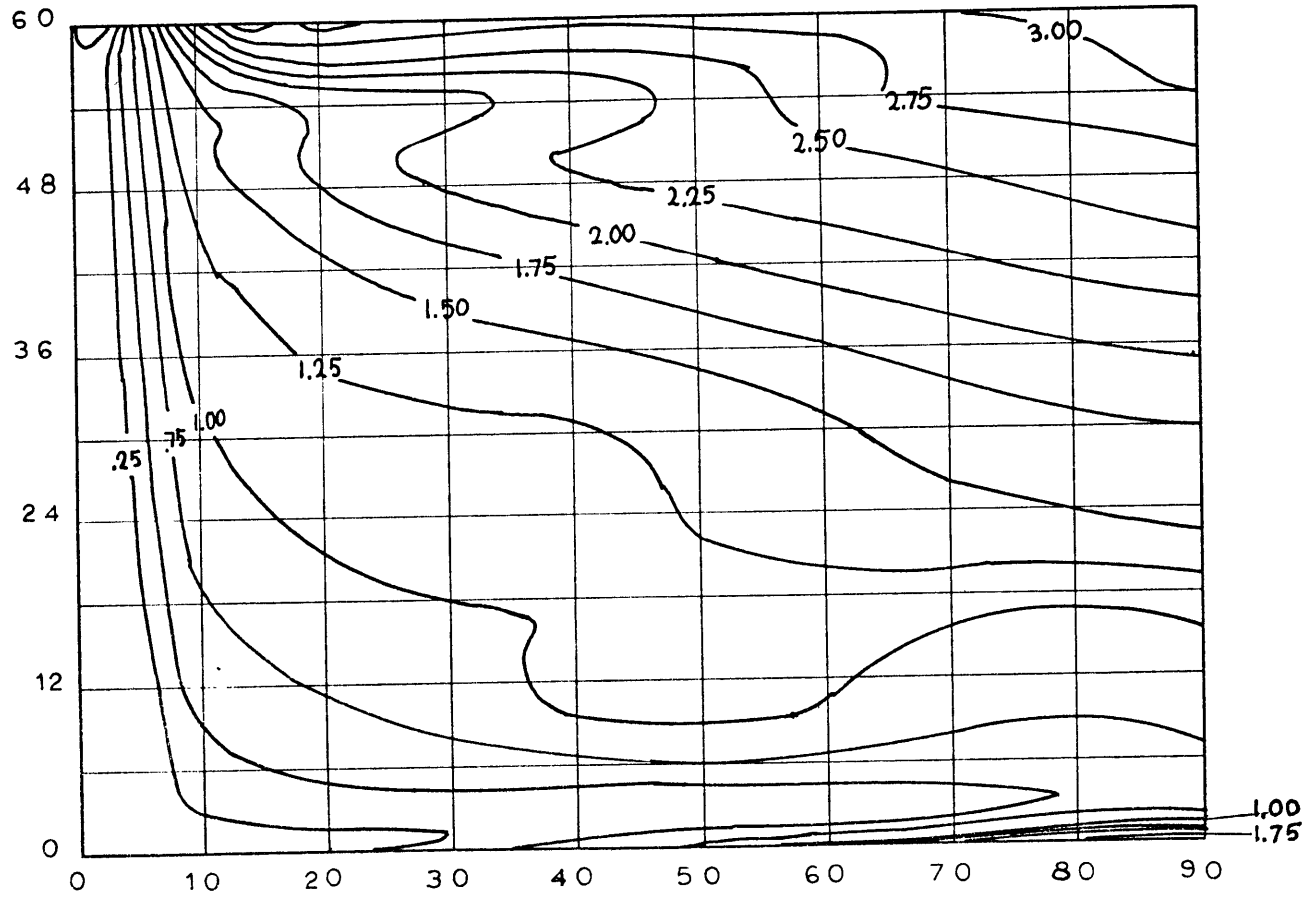
Figure 4.7.7: $AM = (-\Omega a \sin\alpha + \mu)\sin\alpha$ in m/sec.

showing that the meridional circulation has produced a poleward transport of angular momentum in the upper layers. If the flow were non-viscous and symmetric the relative zonal velocity at the equator would be strictly zero. The non-zero u velocity at the equator is due to the existence of horizontal eddy viscosity.

Tables 4.7.1, 4.7.2 and 4.7.3 show the numerical values of the different terms in the vorticity, zonal velocity and thermal equations at 12 grid points (Figure 4.7.8).

Equations (4.2.6), (4.2.1) and (4.2.5) are reproduced below for clarity:

$$\frac{\partial \eta}{\partial t} = - \frac{(v \eta \sin \alpha)_\alpha}{a \sin \alpha} - (\eta w)_z - \frac{f u_z}{\sin \alpha} + \frac{\cot \alpha}{a \sin \alpha} (u^2)_z$$

$$\text{Time Der.} \qquad \text{Hor. Adv.} \qquad \text{Vert. Adv.} \qquad \text{Coriolis} \qquad \text{U-term}$$

(4.7.1)

$$+ \frac{g}{a \sin \alpha} \tilde{\rho}_\alpha + \frac{\nu_H}{a^2} \left[\frac{((\eta \sin \alpha)_\alpha \sin \alpha)_\alpha}{\sin^2 \alpha} - \frac{\eta}{\sin^2 \alpha} \right] + \nu_v \eta_{zz}$$

$$\text{Driving} \qquad \text{Horiz. Visc.} \qquad \text{Vert. Visc.}$$

$$\frac{\partial u}{\partial t} = - \frac{(u v \sin \alpha)_\alpha}{a \sin \alpha} - (u w)_z + f v - \frac{\cot \alpha}{a} \mu v$$

$$\text{Time Der.} \qquad \text{Hor. Adv.} \qquad \text{Vert. Adv.} \qquad \text{Coriolis} \qquad \text{U-term}$$

(4.7.2)

$$+ \frac{\nu_H}{a^2} \left[\frac{(u_\alpha \sin \alpha)_\alpha}{\sin \alpha} - \frac{\mu}{\sin^2 \alpha} \right] + \nu_v \mu_{zz}$$

$$\text{Horiz. Visc} \qquad \qquad \text{Vert. Visc.}$$

$$\frac{\partial \tilde{\rho}}{\partial t} = - \frac{(\tilde{\rho} v \sin \alpha)_\alpha}{a \sin \alpha} - (\tilde{\rho} w)_z + \frac{K_H}{a^2} (\tilde{\rho}_\alpha \sin \alpha)_\alpha + K_v \tilde{\rho}_{zz}$$ (4.7.3)

$$\text{Time Deriv.} \qquad \text{Hor. Adv.} \qquad \text{Vert. Adv.} \qquad \text{Hor. Diff.} \qquad \text{Vert. Diff.}$$
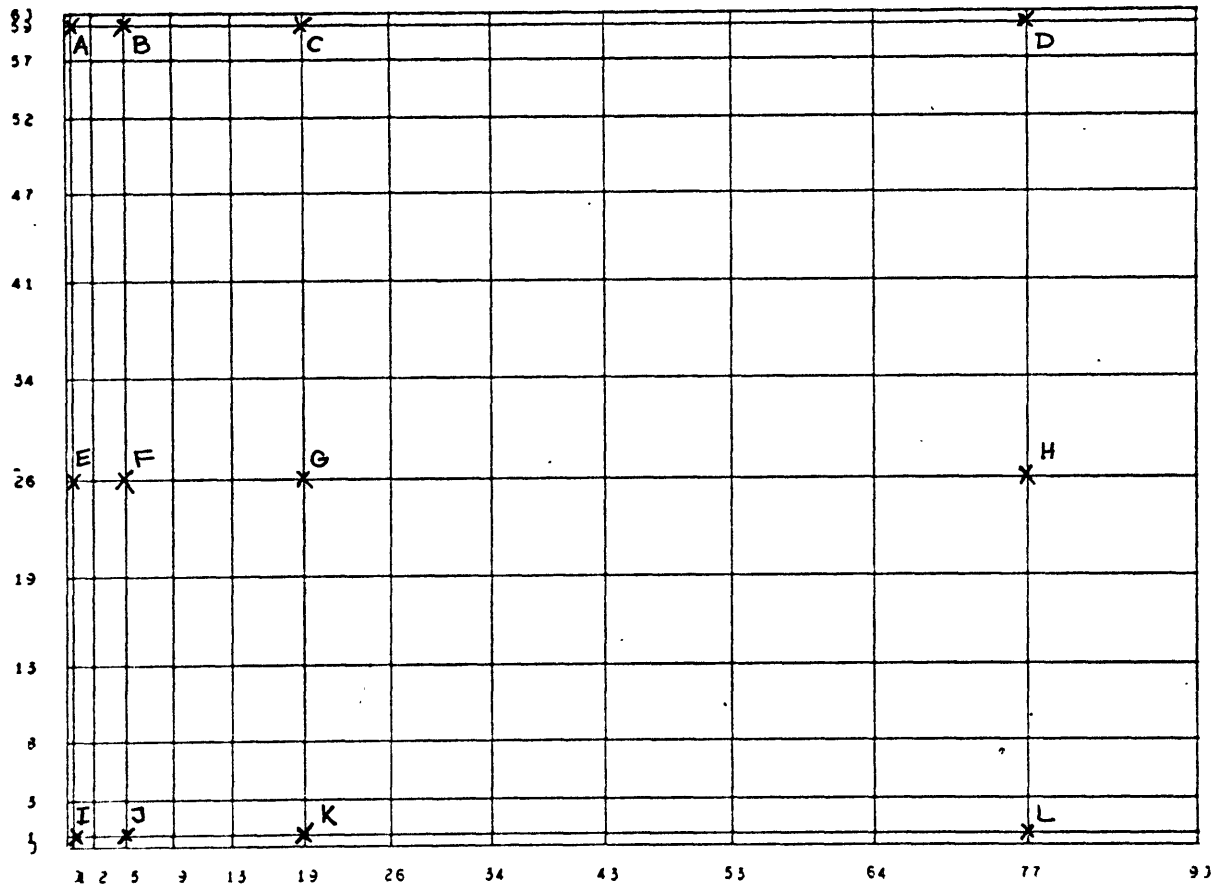
Figure 4.7.8: Position of the 12 points at which the balance of terms in the vorticity, zonal momentum and energy equations are given.

Point	HOR. ADV.	VERT. ADV.	COR. TERM	U. TERM	DRIVING	HOR. VISC.	VERT. VISC.	TIME DERIV.
A	-12480.	954.	-270.	2672.	- 441.	9771.	-213.	-6.
B	- 650.22	-318.71	13.71	786.11	8291.9	-7836.9	-288.86	-3.00
C	220.93	5.25	- 2.65	- 33.91	- 414.28	96.30	132.68	4.25
D	9.64	0.30	0.07	0.05	- 18.92	0.82	9.41	1.37
E	65.30	-120.97	8.89	200.89	16.06	- 171.87	- 0.02	-1.73
F	38.21	26.44	10.26	220.63	18.45	- 314.99	- 0.00	-1.00
G	- 0.78	3.99	0.91	4.09	- 11.22	3.25	0.04	2.74
H	- 0.07	- 0.09	0.05	- 0.00	0.32	- 0.33	- 0.02	0.03
I	- 102.14	0.19	- 0.17	- 0.12	5.81	493.73	-391.39	5.92
J	- 417.69	0.59	0.18	0.09	5.13	767.35	-351.25	4.40
K	- 61.53	- 13.59	3.26	0.26	- 3.17	- 14.43	85.99	-3.22
L	10.13	- 0.71	- 0.76	0.25	- 0.33	- 0.72	- 10.05	-2.18

Table 4.7.1: Balance of terms in the vorticity equation in units of 10 sec^{-2}

Point	HOR. ADV.	VERT. ADV.	CORIOLIS	U. TERM	HOR. VISC.	VERT. VISC.	TIME DERIV.
A	-2761.9	1664.0	- 29.1	- 146.2	1281.7	12.6	- 0.0
B	18775.	-3046.	-326.	-9180.	394	0.9	6618.
C	14.44	- 162.38	49.59	323.65	- 183.43	-36.38	5.48
D	13.20	- 13.46	- 2.42	- 0.87	5.99	1.24	3.68
E	1142.4	- 516.4	7.6	74.3	- 649.0	- 0.0	- 1.1
F	-2488.5	1929.5	61.6	556.9	2062.0	0.0	2121.6
G	212.0	- 210.7	17.8	37.0	- 54.7	- 0.1	1.3
H	1.51	- 16.19	6.97	- 0.57	12.35	- 0.60	3.47
I	61.85	- 13.14	11.70	4.30	- 58.16	- 6.52	0.04
J	- 106.67	2691.	92.07	22.38	64.43	-38.25	58.89
K	26.70	2.97	-135.32	13.18	12.11	82.34	1.98
L	- 0.76	4.28	0.55	- 0.02	0.17	- 3.80	0.42

Table 4.7.2: Balance of terms in the zonal momentum equation in units of 10^{-6}cm/sec^2

Point	HOR. ADV.	VERT. ADV.	HOR. DIFF.	VERT. DIFF.	TIME DERIV.
A	-214.49	141.55	70.53	2.02	-0.39
B	-371.68	201.23	170.26	-0.3	-0.5
C	- 12.52	10.41	- 1.62	3.48	-0.26
D	- 1.02	14.72	- 0.01	13.39	0.24
E	60.88	- 61.29	0.41	-0.00	-0.00
F	28.03	- 28.35	0.31	-0.00	-0.01
G	7.68	- 7.98	0.39	0.00	0.09
H	0.06	0.04	0.01	0.00	0.11
I	92.68	93.06	0.56	0.04	0.22
J	40.97	- 41.03	0.24	0.03	0.20
K	- 6.09	6.41	- 0.10	0.04	0.27
L	1.07	- 1.08	0.02	0.14	0.15

Table 4.7.3: Balance of terms in the thermal equation in units of 10^{-10}sec^{-1}.

It is not possible to make a direct comparison with Stone's and Goody and Robinson's results because they considered a Cartesian geometry, and the convergence of the meridians is very important in the presence of rotation, especially near the poles. The nonlinear terms are important everywhere in the force and heat balance equations, just as in the nonrotating case. Rotation has an important effect on the meridional circulation in the vicinity of the pole; elsewhere the balance of forces in the vorticity equation is similar to that in the nonrotating case.

It is instructive to look at the energy balance in the Boussinesq model with rotation.

We define

$$K_z = 2\pi a^2 \int_0^H \int_0^{\pi/2} \rho_o \frac{u^2}{2} \sin\alpha \, d\alpha \, dz, \tag{4.7.4}$$

the kinetic energy of the zonal motion,

$$K_M = 2\pi a^2 \int_0^H \int_0^{\pi/2} \rho_o \frac{v^2}{2} \sin\alpha \, d\alpha \, dz, \tag{4.7.5}$$

the kinetic energy of the meridional motion, and

$$P = 2\pi a^2 \int_0^H \int_0^{\pi/2} \left(\rho_o \, g \, z + \rho_o \, \tilde{\rho} \, g \, z \right) \sin\alpha \, d\alpha \, dz \tag{4.7.6}$$

the potential energy, separated into its undisturbed value and the perturbation generated after 2×10^7 secs.

From equations (4.2.1) to (4.2.5) we obtain the energy equations

$$\frac{\partial K_z}{\partial t} = CT + UT - D_z \equiv \left\{ KM, KZ \right\} - D_z \tag{4.7.7}$$

$$\frac{\partial K_M}{\partial t} = \left\{ P, K_M \right\} - CT - UT - D_M \equiv \left\{ P, K_M \right\} - \left\{ K_M, K_z \right\} - D_M \tag{4.7.8}$$

$$\frac{\partial P}{\partial t} = G_P - \left\{ P, KM \right\} \tag{4.7.9}$$

where

$$CT = 2\pi a^2 \int_0^H \int_0^{\pi/2} \rho_0 \, f \, v \sin \alpha \, d\alpha \, dz$$

$$UT = -2\pi a^2 \int_0^H \int_0^{\pi/2} \rho_0 \, \frac{\cot \alpha}{a} \, v u^2 \sin \alpha \, d\alpha \, dz$$

$$\left\{ P, KM \right\} = -2\pi a^2 \int_0^H \int_0^{\pi/2} g \, \rho_0 \, \tilde{\rho} \, w \sin \alpha \, d\alpha \, dz$$

$$G_P = 2\pi a^2 \int_0^H \int_0^{\pi/2} g \, \rho_0 \, \frac{d\tilde{\rho}}{dt} \, z \sin \alpha \, d\alpha \, dz \tag{4.7.10}$$

$$D_z = 2\pi a^2 \int_0^H \int_0^{\pi/2} \rho_0 \, u \, F_z \sin \alpha \, d\alpha \, dz \equiv$$

$$\equiv -2\pi a^2 \int_0^H \int_0^{\pi/2} \rho_0 \left\{ \frac{\nu_H}{a^2} \frac{[(u \sin \alpha)_\alpha]^2}{\sin^2 \alpha} + \nu_v (u_z)^2 \right\} \sin \alpha \, d\alpha \, dz$$

$$D_M = 2\pi a^2 \int_0^H \int_0^{\pi/2} \rho_0 \, v \, F_M \sin \alpha \, d\alpha \, dz \equiv$$

$$\equiv -2\pi a^2 \int_0^H \int_0^{\pi/2} \rho_0 \left\{ \frac{\nu_H}{a^2} \frac{[(v \sin \alpha)_\alpha]^2}{\sin^2 \alpha} + \nu_v (v_z)^2 \right\} \sin \alpha \, d\alpha \, dz$$

and F_z and F_M are the eddy friction forces in equations (4.2.1) and (4.2.2).

Paraphrasing Lorenz (1955), we can define unavailable potential energy as the potential energy of a hypothetical state of the atmosphere which has the same statistical distribution of density as the actual model atmosphere but has the least amount of potential energy. In this state of minimum potential energy, surfaces of constant density are horizontal and density never increases upwards. The available potential energy is then defined as the difference between the potential energy of the actual model and the unavailable potential energy. However, in our results the stratification of density is not stable everywhere so that there is not a simple formula to compute the available potential energy and the generation of available potential energy.

We have computed the total generation of potential energy, which includes the generation of both available and unavailable potential energy (Figure 4.7.9). This is why the generation of potential energy is larger than the conversion term from P to K_M. The smallness of the excess of potential energy compared to the initial value shows that the distribution of density has departed very little from the initial neutral stratification.

If the model had completely converged we should have the equalities

$$G_P = \{P, K_M\}$$

$$\{P, K_M\} = \{K_M, K_z\} + D_M$$

$$\{K_M, K_z\} = D_z$$

$G_p = 43.82 \times 10^{21}$

Initial Pot. En.	Excess of Pot. En.
7.022×10^{32}	13.12×10^{27}

$\{P, KM\} =$

14.87×10^{21}

Meridional Kinetic Energy

2.65×10^{27}

$CT = 1.01 \times 10^{21}$

$UT = 6.35 \times 10^{21}$

$\{K_M, K_Z\} = 7.36 \times 10^{21}$

Zonal Kinetic Energy

3.83×10^{27}

$D_M = 9.55 \times 10^{21}$

$D_Z = 7.23 \times 10^{21}$

$D_K = 16.78 \times 10^{21}$
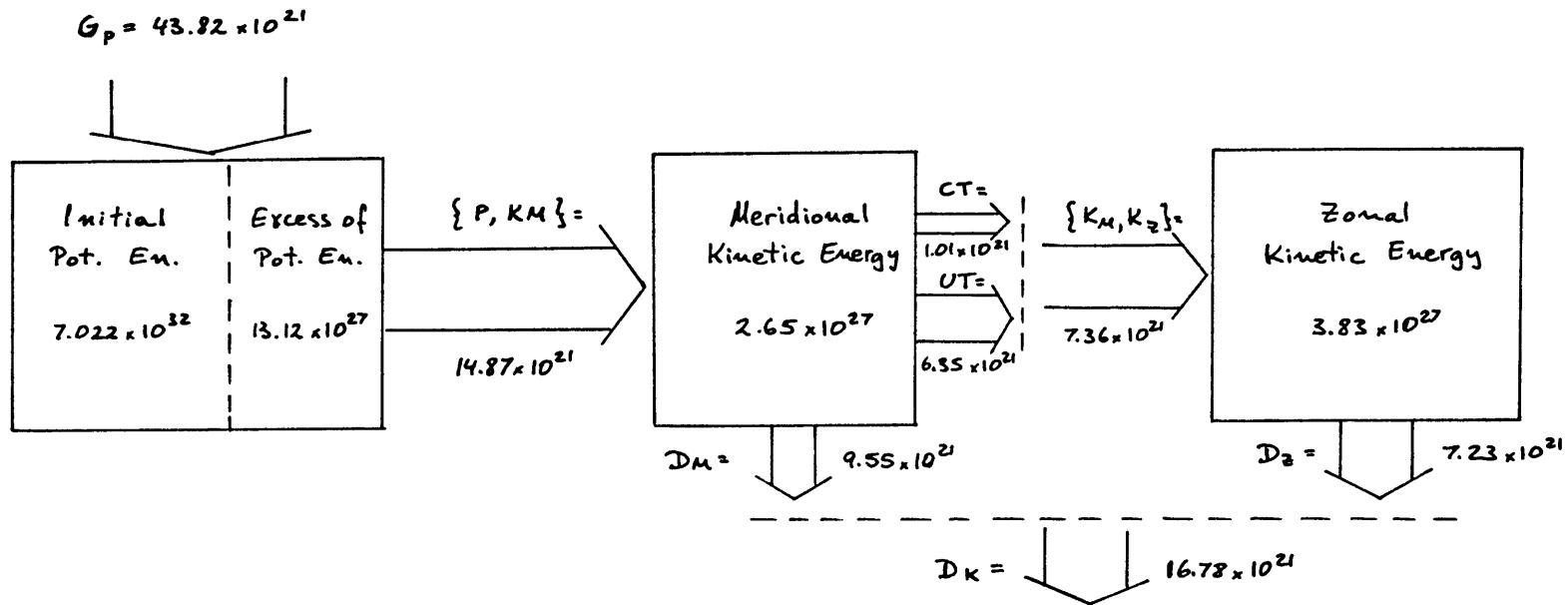
Figure 4.7.9: Balance of energy in the Boussinesq rotating model. Energies are in dynes and conversion terms are in dynes/sec.

Except for the generation of unavailable potential energy which cannot be computed, but whose effect on the total is negligible, these relationships are roughly true in the numerical results indicating that the solution has approximately converged.

It is interesting to note that the zonal kinetic energy is one and a half times larger than the meridional kinetic energy and that the conversion from K_M to K_z is accomplished mainly by the relative rotation term analogous to the Coriolis force and not by the work of the Coriolis force itself.

CHAPTER 5

Quasi-Boussinesq Model with Rotation

5.1 Introduction

In this chapter we describe a numerical model in which,
as in Chapter 4, we assume that the solar heating is symmetrical
about the axis of rotation (a "toroidal Sun"), and we also include
the effect of rotation. As pointed out in the introduction to
Chapter 4, the large thermal capacity of the atmosphere of Venus,
as well as the marked zonal structure of the temperature and cloud
distributions, make this model more realistic than that of a fixed
planet and sun. We make the quasi-Boussinesq approximation instead
of the Boussinesq approximation, so that the effect of a basic-near-
adiabatic stratification of density, pressure and temperature are
included. In this respect the model is similar to that described in
Chapter 3, except that rotation is included, and the finite-difference
treatment of the nonlinear terms has been improved.

In section 5.2 we give the quasi-Boussinesq hydrodynamical
equations. The treatment of radiative transfer is discussed in sec-
tion 5.3, and the boundary conditions in section 5.4. In section 5.5
a vertical stretched coordinate is introduced. In section 5.6 we
describe in some detail a straightforward method for constructing
a conservative, finite-difference scheme for an arbitrarily staggered
placement of dependent variables; the resultant finite-difference
equations are improved with respect to those used in Chapter 3. In
section 5.7 we give the numerical values of the physical parameters
that were used in four different specifications of the model. In

section 5.8 we present the results of the four runs, and conclude
that if most of the solar radiation is absorbed at the cloud top
level, then the circulation driven by differential heating remains
confined to the upper part of the atmosphere; it is not able to main-
tain a lapse-rate close to the adiabatic; this is in contrast to the
finding for the Boussinesq models. However, if there is some pene-
tration of solar radiation, even if only a small percentage of the
solar radiation can reach the surface, there is a double result:
the combination of a partial greenhouse effect and a deeply driven
circulation, which can stir the lower layers of the atmosphere, seems
to be capable of maintaining the observed near-adiabatic lapse rate.
In section 5.9 we present the energy budgets of the four model runs,
and in section 5.10 we derive a simple and rapid method for computing
radiative equilibrium temperatures in a grey atmosphere; the results
of several calculations with varying optical depths are presented.

5.2 Hydrodynamic equations

The following approximations are made:

(a) quasi-Boussinesq

(b) hydrostatic

(c) diurnal effects of the solar heating are neglected,
so that there is axial symmetry around the Equator

(d) semi-gray treatment of radiative transfer

(e) constant horizontal and vertical coefficients of eddy
viscosity and diffusivity; Prandtl number equal to one.

We define the variables $\zeta = z/D$, $\pi = \left(\frac{p}{p_0}\right)^\kappa$, and $\theta = \frac{T}{\pi}$
as in section 3.2, and, as in that section, we separate each dependent

variable into its basic value, corresponding to an adiabatic strati-
fication, (subindex a) and a perturbation (denoted by a prime).

We use coordinates rotating with the planet. In the fol-
lowing equations α is the colatitude, z the elevation from the sur-
face of the planet, u the zonal velocity, positive in the direction
of rotation (i.e., retrograde with respect to the orbital motion),
v is the meridional velocity positive towards the South, and w is the
vertical velocity positive upwards (see Figure 4.2.1).

The rotation period is

$$\tau = 243 \text{ days} = -2.1 \times 10^{7} \text{ sec}$$

so that we define the Coriolis parameter

$$f = 2\Omega \cos\alpha$$

where $\Omega = -2\pi/\tau = -2.99 \times 10^{-7} \text{ sec}^{-1}$

Then the zonal equation of motion is

$$\frac{\partial u}{\partial t} = -\frac{(uv\sin\alpha)_\alpha}{a\sin\alpha} - \frac{(wu\rho_a)_z}{\rho_a} + fv - \frac{\cot\alpha}{a}uv$$

$$+ \frac{\nu_H}{a^2}\left[\frac{(u_\alpha\sin\alpha)_\alpha}{\sin\alpha} - \frac{u}{\sin^2\alpha}\right] + \nu_v\, u_{zz} \qquad (5.2.1)$$

and the meridional equation of motion is

$$\frac{\partial v}{\partial t} = -\frac{(v^2\sin\alpha)_\alpha}{a\sin\alpha} - \frac{(wv\rho_a)_z}{\rho_a} - fu + \frac{\cot\alpha\, u^2}{a} - \frac{C_p\theta_a}{a}\frac{\partial\pi'}{\partial\alpha}$$

$$+ \frac{\nu_H}{a^2}\left[\frac{(v_\alpha\sin\alpha)_\alpha}{\sin\alpha} - \frac{v}{\sin^2\alpha}\right] + \nu_v\, v_{zz} \qquad (5.2.2)$$

Here we have dropped the term $-2w_\alpha$ from the square brackets in the

horizontal eddy viscosity term because it is of order H/a compared to the other terms.

The hydrostatic equation is

$$0 = -\frac{C_p \theta_a}{} \frac{\partial \pi'}{\partial z} + g \frac{\theta'}{\theta_a} \tag{5.2.3}$$

and the continuity equation may be written

$$0 = -\frac{(v \sin \alpha)_\alpha}{a \sin \alpha} + \frac{(w \rho_a)_z}{\rho_a} \tag{5.2.4}$$

since we assume that there is no longitudinal dependence.

The thermal equation is

$$\frac{\partial \theta'}{\partial t} = -\frac{(v \theta' \sin \alpha)_\alpha}{a \sin \alpha} - \frac{(w \theta' \rho_a)_z}{\rho_a} + \frac{K_H}{a^2} \frac{(\theta'_\alpha \sin \alpha)_\alpha}{\sin \alpha}$$

$$+ K_v \theta'_{zz} + \frac{q_v}{C_p \rho_a \pi_a} \tag{5.2.5}$$

where q_v is the radiative energy absorbed per unit volume and unit time, due both to solar and atmospheric radiation.

As in the quasi-Boussinesq model without rotation, (Chapter 3) we define a new variable

$$\eta = \frac{v_z}{\rho_a \sin \alpha} \tag{5.2.6}$$

instead of the vorticity .

From equations (5.2.2) to (5.2.4) and (5.2.6) we obtain an equation for η :

$$\frac{\partial \eta}{\partial t} = -\frac{(v \, \eta \, \sin\alpha)_\alpha}{a \, \sin\alpha} - \frac{(w \, \eta \, \rho_a)_z}{\rho_a} - \frac{g}{a \, \rho_a \, \sin\alpha \, \theta_a} \, \frac{\partial \theta'}{\partial \alpha} - \frac{f \, u_z}{\rho_a \, \sin\alpha}$$

$$+ \frac{\cot\alpha}{a \, \rho_a \, \sin\alpha} \, \frac{\partial u^2}{\partial z} + \frac{\nu_H}{a^2} \left[\frac{((\eta \, \sin\alpha)_\alpha \, \sin\alpha)_\alpha}{\sin^2\alpha} - \frac{\eta}{\sin^2\alpha} \right] + \frac{\nu_v}{\rho_a} (\eta \, \rho_a)_{zz} \qquad (5.2.7)$$

As in Chapter 3, we define a mass stream function ψ such that

$$\left(\frac{\psi_z}{\rho_a}\right)_z = \eta \, \rho_a \, \sin^2\alpha \qquad (5.2.8)$$

Then

$$v \, \sin\alpha \, \rho_a = \psi_z \qquad (5.2.9)$$

and

$$w \, \sin\alpha \, \rho_a = -\frac{\psi_\alpha}{a} \qquad (5.2.10)$$

Equations (5.2.1) and (5.2.5) to (5.2.10), with the boundary conditions and the formulation of q_v , the radiational heating, define the model.

5.3 Radiative transfer

As in Chapter 3, we make a semi-grey assumption, i.e., assume a different constant absorption coefficient for the solar and long wave regions of the spectrum.

(a) Long-wave radiative transfer

This is the same as in the non-rotating model, section 3.3 part (a).

(b) Short-wave radiation.

As in Chapter 3, we assume that the volume extinction coefficient in the short-wave region of the spectrum is proportional to the mean density and is zero above z = H; this implies that any scattered radiation is absorbed at essentially the same level at which it is generated.

The zenith angle of the sun at a point P is, from Figure 5.3.1,

$$
\cos \gamma = \begin{cases} \cos \varphi \cos (\Omega t) + \cos 90° \sin \varphi \sin (\Omega t) & \text{if } |\Omega t| \le \frac{\pi}{2} \quad (\text{day}) \\ 0 & \text{if } |\Omega t| > \frac{\pi}{2} \quad (\text{night}) \end{cases} \tag{5.3.1}
$$

The flux of solar radiation is

$$
\frac{d F_s}{F_s} = - \frac{k_s \, dz}{\cos \gamma} = - \frac{d \tau_s}{\cos \gamma} \tag{5.3.2}
$$

and the flux of solar radiation impinging on the top is

$$
\downarrow F_s (H, \varphi, \Omega t) = \begin{cases} S_0 (1-A) \cos \varphi \cos (\Omega t) & \text{if } |\Omega t| \le \frac{\pi}{2} \\ 0 & \text{if } |\Omega t| > \frac{\pi}{2} \end{cases} \tag{5.3.3}
$$

Hence

$$
\downarrow F_s (z, \varphi, \Omega t) = \begin{cases} S_0 (1-A) \cos \varphi \cos (\Omega t) \, e^{- \frac{\tau_s(z)}{\cos \varphi \cos \Omega t}} & \text{if } |\Omega t| \le \frac{\pi}{2} \\ 0 & \text{if } |\Omega t| > \frac{\pi}{2} \end{cases} \tag{5.3.4}
$$
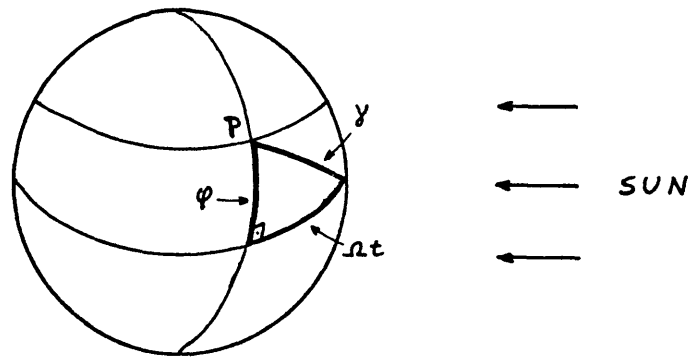
Figure 5.3.1: γ : zenith angle; $\varphi = \frac{\pi}{2} - \alpha$:

latitude; Ωt : hour angle from the local noon.

We neglect diurnal effects in this model, so that the flux of solar radiation over a Venus solar day is averaged:

$$\downarrow F_s (z, \varphi) = \int_{-\pi/2}^{\pi/2} \downarrow F_s (z, \varphi, \Omega t) \, d(\Omega t) \Big/ \int_{-\pi}^{\pi} d(\Omega t)$$

$$= \frac{S_o (1-A) \cos \varphi}{2\pi} \int_{-\pi/2}^{\pi/2} \cos \delta \, e^{-\frac{\tau_s(z)}{\cos \varphi \cos \delta}} \, d\delta \qquad (5.3.5)$$

This integration was carried out numerically using Simpson's rule.

(c) Heating rate

The radiative energy q_v absorbed per unit volume and unit time is

$$q_v = \frac{\partial (\overline{F_s} - F_T)}{\partial z} \qquad (5.3.6)$$

5.4 Boundary conditions

Since the driving is symmetric with respect to the equator, we consider only the northern hemisphere, as in Chapter 4. The boundary conditions for a zero-stress rigid top, a zero-velocity rigid bottom, and symmetry at the equator are as follows:

$$\psi = \left(\frac{\psi_z}{\rho_a}\right)_z = 0 \qquad \text{at} \quad z = H \qquad a$$

$$\psi = \psi_z = 0 \qquad \text{at} \quad z = 0 \qquad b \qquad \Bigg\} \quad (5.4.1)$$

$$\psi = 0 \qquad \text{at} \quad \alpha = 0, \frac{\pi}{2} \qquad c$$

$$\mu_z = 0 \qquad\qquad at\ z = 0$$

$$\mu = 0 \qquad\qquad at\ z = H$$

$$\mu = 0 \qquad\qquad at\ \alpha = 0$$

$$\mu_\alpha = 0 \qquad\qquad at\ \alpha = \frac{\pi}{2}$$

$$(5.4.2)$$

The boundary conditions for the energy equation are similar

to those in Chapter 3 (quasi-Boussinesq model without rotation).

Since we assume that the ground has a negligible heat capacity, the

net heat flux due to solar and thermal radiation and to convection

is zero at the ground. At the equator we assume symmetric conditions.

$$\theta'_z = 0 \qquad\qquad at\ z = H \qquad\qquad a$$

$$-\kappa_v\, \rho_a^*\, C_p\, \theta_z^{'*} + 4\sigma\theta_a^3\left\{\frac{4\kappa}{r z_{T_0}}\,\theta^{'*} + \frac{1}{r}\left(\frac{d\theta'}{dz_T}\right)^{*}\right\}$$

$$= \overline{F_s^*} - F_{ra}^* \qquad at\ z = 0 \qquad\qquad b \qquad (5.4.3)$$

$$\theta'_\alpha = 0 \qquad\qquad at\ \alpha = \frac{\pi}{2} \qquad\qquad c$$

(The left hand side of equation (5.4.3b) is the same as equation

(3.4.4b).

5.5 Equations with the vertical coordinate stretched

For this model we decided to use stretched vertical coor-

dinates and a regular horizontal grid, since from the results obtained

with the Boussinesq model with rotation and from preliminary quasi-

Boussinesq calculations we didn't expect a narrow boundary layer at

the pole.

The vertical stretched coordinate is

$$s = \frac{2}{\pi} \arctan \sqrt{\frac{z}{H-z}} \quad ; \quad \frac{ds}{dz} = \frac{1}{HS} \qquad \text{where} \quad S = \pi \sqrt{\frac{z}{H} \left(1 - \frac{z}{H}\right)} \qquad (5.5.1)$$

The model equations with the vertical stretched coordinates are the zonal momentum equation,

$$\frac{\partial u}{\partial t} = -\frac{(v u \sin \alpha)_\alpha}{a \sin \alpha} - \frac{(w u \, \rho_a)_s}{H S \rho_a} + f v - \frac{\cot \alpha}{a} u v$$

$$+ \frac{\nu_H}{a^2} \left[\frac{(u_\alpha \sin \alpha)_\alpha}{\sin \alpha} - \frac{u}{\sin^2 \alpha} \right] + \frac{\nu_v}{H^2} \frac{1}{S} \left(\frac{u_s}{S} \right)_s , \qquad (5.5.2)$$

the "vorticity" equation, with   ,

$$\frac{\partial \eta}{\partial t} = -\frac{(v \eta \sin \alpha)_\alpha}{a \sin \alpha} - \frac{(w \eta \rho_a)_s}{H S \rho_a} - \frac{g}{a \rho_a \sin \alpha} \frac{\partial \tilde{\theta}}{\partial \alpha} - \frac{f u_s}{\rho_a H S \sin \alpha}$$

$$+ \frac{\cot \alpha}{H S \rho_a \, a \sin \alpha} (u^2)_s + \frac{\nu_H}{a^2} \left[\frac{((\eta \sin \alpha)_\alpha \sin \alpha)_\alpha}{\sin^2 \alpha} - \frac{\eta}{\sin^2 \alpha} \right] + \frac{\nu_v}{H^2} \frac{1}{\rho_a S} \left[\frac{(\rho_a \eta)_s}{S} \right]_s ,$$

$$(5.5.3)$$

the thermal equation,

$$\frac{\partial \tilde{\theta}}{\partial t} = -\frac{(v \tilde{\theta} \sin \alpha)_\alpha}{a \sin \alpha} - \frac{(w \tilde{\theta} \rho_a)_s}{H S \rho_a} + \frac{\kappa_H}{a^2} \left[\frac{(\tilde{\theta}_\alpha \sin \alpha)_\alpha}{\sin \alpha} \right]$$

$$+ \frac{\kappa_v}{H^2} \frac{1}{S} \left(\frac{\theta_s}{S} \right)_s + \frac{q_v}{C_p \theta_a \pi_a \rho_a} \qquad (5.5.4)$$

the definition of the mass stream function

$$\left(\frac{\psi_s}{S \rho_a} \right)_s = \eta \, \rho_a \, S \, \sin^2 \alpha \, H^2 , \qquad (5.5.5)$$

giving the velocity components

$$v = \frac{\psi_s}{H S \rho_a \sin \alpha} ,$$

(5.5.6)

and

$$w = - \frac{\psi_\alpha}{a \sin \alpha \, \rho_a}$$

(5.5.7)

The boundary conditions are:

$$\psi = \eta = 0 \qquad \text{at } s = 1$$

$$\psi = \psi_s = 0 \qquad \text{at } s = 0$$

$$\psi = 0 \qquad \text{at } \alpha = 0, \frac{\pi}{2}$$

(5.5.8)

$$u_s = 0 \qquad \text{at } s = 1$$

$$u = 0 \qquad \text{at } s = 0$$

$$u = 0 \qquad \text{at } \alpha = 0$$

$$u_\alpha = 0 \qquad \text{at } \alpha = \frac{\pi}{2}$$

(5.5.9)

$$\tilde{\theta}_s = 0 \qquad \text{at } s = 1$$

$$- \frac{\kappa_v \, \rho_a \, C_p \theta_a \, \tilde{\theta}_s}{H S} + 4 \sigma \theta_a^3 \left\{ \frac{4 \kappa}{r \, c_{T_0}} \tilde{\theta} + \frac{1}{r} \frac{\partial \tilde{\theta}}{\partial \zeta_r} \right\} = \overline{\overline{F}}_s - \overline{F}_{T_a}$$

$$\text{at } s = 0$$

$$\tilde{\theta}_\alpha = 0 \qquad \text{at } \alpha = \frac{\pi}{2}$$

(5.5.10)

5.6 Finite-difference equations

We used the same staggered grid as in Chapter 3 with u_{ij} located at the same place as v_{ij} (Figure 5.6.1).

The conservative finite-difference equation for the thermal equation is

$$\tilde{\Theta}_{ij}^{m+1} = \tilde{\Theta}_{ij}^{n-1} + 2\Delta t \left\{ - \frac{v_{ij}(\tilde{\Theta}_{ij} + \tilde{\Theta}_{i+1j})SIN'_i - v_{i-1j}(\tilde{\Theta}_{ij} + \tilde{\Theta}_{ij-1})SIN'_{i-1}}{2\Delta\alpha\, a\, SIN_i} \right.$$

$$- \frac{w_{ij}(\tilde{\Theta}_{ij} + \tilde{\Theta}_{ij+1})P'_{aj} - w_{ij-1}(\tilde{\Theta}_{ij} + \tilde{\Theta}_{ij-1})}{2\Delta s\, H\, S_j\, P_{aj}}$$

$$+ \frac{K_{\#}}{a^2}\left[\frac{(\tilde{\Theta}_{i+1j}^{n-1} - \tilde{\Theta}_{ij}^{n-1})/S'_j - (\tilde{\Theta}_{ij}^{n-1} - \tilde{\Theta}_{ij-1}^{n-1})/S'_{j-1}}{\Delta s^2\, S_j} \right]$$

$$+ \left. \frac{F_{ij} - F_{ij-1}}{\Delta s\, H\, S_j\, P_{aj}\, C_p\, \Theta_a\, \pi_{aj}} \right\} \tag{5.6.1}$$

where $i = 2, \dots, IM+1$, $j = 2, \dots, JM+1$

and $F_{ij} = \left(\overline{F_S} - F_{Ta} - F'_T \right)_{ij}$ is the radiative flux.

Equation (5.6.1) coincides with (3.6.1), which was written with a horizontal stretched coordinate, if we make $\Delta y = \Delta\alpha$ and $Y_i = Y'_i = 0.5$. This is an illustration of the advantage of using stretched coordinates defined analytically. It allows a change in the type of stretched coordinate without a change in the finite-difference equations; one only needs to redefine the derivative of the

stretched coordinate with respect to the physical coordinate.

The finite-difference vortex strength equation is here improved in such a way that the truncation errors in the spacial differencing of the nonlinear flux terms are reduced from order $O\left(2\Delta\right)^{2}$ as in Chapter 3, to $O\left(\Delta\right)^{2}$, the same as the truncation errors in the corresponding terms in the thermal equation. We present the derivation in some detail because it gives a simple and general procedure for obtaining a finite-difference analogue of the equation

$$\frac{\partial f}{\partial t} = - \nabla \cdot \left(f \, v\right)$$

which shares the conservation properties of the staggered method (Williams, 1969; Bryan, 1967; Lilly, 1964), i.e., conservation of $\overline{f}$ and $\overline{f^{2}}$, even when the position of the variable f is not at the center of the grid cell at which the finite difference analogue of the continuity equation

$$\nabla \cdot v = 0$$

has been formulated.

This derivation can be used for any model which has a time independent continuity equation and will prevent the development of nonlinear instability. If the continuity equation contains a time derivative a scheme similar to scheme c in section 2.6 can be used.

The idea is to obtain a finite-difference continuity equation defined at the points at which the $f's$ are located, in which the normal velocities are those that should be used in the staggered method. For this purpose the finite difference continuity equations defined exactly at neighboring points should be averaged with weights

<u>proportional to the mass contained in those cells.</u>

From the continuity equation (5.2.4) in stretched coordinates

$$\frac{(v \sin \alpha)_\alpha}{a \sin \alpha} + \frac{(w \, p_a)_s}{H \, S} = 0$$

and the finite-difference equivalent of equations (5.5.6) and (5.5.7) we get

$$v_{ij}^{n+1} = \frac{\psi_{ij}^{n+1} - \psi_{ij-1}^{n+1}}{\Delta s \, H S_j \, p_{aj} \, \sin_i'} \tag{5.6.2}$$

$$w_{ij}^{n+1} = - \frac{\psi_{ij}^{n+1} - \psi_{i-1j}^{n+1}}{\Delta \alpha \, a \, \sin_i \, p_{aj}'} \tag{5.6.3}$$

We see that the finite-difference equivalent of the continuity equation is defined exactly for a cell with center at a " $\tilde{\Theta}_{ij}$ -point" (Figure 5.6.1) as

$$\frac{v_{ij} \, \sin_i' - v_{i-1j} \, \sin_{i-1}'}{\Delta \alpha \, a \, \sin_i} + \frac{w_{ij} \, p_{aj}' - w_{ij-1} \, p_{aj-1}'}{\Delta s \, H \, S_j \, p_{aj}} \tag{5.6.4}$$

The mass of the ring whose cross-section is the cell centered at a " $\tilde{\Theta}_{ij}$ -point" is proportional to $\sin_i \, S_j \, p_{aj}$. To obtain the exact finite-difference continuity equation for a cell centered at an " η_{ij} -point" (the cell limited by a dashed line in Figure 5.6.2), we add the finite-difference continuity equation (5.6.4) defined at the four neighboring points $\tilde{\Theta}_{ij}$, $\tilde{\Theta}_{i+1j}$, $\tilde{\Theta}_{ij+1}$, and $\tilde{\Theta}_{i+1j+1}$ multiplied by the mass of the corresponding cells, and divide by the total mass $4 \sin_i' \, S_j' \, p_{aj}'$:
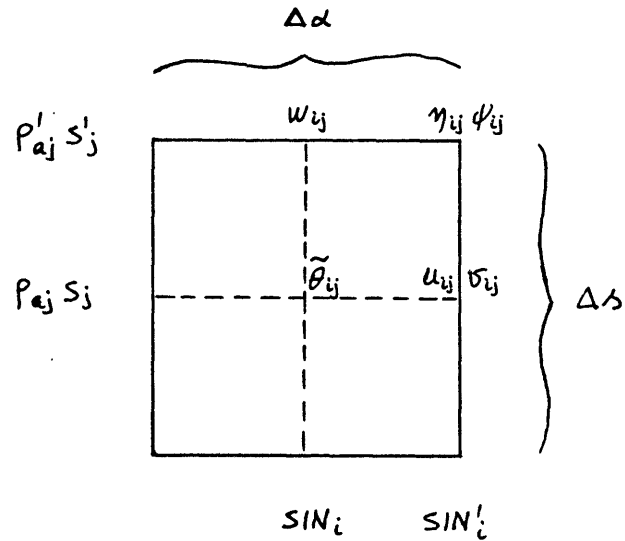
$$\overbrace{\qquad\qquad}^{\Delta\alpha}$$

Figure 5.6.1: Typical cell with the position of the variables and functions having the subindices i,j.
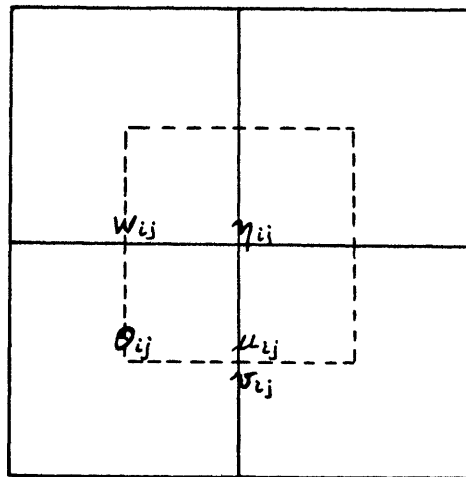

Figure 5.6.2: Cell centered at a " η_{ij} -point" for which a finite-difference continuity equation is found.

$$\frac{\left(A_{ij} + A_{ij+1} + A_{i+1j} + A_{i+1j+1}\right) - \left(A_{i-1j} + A_{i-1j+1} + A_{ij} + A_{ij+1}\right)}{4\Delta\alpha\, a\, \text{SIN}'_i\, S'_j\, \varphi'_{aj}}$$

$$+ \frac{\left(B_{ij} + B_{ij+1} + B_{i+j} + B_{i+1j+1}\right) - \left(B_{ij-1} + B_{ij} + B_{i+1j-1} + B_{i+1j}\right)}{4\Delta_\rho} = 0 \qquad (5.6.5)$$

where

$$A_{ij} = \sigma_{ij}\, SIN'_i\, S_j\, \varphi_{aj}$$

$$B_{ij} = w_{ij}\, SIN_i\, \varphi'_{aj}$$

If we cancel the terms A_{ij} , A_{ij+1} , B_{ij} , and B_{i+1j} in

(5.6.5), as we did in the quasi-Boussinesq model without rotation,

(5.6.5) becomes the continuity equation valid at the large cell

composed of the four smaller cells in Figure (5.6.2), but as it is,

equation (5.6.5) corresponds to the small dashed cell.

Analogously, to develop a conservative scheme for u, we

need the finite-difference continuity equation for a cell centered

at a " μ_{ij} -point" (Figure 5.6.3). Here it is necessary to average

the continuity equation at only two neighboring cells, and we obtain

$$\frac{\left(A_{ij} + A_{i+1j}\right) - \left(A_{i-1j} + A_{ij}\right)}{2\Delta\alpha\, a\, SIN'_i\, S_j\, \varphi_{aj}} + \frac{\left(B_{ij} + B_{i+1j}\right) - \left(B_{ij-1} + B_{i+1j-1}\right)}{2\Delta_\rho H\, SIN'_i\, S_j\, \varphi_{aj}} = 0 \qquad (5.6.6)$$

In equations (5.6.5) and (5.6.6), each parenthesis repre-

sents the normal flux of mass that has to be used in the conservative

scheme. Accordingly the finite-difference vorticity equation equi-
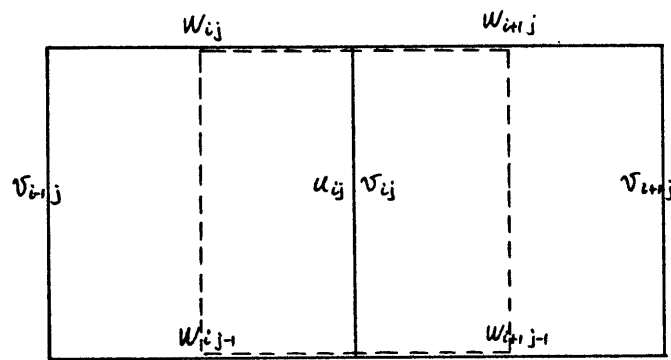
valent to (5.5.3) is

Figure 5.6.3: Cell centered at a " μ_{ij} - point" for which a finite-difference continuity equation is found.

$$\eta_{ij}^{m+1} = \eta_{ij}^{m-1} + 2\Delta t \left\{ -\left\langle \left[\left(\nu_{ij} S_j P_{a_j} + \nu_{ij+1} S_{j+1} P_{a_{j+1}} \right) SIN_i' + \left(\nu_{i+1j} S_j P_{a_j} \right. \right. \right.\right.$$

$$\left. + \nu_{i+1j+1} P_{a_{j+1}} S_{j+1} \right) SIN_{i+1}' \right] \left(\eta_{ij} + \eta_{i+1j} \right) - \left[\left(\nu_{i-1j} S_j P_{a_j} + \nu_{i-1j+1} S_{j+1} P_{a_{j+1}} \right) \right.$$

$$SIN_{i-1}' + \left(\nu_{ij} S_j P_{a_j} + \nu_{ij+1} S_{j+1} P_{a_{j+1}} \right) SIN_i' \right] \left(\eta_{i-1j} + \eta_{ij} \right) \Big\rangle / \left(8\Delta\alpha a \, SIN_i' S_j' P_{a_j}' \right)$$

$$- \left\langle \left[\left(W_{ij} SIN_i + W_{i+1j} SIN_{i+1} \right) P_{a_j}' + \left(W_{ij+1} SIN_i + W_{i+1j+1} SIN_{i+1} \right) P_{a_{j+1}}' \right] \right.$$

$$\left(\eta_{ij} + \eta_{ij+1} \right) - \left[\left(W_{ij-1} SIN_i + W_{i+1j-1} SIN_{i+1} \right) P_{a_{j-1}}' + \left(W_{ij} SIN_i + W_{i+1j} SIN_{i+1} \right) P_{a_j}' \right]$$

$$\left(\eta_{ij-1} + \eta_{ij} \right) \Big\rangle / \left(8\Delta_s H \, SIN_i' S_j' P_{a_j}' \right) - g / \left(2\Delta\alpha a \, SIN_i' P_{a_j}' \right) \times$$

$$\left[\bar{\theta}_{i+1j} + \bar{\theta}_{i+1j+1} - \tilde{\theta}_{ij} - \bar{\theta}_{ij+1} \right] - f_i' \left(\mu_{ij+1} - \mu_{ij} \right) / \left(\Delta_s H \, S_j' P_{a_j}' \, SIN_i' \right)$$

$$+ COT_i / \left(\Delta_s H \, a \, S_j' P_{a_j}' \, SIN_i' \right) \left(\mu_{ij+1}^2 - \mu_{ij}^2 \right)$$

$$+ \frac{\nu_H}{a^2} \left\langle \left[\left(\eta_{i+1j}^{m-1} SIN_{i+1}' - \eta_{ij}^{m-1} SIN_i' \right) SIN_{i+1} - \left(\eta_{ij}^{m-1} SIN_i' - \eta_{i-1j}^{m-1} SIN_{i-1}' \right) SIN_i \right] \right.$$

$$\left. / \left[(\Delta\phi)^2 SIN_i'^2 \right] - \eta_{ij}^{m-1} / SIN_i'^2 \right\rangle + \frac{\nu_\nu}{H^2} \left[\left(\eta_{ij+1}^{m-1} P_{a_{j+1}}' - \eta_{ij}^{m-1} P_{a_j}' \right) / S_{j+1} \right.$$

$$\left. - \left(\eta_{ij}^{m-1} P_{a_j}' - \eta_{ij-1}^{m-1} P_{a_{j-1}}' \right) / S_j \right] / \left(\Delta_s^2 S_j' P_{a_j}' \right) \right\} \tag{5.6.7}$$

where $i = 2, \ldots, IM$

$j = 2, \ldots, JM$

and the forecast equation for u is

$$u_{ij}^{n+1} = u_{ij}^{n-1} + 2\Delta t \left\{ - \left[(\sigma_{ij} SIN_i' + \sigma_{i+1j} SIN_{i+1}')(u_{ij} + u_{i+1j}) - \right. \right.$$

$$(\sigma_{i-1j} SIN_{i-1}' + \sigma_{ij} SIN_i')(u_{i-1j} + u_{ij}) \left] / (4\Delta\alpha a\, SIN_i') \right.$$

$$- \left[(w_{ij} SIN_i + w_{i+1j} SIN_{i+1}) P_{aj}'(u_{ij} + u_{ij+1}) - (w_{ij-1} SIN_i + w_{i+1j-1} SIN_{i+1}) \times \right.$$

$$\times P_{aj-1}'(u_{ij} + u_{ij-1}) \left] / (4\Delta\lambda H\, SIN_i'\, S_j\, P_{aj}) + f_i'\, \sigma_{ij} - \frac{COT_i}{a}\, u_{ij}\, \sigma_{ij} \right.$$

$$+ \frac{\gamma_H}{a^2} \left\langle \left[(u_{i+1j}^{n-1} - u_{ij}^{n-1}) SIN_{i+1} - (u_{ij}^{n-1} - u_{i-1j}^{n-1}) SIN_i \right] / (\Delta\alpha\, SIN_i') \right.$$

$$\left. - \frac{u_{ij}^{n-1}}{SIN_i'^2} \right\rangle + \frac{\gamma_v}{H^2} \left[(u_{ij+1}^{n-1} - u_{ij}^{n-1})/S_j' - (u_{ij}^{n-1} - u_{ij-1}^{n-1})/S_{j-1}' \right] \right\}$$

(5.6.8)

where $\quad i = 2, \ldots, IM\ ;\ j = 2, \ldots, JM+1$

Equation (5.5.5) in finite-difference form is written as in the non-rotating model

$$\psi_{ij+1}^{n+1} - \psi_{ij}^{n+1}\left(1 + \frac{P_{aj+1}\, S_{j+1}}{P_{aj}\, S_j} \right) + \frac{P_{aj+1}\, S_{j+1}}{P_{aj}\, S_j}\, \psi_{ij-1} = $$

$$= \left(\Delta_\lambda^2\, H^2\, S_j'\, P_{aj}'\, S_{j+1}\, P_{aj+1}\, SIN_i' \right) \eta_{ij}^{n+1} \qquad (5.6.9)$$

where $\quad i = 2, \ldots, IM;\ j = 2, \ldots, JM$

Equation (5.6.9) is solved as described in the non-rotating model

(equation 3.6.9):

The boundary conditions in finite differences are

$$\psi_{i1}^{n+1} = \psi_{iJM+1}^{n+1} = 0 \qquad \text{where } i = 2,\ldots,IM$$

$$\psi_{1j}^{n+1} = \psi_{IM+1\,j}^{n+1} = 0 \qquad \text{where } j = 2,\ldots,JM$$

$$\left.\begin{array}{l}\end{array}\right\} \qquad (5.6.10)$$

$$\eta_{1j}^{n+1} = \eta_{IM+1\,j}^{n+1} = 0 \qquad \text{where } j = 2,\ldots,JM$$

$$\eta_{i\,JM+1}^{n+1} = 0$$

$$\left.\begin{array}{l}\end{array}\right\} \qquad (5.6.11)$$

$$\eta_{i1}^{n+1} = \left[\frac{2z_2}{z_1^2(z_2-z_1)} \psi_{i2}^{n+1} - \frac{2z_1}{z_1^2(z_2-z_1)} \psi_{i3}^{n+1} \right] \Big/ \left(\rho_{a_1}^{\prime\,2} \sin_i^{\prime\,2} \right)$$

$$\text{where } i = 2,\ldots,IM$$

$$(5.6.12)$$

$$u_{i1}^{n+1} = -u_{i2}^{n+1}$$

$$u_{i\,JM+2}^{n+1} = u_{i\,JM+1}^{n+1} \qquad \text{where } i = 2,\ldots, IM$$

$$u_{1j}^{n+1} = 0$$

$$u_{IM+1\,j}^{n+1} = u_{IM\,j}^{n+1} \qquad \text{where } j = 2,\ldots,JM+1$$

$$\left.\begin{array}{l}\end{array}\right\}$$

$$\tilde{\theta}_{i\ JM+2}^{m+1} = \tilde{\theta}_{i\ JM+1}^{m+1}$$

$$C_1\ \tilde{\theta}_{i1}^{m+1} = C_2\ \tilde{\theta}_{i2}^{m+1} + \left(\overline{F}_s - F_{Ta}\right)_{i,1}, \qquad \text{where } i = 2,\cdots,IM+1$$

$$\tilde{\theta}_{IM2,j}^{m+1} = \tilde{\theta}_{IM+1,j}^{m+1} \qquad\qquad \text{where } j = 2,\cdots,JM+1,$$

$\tag{5.6.13}$

C_1 and C_2 are defined in (3.6.13b).

5.7 Physical data

We made several runs with this model. The following numerical values for the physical parameters were unchanged.

$$a = 6.05 \times 10^8 \ cm$$

$$H = 5.3 \times 10^6 \ cm$$

$$g = 8.5 \times 10^2 \ cm/sec^2$$

$$C_p = 8.5 \times 10^6 \ cm^2/(sec^2\ {}^\circ K)$$

$$\Gamma = g/C_p = 10^{-4}\ {}^\circ K/cm$$

$$R = 1.9 \times 10^6 \ cm^2/(sec^2\ {}^\circ K)$$

$$\sigma = 5.67 \times 10^{-5} \ g/(sec^3\ {}^\circ K^4)$$

$$T_{e\parallel} = 230\ {}^\circ K$$

$$\theta_a = \overline{T}(z=0) = 730\ {}^\circ K$$

$$p_0 = 100 \ atm = 1.013 \times 10^8 \ dyne/cm^2$$

$$z_T^* = 222$$

$$f_0 = -5.984 \times 10^{-7} \ sec^{-1}$$

The above values coincide with the values used in the nonrotating model (Chapter 3).

The other parameters were varied in the following way:

Run I $\quad \nu_H = K_H = 10^{10} \ cm^2/sec$

$\qquad\qquad \nu_V = K_V = 10^4 \ cm^2/sec$

$\qquad\qquad \zeta_s^* = 55$

Run II $\quad \nu_H = K_H = 10^{11} \ cm^2/sec$

$\qquad\qquad \nu_V = K_V = 10^4 \ cm^2/sec$

$\qquad\qquad \zeta_s^* = 55$

Run III $\quad \nu_H = K_H = 10^{10} \ cm^2/sec$

$\qquad\qquad \nu_V = K_V = 10^3 \ cm^2/sec$

$\qquad\qquad \zeta_6^* = 55.$

Run IV $\quad \nu_H = K_H = 10^{10} \ cm^2/sec$

$\qquad\qquad \nu_V = K_V = 10^4 \ cm^2/sec$

$\qquad\qquad \zeta_s^* = 2.3$

5.8 Results

Figure 5.8.1 shows the basic heating of the atmosphere assuming an adiabatic stratification and the optical depths of $\zeta_T^* = 222$ for the long wave part of the spectrum and $\zeta_s^* = 55$ for the solar radiation. It may be seen that the maximum heating contrast between equator and poles occurs very near the top; in this respect the situation is similar to the one assumed in the Boussinesq model (Chapter 4). This basic heating was used in the first three runs.
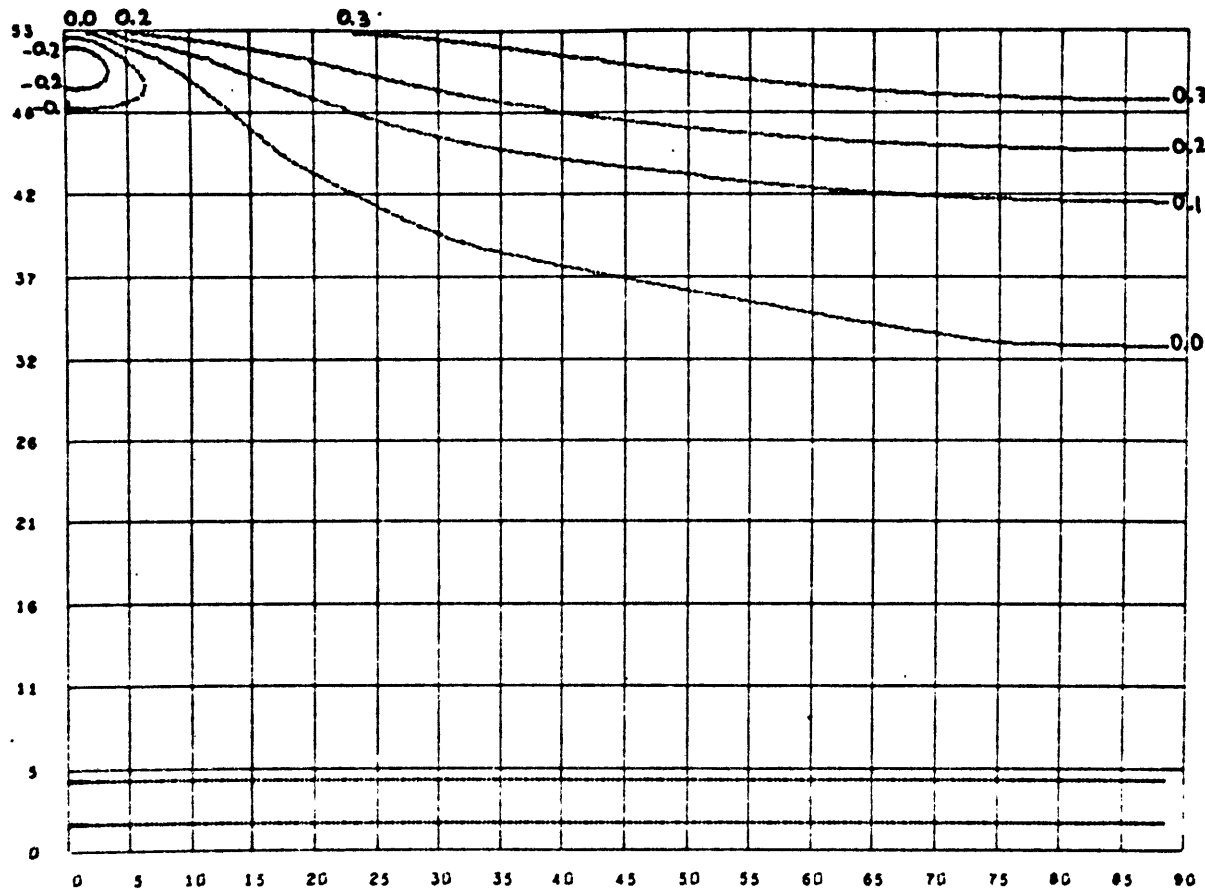
Figure 5.8.1: Basic heating for an adiabatic stratification
used in Runs I, II and III.

<u>Run I</u>: The values of the coefficients of eddy viscosity and diffusivity are those suggested by Goody and Robinson. Figures 5.8.2 to 5.8.8 show the results obtained after running the equivalent of 3.94×10^7 secs. At this time the velocities and temperatures had practically converged at the upper and middle levels, but not quite near the bottom. The most striking result is that the circulation remains confined to the top 10 km or so of the atmosphere. The velocities are of the same order of magnitude as those obtained in the Boussinesq model but somewhat larger. The maximum zonal velocity is about 19 m/s and the maximum meridional velocity about 12 m/s, as compared to 14 m/s and 10 m/s respectively in the Boussinesq model. The indirect cell near the pole is present but is weaker than in the Boussinesq model, perhaps because in the Boussinesq calculation there was better resolution near the pole. The return meridional flow has a maximum velocity of 60 cm/s at a depth of 6 km from the top. In the interior the meridional velocities are of the order of a few cm/sec and the zonal velocities are even smaller. In accordance with the existence of a counter cell, the downward jet is located at about 8° colatitude from the pole, with a maximum speed of about 28 cm/sec.

The temperature contrast $\Delta \tilde{\theta}$ between equator and pole is 1.1% or about 2°K.

Tables 5.8.1, 5.8.2, and 5.8.3 show the balance of terms in the vorticity, zonal momentum and thermal equation respectively at nine points. The position of the points is indicated in Figure 5.8.9.
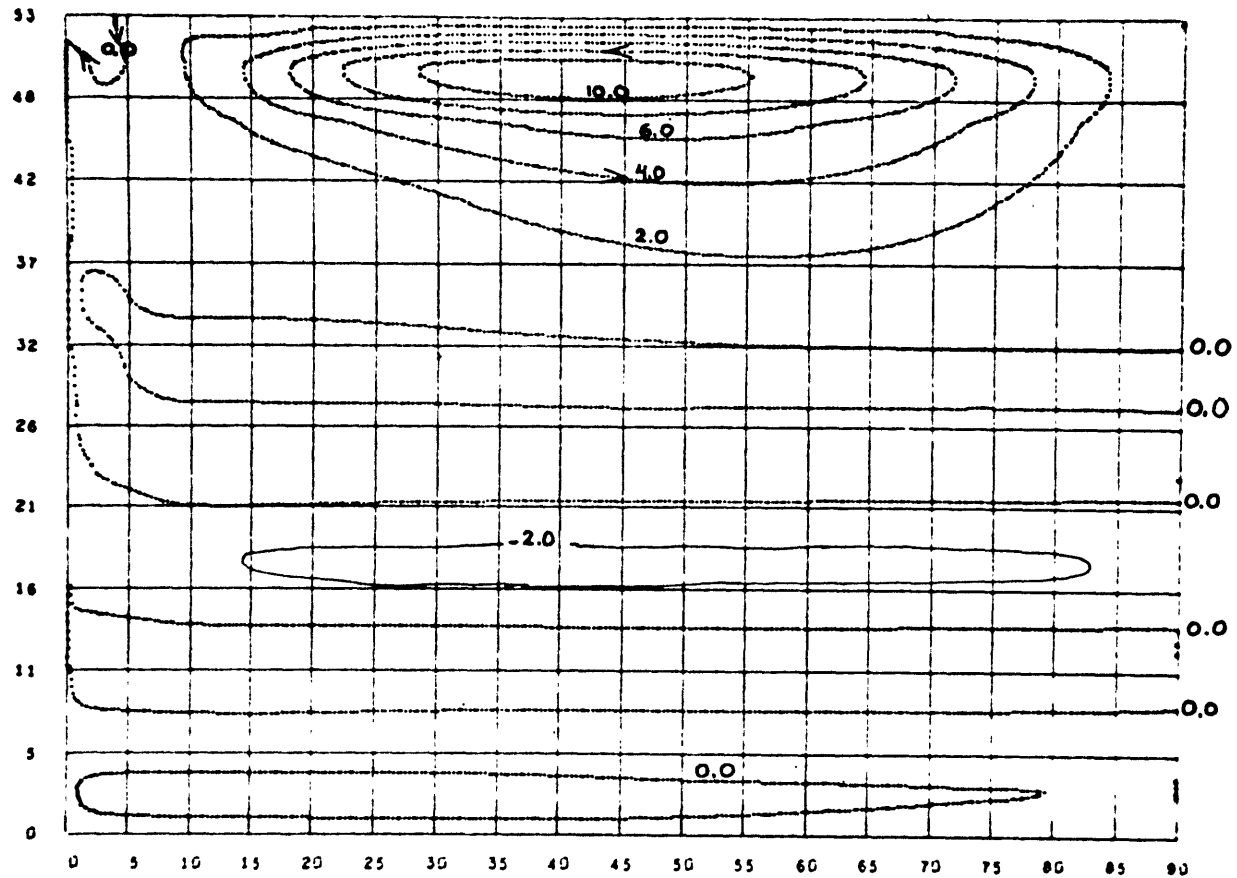
Figure 5.8.2: Meridional mass stream function ψ corresponding to Run I
after a time of 3.94×10^7sec.
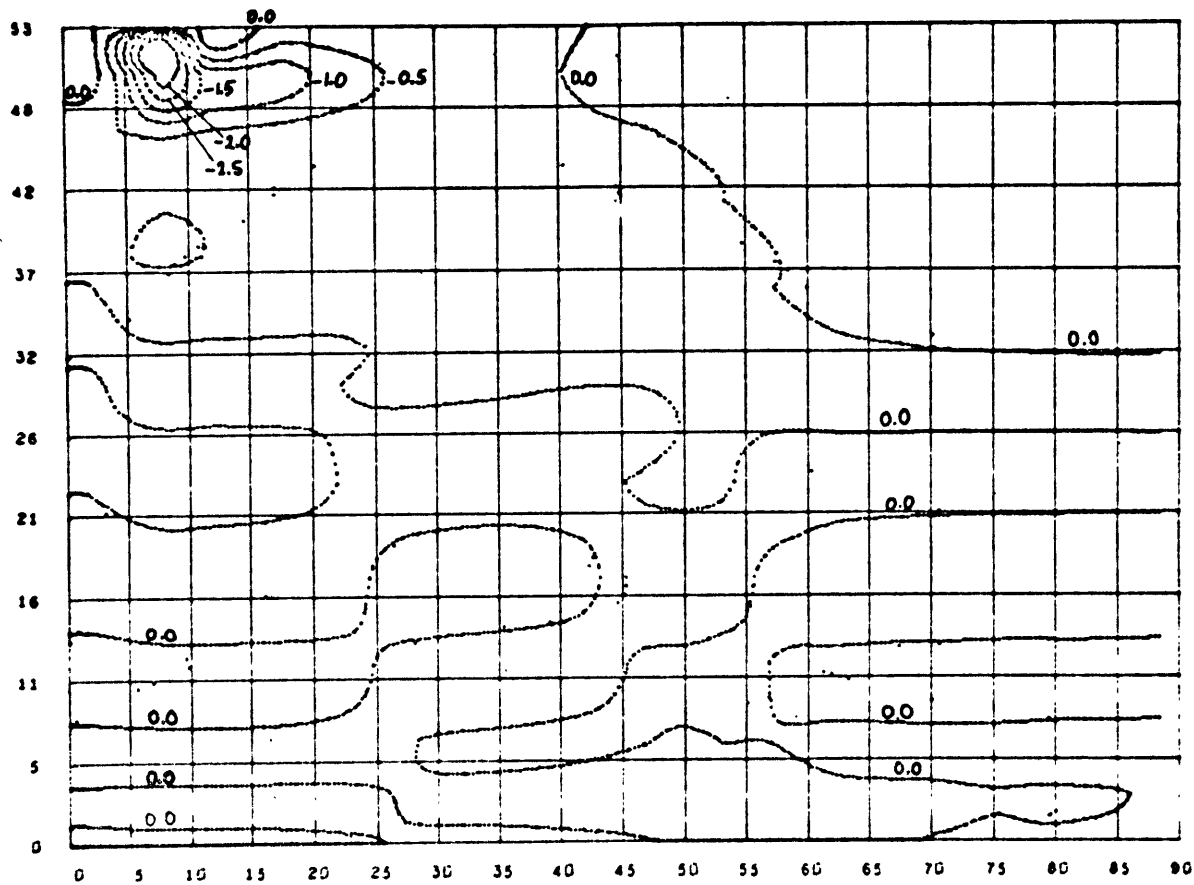
Figure 5.8.3: Zonal vortex strength η for Run I in units of 10 $cm^3sec^{-1}g^{-1}$.
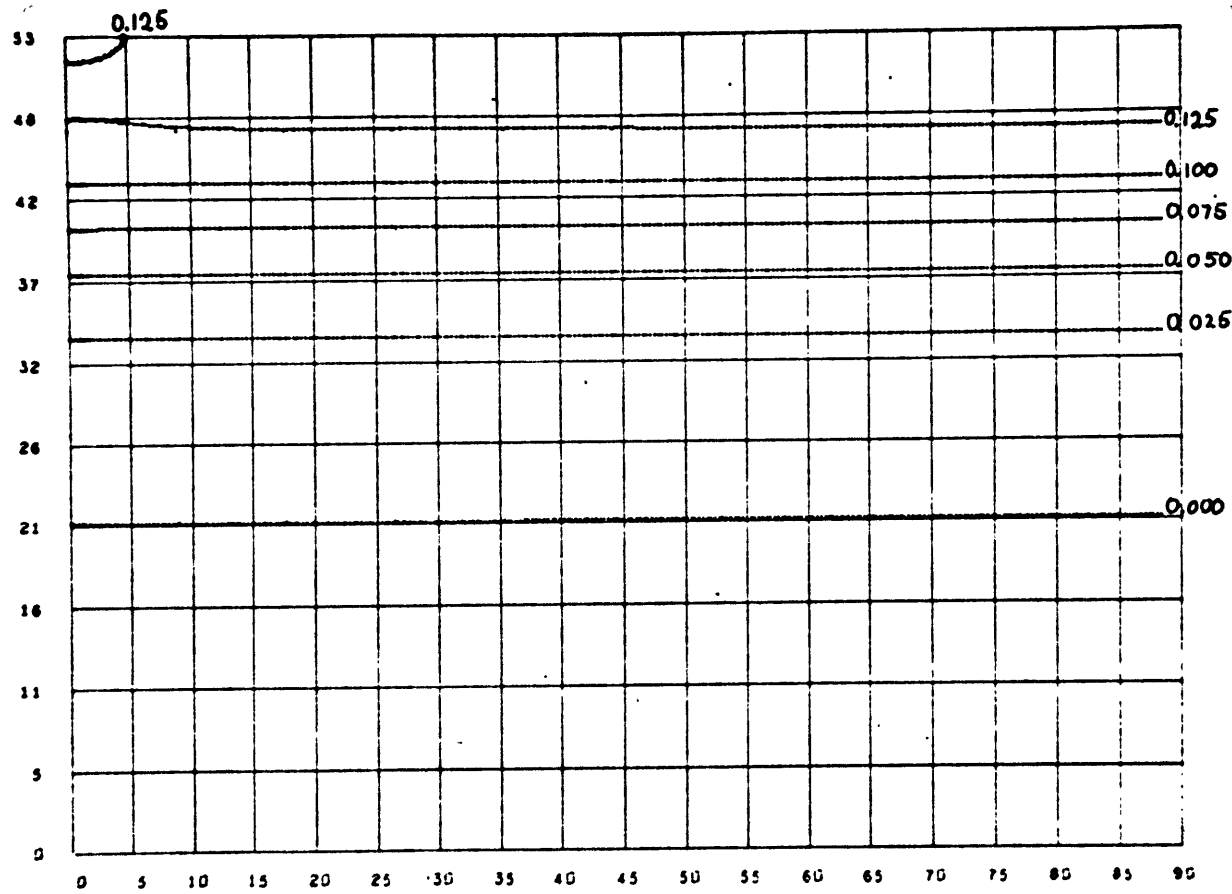
Figure 5.8.4: Relative potential temperature departure in Run I.
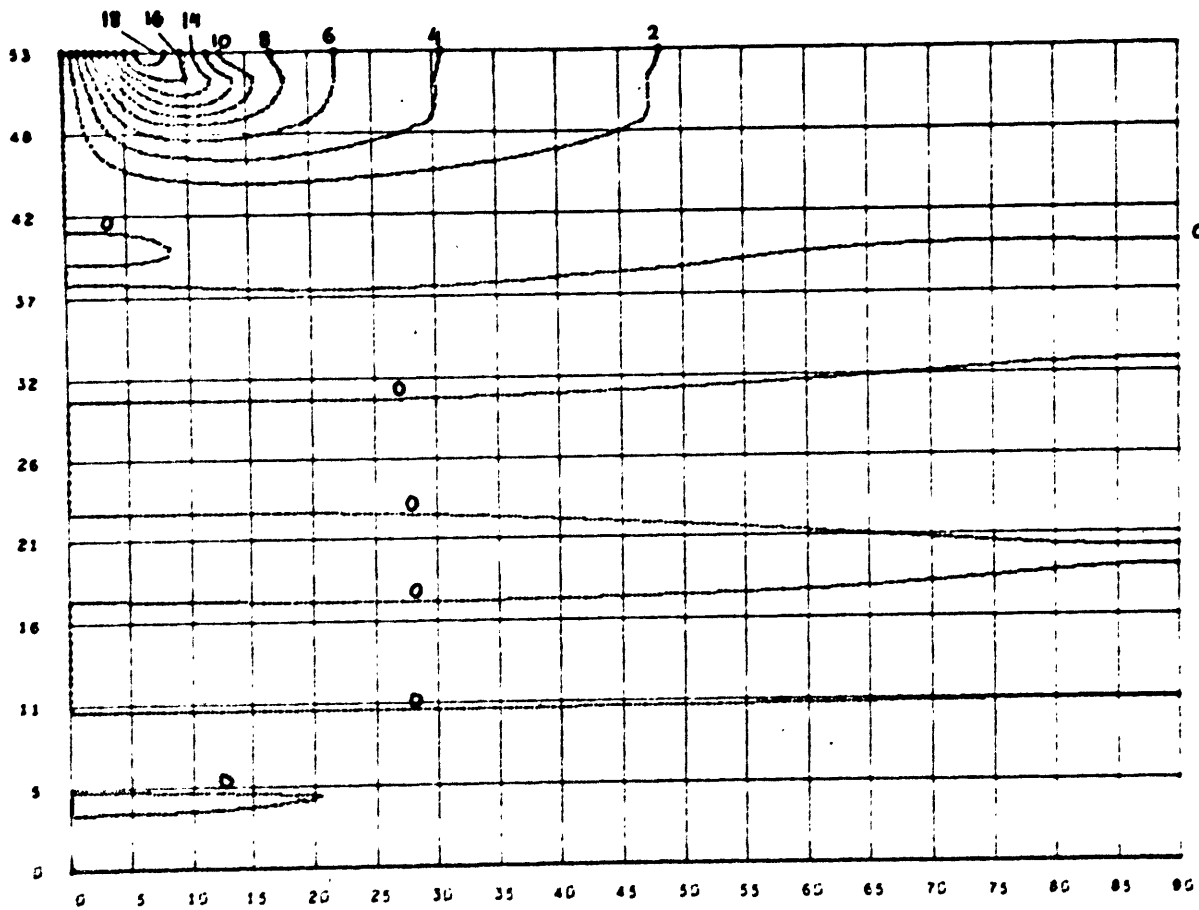
Figure 5.8.5: Zonal velocity u in m/sec. Run I.
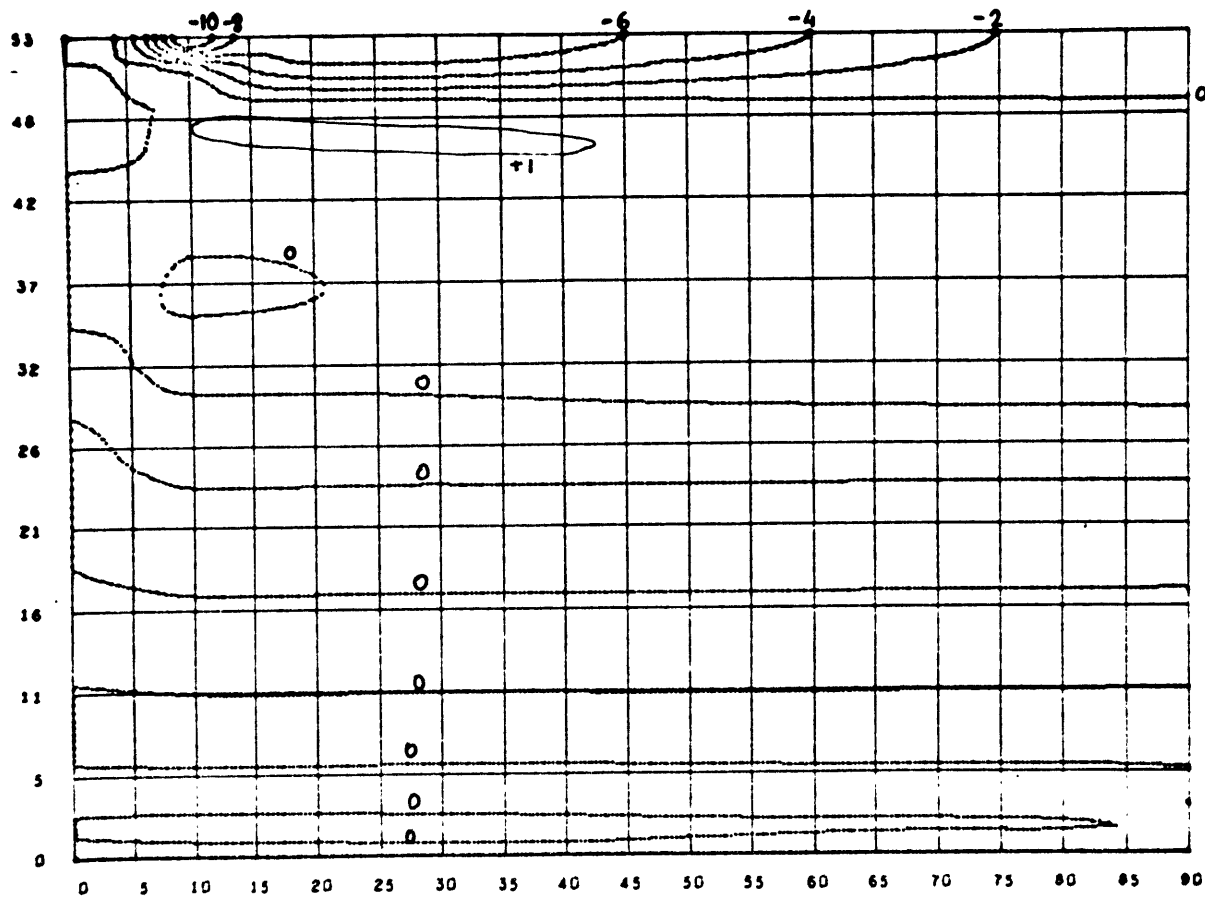
Figure 5.8.6: Meridional vleocity v in m/sec. Run I.
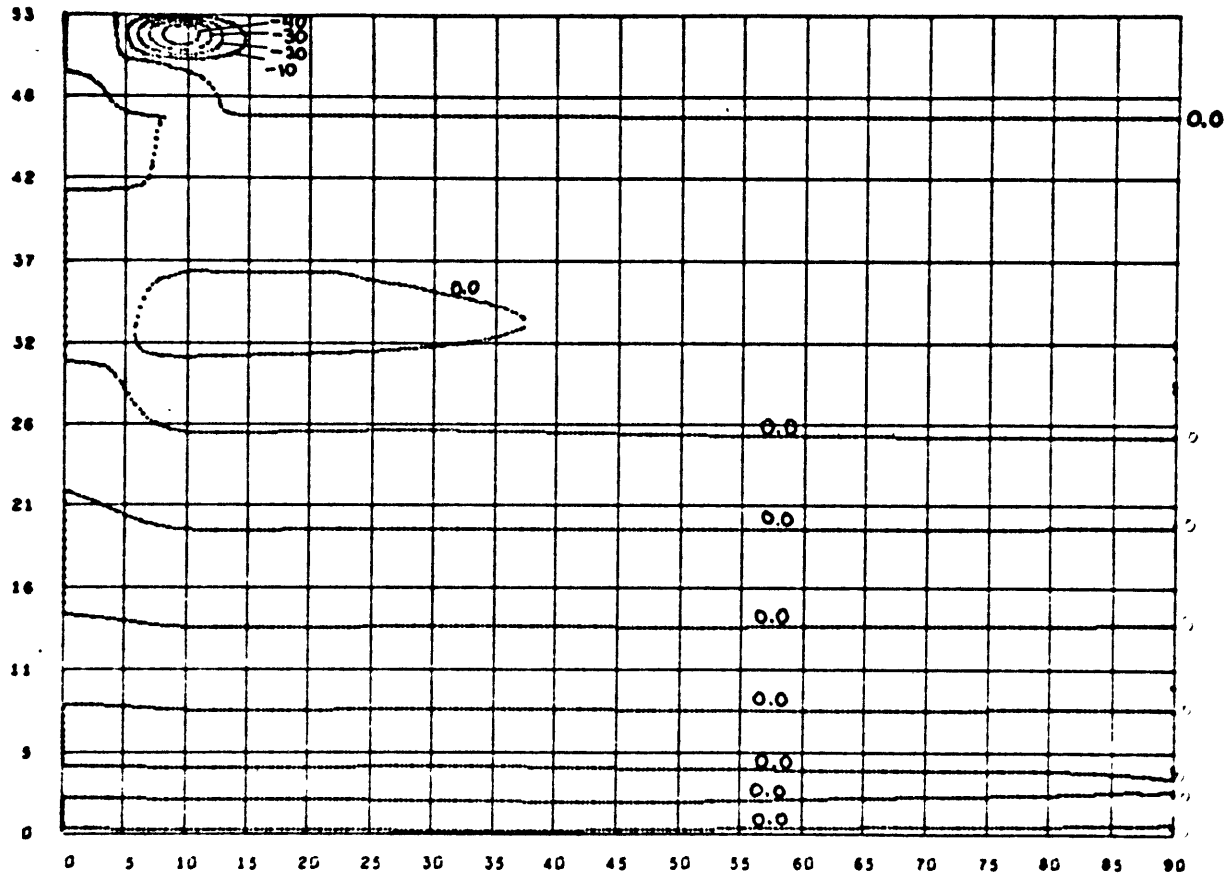
Figure 5.8.7: Vertical velocity w in cm/sec. Run I.
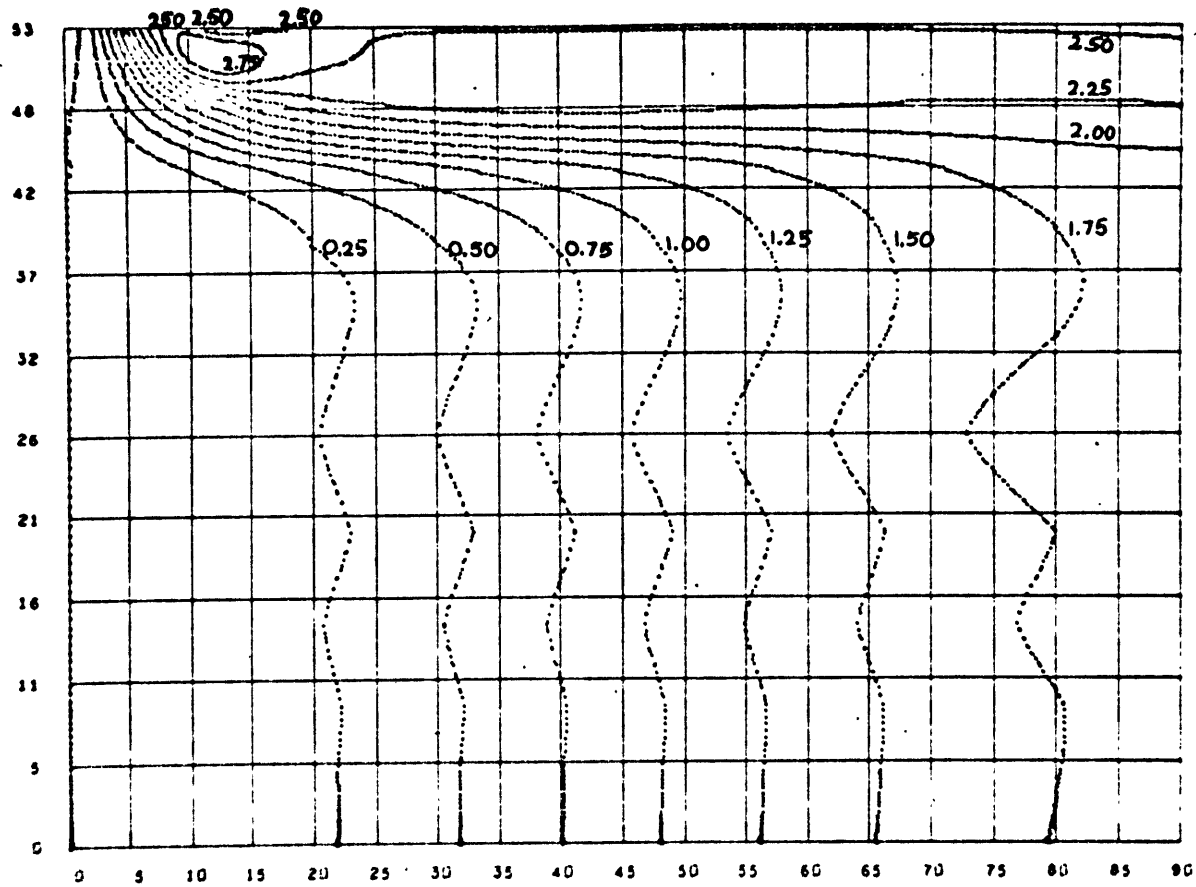
Figure 5.8.8: Angular momentum AM = $\left(-\Omega a \sin \alpha + u\right)\sin \alpha$ in m/sec. Run I.
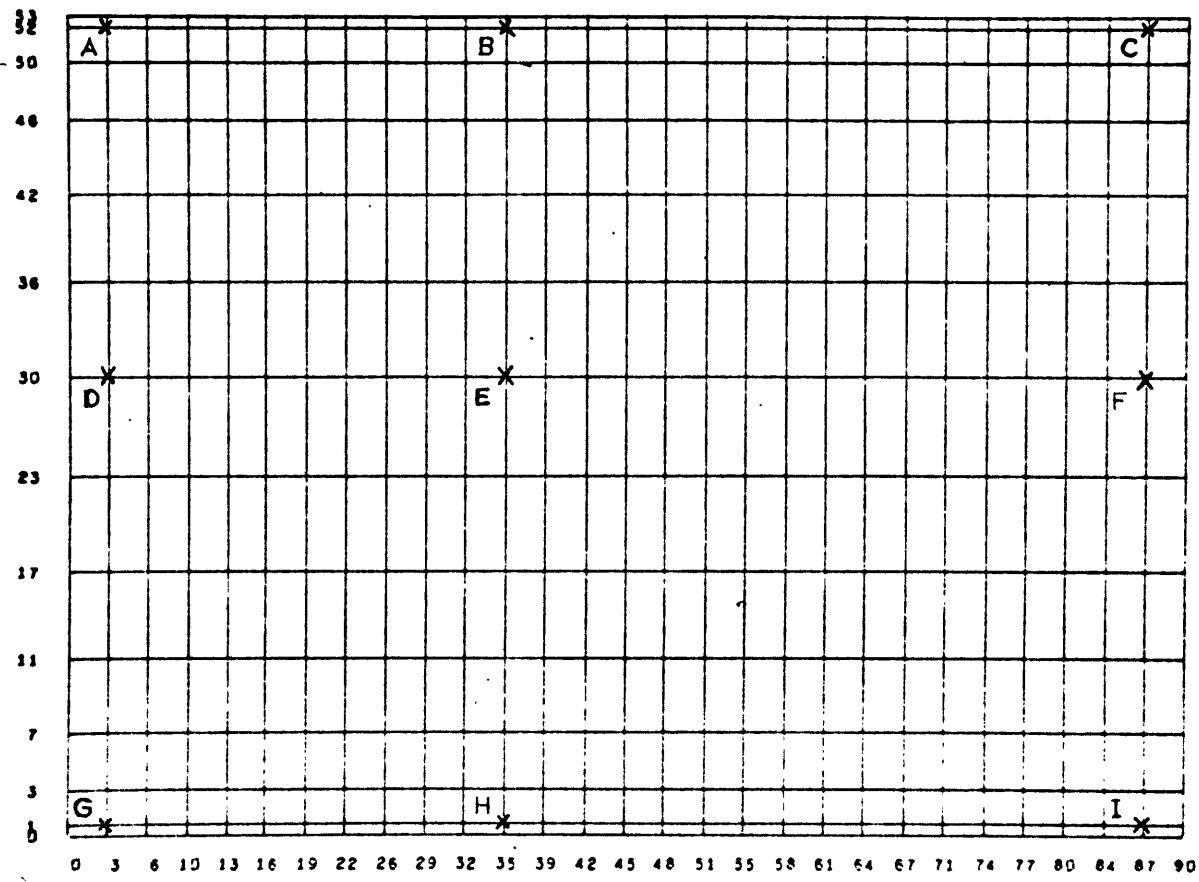
Figure 5.8.9: Position of the nine points at which the balance of terms in the vorticity, zonal momentum and energy equations is given.

Point	HOR. ADV.	VERT. ADV.	HOR. VISC.	VERT. VISC.	CORIOLIS	U. TERM	SO
A	-1.47×10^{-5}	-1.41×10^{-5}	-74.88×10^{-5}	-0.69×10^{-5}	2.10×10^{-5}	185.15×10^{-5}	-108
B	192.25×10^{-8}	145.07×10^{-8}	36.75×10^{-8}	69.92×10^{-8}	3.94×10^{-8}	12.24×10^{-8}	-461
C	16.64×10^{-8}	-10.20×10^{-8}	0.72×10^{-8}	5.07×10^{-8}	0.19×10^{-8}	0.07×10^{-8}	-12
D	0.16×10^{-10}	0.15×10^{-10}	807.53×10^{-10}	1.45×10^{-10}	-36.48×10^{-10}	-1.58×10^{-10}	-767
E	-0.10×10^{-10}	0.08×10^{-10}	1.44×10^{-10}	-0.92×10^{-10}	-16.96×10^{-10}	-0.38×10^{-10}	14
F	0.03×10^{-11}	-0.02×10^{-11}	-2.12×10^{-11}	-0.54×10^{-11}	-4.62×10^{-11}	-0.12×10^{-11}	6
G	-0.45×10^{-12}	-0.13×10^{-12}	-153.93×10^{-12}	-462.39×10^{-12}	-44.94×10^{-12}	0.12×10^{-12}	614
H	0.04×10^{-12}	0.005×10^{-12}	0.91×10^{-12}	-73.46×10^{-12}	-23.80×10^{-12}	0.00×10^{-12}	89
I	-0.04×10^{-14}	0.04×10^{-14}	-118.01×10^{-14}	-1035.0×10^{-14}	-134.74×10^{-14}	0.20×10^{-14}	1061

Table 5.8.1: Balance of terms in the vorticity equation at nine points. Run I:

Point	HOR. ADV.	VERT. ADV.	HOR. VISC.	VERT. VISC.	CORIOLIS	U. TERM	TIME DERIV.
A	50.15×10^{-6}	772.66×10^{-6}	-579.39×10^{-6}	28.82×10^{-6}	-7.14×10^{-6}	-264.85×10^{-6}	0.26×10^{-6}
B	-593.12×10^{-6}	-125.03×10^{-6}	7.11×10^{-6}	1.38×10^{-6}	279.67×10^{-6}	429.57×10^{-6}	-0.42×10^{-6}
C	-60.16×10^{-6}	47.46×10^{-6}	11.31×10^{-6}	-0.14×10^{-6}	1.05×10^{-6}	0.19×10^{-6}	-0.30×10^{-6}
D	9.72×10^{-8}	-0.97×10^{-8}	0.82×10^{-8}	-13.82×10^{-8}	-0.04×10^{-8}	-0.003×10^{-8}	-4.30×10^{-8}
E	-2.64×10^{-8}	0.74×10^{-8}	-103.45×10^{-8}	-76.40×10^{-8}	134.86×10^{-8}	6.39×10^{-8}	-40.49×10^{-8}
F	-6.04×10^{-8}	2.89×10^{-8}	-16.48×10^{-8}	-50.64×10^{-8}	0.70×10^{-8}	0.02×10^{-8}	-69.55×10^{-8}
G	-0.09×10^{-10}	0.32×10^{-10}	-1.76×10^{-10}	-109.61×10^{-10}	162.23×10^{-10}	-0.03×10^{-10}	51.05×10^{-10}
H	0.03×10^{-10}	-0.21×10^{-10}	35.69×10^{-10}	-80.63×10^{-10}	132.10×10^{-10}	-0.02×10^{-10}	86.94×10^{-10}
I	0.23×10^{-10}	-1.15×10^{-10}	33.90×10^{-10}	26.73×10^{-10}	6.85×10^{-10}	-0.00×10^{-10}	66.56×10^{-10}

Table 5.8.2: Balance of terms in the zonal momentum equation. Run I.

Point	HOR. ADV.	VERT. ADV.	HOR. DIFF.	VERT. DIFF.	RADIATION (BASIC)	RADIATION (PERT.)	TIME DERIV.
A	- 882.27	909.20	349.27	- 4.99	-241.62	-117.46	6.13
B	788.77	- 760.76	0.10	-15.40	301.76	-308.25	6.22
C	-1248.6	1225.6	- 0.40	-15.88	365.11	-319.53	6.38
D	- 0.002	0.74	- 0.93	3.01	- 1.46	0.89	2.25
E	- 0.21	0.21	- 0.02	2.97	- 1.46	0.85	2.33
F	- 0.29	0.34	- 0.02	2.94	- 1.32	0.84	2.49
G	- 0.20	0.18	- 0.01	7.38	- 11.15	2.06	-1.74
H	0.016	- 0.014	- 0.000	7.36	- 11.15	2.05	-1.73
I	0.03	- 0.03	0.00	7.36	- 11.15	2.05	-1.73

Table 5.8.3: Balance of terms in the thermal equation at 9 points. Units of 10^{-10}sec^{-1}. Run I.

The most important result is that the nonlinear terms corresponding to large scale advection of momentum and temperature are negligible in the interior and near the bottom (points D to I). In particular the balance in the thermal equation tends to be radiative-diffusive, and not advective, except near the top. Furthermore the system has not reached a steady state in the deep atmosphere since the relaxation time is radiative and not advective, and is much larger than 10^7 sec (at least $\sim 10^9$ sec). As was stated before, there is little justification for the use of a vertical coefficient of eddy diffusivity as large as $10^4 \frac{cm^2}{sec}$ in the interior, where radiation tends to produce a strongly stable lapse-rate.

Run II: $\mathcal{V}_H = K_H = 10^{11} cm^2/sec$ instead of $10^{10} cm^2/sec$. This run was made for the purpose of comparison, since even $\mathcal{V}_H = 10^{10}$ cm^2/sec is probably excessive, especially in the interior. Figures 5.8.10 to 5.8.16 reproduce the fields obtained after $1.8 \times 10^7 sec$. Note that some intermediate isolines have been drawn to improve the resolution.

The results are similar to those of Run I except that the circulation is slowed down by the large horizontal viscosity. The maximum zonal and meridional velocities are 2.0 m/s and 4.6 m/s as compared to 18.7 m/s and 11.7 m/s respectively in Run I. The counter cell near the pole is not present any longer because before a ring of air has reached the pole, the horizontal eddy viscosity has dissipated most of its angular momentum.

If we compare the streamlines in Figures 5.8.10 or 5.8.2 with those obtained for the nonrotating case (Figure 3.9.1) we see
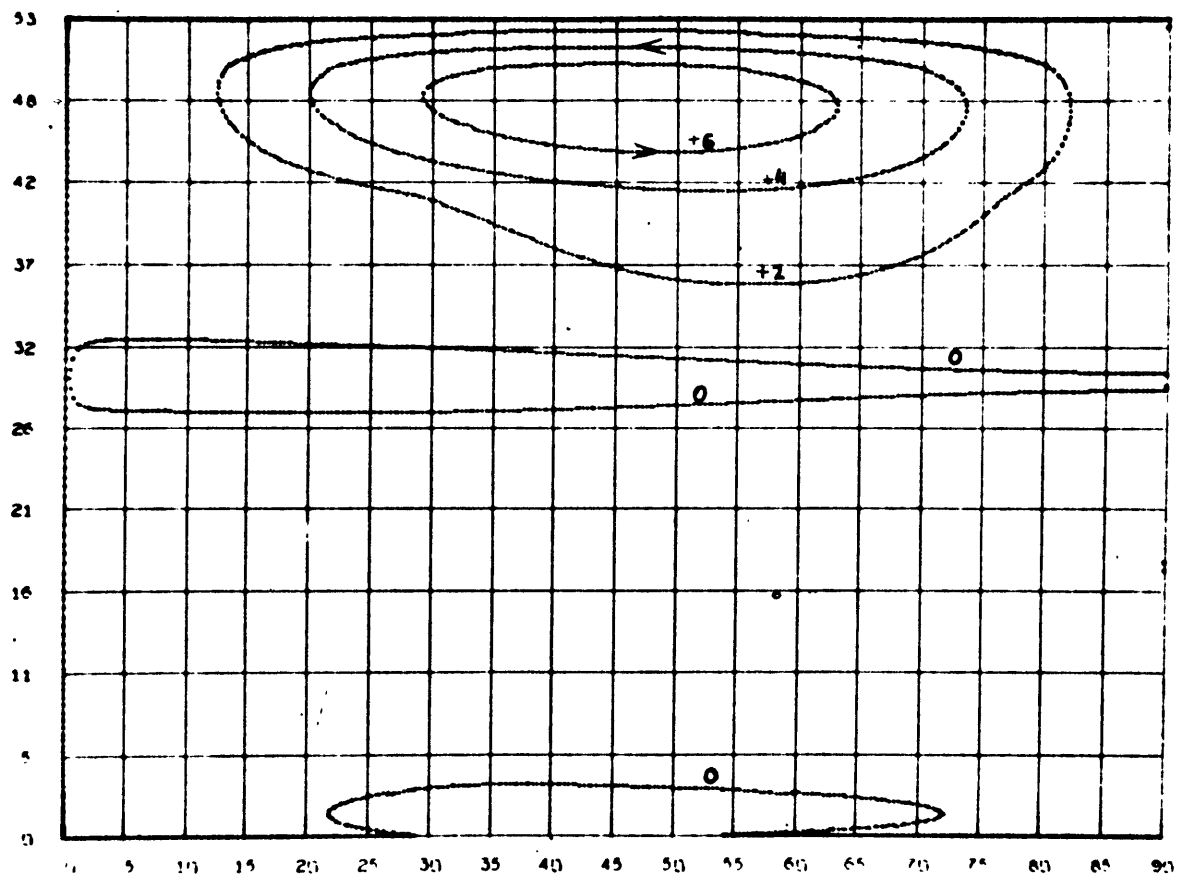
Figure 5.8.10: Meridional mass stream function ψ corresponding to Run II after a time $t = 1.8 \times 10^7$ sec.
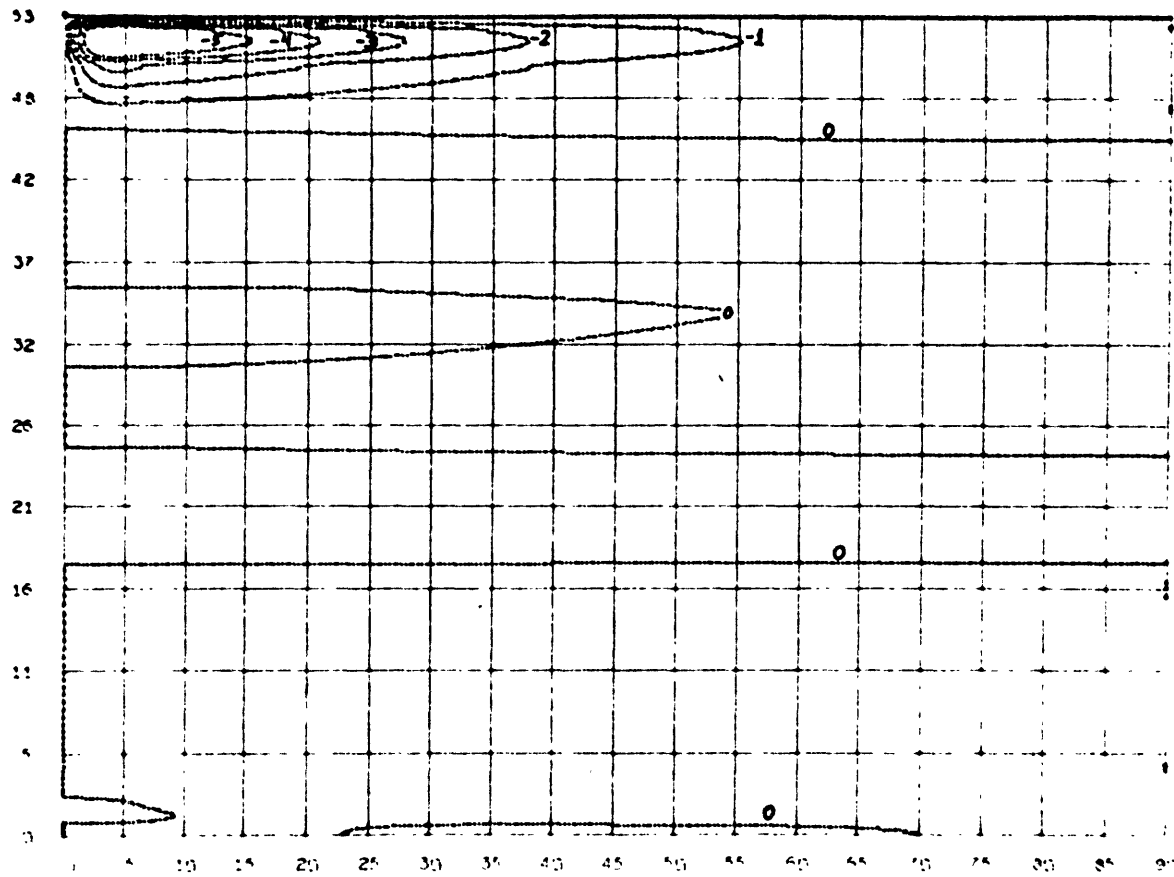
Figure 5.8.11: Zonal vortex strength $\eta = \dfrac{v_z}{\rho_a \sin \alpha}$ in $cm^3 g^{-1} sec^{-1}$. Run II.
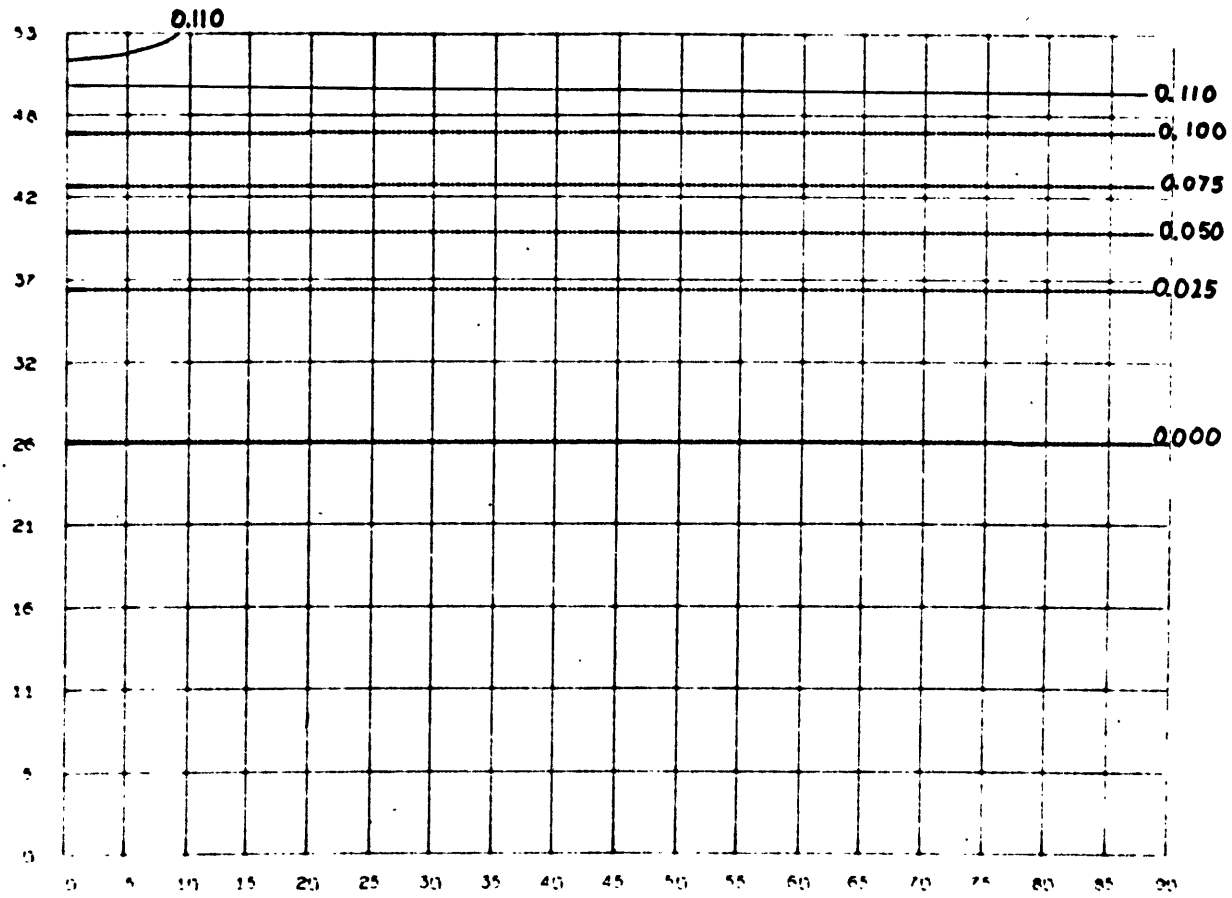
Figure 5.8.12: Relative potential temperature departure $\tilde{\theta}$ in Run II.
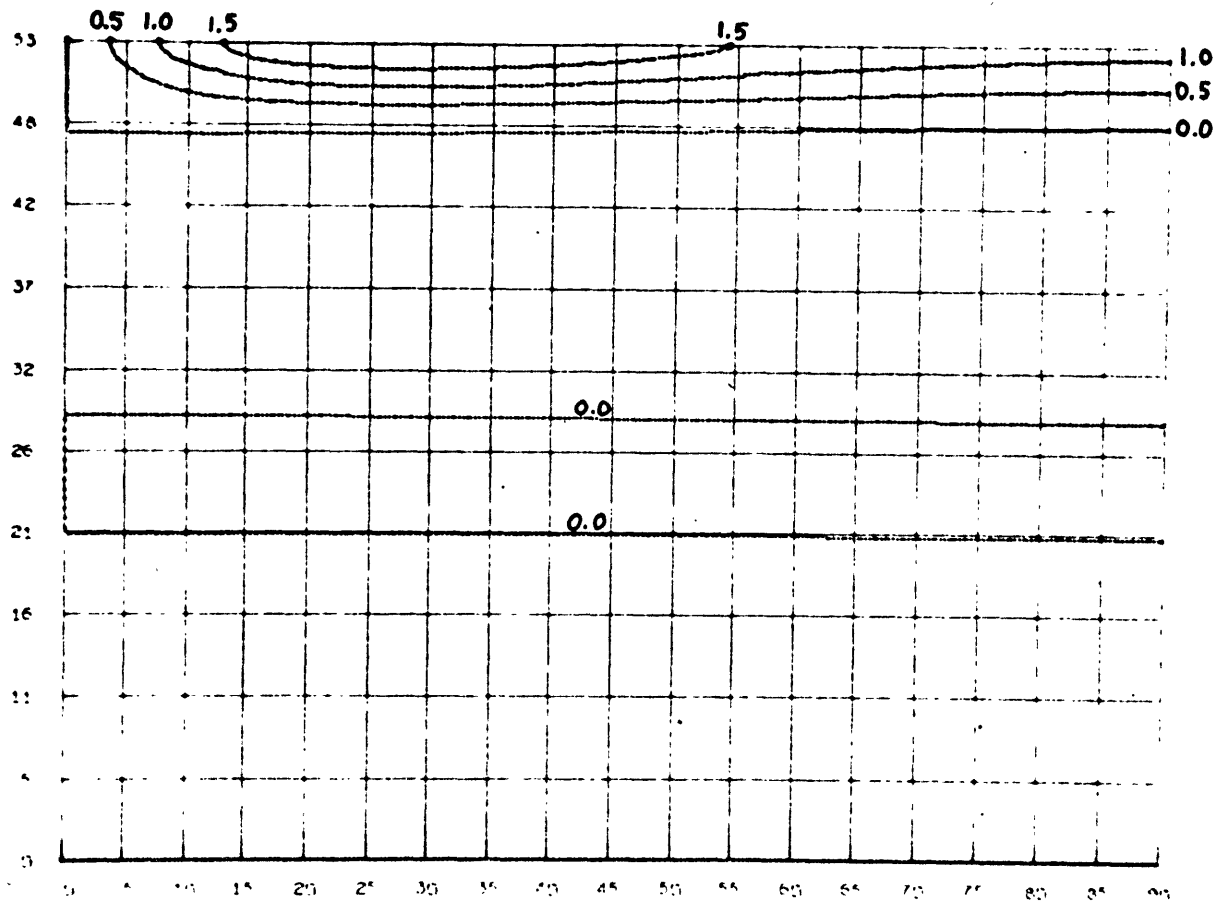
Figure 5.8.13: Zonal velocity u in m/sec. Run II.
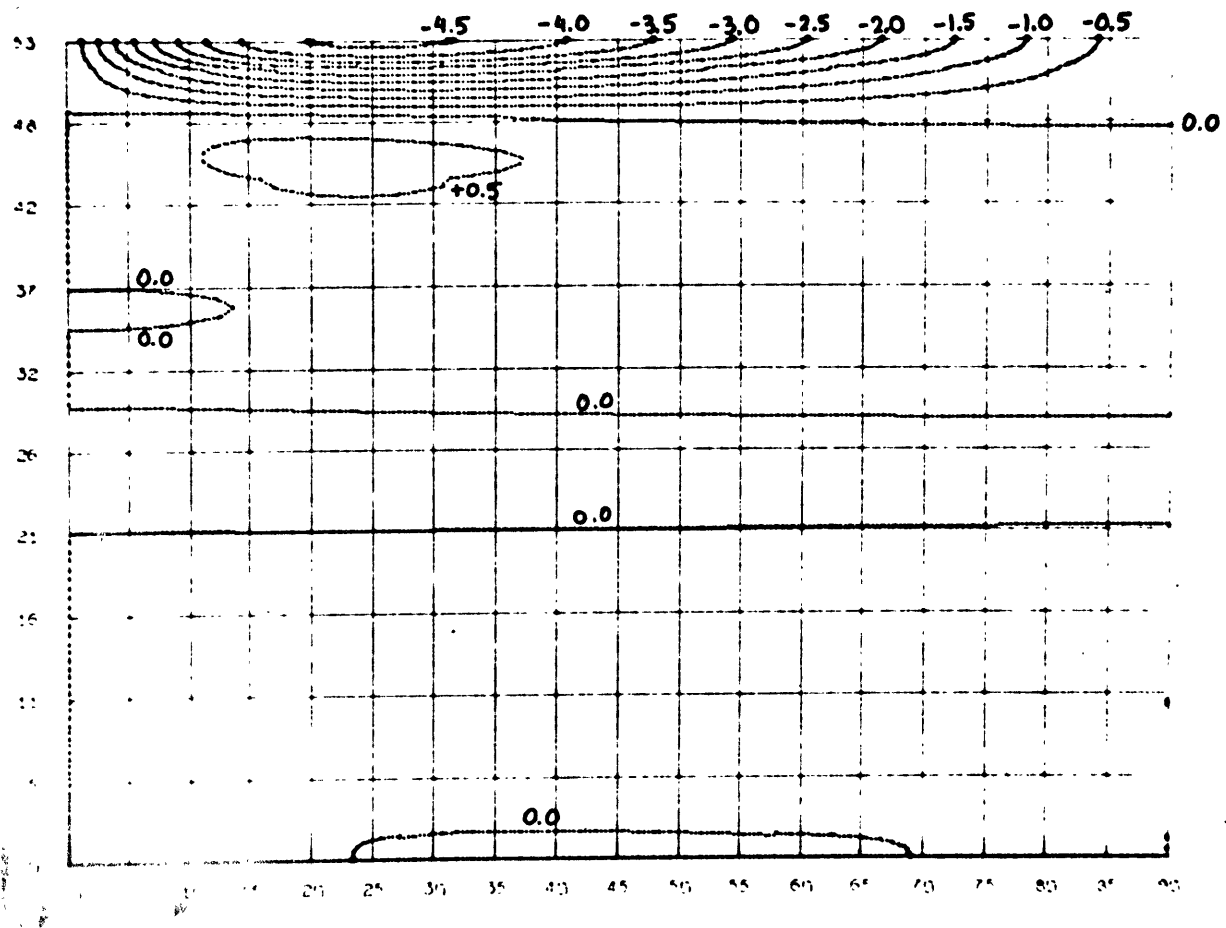
Figure 5.8.14: Meridional velocity v in m/sec. Run II.
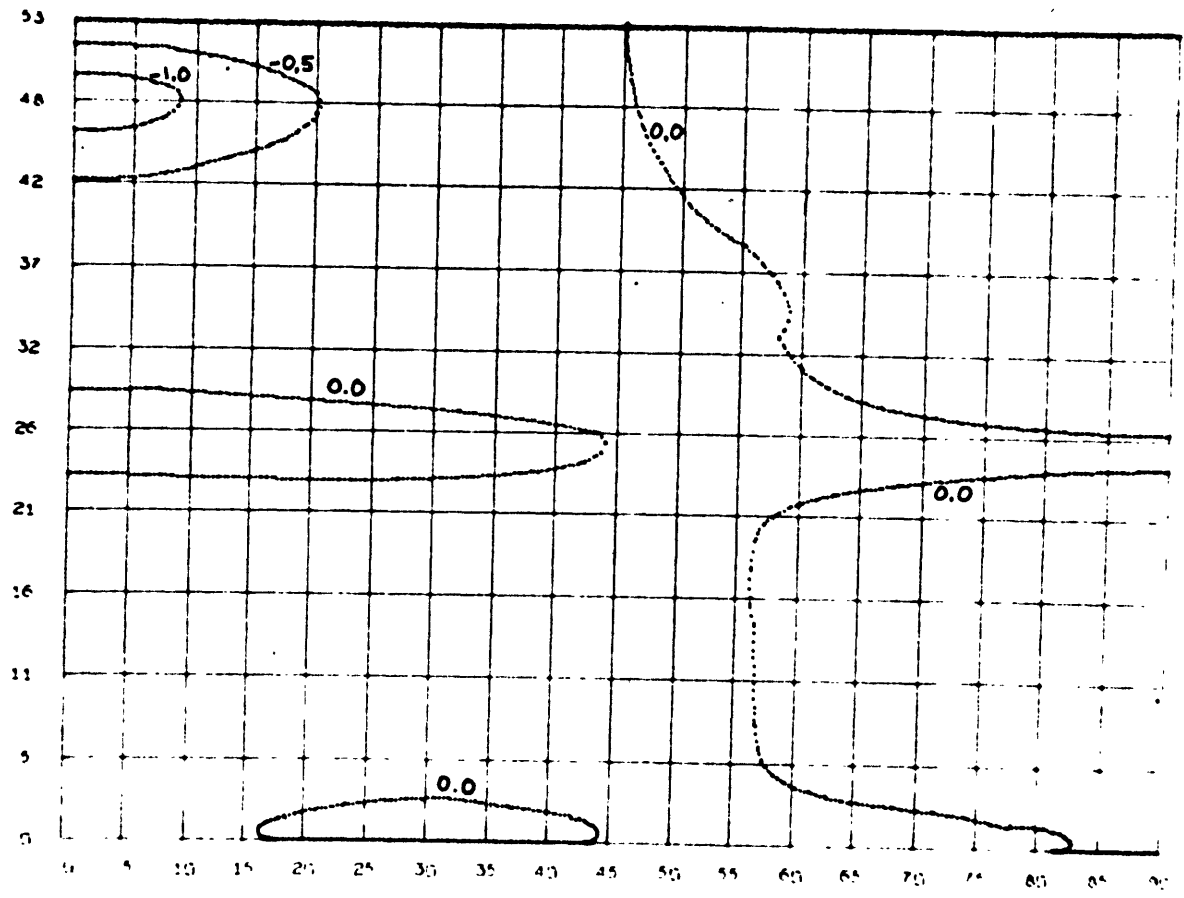
Figure 5.8.15: Vertical velocity w in m/sec. Run II.
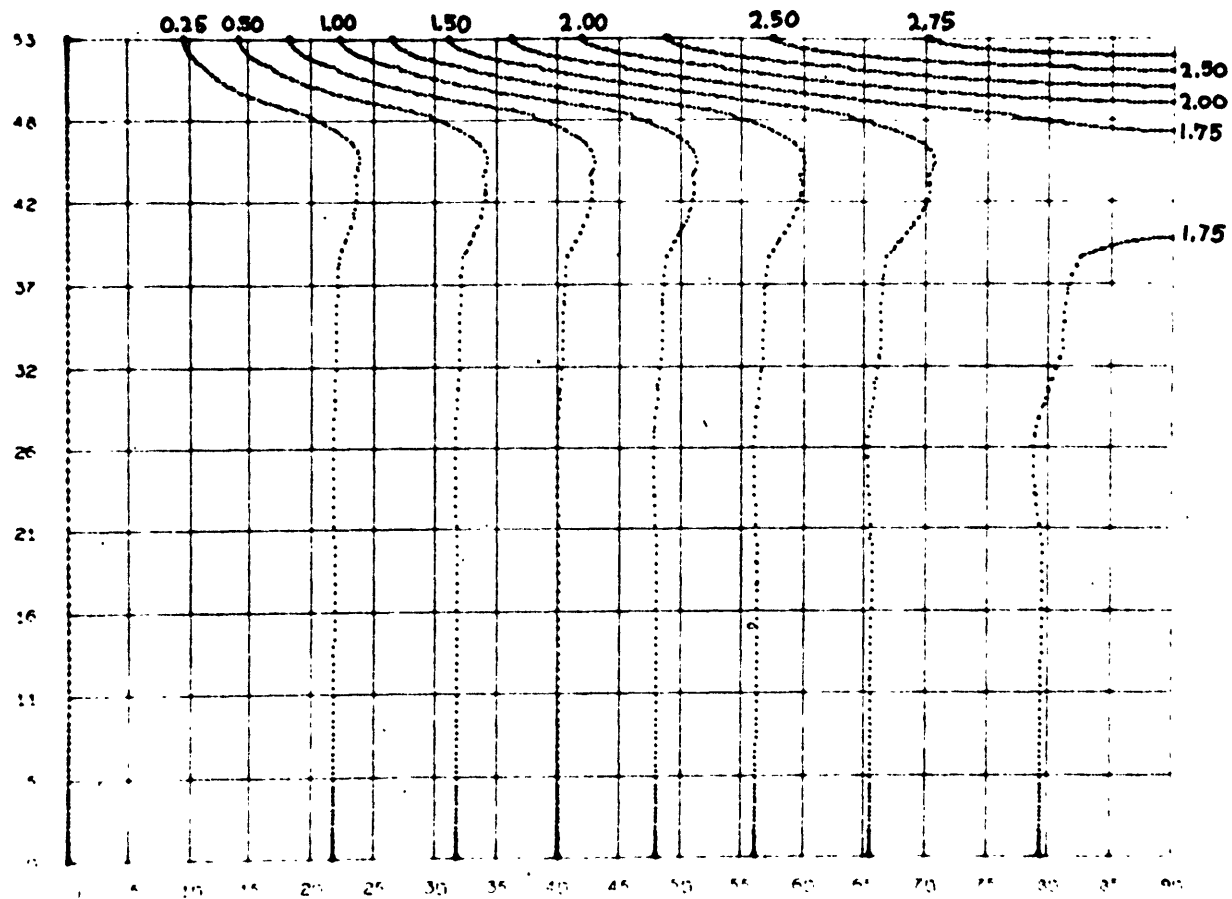
Figure 5.8.16: Angular momentum $AM = \left(-\Omega a \sin\alpha + u\right)\wind$ in m/sec.

that the effect of rotation is to reduce still further the penetration depth of the circulation. The upper part of the direct cell is the most compressed because the stabilizing effect of the relative rotation is greatest where the relative rotation is strongest.

The balance of terms in the forecast equations at the 9 points of Figure 5.8.9 is presented in Tables 5.8.4 to 5.8.7. The balance is basically similar to that of Run I, except that the horizontal viscosity is important even in the interior. In the thermal equation, however, the temperature is so strongly stratified horizontally that horizontal diffusivity remains unimportant except near the pole.

Run III: $\nu_v = K_v = 10^3 \text{cm}^2/\text{sec}$ instead of $10^4 \text{cm}^2/\text{sec}$. From the results of Runs I and II, and the nonrotating quasi-Boussinesq model, it became clear that if most of the solar radiation is absorbed at the top, the large scale circulation is not enough to stir the deep atmosphere and maintain an adiabatic or quasi-adiabatic lapse rate. In that case, a vertical coefficient of diffusivity of $10^4 \text{cm}^2/\text{sec}$ is excessive since the interior of the atmosphere would be stable.

The vertical radiative-diffusive equilibrium state of the atmosphere was calculated for several values of the vertical coefficient of eddy diffusivity, with radiation (treated in the same linearized fashion as in the two-dimensional model). Figure 5.8.17 shows the vertical profile obtained for the relative potential temperature departure. It may be observed that $K_v = 10^4 \text{cm}^2/\text{sec}$ forces the lower atmosphere to remain adiabatically stratified, whereas

$K_v = 10^3 \text{cm}^2/\text{sec}$, a more realistic value in a stable atmosphere,

Point	HOR. ADV.	VERT. ADV.	HOR. VISC.	VERT. VISC.	CORIOLIS	U. TERM	SOLENOI
A	-3.21×10^{-5}	2.64×10^{-5}	11.78×10^{-5}	0.51×10^{-5}	0.09×10^{-5}	0.36×10^{-5}	$-12.17\times1($
B	148.46×10^{-8}	73.63×10^{-8}	269.24×10^{-8}	139.60×10^{-8}	28.31×10^{-8}	44.99×10^{-8}	$-705.75\times1($
C	7.67×10^{-8}	-3.74×10^{-8}	2.77×10^{-8}	4.63×10^{-8}	0.72×10^{-8}	0.37×10^{-8}	$-12.49\times1($
D	-0.002×10^{-10}	0.08×10^{-10}	-14.47×10^{-10}	-0.70×10^{-10}	-4.10×10^{-10}	0.02×10^{-10}	$17.47\times1($
E	-0.03×10^{-10}	0.06×10^{-10}	-30.23×10^{-10}	-0.78×10^{-10}	-2.81×10^{-10}	0.01×10^{-10}	$33.58\times1($
F	0.04×10^{-11}	-0.02×10^{-11}	-14.15×10^{-11}	-0.57×10^{-11}	-1.14×10^{-11}	-0.00×10^{-11}	$15.70\times1($
G	-0.00×10^{-13}	-0.00×10^{-13}	-51.80×10^{-13}	49.53×10^{-13}	-3.65×10^{-13}	0.00×10^{-13}	0.00×10
H	0.00×10^{-13}	-0.00×10^{-13}	0.20×10^{-13}	-2.64×10^{-13}	-2.79×10^{-13}	0.00×10^{-13}	0.00×10
I	0.00×10^{-15}	0.00×10^{-15}	-72.75×10^{-15}	60.16×10^{-15}	-17.36×10^{-15}	0.00×10^{-15}	0.00×10

Table 5.8.4: Balance of terms in the vorticity equation. Run II:

Point	HOR. ADV.	VERT. ADV.	HOR. VISC.	VERT. VISC.	CORIOLIS	U. TERM	TIME DERIV.
A	23.55×10^{-5}	-4.29×10^{-5}	-30.89×10^{-5}	-0.54×10^{-5}	4.50×10^{-5}	7.22×10^{-5}	0.03×10^{-5}
B	24.29×10^{-6}	-21.05×10^{-6}	-238.89×10^{-6}	-4.45×10^{-6}	143.39×10^{-6}	97.60×10^{-6}	0.88×10^{-6}
C	-45.27×10^{-6}	13.87×10^{-6}	32.63×10^{-6}	-1.86×10^{-6}	0.65×10^{-6}	0.14×10^{-6}	0.15×10^{-6}
D	0.25×10^{-8}	-0.01×10^{-8}	-16.49×10^{-8}	-0.98×10^{-8}	16.90×10^{-8}	0.07×10^{-8}	-0.26×10^{-8}
E	0.69×10^{-8}	-0.11×10^{-8}	-104.78×10^{-8}	-8.39×10^{-8}	109.96×10^{-8}	0.38×10^{-8}	-2.23×10^{-8}
F	-0.44×10^{-8}	0.14×10^{-8}	5.80×10^{-8}	-8.39×10^{-8}	0.73×10^{-8}	0.00×10^{-8}	-2.17×10^{-8}
G	0.00×10^{-10}	-0.00×10^{-10}	3.93×10^{-10}	0.24×10^{-10}	-4.12×10^{-10}	0.00×10^{-10}	0.05×10^{-10}
H	-0.00×10^{-10}	0.00×10^{-10}	1.40×10^{-10}	-2.39×10^{-10}	4.07×10^{-10}	-0.00×10^{-10}	3.08×10^{-10}
I	-0.00×10^{-10}	0.00×10^{-10}	3.23×10^{-10}	-0.98×10^{-10}	-4.20×10^{-10}	0.00×10^{-10}	2.21×10^{-10}

Table 5.8.5: Balance of terms in the zonal momentum equation for run II.

Point	HOR. ADV.	VERT. ADV.	HOR. DIF.	VERT. DIFF.	RADIATION (BASIC)	RADIATION (PERT.)	TIME DERIV.
A	4917.7	-4865.8	428.26	-10.19	-241.62	-211.35	17.06
B	574.47	- 546.83	- 8.70	-14.30	301.76	-288.95	17.46
C	-649.74	631.05	- 3.90	-15.32	365.11	-309.62	17.58
D	- 0.01	- 0.14	0.18	2.01	- 1.46	0.91	1.50
E	- 0.00	- 0.03	0.08	2.01	- 1.46	0.91	1.50
F	0.00	- 0.01	- 0.06	2.00	- 1.32	0.90	1.51
G	0.00	- 0.00	0.00	6.92	- 11.15	1.81	-2.42
H	- 0.00	0.00	0.00	6.92	- 11.15	1.81	-2.42
I	- 0.00	0.00	0.00	6.92	- 11.15	1.81	-2.42

Table 5.8.6: Balance of terms in the thermal equation for Run II. Units of $10^{-10}sec^{-1}$.
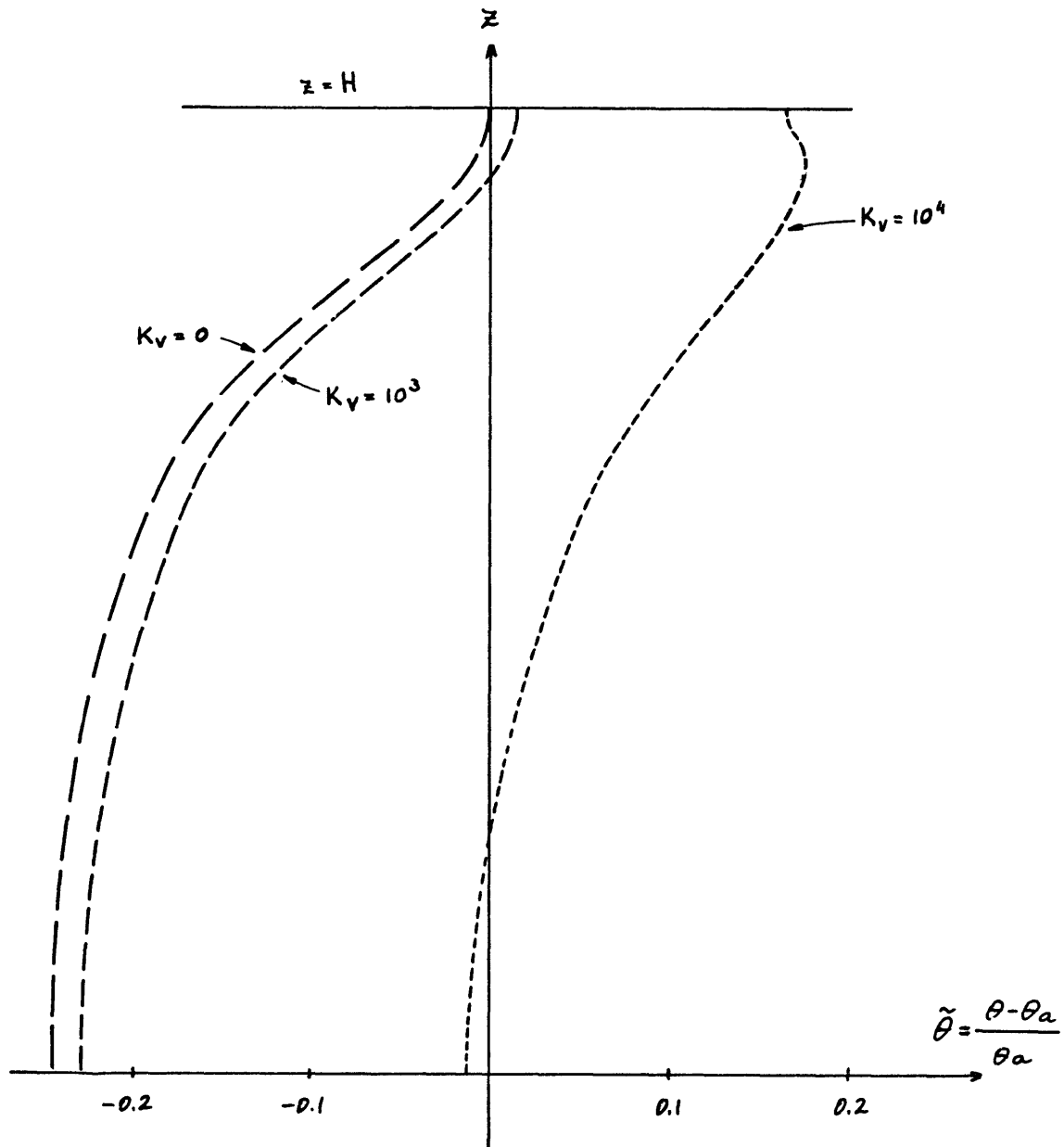
Figure 5.8.17: Unidimensional computation of the radiative diffusive equilibrium profile of $\tilde{\theta} = \dfrac{\theta - \theta_a}{\theta_a}$ for several values of K_v.

has relatively little effect. The potential temperature at the sur-

face is here 25% lower than its initial adiabatic value, 730°K; hence

the linearization procedure used for radiation is inaccurate, and

the original radiative transfer equations should have been used.

This is actually done in section 5.10 for a purely radiative model.

The results of Run III after 3.6×10^7 sec are shown in

Figures 5.8.18 to 5.8.24.

The direct cell at the top of the atmosphere is quite

similar to that obtained in Run I. The main difference is that

the circulation in the interior is stronger, with horizontal velo-

cities of the order of 10 cm/sec instead of 1 cm/sec.

The maximum zonal and meridional velocities are 18.3 m/sec

and 10.4 m/sec respectively, about the same as those in Run I. The

reverse cell is also observed at the pole, and the maximum downward

velocity is 2.8 cm/sec and occurs at 8° colatitude from the pole in

both runs.

The balance of terms in the forecast equations is presented

in Tables (5.8.7) to (5.8.9). The balance in the vorticity equa-

tion is quite similar to that of Run I; the nonlinear terms are still

negligible in the interior. In the zonal momentum equation the non-

linear terms are important in the interior but not near the bottom,

and this is also true in the thermal equation. In any case the ad-

vective terms in the interior (which tend to cancel each other be-

cause the streamlines are rather parallel to the isotherms) are of

the same order as the vertical diffusion term and smaller than the

radiative terms. Near the bottom they become completely negligible.

Both in Run I and in Run III the zonal momentum equation
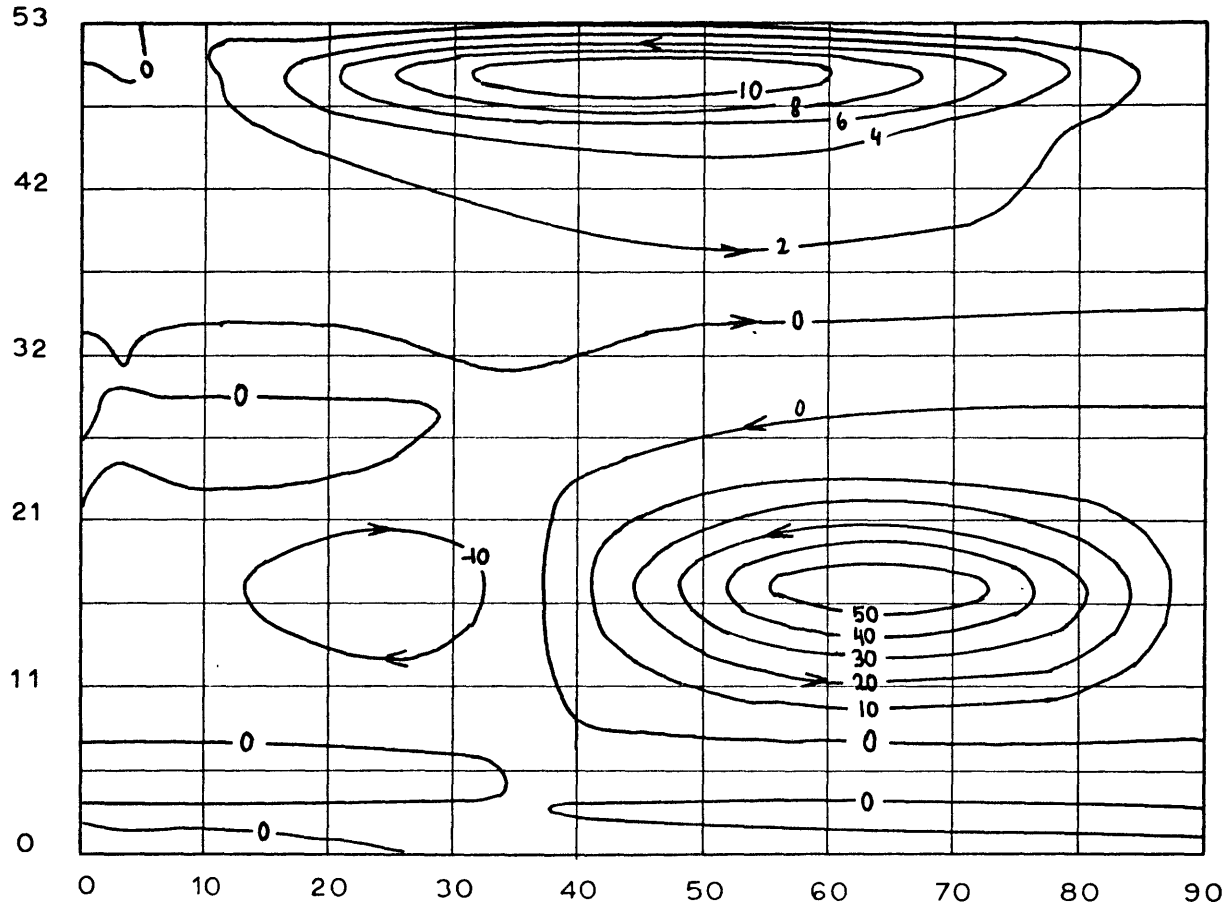
Figure 5.8.18: Meridional stream function corresponding to Run III after a time t = 3.6 × 10⁷sec.
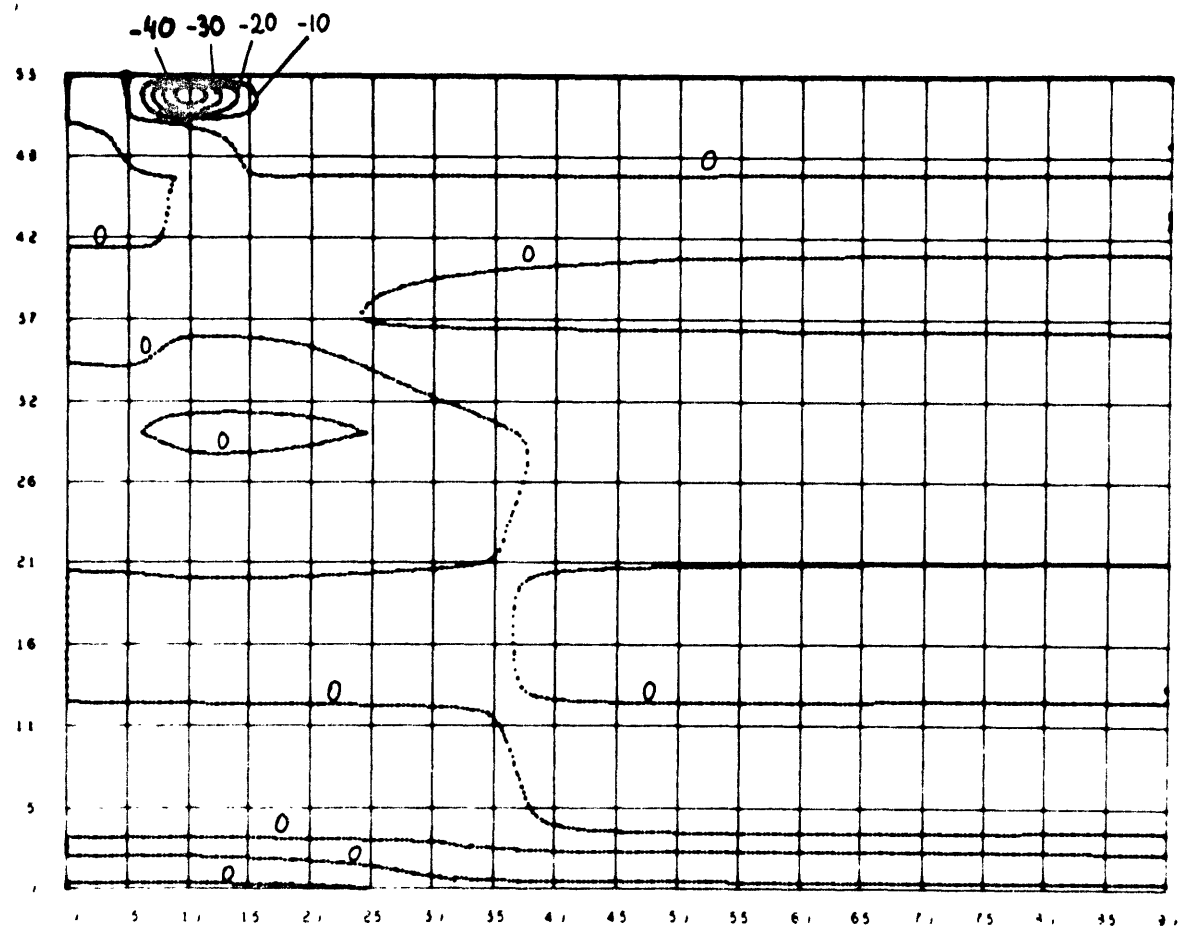
Figure 5,8.19: Zonal vortex strength $\eta = \dfrac{v_\varphi}{\rho_a \sin \alpha}$ in 10 cm^{3}g^{-1}sec^{-1}. Run III.
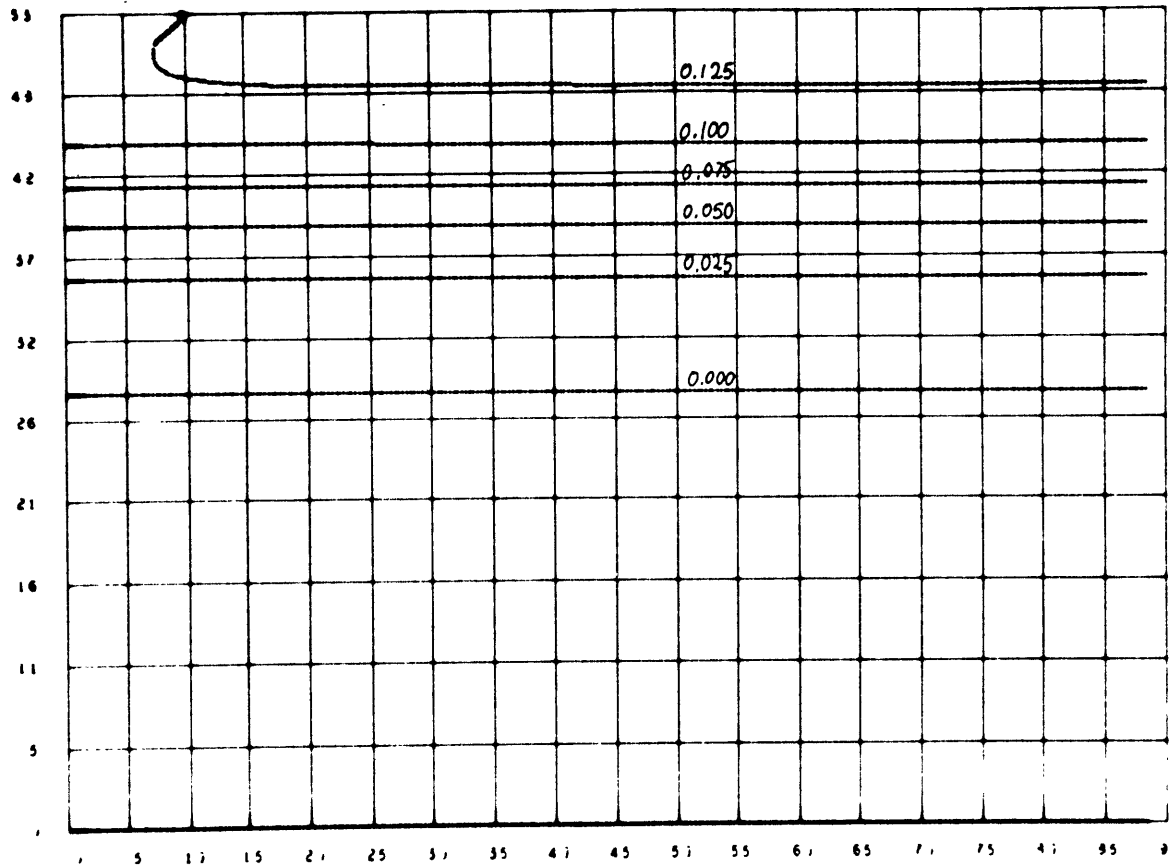
Figure 5.8.20: Potential temperature departure $\widetilde{\theta}$. Run III.
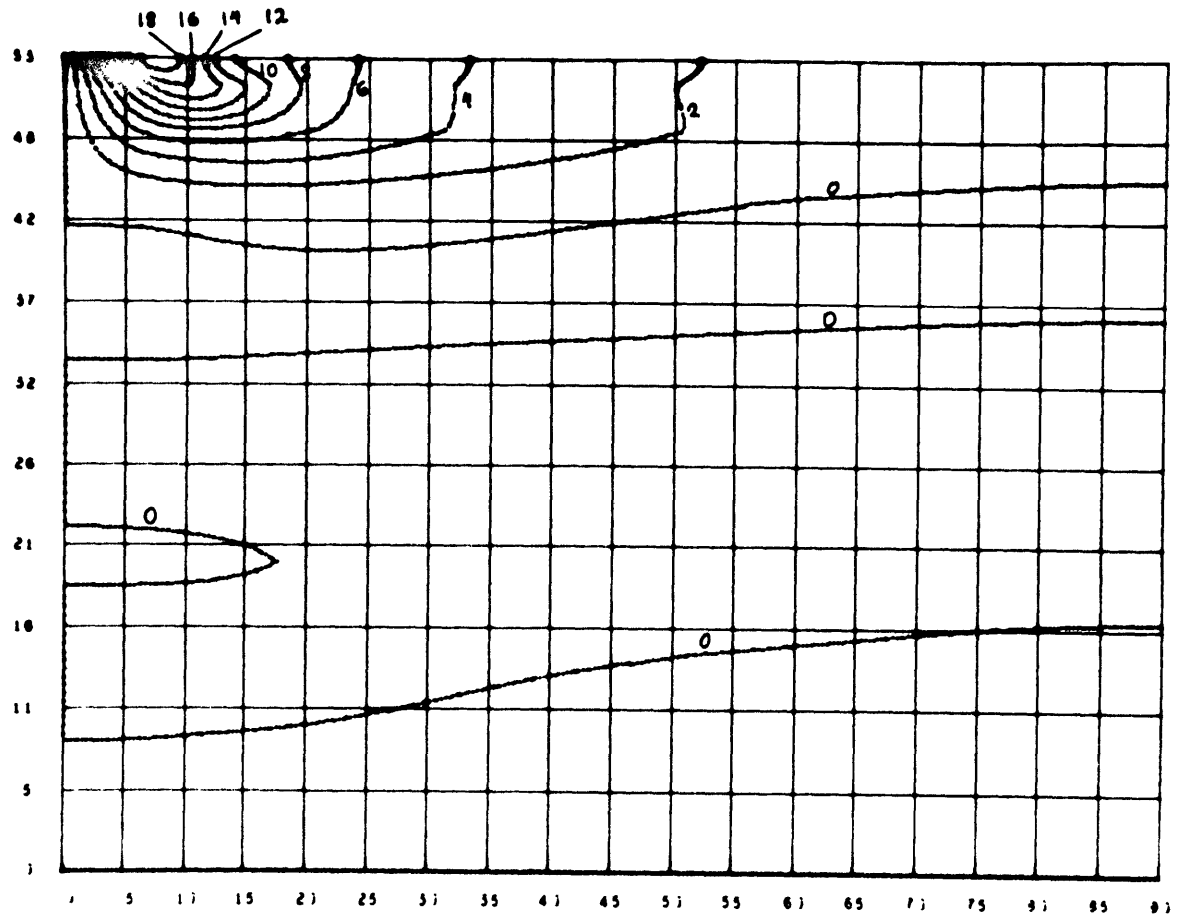
Figure 5.8.21:   Zonal velocity u in m/sec.   Run III.
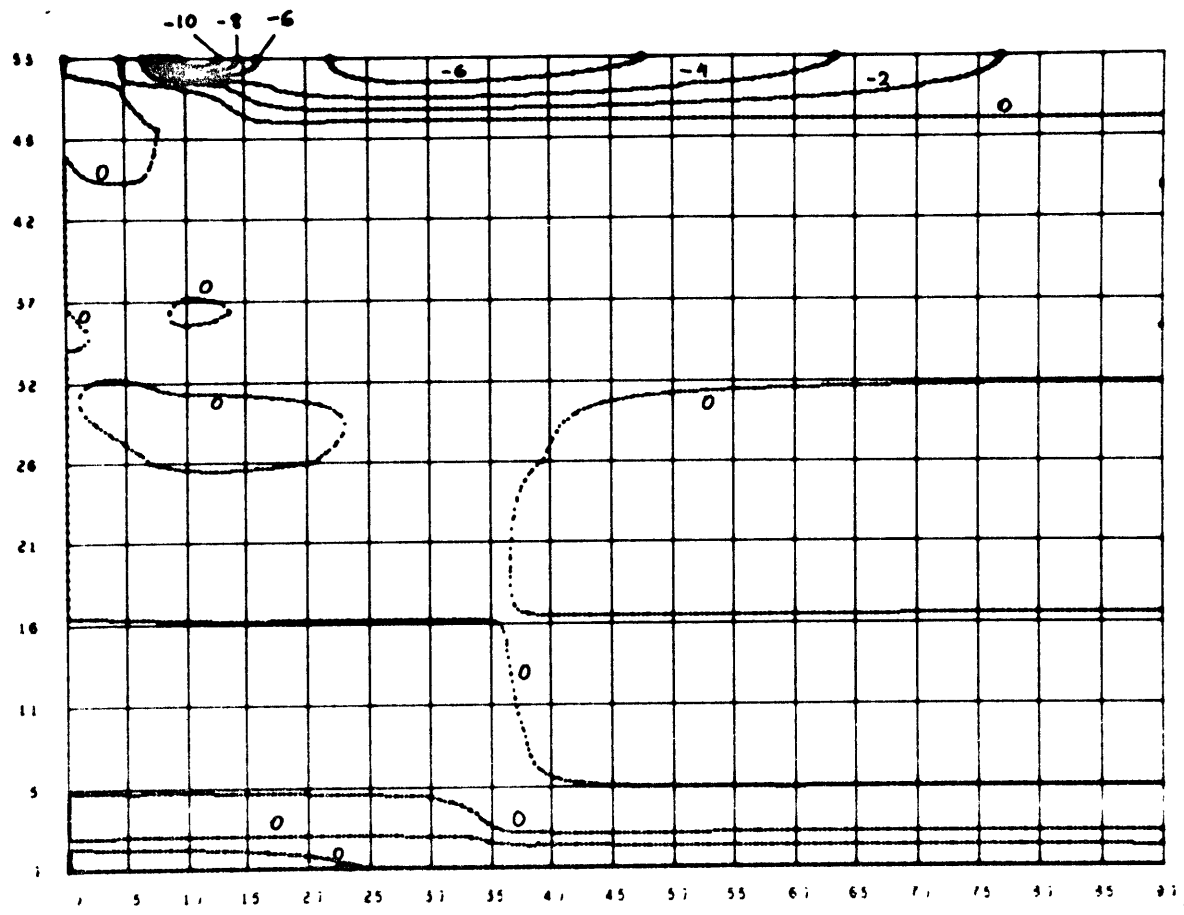
Figure 5.8.22:   Meridional velocity v in m/sec.   Run III.
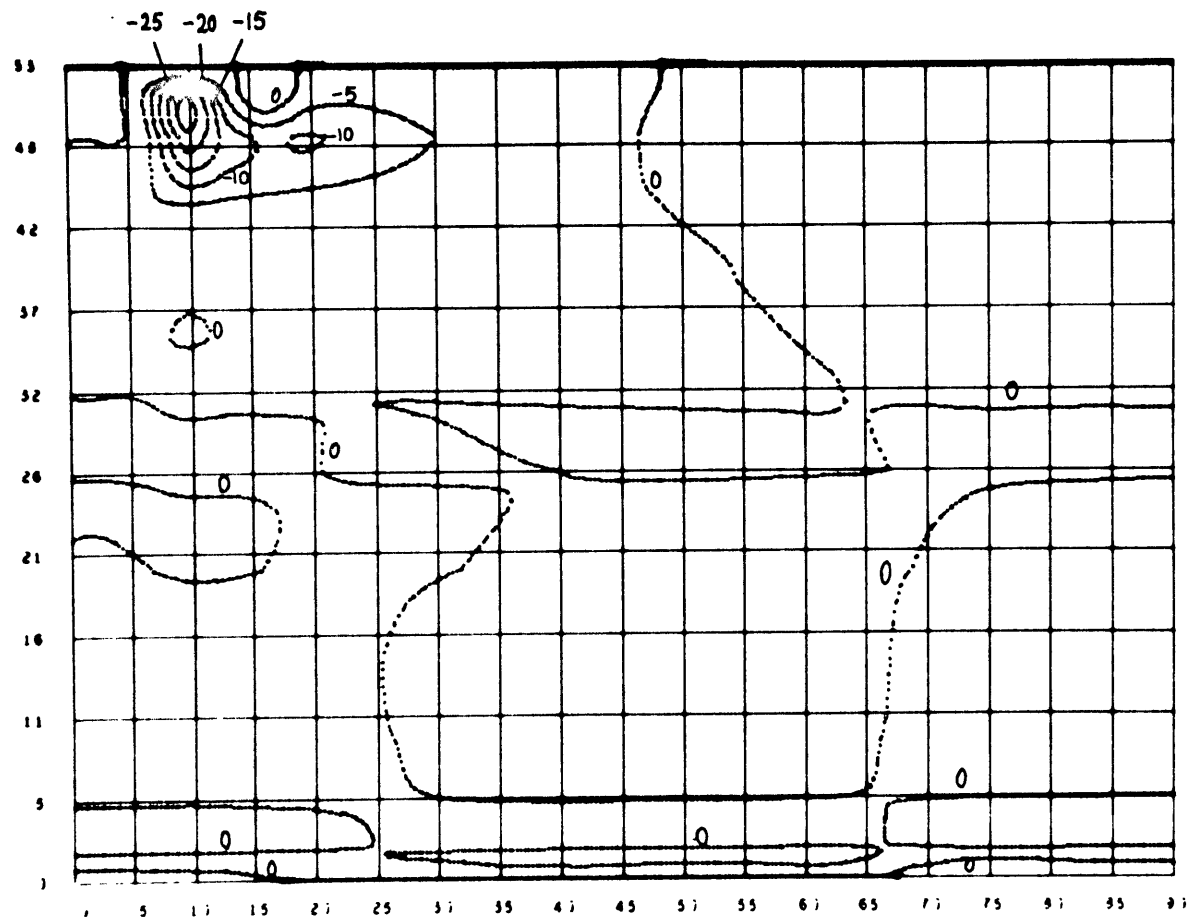
Figure 5.8.23: Vertical velocity w in cm/sec. Run III.
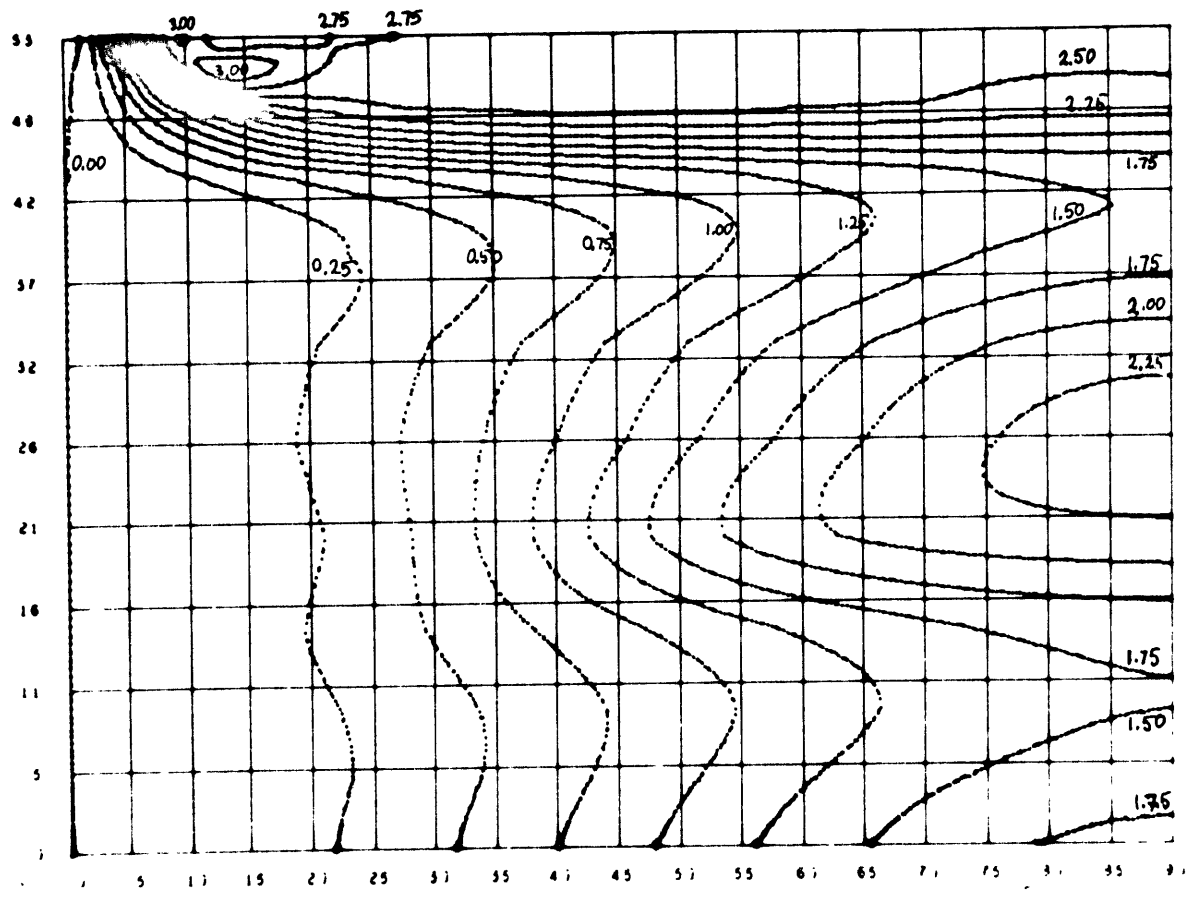
Figure 5.8.24: Angular momentum AM $= \left(-\Omega a \sin\alpha + u\right)\sin\alpha$ in m/sec.   Run III.

Point	HOR. ADV.	VERT. ADV.	HOR. VISC.	VERT. VISC.	CORIOLIS	U. TERM	SOLENOID	TIME DERIV.
A	$- \ 0.22 \times 10^{-5}$	$- \ 0.45 \times 10^{-5}$	$- \ 45.72 \times 10^{-5}$	$- \ 0.07 \times 10^{-5}$	1.89×10^{-5}	154.21×10^{-5}	-109.63×10^{-5}	0.03×10^{-5}
B	-107.58×10^{-8}	287.25×10^{-8}	36.50×10^{-8}	2.17×10^{-8}	11.02×10^{-8}	37.61×10^{-8}	-266.58×10^{-8}	0.39×10^{-8}
C	22.45×10^{-8}	$- \ 15.08 \times 10^{-8}$	1.09×10^{-8}	0.51×10^{-8}	0.36×10^{-8}	0.17×10^{-8}	$- \ 9.59 \times 10^{-8}$	$- \ 0.09 \times 10^{-8}$
D	0.05×10^{-10}	$- \ 0.83 \times 10^{-10}$	438.11×10^{-10}	$- \ 0.29 \times 10^{-10}$	$- \ 34.72 \times 10^{-10}$	$- \ 7.29 \times 10^{-10}$	-405.96×10^{-10}	$- \ 10.93 \times 10^{-10}$
E	$- \ 0.22 \times 10^{-10}$	0.10×10^{-10}	15.94×10^{-10}	0.07×10^{-10}	$- \ 22.52 \times 10^{-10}$	$- \ 5.10 \times 10^{-10}$	9.82×10^{-10}	$- \ 1.92 \times 10^{-10}$
F	2.62×10^{-11}	1.41×10^{-11}	$- \ 16.10 \times 10^{-11}$	0.00×10^{-11}	$- \ 11.13 \times 10^{-11}$	$- \ 2.63 \times 10^{-11}$	28.65×10^{-11}	$- \ 2.43 \times 10^{-11}$
G	$- \ 0.04 \times 10^{-12}$	$- \ 0.02 \times 10^{-12}$	8.33×10^{-12}	20.46×10^{-12}	-274.87×10^{-12}	4.91×10^{-12}	248.18×10^{-12}	6.95×10^{-12}
H	$- \ 0.00 \times 10^{-12}$	$- \ 0.00 \times 10^{-12}$	14.80×10^{-12}	$- \ 6.53 \times 10^{-12}$	-238.43×10^{-12}	4.34×10^{-12}	249.64×10^{-12}	23.82×10^{-12}
I	1.07×10^{-14}	0.24×10^{-14}	-213.28×10^{-14}	-277.29×10^{-14}	-1610.1×10^{-14}	28.64×10^{-14}	2389.3×10^{-14}	318.58×10^{-14}

Table 5.8.7: Balance of terms in the vorticity equation. Run III

Point	HOR. ADV.	VERT. ADV.	HOR. VISC.	VERT. VISC.	CORIOLIS	U. TERM	TIME DERIV.
A	-78.10×10^{-6}	470.97×10^{-6}	-544.13×10^{-6}	2.28×10^{-6}	4.02×10^{-6}	138.93×10^{-6}	6.03×10^{-6}
B	-466.11×10^{-6}	-292.59×10^{-6}	10.63×10^{-6}	0.47×10^{-6}	280.66×10^{-6}	466.43×10^{-6}	-0.41×10^{-6}
C	-84.01×10^{-6}	69.48×10^{-6}	12.56×10^{-6}	0.23×10^{-6}	1.24×10^{-6}	0.03×10^{-6}	-0.25×10^{-6}
D	-8.10×10^{-8}	0.27×10^{-8}	34.52×10^{-8}	-1.76×10^{-8}	-42.30×10^{-8}	-7.01×10^{-8}	-24.37×10^{-8}
E	106.22×10^{-8}	-143.82×10^{-8}	14.63×10^{-8}	-2.93×10^{-8}	-110.46×10^{-8}	-17.82×10^{-8}	-154.18×10^{-8}
F	-359.15×10^{-8}	304.97×10^{-8}	-41.24×10^{-8}	-10.16×10^{-8}	7.62×10^{-8}	1.16×10^{-8}	-96.80×10^{-8}
G	0.58×10^{-10}	-1.43×10^{-10}	67.33×10^{-10}	46.88×10^{-10}	-86.46×10^{-10}	0.18×10^{-10}	27.08×10^{-10}
H	-3.30×10^{-10}	14.05×10^{-10}	285.28×10^{-10}	-14.89×10^{-10}	321.10×10^{-10}	-0.59×10^{-10}	601.65×10^{-10}
I	6.79×10^{-10}	-3.47×10^{-10}	432.57×10^{-10}	-129.19×10^{-10}	12.09×10^{-10}	-0.02×10^{-10}	287.55×10^{-10}

Table 5.8.8: Balance of terms in the zonal momentum equation. Run III.

Point	HOR. ADV.	VERT. ADV.	HOR. DIFF.	VERT. DIFF.	RADIATION (BASIC)	RADIATION (PERT.)	TIME DERIV.
A	478.79	- 464.51	363.04	-0.57	-241.62	-129.77	5.36
B	1396.9	-1360.9	0.10	-1.68	301.76	-330.89	5.29
C	-1417.8	1386.9	- 0.28	-1.63	36.51	- 32.66	5.75
D	0.54	- 0.75	0.01	-1.46	1.30	0.27	-0.09
E	- 0.33	0.51	- 0.22	0.26	- 1.46	1.24	0.02
F	0.81	- 0.87	- 0.07	0.27	- 1.32	1.29	0.24
G	0.20	0.16	- 0.03	1.25	- 11.15	6.31	-3.58
H	- 0.16	0.13	0.00	1.26	- 11.15	6.33	-3.59
I	0.26	- 0.21	- 0.01	1.25	- 11.15	6.31	-3.55

Table 5.8.9: Balance of terms in the thermal equation. Units of 10^{-10}sec^{-1}. Run III.

shows a lack of convergence in the interior and near the bottom.
However this is not really important since the zonal velocities them-
selves are very small except near the top.

Run IV: $\nu_H = K_H = 10^{10} \; cm^2/sec$

$\nu_v = K_v = 10^4 \; cm^2/sec$

$\zeta_s^* = 2.3$

In this run we allowed a deeper penetration of solar radi-
ation, and consequently a deeper circulation. An optical depth
$\zeta_s^* = 2.3$ allows 10% of the solar radiation to reach the surface
when the zenith angle is zero; when the radiation is averaged over
a day, 6% of the normal radiation reaches the surface at the equator,
3% at 45° and none near the pole. Figure 5.8.25 shows the basic
"adiabatic" heating field obtained with $\zeta_s^* = 2.3$. (Unfortunately,
even though the model was free from nonlinear instability, a "nood-
ling" effect appeared and though there was a tendency to settle down,
the smaller-scale details are obviously not real.)

In Figures 5.8.26 and 5.8.27 we present the temperature
and meridional velocity v fields obtained after 1.8×10^7 secs.

Besides the "noodling", the most important observation is
that the velocities are much stronger both in the interior and near
the top, and that the circulation is able to maintain the temperature
close to an adiabatic stratification everywhere.

Even though the numerical values don't deserve confidence
because of the noodling, we present in Tables 5.8.10 to 5.8.12 the
"balance" of terms in the forecast equations, because they may give
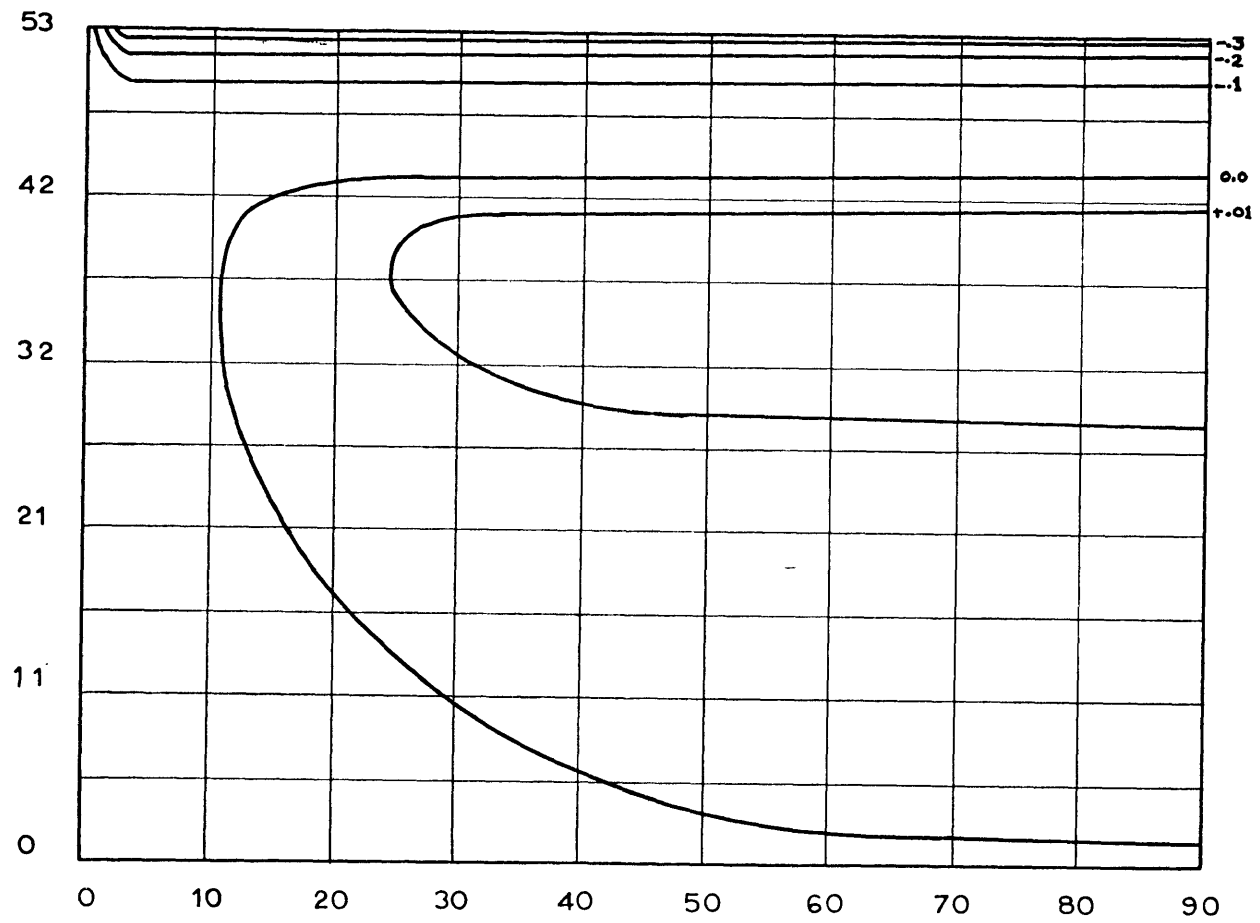
Figure 5.8.25: Heating rate in an adiabatic stratification with $\tau_s^* = 2.3$

Units of 10^{-7}sec^{-1}. Run IV.
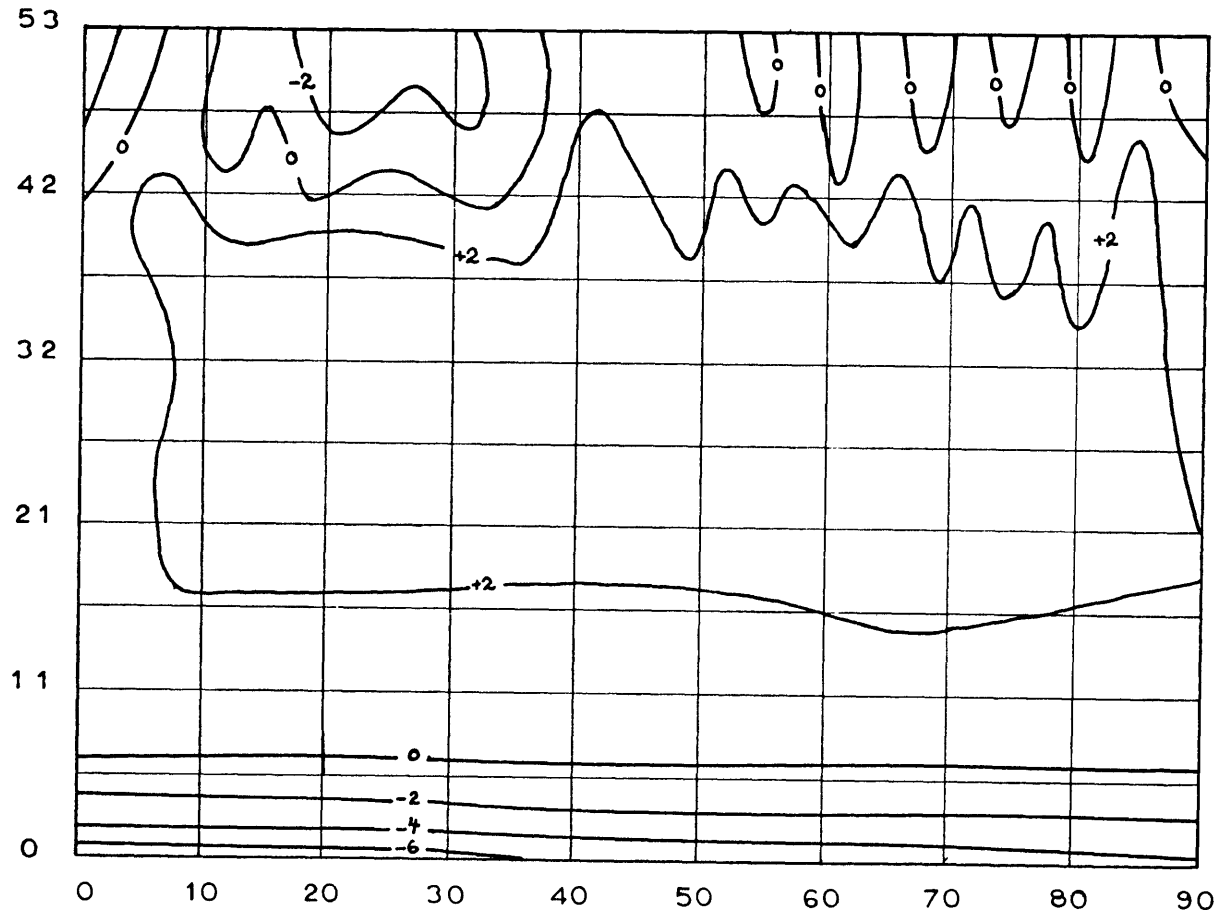
Figure 5.8.26: Relative potential temperature departure $\tilde{\theta}$ in units of 10^{-3}. Time t = 1.8×10^7. Run IV.
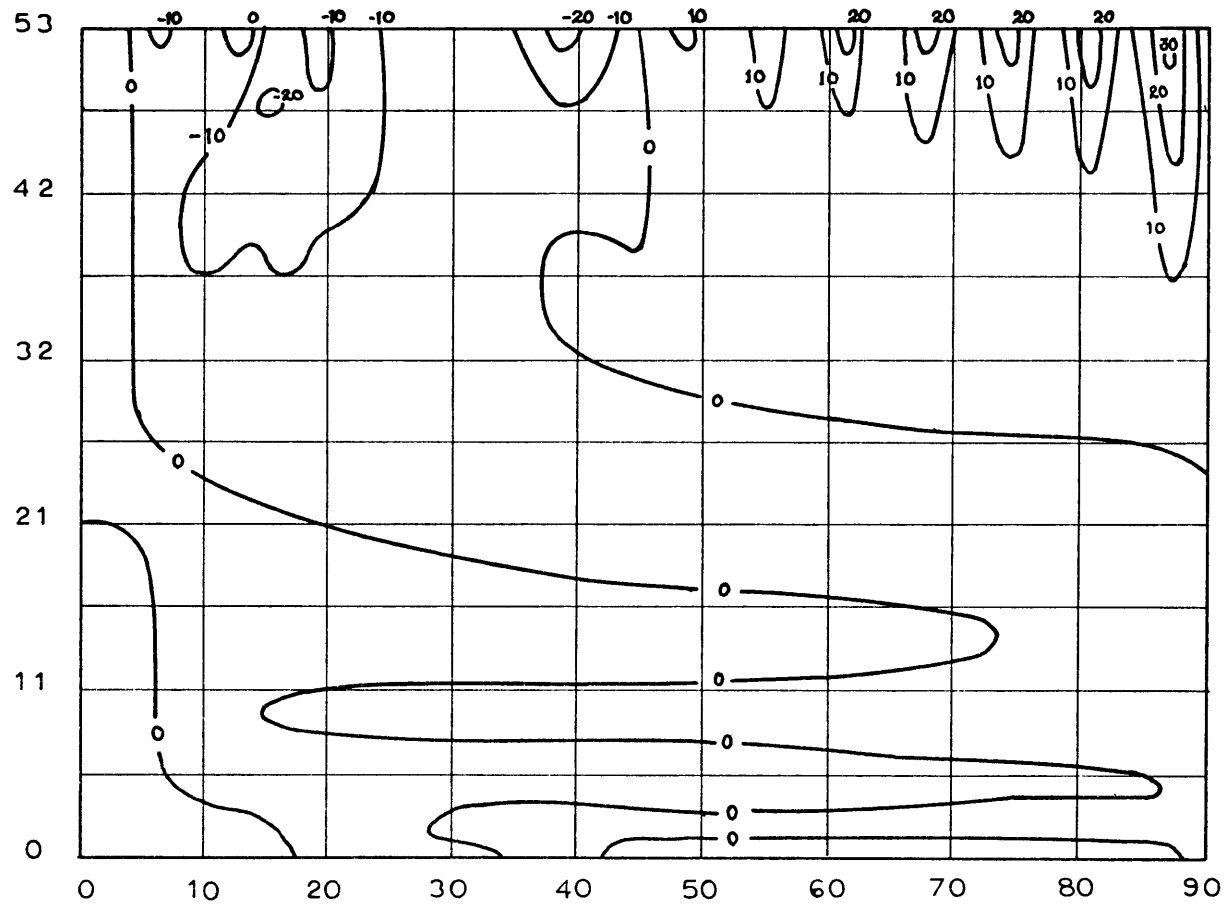
Figure 5.8.27: Meridional velocity v in m/sec. Run IV.

Point	HOR. ADV.	VERT. ADV.	HOR. VISC.	VERT. VISC.	CORIOLIS	U. TERM	SOLENOID	TIME DERIV.
A	$- 70.22 \times 10^{-5}$	$- 59.45 \times 10^{-5}$	$- 17.41 \times 10^{-5}$	3.85×10^{-5}	$- 0.04 \times 10^{-5}$	6.20×10^{-5}	$- 77.92 \times 10^{-5}$	$- 61.19 \times 10^{-5}$
B	-131.99×10^{-6}	105.64×10^{-6}	47.00×10^{-6}	3.78×10^{-6}	0.00×10^{-6}	0.00×10^{-6}	$- 80.64 \times 10^{-6}$	$- 56.20 \times 10^{-6}$
C	$- 22.26 \times 10^{-6}$	$- 1.85 \times 10^{-6}$	2.80×10^{-6}	1.11×10^{-6}	0.00×10^{-6}	$- 0.00 \times 10^{-6}$	28.10×10^{-6}	1.99×10^{-6}
D	2.50×10^{-6}	4.43×10^{-6}	$- 40.70 \times 10^{-6}$	$- 0.04 \times 10^{-6}$	$- 0.52 \times 10^{-6}$	41.97×10^{-6}	9.40×10^{-6}	18.08×10^{-6}
E	154.79×10^{-10}	620.93×10^{-10}	309.36×10^{-10}	$- 8.99 \times 10^{-10}$	5.00×10^{-10}	6.19×10^{-10}	-1779.5×10^{-10}	$- 692.26 \times 10^{-10}$
F	307.37×10^{-9}	535.99×10^{-9}	-111.37×10^{-9}	$- 1.27 \times 10^{-9}$	$- 0.01 \times 10^{-9}$	0.00×10^{-9}	289.06×10^{-9}	17.50×10^{-9}
G	17.96×10^{-8}	$- 11.24 \times 10^{-8}$	42.07×10^{-8}	-104.52×10^{-8}	$- 0.21 \times 10^{-8}$	0.00×10^{-8}	$- 25.62 \times 10^{-8}$	$- 182.68 \times 10^{-8}$
H	$- 0.73 \times 10^{-10}$	$- 2.20 \times 10^{-10}$	$- 1.49 \times 10^{-10}$	10.25×10^{-10}	$- 1.06 \times 10^{-10}$	0.01×10^{-10}	$- 45.05 \times 10^{-10}$	$- 40.27 \times 10^{-10}$
I	0.45×10^{-10}	$- 0.14 \times 10^{-10}$	41.64×10^{-10}	4.41×10^{-10}	$- 0.20 \times 10^{-10}$	0.00×10^{-10}	$- 61.84 \times 10^{-10}$	$- 15.68 \times 10^{-10}$

Table (5.8.10) Balance of terms in the vorticity equation after 2×10^{7} Run IV.

Point	HOR. ADV.	VERT. ADV.	HOR. VISC.	VERT. VISC.	CORIOLIS	U. TERM	TIME DERIV.
A	32.49×10^{-3}	-34.35×10^{-3}	10.18×10^{-3}	0.03×10^{-3}	-0.25×10^{-3}	-22.20×10^{-3}	-34.47×10^{-3}
B	34.12×10^{-4}	-31.82×10^{-4}	0.21×10^{-4}	0.00×10^{-4}	4.40×10^{-4}	2.91×10^{-4}	9.83×10^{-4}
C	-41.14×10^{-5}	46.70×10^{-5}	2.12×10^{-5}	0.10×10^{-5}	10.06×10^{-5}	1.06×10^{-5}	-1.22×10^{-5}
D	-4.90×10^{-5}	431.29×10^{-5}	-396.70×10^{-5}	0.14×10^{-5}	-8.01×10^{-5}	-252.42×10^{-5}	-230.60×10^{-5}
E	-115.20×10^{-6}	13.77×10^{-6}	20.15×10^{-6}	-0.03×10^{-6}	54.13×10^{-6}	32.96×10^{-6}	5.79×10^{-6}
F	12.06×10^{-6}	-31.29×10^{-6}	23.29×10^{-6}	0.03×10^{-6}	-1.76×10^{-6}	0.15×10^{-6}	2.48×10^{-6}
G	8.19×10^{-6}	0.65×10^{-6}	-7.43×10^{-6}	-8.05×10^{-6}	88.48×10^{-6}	4.08×10^{-6}	85.92×10^{-6}
H	-5.12×10^{-8}	8.99×10^{-8}	1.14×10^{-8}	275.08×10^{-8}	122.98×10^{-8}	-0.34×10^{-8}	402.74×10^{-8}
I	-4.22×10^{-8}	21.49×10^{-8}	16.55×10^{-8}	10.93×10^{-8}	1.55×10^{-8}	0.00×10^{-8}	24.03×10^{-8}

Table 5.8.11: Balance of terms in the zonal momentum equation after 2×10^{7} sec. Run IV.

Point	HOR. ADV.	VERT. ADV.	HOR. DIFF.	VERT. DIFF.	RADIATION (BASIC)	RADIATION (PERT.)	TIME DERIV.
A	362.56	-367.20	223.62	-0.98	-246.13	0.84	-27.29
B	- 42.55	31.79	158.77	-3.49	-240.93	66.34	-23.04
C	-515.78	1016.3	-231.58	-1.30	-240.79	-13.31	13.48
D	- 94.84	252.09	- 82.19	-0.03	- 1.46	0.00	73.58
E	5.98	- 8.22	- 0.18	-0.06	4.66	- 0.07	2.10
F	- 35.00	19.93	7.64	0.05	7.23	0.02	- 0.14
G	-548.63	450.31	5.42	8.79	- 11.15	1.97	-93.27
H	- 5.45	4.57	- 0.11	6.92	- 11.09	1.73	- 3.44
I	- 7.24	6.10	0130	8.48	- 10.71	1.73	- 1.32

Table 5.8.12: Balance of terms in the thermal equation after 2×10^7 sec. Units are $10^{-10} sec^{-1}$.

Run IV.

an indication of what would be the dominant terms in balance in a

correct solution. It may be inferred that a solar optical depth

of $\tau_s^* = 2.3$ or smaller will give rise to a circulation that is

strong enough to stir the whole atmosphere and maintain an adiabatic

or quasi-adiabatic stratification. In particular, from Table 5.8.12,

we see that nonlinear terms in the thermal equation are of the

same order or larger than the radiative terms even near the ground.

Other runs: In several runs it was observed that poor resolution

may give rise to large-scale oscillations that are not damped out

with time. These spurious oscillations may be due to a physically

unstable situation produced by truncation errors especially in the

advective terms. For example in one run very regular oscillations

were observed in the meridional circulation with the suggestive period

of 4 1/2 earth days (the same as the observed rotation period of

the clouds). It was thought that this was related to an inertial

period corresponding to the high relative rotation, until it was

found that increasing the resolution caused the oscillations to dis-

appear! In this case the oscillations were associated with a highly

unstable distribution of angular momentum, which also disappeared

as the number of grid points was increased.

5.9 Energy budget

We define the kinetic energy of the zonal motion as

$$K_z = 2\pi a^2 \int_0^H \int_0^{\pi/2} \rho_a \frac{u^2}{2} \sin\alpha \, d\alpha \, dz , \qquad (5.9.1)$$

the kinetic energy of the meridional motion as:

$$K_M = 2\pi a^2 \int_0^H \int_0^{\pi/2} \rho_a \frac{v^2}{2} \sin\alpha \, d\alpha \, dz \, , \tag{5.9.2}$$

and the potential energy separated in its initial (adiabatically-stratified) value and the excess of potential energy generated during the run by

$$P = 2\pi a^2 \int_0^H \int_0^{\pi/2} \left(\rho_a \, g \, z - \rho_a \, \tilde{\theta} g \, z \right) \sin\alpha \, d\alpha \, dz \tag{5.9.3}$$

Then, from equations (5.2.1) to (5.2.5) we obtain the energy equations:

$$\frac{\partial K_z}{\partial t} = CT + UT - D_z \equiv \{ K_M, K_z \} - D_z \tag{5.9.4}$$

$$\frac{\partial K_M}{\partial t} = \{ P, K_M \} - CT - UT - D_M = \{ P, K_M \} - \{ K_M, K_z \} - D_M \tag{5.9.5}$$

$$\frac{\partial P}{\partial t} = G_P - \{ P, K_M \} \tag{5.9.6}$$

where

$$CT = 2\pi a^2 \int_0^H \int_0^{\pi/2} \rho_a \, f \, v \, u \, \sin\alpha \, d\alpha \, dz \tag{5.9.7}$$

$$UT = -2\pi a^2 \int_0^H \int_0^{\pi/2} \rho_a \, \frac{\cot\alpha}{a} \, u^2 \, v \, \sin\alpha \, d\alpha \, dz \tag{5.9.8}$$

$$D_z = -2\pi a^2 \int_0^H \int_0^{\pi/2} \rho_a \left\{ \frac{\nu_H}{a^2} \frac{[(u\sin\alpha)_\alpha]^2}{\sin^2\alpha} + \nu_v \, (u_z)^2 \right\} \sin\alpha \, d\alpha \, dz \tag{5.9.9}$$

$$\mathcal{D}_M = -2\pi a^2 \int_0^H \int_0^{\pi/2} \rho_a \left\{ \frac{\nu_H}{a^2} \frac{[(v \sin\alpha)_\alpha]^2}{\sin^2\alpha} + \nu_v (v_z)^2 \right\} \sin\alpha \, d\alpha \, dz \qquad (5.9.10)$$

$$\{P, K_M\} = -2\pi a^2 \int_0^H \int_0^{\pi/2} g w \, \tilde{\theta} \rho_a \sin\alpha \, d\alpha \, dz \qquad (5.9.11)$$

$$G_P = -2\pi a^2 \int_0^H \int_0^{\pi/2} g \rho_a \frac{d\tilde{\theta}}{dz} z \sin\alpha \, d\alpha \, dz$$

$$= -2\pi a^2 \int_0^H \int_0^{\pi/2} g \rho_a z \left\{ \frac{K_H}{a^2} \frac{(\tilde{\theta}_\alpha \sin\alpha)_\alpha}{\sin\alpha} + K_v \tilde{\theta}_{zz} + \frac{q_v}{C_p \rho_a \pi_a \theta_a} \right\} \sin\alpha \, d\alpha \, dz \qquad (5.9.12)$$

These equations are completely similar to the energy equations in the Boussinesq model (section 4.7), except that the mean constant density ρ_0, is replaced in the quasi-Boussinesq model by the mean adiabatic density ρ_a, and the relative density departure $\tilde{\rho}$ by $-\tilde{\theta}$, the negative of the relative potential temperature departure.

Figures 5.9.1 to 5.9.4 show the energy budgets of the model atmosphere at the end of the four runs. It is interesting to compare the results with those obtained in the Boussinesq model with rotation (section 4.7).

The initial potential energy in the quasi-Boussinesq model is less than half the potential energy in the Boussinesq model where the density is constant and therefore the center of gravity is higher. The excess (or deficit) of potential energy over that of the basic

$G_P = -4850 \times 10^{19}$

Basic Pot. En. 306.8×10^{30} | Excess of Pot. En. -4.4×10^{30}

$\{P, KM\} =$ 25.52 $\times 10^{19}$

Meridional Kinetic Energy 6.16×10^{25}

$CT = 2.05 \times 10^{19}$

$UT = 17.52 \times 10^{19}$

$\{K_M, K_z\} = 19.57 \times 10^{19}$

Zonal Kinetic Energy 10.13×10^{25}

$D_M = 6.00 \times 10^{19}$

$D_z = 19.61 \times 10^{19}$

$D_K = 25.61 \times 10^{19}$
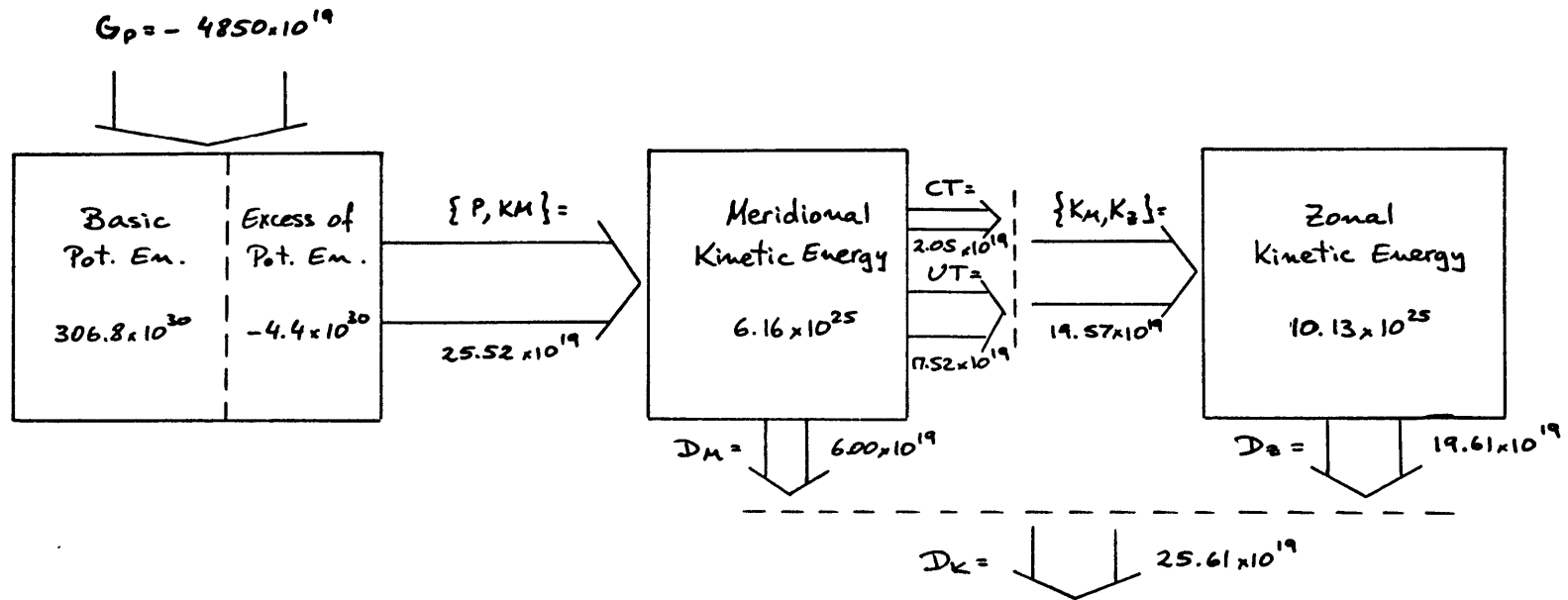
Figure 5.9.1: Balance of energy in the quasi-Boussinesq rotating model, Run I. Energies are in dynes and conversion terms in dynes/sec.

$G_P = -8970 \times 10^{19}$

Initial Pot. Em.	Excess of Pot. Em.
306.8×10^{30}	-3.0×10^{30}

$\{P, KM\} = $

9.376×10^{19}

Meridional Kinetic Energy

1.88×10^{25}

$CT = $

$.772 \times 10^{19}$

$UT = $

$.560 \times 10^{19}$

$\{K_M, K_Z\} = $

1.332×10^{19}

Zonal Kinetic Energy

0.534×10^{25}

$D_M = 8.060 \times 10^{19}$

$D_Z = 1.332 \times 10^{19}$

$D_K = 9.392 \times 10^{19}$
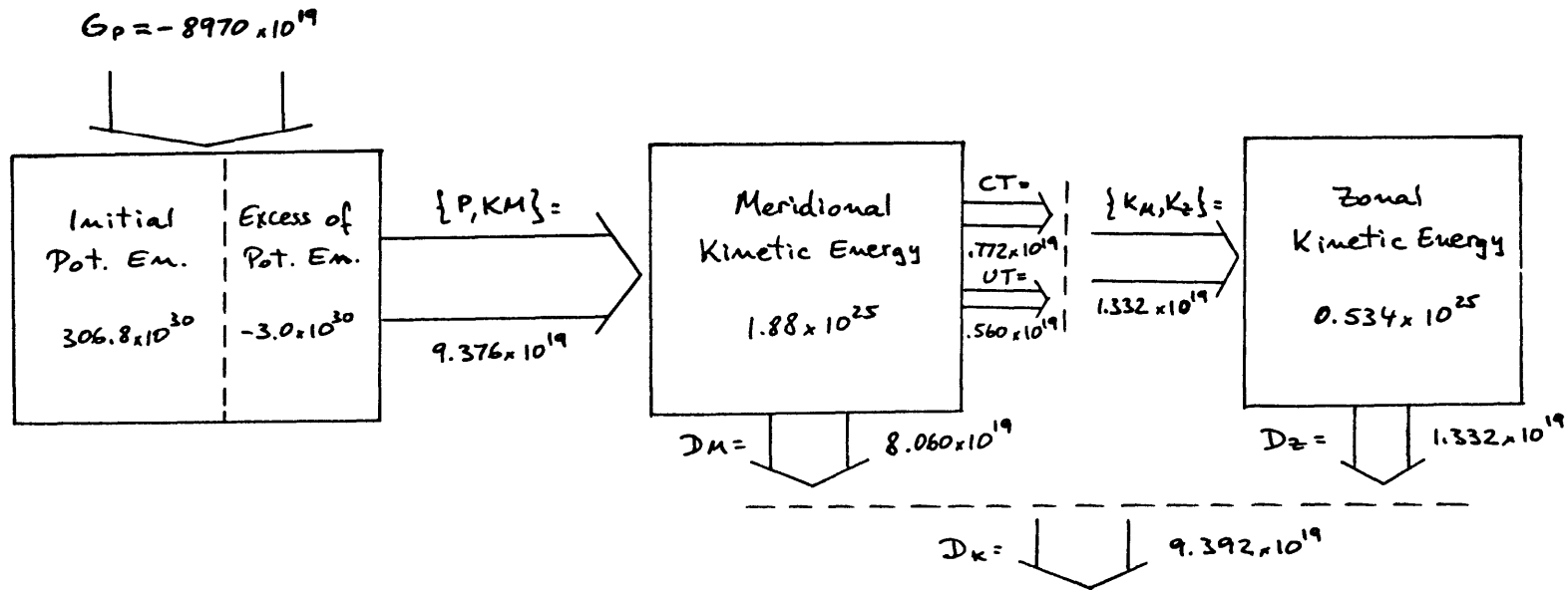
Figure 5.9.2: Balance of energy. Run II.

$G_P = -1965 \times 10^{19}$

Initial Pot. En.	Excess of Pot. En.
306.8×10^{30}	-3.2×10^{30}

$\{P, KM\} =$

25.65×10^{19}

Meridional Kinetic Energy

8.29×10^{25}

$CT = 3.42 \times 10^{19}$

$UT = 16.70 \times 10^{19}$

$\{K_M, K_2\} =$

20.12×10^{19}

Zonal Kinetic Energy

21.01×10^{25}

$D_M = 5.69 \times 10^{19}$

$D_Z = 20.46 \times 10^{19}$

$D_K = 26.15 \times 10^{19}$
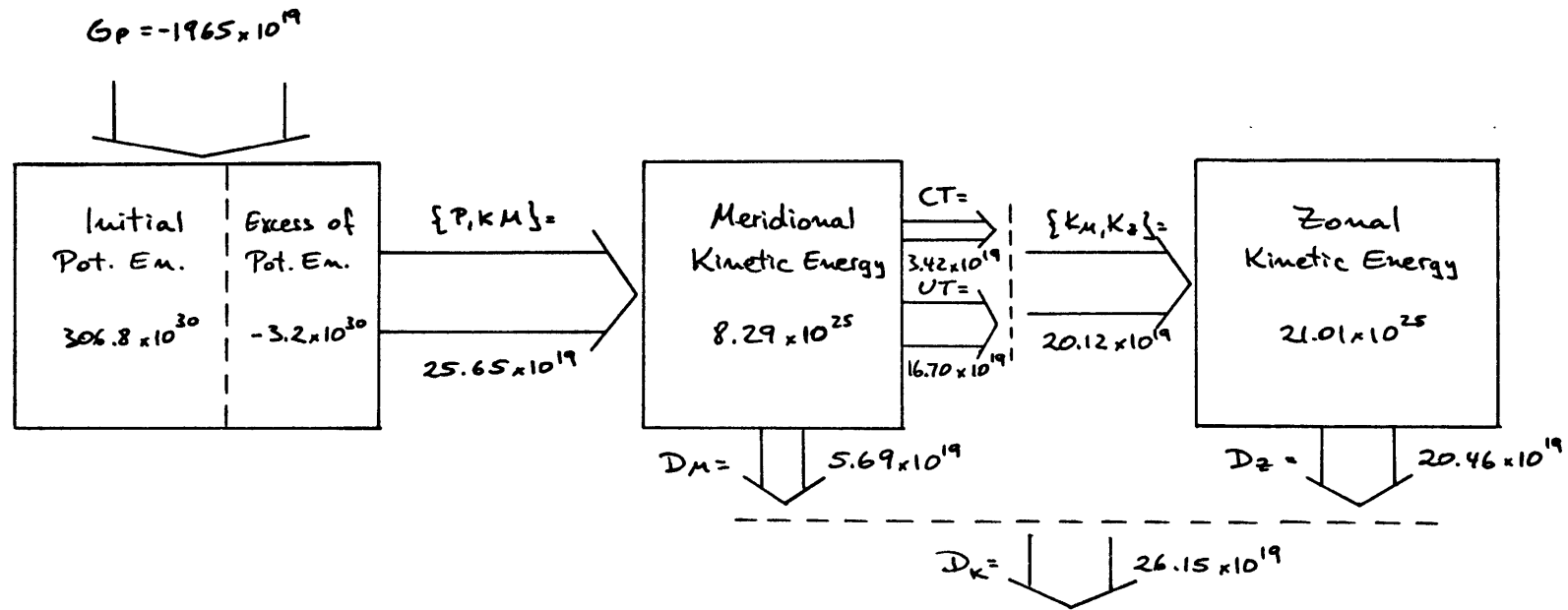
Figure 5.9.3: Balance of energy. Run III.

$G_P = 3620 \times 10^{19}$

| Initial
Pot. En.

306.8×10^{30} | Excess of
Pot. En.

-0.4×10^{30} |

$\{P_1 K_M\} =$

5853×10^{19}

Meridional
Kinetic Energy

737.0×10^{25}

$CT =$
4296×10^{19}

$UT =$
400.1×10^{19}

$\{K_M, K_Z\} =$

447.1×10^{19}

Zonal
Kinetic Energy

145.5×10^{25}

$D_M = \quad 6497 \times 10^{19}$

$D_Z = \quad 902.1 \times 10^{19}$

$D_K = \quad 7309 \times 10^{19}$
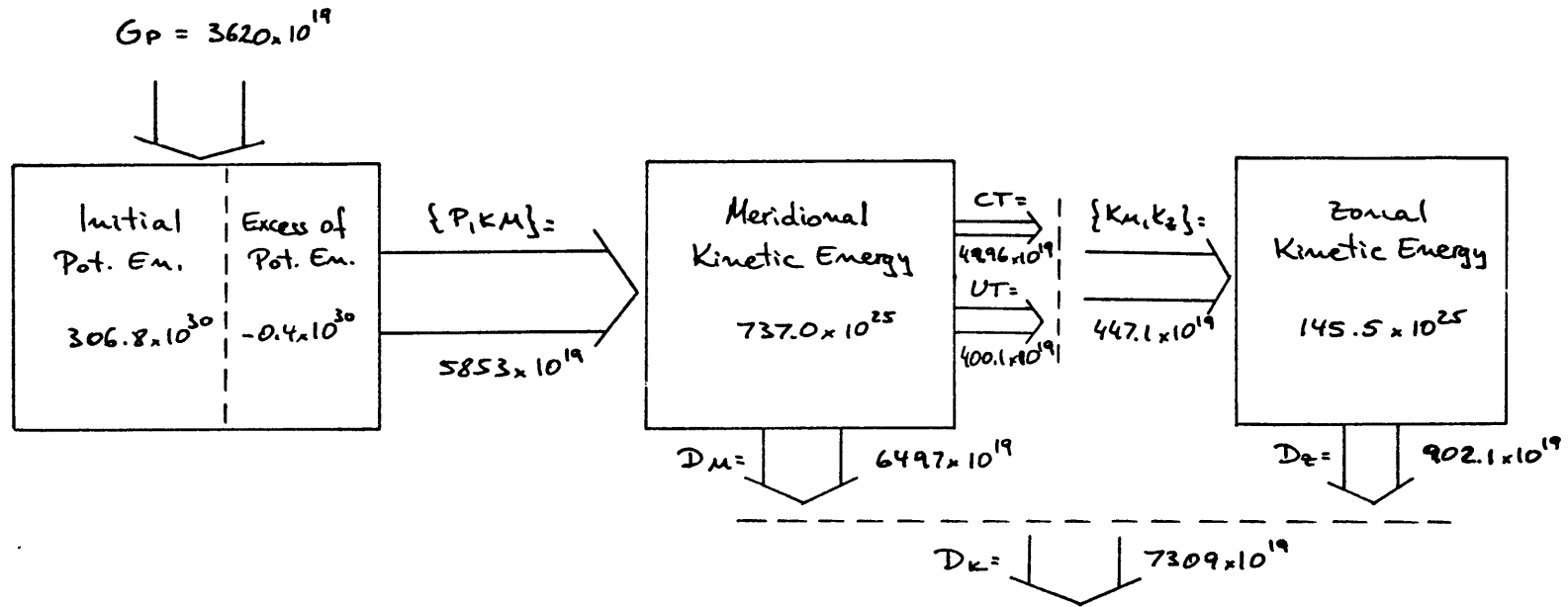
Figure 5.9.4: Balance of energy. Run IV

stratification is two orders of magnitude larger in Runs I, II and

III, and one order of magnitude larger in Run IV, than that of the

Boussinesq model. This result reflects the fact that radiation has

affected the deep atmosphere in the quasi-Boussinesq models, making

it more stable and decreasing by a large amount the unavailable po-

tential energy, whereas in the Boussinesq model the interior density

remained essentially unperturbed.

In the Boussinesq model the G_p term was about twice as

large as the $\{P, K_M\}$ term, indicating that only half of the poten-

tial energy generated was unavailable. Here the ratio $G_p / \{P, K_M\}$

is of the order of 100 or more in Runs I, II and III. Again, this

is due to the fact that the general circulation is confined mainly

to the top, and in the interior there is a tendency to have radiative

equilibrium, which obviously has not yet been reached. G_p is

negative because radiation is continuing to decrease the unavailable

potential energy by much more than available potential energy is

being generated and converted to kinetic energy.

In Run I, and in the Boussinesq model, in which $\nu_H = 10^{10} \, cm^2/sec$

and $\nu_V = 10^4 \, cm^2/sec$, the ratio of the zonal kinetic energy to the

meridional kinetic energy is roughly 10:6. In Run II, where the hori-

zontal coefficient of eddy viscosity was increased to $10^{11} \, cm^2/sec$

this ratio decreased to 10:30, and in Run III, where the vertical

coefficient of eddy viscosity was reduced to $10^3 \, cm^2/sec$, the ratio

increased to 10:4. This suggests that if smaller (and probably more

realistic) values for the horizontal and vertical coefficients of

eddy viscosity were used, the zonal kinetic energy would become

even larger.

The confinement of the circulation to the top in Runs I, II, and III is also apparent in the magnitude of the kinetic energy which is roughly 40 times smaller in the quasi-Boussinesq than in the Boussinesq case. In Run IV, in which the circulation penetrates deeply into the atmosphere, the kinetic energy is of the same order as in the Boussinesq case.

If the models had converged we should have observed the following equalities:

$$G_\rho = \{P, K_M\}$$

$$\{P, K_M\} = \{K_M, K_z\} + D_M \qquad (5.9.13)$$

$$\{K_M, K_z\} = D_z$$

Of these, only the last two equations have been satisfied with good approximation in Runs I, II and III. The first equation is very far from being satisfied because of the tendency of the interior to reach radiative equilibrium with a much larger relaxation time than the times for which the integrations were made.

Figure 5.9.4 corresponding to Run IV with $\tau_s^* = 2.3$ presents a much different picture. The effect of a deeper penetration of the solar radiation is twofold: there is a greenhouse effect, and a deeper circulation is driven; the combination of the two effects is apparently capable of maintaining a near-adiabatic lapse rate. Thus in Figure 5.9.4 we see that even though there is no sign of convergence, the values of G_ρ and $\{P, K_M\}$ are of the same order, and

that the extra potential energy generated is 10 times smaller, and
the kinetic energy 100 times larger, than in Runs I, II and III,
in which solar radiation was absorbed mainly at the top.

5.10 Radiative equilibrium in a semi-grey atmosphere

The results of Runs I, II and III, as well as those ob-
tained in the nonrotating quasi-Boussinesq model, show that if solar
radiation is absorbed mainly at the cloud top level, then the large-
scale circulation is not able to maintain an adiabatic or close to
adiabatic temperature stratification in the interior. In that case
the thermal balance will be mainly radiative and the temperature will
tend to become isothermal in the interior. In this case the quasi-
Boussinesq approximation and the linearized treatment of radiation
become inaccurate.

To find what the radiative balance would be if large-scale
convection and turbulent diffusion were negligible, a simple and rapid
method was developed to evaluate the radiative fluxes in a semi-grey,
constant composition atmosphere.

For a semi-grey atmosphere, the thermal and solar radiative
fluxes are respectively (Gierasch and Goody, 1970)

$$F_T(\tau_T) = \int_{\tau_T}^{\tau_T^*} \sigma T^4(t)\, e^{-r(t-\tau_T)}\, r\,dt + \sigma T^{*4}\, e^{-r(\tau_T^* - \tau_T)}$$

$$- \int_0^{\tau_T} \sigma T^4(t)\, e^{r(t-\tau_T)}\, r\,dt, \qquad\qquad (5.10.1)$$

$$F_s(\tau_s) = F_s(0)\, e^{-\tau_s} \qquad\qquad (5.10.2)$$

which are seen to coincide with equations (3.3.1) and (3.3.18). As before we consider τ_s to be the effective solar optical depth.

If we assume that the volume absorption coefficients both for solar and thermal radiation are proportional to the density, but with different constants of proportionality (semi-grey assumption), then from the hydrostatic equation, we obtain that the optical depths are proportional to the pressure:

$$\frac{p - p_H}{p_0} = \frac{\tau_T - \tau_{T_H}}{\tau_{T_0}} = \frac{\tau_s - \tau_{s_H}}{\tau_{s_0}} \tag{5.10.3}$$

where p_H, τ_{T_H}, and τ_{s_H} are the values of the pressure and the thermal and solar optical depths at the top of the atmosphere, and may, in particular, be zero.

The heating rate is given by

$$\frac{\partial T}{\partial t} = \frac{1}{C_p \rho} \frac{\partial (F_s - F_T)}{\partial z} \tag{5.10.4}$$

or, using the hydrostatic approximation

$$\frac{\partial T}{\partial t} = -\frac{g}{C_p} \frac{\partial (F_s - F_T)}{\partial p} \tag{5.10.5}$$

We introduce (5.10.3) into (5.10.1) and (5.10.2) and obtain

$$F_T(p) = \int_p^{p_0} \sigma T^4(P) e^{-r C_T (P-p)} r C_T \, dP + \sigma T^{*4} e^{-r C_T (p_0 - p)}$$

$$- \int_{p_H}^p \sigma T^4(P) e^{r C_T (P-p)} r C_T \, dP \tag{5.10.6}$$

$$F_s(\mu) = F_s(\mu_H) \, e^{-C_s(\mu - \mu_H)} \qquad (5.10.7)$$

where $C_T = \dfrac{\tau_{T_0}}{\mu_0}$ and $C_s = \dfrac{\tau_{S_0}}{\mu_0}$

Equations (5.10.5) to (5.10.7) and the boundary conditions

$$F_s - F_T = 0 \qquad\qquad at \quad \mu = \mu_0, \mu_H \qquad (5.10.8)$$

are simple to integrate numerically by successive iterations.

If the atmosphere has a large thermal optical depth, τ_{T_0}, the rapid variation of the exponentials in equation (5.10.6) may produce problems in the numerical approximation. However, in that case we can make the following simplification (Figure 5.10.1):

Divide the atmosphere into pressure layers $\Delta \mu$ and assume that the temperature varies linearly with pressure within each layer i.e., at each layer n, set

$$T = T_n + (T_{n+1} - T_n) \frac{q}{\Delta q} \qquad (5.10.9)$$

where
$$q = r \, C_T \, (\mu - \mu_n)$$
$$\Delta q = r \, C_T \, \Delta \mu$$

Then, if we assume that the temperature varies continuously, and neglect $e^{-\Delta q} \ll 1$, we can integrate (5.10.6) directly and obtain the finite-difference system of equations

$n = N \quad z = H$ ────────────────

─ ─ ─ ─ ─ ─ ─ ─ ─

n^{th} layer $\Biggl\{$ ──────────────── $T_{n+1}, F_{T_{n+1}}, F_{S_{n+1}}$

──── T'_{n}

──────────────── $T_{n}, F_{T_{n}}, F_{S_{n}}$

─ ─ ─ ─ ─ ─ ─ ─

$n = 1 \quad z = 0$ ///////////////
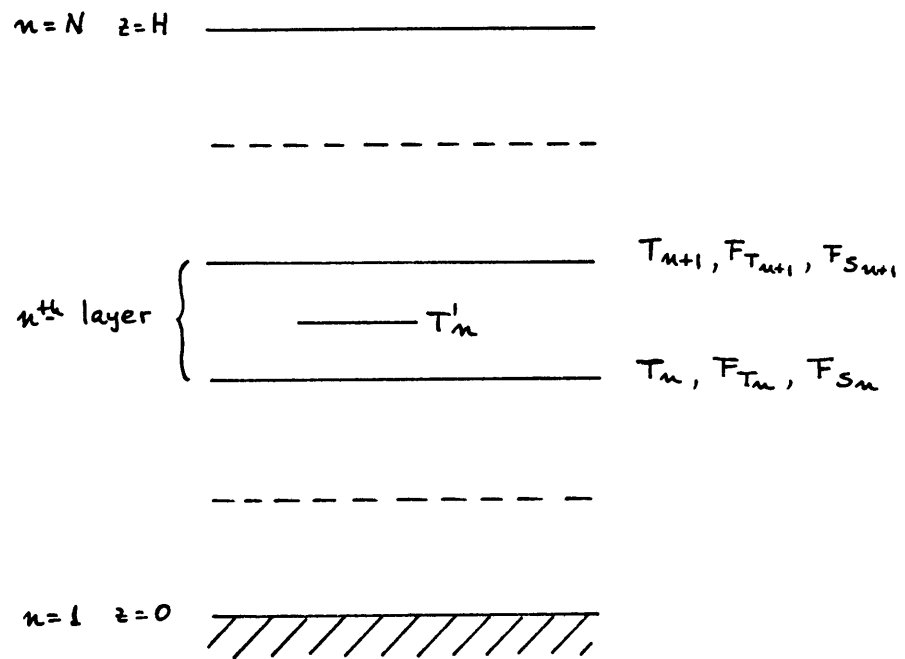
Figure 5.10.1: Computation of radiative equilibrium.

$$F_{T_m} = \sigma \left[f\left(T_m, \frac{T_{m-1} - T_m}{\Delta q}\right) - f\left(T_m, \frac{T_{m+1} - T_m}{\Delta q}\right) \right] \quad \text{for } m = 2, \ldots, N-1$$

$$F_{T_1} = \sigma \left[T_1^4 - f\left(T_1, \frac{T_2 - T_1}{\Delta q}\right) \right]$$

$$F_{T_N} = \sigma \, f\left(T_N, \frac{T_{N-1} - T_N}{\Delta q}\right)$$

$$F_{S_m} = F_{S_N} \, e^{-[(N-m) C_S \Delta q]} \quad \text{for } m = 1, \ldots, N-1$$

<div align="right">(5.10.10)</div>

$$T_m' = T_m' + \frac{\Delta t \, g}{C_p \Delta p} \left[F_{S_{m+1}} - F_{T_{m+1}} - F_{S_n} + F_{T_n} \right]$$

<div align="right">for $m = 1, \ldots, N-1$</div>

$$T_m = \frac{(T_m' + T_{m-1}')}{2}$$

$$T_N = T_{N-1}' + \frac{1}{2}\left(T_{N-1}' - T_{N-2}'\right)$$

$$F_{T_1} = F_{S_1}$$

where

$$f(T, \beta) = T^4 + 4\beta T^3 + 12\beta^2 T^2 + 24\beta^3 T + 24\beta^4 \qquad (5.10.11)$$

The numerical integration of the system (5.10.10) to convergence is simple and rapid. Once the final solution $T(p)$ is known, the corresponding function $T(z)$ may be obtained from a combination of the hydrostatic equation and the perfect gas law:

$$dz = -\frac{RT}{g}\frac{dp}{p} \qquad (5.10.12)$$

Table 5.10.1 shows the surface temperature obtained at radiative equilibrium for some combinations of ζ_s^* and ζ_τ^* . Gierasch and Goody's (1970) radiative diffusive equilibrium calculations gave a surface temperature of 464°K when $\zeta_s^* \simeq 2.4$ and $\zeta_\tau^* = 50$; this coincides with our radiative equilibrium result.

The combination $\zeta_\tau^* = 222$ and $\zeta_s^* = 55$, which was used in Runs I, II and III, gives a radiative equilibrium surface temperature of 271°K. We quote Mintz (1960) as saying that it is like a greenhouse with very dirty glass which will not work. If the circulation is included, the results of Runs I to III indicate that it will be able to maintain the lapse-rate close to adiabatic only in roughly the upper half of the atmosphere. In the lower half the thermal balance will be radiative, and we would expect the surface temperature to have an intermediate temperature of about 500°K, considerably lower than the 748°K observed by Venera 7 (Avduevsky et al., 1971).

The combination $\zeta_\tau^* = 222$ and $\zeta_s^* = 2.3$, which was used in Run IV, gives a surface temperature of 664°K, so that even if 90% or more of the solar radiation is absorbed before it reaches the surface, there is a considerable greenhouse effect, although not enough to explain the Venera 7 observations. But the results of Run IV show that in this case the combined effect of a deep circulation, which penetrates to the ground, and a partial greenhouse effect can explain the adiabatic lapse rate throughout the atmosphere and therefore the high surface temperature observed by Venera 7.

ζ_T^* \ ζ_s^*	1.0	2.3	4.6	9.2	55
50	522	464	401	341	241
100	617	548	470	395	252
150	680	604	517	431	261
200	$\sim$ 730	647	553	460	268
222	$\sim$ 750	664	567	469	272
250	$\sim$ 770	684	584	483	275
300	$\sim$ 800	715	610	504	281
350	$\sim$ 830	742	633	522	287
400	$\sim$ 860	767	653	538	292
450	$\sim$ 880	789	672	553	297
500	$\sim$ 900	810	689	567	301

Table 5.10.1: Surface temperature for radiative equilibrium in a grey atmosphere. These values have been computed assuming the solar radiation to be normal and equal to $F_s = \sigma T_{eff}^4 = \frac{S_o(1-A)}{4}$. If the zenith angle is different from zero, a correspondingly larger value of ζ_s^* should be taken.

CHAPTER 6

Summary and Conclusions

In this thesis the behavior of two-dimensional models of
the atmosphere of Venus is studied. Two extreme cases are consid-
ered: first, we neglect (following Goody and Robinson) the effects
of planetary rotation and assume that the subsolar and antisolar points
remain fixed, and second, we include the planetary rotation but as-
sume that the effects of the diurnal variation of solar heating are
negligible. In each case we develop a Boussinesq model, in which
there is no basic stratification of density, and a quasi-Boussinesq
model, in which the effect of stratification of density is included.

The Boussinesq model without rotation does not include
radiation, since the transfer of heat is assumed to be effected only
by eddy diffusivity and large-scale advection. The model is thus
more similar to Stone's than to Goody and Robinson's model. The re-
sults obtained show an overall agreement with those of Stone and
Goody and Robinson. An asymmetric cell develops, with a strong cur-
rent at the top directed from the subsolar to the antisolar points
and a strong downward jet at the antisolar point ("mixing region").
In Goody and Robinson's calculations, the downward motion is confined
to the narrow mixing region, a phenomenon which would explain the
almost complete cloud coverage of the surface of Venus, if the clouds
were of condensational origin. However, our results differ from
theirs in that weak downward motion occurs over most of the dark
hemisphere, not only in the mixing region.

The convergence time is given by the interior advective

time $\alpha/\bar{v}_{int} \sim 10^{7} sec$, or approximately one Venus solar day. This shows that the approximation in which the subsolar point is assumed to be fixed is not really justified. The approximation is even less justified for the quasi-Boussinesq model, in which the interior velocities are much weaker and the relaxation time for the deep atmosphere consequently much longer.

In the Boussinesq model without rotation, the stratification remains neutrally stable except in the top boundary layer, but this fact is not really signficant, for radiation is not taken into account, except for the influx and outflux of heat at the top, and it is the vertical eddy diffusivity, which is very probably too large, that tends to maintain the density neutrally stratified.

In the Boussinesq model with rotation, in which the solar heating is averaged over a Venus solar day, the result obtained is essentially a direct Hadley cell in each hemisphere and a smaller reverse cell near the poles, the latter occuring because the rings of air near the top of the atmosphere tend to increase their speed of rotation as they move polewards with decreasing radius of rotation, until the centrifugal force urges them back before reaching the pole. Angular momentum is transported polewards in the upper atmosphere with the result that in most of the atmosphere there is a shear of the zonal momentum in the same direction as the planetary rotation with a maximum near the pole. As in the Boussinesq model without rotation, the circulation penetrates the atmosphere and the return flow has its maximum intensity near the bottom. The stratification also remains neutral in the interior.

In the quasi-Boussinesq models, two important factors are

introduced: (a) the basic stratification of density in the deep atmosphere of Venus is included, and (b) radiation is introduced through a semi-grey approximation, i.e., constant absorption coefficients are assumed for both the solar and thermal radiation. The thermal radiative fluxes are linearized about the values they would have in an adiabatic atmosphere. This linearization is introduced in order to obtain a simple expression for the thermal fluxes. If the stratification does not remain nearly adiabatic, the approximation becomes inaccurate; this is probably the least accurate approximation of the model.

In the quasi-Boussinesq model without rotation most of the solar radiation is assumed to be absorbed near the top, as was the case in the Boussinesq model. The results obtained are similar to those for the Boussinesq model, except that the stratification of density confines the circulation to the upper part of the atmosphere. In the interior only a weak frictionally-driven circulation with velocities of the order of a few cm/sec are found. Hence the large-scale circulation is unable to maintain an adiabatic stratification in the interior. The thermal equilibrium in the lower atmosphere is radiative-diffusive, with a much longer relaxation time (of the order of 10^9 sec or 100 Venus solar days). The confinement of the circulation to the upper atmosphere was also obtained by Hess in a numerical model in which pressure was used as a vertical coordinate and with radiation absorbed and emitted at the top of the atmosphere as in our Boussinesq model.

In the quasi-Boussinesq model with rotation and symmetric heating, several cases were run, with varying horizontal and vertical

coefficients of eddy viscosity and diffusivity and varying penetration depths of solar radiation.

As in the non-rotating quasi-Boussinesq model, it was found that if most of the solar radiation is absorbed near the top ($\zeta_T^* = 55$) then the large scale circulation remains confined to the upper atmosphere and cannot maintain an adiabatic stratification in the interior (Run I). However, when some penetration of the solar radiation is allowed ($\zeta_S^* = 2.3$), even though only 6% of the solar radiation reaches the surface at the equator, and much less at higher latitudes, the circulation is able to penetrate the interior of the atmosphere (Run IV). In this case it is found that the combination of a deep large-scale circulation, and some greenhouse effect can maintain an adiabatic or nearly adiabatic lapse rate.

The effect of increasing the horizontal coefficient of eddy viscosity is to slow down the intensity of the circulation, especially the zonal velocities. With $\nu_H = 10^{10} cm^2/sec$ (Run I) the maximum relative zonal velocity is found to be 18 m/sec, whereas it is only 2.0 m/sec when $\nu_H = 10^{11} cm^2/sec$ (Run II). Smaller (and probably more realistic) values of the horizontal coefficients of eddy viscosity would allow larger zonal velocities, perhaps of the order of 100 m/sec, although not near the equator.

When lower values of the vertical coefficients of eddy viscosity and diffusivity are used (Run III), as being more appropriate for the slow velocities and stable stratification of the interior, the frictionally-driven interior circulation becomes somewhat stronger with velocities of the order of 10 cm/sec; the thermal equilibrium is now radiative-advective rather than radiative-diffusive; otherwise

the results are essentially the same.

It is found that the planetary rotation has a considerable effect on the circulation even though the rotation period is very long (243 earth days). In the interior the relative velocities are very small, and therefore the Rossby number is small compared to unity (except in Run IV, where the interior velocities are of the order of a few meters per second and the Rossby number is of order 1). Near the top the relative rotation due to the transport of angular momentum towards the pole is important.

We should note here that each of the runs described required several hours of computer time in the very fast IBM/360-95 computer at the Goddard Institute for Space Studies at New York.

The apparent rotation of the sun, Ω_S , is given by

$$\Omega_S = \Omega_Y - \Omega_R$$

where Ω_Y is the angular velocity of Venus corresponding to its yearly revolution around the sun and Ω_R the angular velocity corresponding to its sidereal rotation. The prograde revolution of Venus with a period of 225 earth days, and its retrograde rotation with a period of 243 earth days, combine to give a prograde apparent rotation of the sun with a period of 117 earth days. If solar radiation is assumed to be absorbed near the top, then the effect of the prograde motion of the sun would be to tilt the convection cells in such a way that there would be an upward transport of prograde zonal momentum. Only if the frictional effect of the ground is strong enough can retrograde motion be produced at the top (Schubert, Young and Hinch, 1971). Therefore it is felt that the mechanism proposed by Schubert and

Whitehead to explain the observed high zonal velocities at the cloud

top level is not probable, since the effect of the ground is unlikely

to be significant at high levels, especially when the basic strati-

fication of the density is considered.

A more probable explanation seems to be a combination of the

assumption of symmetrical heating introduced in Chapters 4 and 5, and

the Malkus-Thompson idea that an initial zonal flow can amplify beyond

the linear limit by Reynolds stress interaction with the tilted

thermally-induced disturbances in such a manner that the velocity of

the zonal flow becomes much larger than the apparent velocity of the

sun, so that the direction of the solar rotation becomes immaterial.

Let us assume that the main effect of the sun is to produce

a direct Hadley cell in each hemisphere, and a corresponding shear

of the zonal momentum, with maximum retrograde velocities at the top

of the atmosphere as in our quasi-Boussinesq model with rotation.

The diurnal contrast of heating between the day and night hemispheres

will be important only near the top of the atmosphere. There, as

Thompson has suggested, the basic shear of the zonal velocities

can tilt the convection cells in such a manner as to increase the

shear and produce even stronger zonal velocities at the top. Although

the zonal shear produced by the Hadley cells is a minimum at the equa-

tor, the heating contrast is a maximum so that both effects may combine

to give an appearance of near solid rotation. Furthermore, the ultra-

violet cloud pictures show that the motion is actually three-dimen-

sional, with the bifurcated horizontal Y pattern suggesting that

there is eddy transport of retrograde zonal momentum from middle to

low latitudes.

It is felt that only a three-dimensional, non-linear, non-Boussinesq model of the Venus atmosphere will adequately test the validity of the hypotheses offered to explain the high zonal velocities. A simple model suggested by J. G. Charney and R. T. Thompson that will retain the characteristics of three-dimensionality without consuming a prohibitive amount of computer time is proposed in Appendix A. Some preliminary computations were actually made but were ruined by non-linear instabilities inherent in an earlier version of the finite-difference equations. It is felt that the procedure discussed in sections 2.5 and 5.6 will eliminate these instabilities.

A very fast procedure has been found to obtain the radiative flux and the corresponding radiational heating in a semi-grey atmosphere when pressure is used as vertical coordinate (section 5.10). The use of pressure as vertical coordinate has the advantage, furthermore, that it provides a time-independent continuity equation without the need of the quasi-Boussinesq approximation. These characteristics make desirable the use of pressure as vertical coordinate in future models. The only disadvantage is that it gives poor resolution in the upper atmosphere, but this might be corrected with the use of a suitable vertical stretched coordinate defined in terms of the pressure. Other improvements that should probably be introduced are the use of nonconstant coefficients of eddy viscosity and diffusivity dependent on the local Richardson number and the horizontal deformation field.

In the course of this investigation it was realized that in order to keep the computation time within reasonable limits it was necessary to use non-uniform grids in order to be able to resolve

the boundary layers. A study of the truncation errors introduced by the use of such grids was made (Appendix B). It was found that a suitable choice of the stretched coordinate gives a decided advantage over other variable grid methods.

APPENDIX A

A Truncated Fourier Series Model

For the Three-Dimensional Circulation of the Atmosphere of Venus

A.1 Introduction

Our approach to the study of the circulation of the atmosphere of Venus was to try to obtain a steady state numerical solution for a series of simple two-dimensional models. These solutions, which include nonlinear interactions, are more complete than the schematic solutions obtained by scale analysis in previous studies (Goody and Robinson, 1966 and Stone, 1968). They have shown that some penetration of the solar radiation through the atmosphere is necessary in order to maintain an adiabatic stratification. However it has become clear that a two-dimensional model cannot explain some observations of the atmosphere of Venus, in particular the high zonal velocities observed at the cloud top level (Dollfus, 1968; Smith, 1967). The cloud observations also indicate that the circulation is three-dimensional and unsteady.

The recent theories developed by Schubert (1969), Malkus (1970) and Thompson (1970) make it plausible that the large zonal velocities observed may be due to the apparent motion of the sun during a Venus solar day. Thompson's model requires a basic zonal flow with a vertical shear. The relative motion of the sun is not essential. The basic zonal flow can be explained by neglecting diurnal variations as a first approximation, and considering a two-dimensional model symmetric around the equator, as was done in Chapters 4 and 5. But it is obvious that a three-dimensional model will be

necessary to adequately test the validity of the theories of Schubert, Malkus and Thompson.

The possibility of developing a fully three-dimensional numerical model for the atmosphere of Venus is remote now, because it would require an enormous consumption of computer time, probably comparable to that required for the complex models of the three-dimensional atmospheric circulation developed, for example, by Smagorinsky et al. (1965). It would not be reasonable to construct such a model now in view of the sparcity of data on the constitution of the atmosphere of Venus, its aerosols, and its circulation. We propose instead to develop a simple model that will retain some characteristics of three-dimensionality while requiring only a little more than three times the amount of computer time used by a two-dimensional model.

The model proposed is one in which zonal variations are expressed by a Fourier expansion with only a few components retained, and a finite-difference method is used to solve the differential equations in the meridional and vertical directions (similar to the one used in Chapter 5).

The expansion in Fourier series for the zonal dependence, when only a small number of components are retained, has several advantages: (a) the boundary condition of periodicity in the zonal direction makes the expansion in orthogonal (Fourier) series especially simple; (b) for very few (say 3) components the Fourier method is about as efficient, computationally speaking, as a finite-difference method with the same number of grid points; (c) for a moderately large number of components, the Fourier method is much more accurate than a finite-difference scheme with the same number of grid points

(Orszag, 1970). With few components, this becomes even more true, since finite-difference methods become meaningless as the number of points decreases and the Fourier representation retains the basic characteristics of the nonlinear interactions; (d) the Fourier representation has conservation properties of energy and momentum similar to those of the continuous equations (Lorenz, 1960).

In the meridional and vertical directions it would not be convenient to use an expansion in orthogonal functions because there it would be necessary to retain many more components to obtain a reasonable resolution and this would require much more computer time.

We present here the basic equations and a method of solution for a numerical model in which the meridional and vertical directions are resolved by finite difference and in which diurnal variations are taken into account by retaining only three Fourier components: the zonally-symmetric component and the sine and cosine components with longitudinal wave number unity.

A.2 Three-dimensional quasi-Boussinesq model

(a) Continuous equations

The quasi-Boussinesq equations are written in spherical coordinates, where λ is the longitude, increasing in the retrograde direction, α the colatitude and z the height: The zonal momentum equation is

$$\frac{\partial u}{\partial t} = - \frac{u}{a \sin \alpha} u_\lambda - \frac{v}{a} u_\alpha - w u_z - \frac{c_p \theta_a}{a \sin \alpha} \pi'_\lambda - \frac{\cot \alpha}{a} uv + fv$$

$$+ \frac{\nu_H}{a^2} \left[\frac{u_{\lambda\lambda}}{\sin^2 \alpha} + \frac{1}{\sin \alpha} \left(\sin \alpha\, u_\alpha \right)_\alpha + \frac{2 w_\lambda}{\sin \alpha} + \frac{2 \cos \alpha}{\sin^2 \alpha} v_\lambda - \frac{u}{\sin^2 \alpha} \right] + \nu_V u_{zz} \qquad (A.2.1)$$

the meridional momentum equation is

$$\frac{\partial v}{\partial t} = - \frac{u}{a \sin \alpha} v_\lambda - \frac{v}{a} v_\alpha - w v_z - \frac{C_p \theta_a}{a} \pi'_\alpha + \frac{\cot \alpha}{a} u^2 - f u$$

$$+ \frac{V_H}{a^2} \left[\frac{v_{\lambda\lambda}}{\sin^2 \alpha} + \frac{(v_\alpha \sin \alpha)_\alpha}{\sin \alpha} + 2 w_\alpha - \frac{v}{\sin^2 \alpha} - \frac{2 \cos \alpha}{\sin^2 \alpha} u_\lambda \right] + V_v v_{zz} \qquad \text{(A.2.2)}$$

the hydrostatic equation is

$$0 = - C_p \theta_a \pi'_z + g \frac{\theta'}{\theta_a} \qquad \text{(A.2.3)}$$

the thermal equation is

$$\frac{\partial \theta'}{\partial t} = - \frac{u}{a \sin \alpha} \theta'_\lambda - \frac{v}{a} \theta'_\alpha - w \theta'_z + \frac{K_H}{a^2} \left[\frac{\theta'_{\lambda\lambda}}{\sin^2 \alpha} + \frac{(\theta'_\alpha \sin \alpha)_\alpha}{\sin \alpha} \right]$$

$$+ K_v \theta'_{zz} + \frac{q_v}{C_p \pi_a \rho_a} \qquad \text{(A.2.4)}$$

and the continuity equation is

$$\frac{u_\lambda}{a \sin \alpha} + \frac{(v \sin \alpha)_\alpha}{a \sin \alpha} + \frac{(w \rho_a)_z}{\rho_a} = 0 \qquad \text{(A.2.5)}$$

(b)   Expansion in a finite Fourier series

The variables u, v, w, θ', π', and q_v are now expanded as follows:

$$f(\lambda, \alpha, z, t) = f_0(\alpha, z, t) + f_c(\alpha, z, t) \cos \lambda + f_s(\alpha, z, t) \sin \lambda \qquad \text{(A.2.6)}$$

We introduce (A.2.6) into equations (A.2.1) to (A.2.5)
and, by integrating them with respect to λ between 0 and 2π,
obtain the zonally-averaged mean field equations. Similarly, equations for f_c and f_s are obtained by multiplying (A.2.1) to (A.2.5)
by $\cos\lambda$ and $\sin\lambda$ and integrating between 0 and 2π.

The following equations for the mean fields and the Fourier components are obtained:

The three zonal momentum equations:

$$\frac{\partial u_0}{\partial t} = -\frac{v_0}{a} u_{0\alpha} - w_0 u_{0z} - \frac{v_c u_{c\alpha} + v_s u_{s\alpha}}{2a} - \frac{w_c u_{cz} + w_s u_{sz}}{2}$$

$$- \frac{\cot\alpha}{a}\left[u_0 v_0 + \frac{u_c v_c + u_s v_s}{2}\right] + f v_0 + \frac{\nu_H}{a^2}\left[\frac{(u_{0\alpha}\sin\alpha)_\alpha}{\sin\alpha} - \frac{u_0}{\sin^2\alpha}\right] + \nu_V u_{0zz}$$

(o)

$$\frac{\partial u_c}{\partial t} = -\frac{u_0 u_s}{a\sin\alpha} - \frac{v_0}{a} u_{c\alpha} - \frac{v_c}{a} u_{0\alpha} - w_0 u_{cz} - w_c u_{0z} - \frac{C_p \theta_a}{a\sin\alpha}\pi'_s$$

$$- \frac{\cot\alpha}{a}\left[u_0 v_c + u_c v_0\right] + f v_c + \frac{\nu_H}{a^2}\left[\frac{(u_{c\alpha}\sin\alpha)_\alpha}{\sin\alpha} - \frac{2u_c}{\sin^2\alpha} + \frac{2\cos\alpha}{\sin^2\alpha} v_s\right] + \nu_V u_{czz}$$

(c)

(A.2.7)

$$\frac{\partial u_s}{\partial t} = \frac{u_0 u_c}{a\sin\alpha} - \frac{v_0}{a} u_{s\alpha} - \frac{v_s}{a} u_{0\alpha} - w_0 u_{0z} - w_s u_{0z} + \frac{C_p \theta_a}{a\sin\alpha}\pi'_c$$

$$- \frac{\cot\alpha}{a}\left[u_0 v_s + u_s v_0\right] + f v_s + \frac{\nu_H}{a^2}\left[\frac{(u_{s\alpha}\sin\alpha)_\alpha}{\sin\alpha} - \frac{2u_s}{\sin^2\alpha} - \frac{2\cos\alpha}{\sin^2\alpha} v_c\right] + \nu_V u_{szz}$$

(s)

The meridional equations of motion are:

$$\frac{\partial v_0}{\partial t} = \frac{(-u_c v_s + u_s v_c)}{2a\sin\alpha} - \frac{v_0}{a} v_{0\alpha} - w_0 v_{0z} - \frac{v_c v_{c\alpha} + v_s v_{s\alpha}}{2a} - \frac{w_c v_{cz} + w_s v_{sz}}{2}$$

$$- \frac{C_p\theta_a}{a}\pi'_{0\alpha} + \frac{\cot\alpha}{a}\left[u_0^2 + \frac{u_c^2 + u_s^2}{2}\right] - f u_0 + \frac{\nu_H}{a^2}\left[\frac{(v_{0\alpha}\sin\alpha)_\alpha}{\sin\alpha} - \frac{v_0}{\sin^2\alpha}\right] + \nu_V v_{0zz}$$

(o)

$$\frac{\partial v_c}{\partial t} = -\frac{u_o v_s}{a \sin \alpha} - \frac{v_o}{a} v_{c_\alpha} - \frac{v_c}{a} v_{o_\alpha} - w_o v_{c_z} - w_c v_{o_z} - \frac{c_p \theta_a \pi'_{c_\alpha}}{a} + \frac{\cot \alpha}{a} 2 u_o u_c$$

$$- f u_c + \frac{\nu_H}{a^2} \left[\frac{(v_{c_\alpha} \sin \alpha)_\alpha}{\sin \alpha} - \frac{2 v_c}{\sin^2 \alpha} - \frac{2 \cos \alpha}{\sin^2 \alpha} u_s \right] + \nu_v v_{c_{zz}} \qquad (c) \qquad (A.2.8)$$

$$\frac{\partial v_s}{\partial t} = \frac{u_o v_c}{a \sin \alpha} - \frac{v_o}{a} v_{s_\alpha} - v_s v_{o_\alpha} - w_o v_{s_z} - w_s v_{o_z} - \frac{c_p \theta_a \pi'_{s_\alpha}}{a} + \frac{\cot \alpha}{a} 2 u_o u_s$$

$$- f u_s + \frac{\nu_H}{a^2} \left[\frac{(v_{o_\alpha} \sin \alpha)_\alpha}{\sin \alpha} - \frac{2 v_s}{\sin^2 \alpha} + \frac{2 \cos \alpha}{\sin^2 \alpha} u_c \right] + \nu_v v_{s_{zz}} \qquad (s)$$

In these equations the w-terms in the expressions for the horizontal viscosity are neglected. The hydrostatic equation components are:

$$0 = -c_p \theta_a \pi'_{o_z} + g \frac{\theta'_o}{\theta_a} \qquad (o)$$

$$0 = -c_p \theta_a \pi'_{c_z} + g \frac{\theta'_c}{\theta_a} \qquad (c) \qquad (A.2.9)$$

$$0 = -c_p \theta_a \pi'_{s_z} + g \frac{\theta'_s}{\theta_a} \qquad (s)$$

The thermal equation components are:

$$\frac{\partial \theta'_o}{\partial t} = \frac{-u_c \theta'_s + u_s \theta'_c}{2 a \sin \alpha} - \frac{v_o}{a} \theta'_{o_\alpha} - w_o \theta'_{o_z} - \frac{v_c \theta'_{c_\alpha} + v_s \theta'_{s_\alpha}}{2a} - \frac{w_c \theta'_{c_z} + w_s \theta'_{s_z}}{2}$$

$$+ \frac{K_H}{a^2} \left[\frac{(\theta'_{o_\alpha} \sin \alpha)_\alpha}{\sin \alpha} \right] + K_v \theta'_{o_{zz}} + \frac{q v_o}{c_p \pi_a \rho_a} \qquad (o)$$

$$\frac{\partial \theta'_c}{\partial t} = -\frac{u_o \theta'_s}{a \sin \alpha} - \frac{v_o}{a} \theta'_{c_\alpha} - \frac{v_c}{a} \theta'_{o_\alpha} - w_o \theta'_{c_z} - w_c \theta'_{o_z}$$

$$+ \frac{K_H}{a^2} \left[\frac{(\sin \alpha\, \theta'_{c_\alpha})_\alpha}{\sin \alpha} - \frac{\theta'_c}{\sin^2 \alpha} \right] + K_v \theta'_{c_{zz}} + \frac{q v_c}{c_p \pi_a \rho_a} \qquad (c) \qquad (A.2.10)$$

$$\frac{\partial \theta'_s}{\partial t} = \frac{u_o \theta'_c}{a \sin \alpha} - \frac{v_o}{a} \theta'_{s\alpha} - \frac{v_s}{a} \theta'_{o\alpha} - w_o \theta'_{s_z} - w_s \theta'_{o_z}$$

$$+ \frac{k_H}{a^2} \left[\frac{(\theta'_{s\alpha} \sin \alpha)_\alpha}{\sin \alpha} - \frac{\theta'_s}{\sin^2 \alpha} \right] + k_V \theta'_{s_{zz}} + \frac{q_{V_s}}{C_p \pi_a \rho_a} \qquad \text{(s)}$$

and the continuity equation

$$\frac{(v_o \sin \alpha)_\alpha}{a \sin \alpha} + \frac{(w_o \rho_a)_z}{\rho_a} = 0 \qquad \text{(o)}$$

$$\frac{u_s}{a \sin \alpha} + \frac{(v_c \sin \alpha)_\alpha}{a \sin \alpha} + \frac{(w_c \rho_a)_z}{\rho_a} = 0 \qquad \text{(c)} \qquad \text{(A.2.11)}$$

$$-\frac{u_c}{a \sin \alpha} + \frac{(v_s \sin \alpha)_\alpha}{a \sin \alpha} + \frac{(w_s \rho_a)_z}{\rho_a} = 0 \qquad \text{(s)}$$

Equations (A.2.7), (A.2.8) and (A.2.11) can be solved numerically by a finite difference method; it may be useful to use stretched coordinates, especially near the top of the atmosphere.

At each time step after advancing u, v and θ , the new value of π' can be obtained in the following way:

We define

$$\bar{\rho}_a = \frac{1}{H} \int_0^H \rho_a \, dz \qquad \text{(A.2.12)}$$

and

$$\bar{\pi}'(\alpha) = \frac{1}{\bar{\rho}_a H} \int_0^H \pi'(\alpha, z) \rho_a \, dz \qquad \text{(A.2.13)}$$

From the continuity equation (A.2.11o) and the boundary condition $W_o = 0$ at $z = 0, H$, we have

$$\frac{\partial}{\partial \alpha}\left[\sin\alpha \int_0^H v_o \rho_a \, dz \right] = 0$$

and since $v_o \sin\alpha = 0$ at the pole

$$\int_0^H v_o \rho_a \, dz = \frac{\partial}{\partial t}\int_0^H v_o \rho_a \, dz = 0$$

Then we can integrate equation (A.2.8.o) from top to bottom and obtain

$$\frac{C_p \theta_a}{a}\frac{\partial \overline{\pi}_o'}{\partial \alpha} = \frac{1}{H\overline{\rho}_a}\int_0^H \left(\frac{\partial v_o}{\partial t} + \frac{C_p \theta_a}{a}\frac{\partial \pi_o'}{\partial \alpha} \right) \rho_a \, dz \qquad \text{(A.2.14o)}$$

where the parenthsis in integral is a shorthand that stands for the right hand side of equation (A.2.8.o) without the pressure term.

Similarly from the continuity equation (A.2.11c) and the boundary conditions $W_c = 0$ at $z = 0, H$, we get

$$\int_0^H \left(u_s + \frac{\partial(v_c \sin\alpha)}{\partial \alpha} \right) \rho_a \, dz = 0$$

We can combine equations (A.2.7s) and (A.2.8c) to obtain

$$\frac{C_p \theta_a}{a}\left[\frac{\partial}{\partial \alpha}\left(\sin\alpha \frac{\partial \overline{\pi}_c'}{\partial \alpha} \right) - \frac{\overline{\pi}_c'}{\sin\alpha} \right] =$$

$$= \frac{1}{\overline{\rho}_a H}\int_0^H \left\{ \frac{\partial}{\partial \alpha}\left[\left(\frac{\partial v_c}{\partial t} + \frac{C_p \theta_a}{a}\frac{\partial \pi_c'}{\partial \alpha} \right)\sin\alpha \right] + \left(\frac{\partial u_s}{\partial t} - \frac{C_p \theta_a}{a}\frac{\pi_c'}{\sin\alpha} \right) \right\} \rho_a \, dz \qquad \text{(A.2.14c)}$$

which is an elliptical equation that can be solved for $\overline{\pi}'_c$. Again

the two parentheses in the integral of (A.2.14c) stand for the right

hand side of equations (A.2.7s) and (A.2.8c) without the pressure

terms.

Similarly, from equation (A.2.11s) we get

$$\int_0^H \left[-u_c + (v_s \sin \alpha)_\alpha \right] \rho_a \, dz = 0$$

and from equations (A.2.7c) and (A.2.8s)

$$\frac{C_p \theta_a}{a} \left[\frac{\partial}{\partial \alpha} \left(\sin \alpha \frac{\partial \overline{\pi}'_s}{\partial \alpha} \right) - \frac{\overline{\pi}'_s}{\sin \alpha} \right] =$$

$$= \frac{1}{\rho_a H} \int_0^H \left\{ \frac{\partial}{\partial \alpha} \left[\left(\frac{\partial v_s}{\partial t} + \frac{C_p \theta_a}{a} \frac{\partial \pi'_s}{\partial \alpha} \right) \sin \alpha \right] - \left(\frac{\partial u_c}{\partial t} + \frac{C_p \theta_a}{a} \frac{\pi'_s}{\sin \alpha} \right) \right\} \rho_a \, dz \qquad \text{(A.2.14s)}$$

The functions $\overline{\pi}'_o$, $\overline{\pi}'_c$, and $\overline{\pi}'_s$ are obtained

from equations (A.2.14). From the hydrostatic equations (A.2.9)

$$\pi'(\alpha, z) = \pi'(\alpha, H) + \pi'^u(\alpha, z) \qquad \text{(A.2.15)}$$

where $\pi'^u(\alpha, z)$, the "uncorrected π' " is defined as

$$\pi'^u(\alpha, z) = -\frac{g}{C_p \theta_a} \int_z^H \frac{\theta'(\alpha, z)}{\theta_a} \, dz \qquad \text{(A.2.16)}$$

Then integrating (A.2.15) multiplied by ρ_a between z = 0 and z = H,

we get

$$\pi'(\alpha, H) = \overline{\pi}'(\alpha) - \frac{1}{\overline{\rho}_a H} \int_0^H \pi'^u(\alpha, z) \rho_a dz \qquad (A.2.17)$$

and replacing in (A.2.15)

$$\pi'(\alpha, z) = \overline{\pi}'(\alpha) - \frac{1}{\overline{\rho}_a H} \int_0^H \pi'^u(\alpha, z) \rho_a dz + \pi'^u(\alpha, z) \qquad (A.2.18)$$

Computations were begun with an earlier version of the model described here, but had to be stopped because of numerical instabilities. It is thought that these instabilities can be avoided by the use of the finite-differences scheme (2.5.b) and the conservative method described in Section (5.6). I plan to go on working on this model in the future.

APPENDIX B

On the Use of Nonuniform Grids in Finite-difference Equations

Finite-difference schemes that use grids with uniform spacing are the simplest and most accurate, but they are not satisfactory in problems with boundary layers. If the number of points is not large enough to resolve the boundary layer (at least two or three points within it) then the numerical solution is apt to have gross errors even in the interior. The use of enough grid points to resolve the boundary layer then makes the total computation time unacceptably large. The problem can be solved by the introduction of an irregular net with smaller spacing near the boundary.

One possibility is to divide the grid intervals by two or more within the region of interest. This method has two disadvantages: first, it is necessary to interpolate values of the variables or their derivatives at intermediate points and weak numerical instabilities usually arise at the boundary between the large and small grid size, and second, this method cannot give really small grid intervals without greatly increasing the number of intermediate interpolations. Crowder and Dalton (1971) have shown that, in a boundary layer problem, the use of grids with discontinuously varying resolution gives worse overall errors than a regular grid with the same number of points. Another possibility is to vary the grid intervals continuously, avoiding the necessity of intermediate interpolations. Consider, for example, a function $f(x)$ defined on a non-uniform grid (Figure B.1).

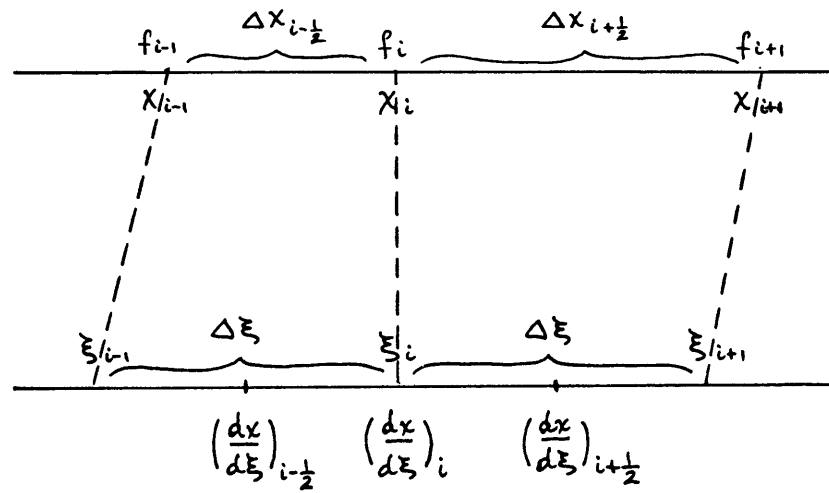Making a Taylor expansion about the center point x_i ,

Figure B.1: Non-uniform grid defined through the use of a stretched coordinate.

there are two "centered" combinations of the function at three

points that give an approximation of the first derivative f'_i :

$$\frac{f_{i+1}-f_{i-1}}{\Delta X_{i+\frac{1}{2}}+\Delta X_{i-\frac{1}{2}}} = f'_i + \frac{(\Delta X_{i+\frac{1}{2}}-\Delta X_{i-\frac{1}{2}})}{2}f''_i + \frac{\Delta X^2_{i+\frac{1}{2}}-\Delta X_{i+\frac{1}{2}}+\Delta X_{i-\frac{1}{2}}+\Delta X^2_{i-\frac{1}{2}}}{6}f'''_i + \cdots \quad (B.1)$$

which has first order errors, and

$$\frac{\Delta X_{i-\frac{1}{2}}}{(\Delta X_{i+\frac{1}{2}}+\Delta X_{i-\frac{1}{2}})\Delta X_{i+\frac{1}{2}}}f_{i+1} - \frac{\Delta X_{i+\frac{1}{2}}}{(\Delta X_{i+\frac{1}{2}}+\Delta X_{i-\frac{1}{2}})\Delta X_{i-\frac{1}{2}}}f_{i-1} - \frac{\Delta X_{i+\frac{1}{2}}-\Delta X_{i-\frac{1}{2}}}{\Delta X_{i+\frac{1}{2}}\Delta X_{i-\frac{1}{2}}}f_i = f'_i + \frac{\Delta X_{i+\frac{1}{2}}\Delta X_{i-\frac{1}{2}}}{6}f'''_i + \cdots \quad (B.2)$$

which has second-order errors. If $\Delta X_{i+\frac{1}{2}}=\Delta X_{i-\frac{1}{2}}$, both (B.1) and

(B.2) reduce to the usual centered-difference scheme. However, there

is only one combination of the three points that gives an approxi-

mation of the second derivative f''_i ,

$$\frac{f_{i+1}-f_i}{\Delta X_{i+\frac{1}{2}}\frac{(\Delta X_{i+\frac{1}{2}}+\Delta X_{i-\frac{1}{2}})}{2}} - \frac{f_i-f_{i-1}}{\Delta X_{i-\frac{1}{2}}\frac{(\Delta X_{i+\frac{1}{2}}+\Delta X_{i-\frac{1}{2}})}{2}} = f''_i + \frac{\Delta X_{i+\frac{1}{2}}-\Delta X_{i-\frac{1}{2}}}{3}f'''_i + \frac{\Delta X^2_{i+\frac{1}{2}}-\Delta X_{i+\frac{1}{2}}+\Delta X_{i-\frac{1}{2}}+\Delta X^2_{i-\frac{1}{2}}}{12}f^{IV}_i + \cdots$$
$$(B.3)$$

which has first order errors. Note that the second term of the right

hand side of equations (B.1) and (B.3) is the "extra error" intro-

duced by the use of a non-uniform grid, while the following terms

are equivalent to the second order errors that are made when constant

spacing is used.

Sundqvist and Veronis (1970) reduced the "extra error" in

equation (B.3) to second order by choosing the intervals such that

$$\Delta X_{i+\frac{1}{2}} - \Delta X_{i-\frac{1}{2}} = O\left(\Delta X_{i-\frac{1}{2}}\right)^2 \quad (B.4)$$

but they still use (B.2) instead of (B.1). This method allows some

improvement of the resolution near the boundary but it still requires a large number of points to significantly reduce the grid intervals there.

Suppose now that we vary the grid intervals by defining a stretched coordinate ξ ,

$$x = x(\xi) \tag{B.5}$$

in such a way that the grid intervals $\Delta\xi$ are constant. If we are studying a function defined in a region $0 \leq x \leq 1$ with a boundary layer at x = 0, then $x(\xi)$ should have the following properties:

(a) $\frac{dx}{d\xi}$ should be finite over the whole interval. If $\frac{dx}{d\xi}$ becomes infinite at some point then the mapping $x = x(\xi)$ will give a poor resolution near that point, which cannot be improved by increasing the number of points, since $\Delta x \simeq \frac{dx}{d\xi}\Delta\xi$.

(b) $\frac{dx}{d\xi} = 0$ at $x = 0$. This will insure a high resolution near x = 0.

Making a Taylor series expansion of x about x_i we find

$$\Delta x_{i+\frac{1}{2}} = x_{i+1} - x_i = \Delta\xi\left(\frac{dx}{d\xi}\right)_i + \frac{(\Delta\xi)^2}{2}\left(\frac{d^2x}{d\xi^2}\right)_i + \frac{(\Delta\xi)^3}{6}\left(\frac{d^3x}{d\xi^3}\right)_i + \frac{(\Delta\xi)^4}{24}\left(\frac{d^4x}{d\xi^4}\right)_i + \cdots$$

$$= \Delta\xi\left(\frac{dx}{d\xi}\right)_{i+\frac{1}{2}} + \frac{(\Delta\xi)^3}{24}\left(\frac{d^3x}{d\xi^3}\right)_i + \frac{(\Delta\xi)^4}{48}\left(\frac{d^4x}{d\xi^4}\right)_i + \cdots \tag{B.6}$$

$$\Delta x_{i-\frac{1}{2}} = x_i - x_{i-1} = \Delta\xi\left(\frac{dx}{d\xi}\right)_i - \frac{(\Delta\xi)^2}{2}\left(\frac{d^2x}{d\xi^2}\right)_i + \frac{(\Delta\xi)^3}{6}\left(\frac{d^3x}{d\xi^3}\right)_i - \frac{(\Delta\xi)^4}{24}\left(\frac{d^4x}{d\xi^4}\right)_i + \cdots$$

$$= \Delta\xi\left(\frac{dx}{d\xi}\right)_{i-\frac{1}{2}} + \frac{(\Delta\xi)^3}{24}\left(\frac{d^3x}{d\xi^3}\right)_i - \frac{(\Delta\xi)^4}{48}\left(\frac{d^4x}{d\xi^4}\right)_i + \cdots \tag{B.7}$$

since

$$\left(\frac{dx}{d\xi}\right)_{i+\frac{1}{2}} = \left(\frac{dx}{d\xi}\right)_i + \left(\frac{d^2x}{d\xi^2}\right)_i \frac{\Delta\xi}{2} + \left(\frac{d^3x}{d\xi^3}\right)_i \frac{(\Delta\xi)^2}{8} + \left(\frac{d^4x}{d\xi^4}\right)_i \frac{(\Delta\xi)^3}{48} + \cdots$$

$$\left(\frac{dx}{d\xi}\right)_{i-\frac{1}{2}} = \left(\frac{dx}{d\xi}\right)_i - \left(\frac{d^2x}{d\xi^2}\right)_i \frac{\Delta\xi}{2} + \left(\frac{d^3x}{d\xi^3}\right)_i \frac{(\Delta\xi)^2}{8} - \left(\frac{d^4x}{d\xi^4}\right)_i \frac{(\Delta\xi)^3}{48} + \cdots$$

Therefore

$$\Delta X_{i+\frac{1}{2}} + \Delta X_{i-\frac{1}{2}} = \Delta\xi \left[2\left(\frac{dx}{d\xi}\right)_i + \frac{(\Delta\xi)^2}{3}\left(\frac{d^3x}{d\xi^3}\right)_i + \cdots \right] \tag{B.8}$$

$$\Delta X_{i+\frac{1}{2}} - \Delta X_{i-\frac{1}{2}} = (\Delta\xi)^2 \left[\left(\frac{d^2x}{d\xi^2}\right)_i + \frac{(\Delta\xi)^2}{12}\left(\frac{d^4x}{d\xi^4}\right)_i + \cdots \right] \tag{B.9}$$

Introducing (B.6) to (B.9) into (B.1) and (B.3) we get

$$\frac{f_{i+1} - f_{i-1}}{2\Delta\xi \left(\frac{dx}{d\xi}\right)_i} = f'_i \left[1 + \frac{(\Delta\xi)^2}{6}\left(\frac{d^3x}{d\xi^3}\right)_i \Big/ \left(\frac{dx}{d\xi}\right)_i \right]$$

$$+ f''_i \frac{(\Delta\xi)^2}{2}\left[\left(\frac{d^2x}{d\xi^2}\right)_i + \frac{(\Delta\xi)^2}{6}\left(\frac{1}{4}\left(\frac{d^4x}{d\xi^4}\right)_i + \left(\frac{d^3x}{d\xi^3}\right)_i \Big/ \left(\frac{dx}{d\xi}\right)_i \right) \right] \tag{B.10}$$

$$+ f'''_i \frac{(\Delta\xi)^2}{6}\left[\left(\frac{dx}{d\xi}\right)_i^2 + \frac{(\Delta\xi)^2}{2}\left(\left(\frac{d^3x}{d\xi^3}\right)_i\left(\frac{dx}{d\xi}\right)_i + \frac{3}{2}\left(\frac{d^2x}{d\xi^2}\right)_i^2 \right) \right] + O(\Delta\xi^5)$$

and

$$\frac{\dfrac{f_{i+1}-f_i}{\left(\frac{dx}{d\xi}\right)_{i+\frac{1}{2}}} - \dfrac{f_i-f_{i-1}}{\left(\frac{dx}{d\xi}\right)_{i-\frac{1}{2}}}}{\Delta\xi^2 \left(\frac{dx}{d\xi}\right)_i} = f_i'' \left[1 + \frac{5}{24}\Delta\xi^2 \left(\frac{d^3x}{d\xi^3}\right)_i \Big/ \left(\frac{dx}{d\xi}\right)_i\right]$$

$$+ f_i''' \frac{\Delta\xi^2}{3}\left[\left(\frac{d^2x}{d\xi^2}\right)_i + \frac{\Delta\xi^2}{12}\left(\left(\frac{d^4x}{d\xi^4}\right)_i + \frac{5}{2}\left(\frac{d^3x}{d\xi^3}\right)_i \left(\frac{dx}{d\xi}\right)_i\right)\right]$$

$$+ f_i^{IV} \frac{\Delta\xi^3}{12}\left[\left(\frac{dx}{d\xi}\right)_i^2 + \frac{\Delta\xi^2}{4}\left(\frac{13}{6}\left(\frac{d^3x}{d\xi^3}\right)_i \left(\frac{dx}{d\xi}\right)_i + 3\left(\frac{d^2x}{d\xi^2}\right)_i^2\right)\right]$$

$$+ O(\Delta\xi^3) \tag{B.11}$$

Equations (B.10) and (B.11) show that <u>any smooth function</u> <u>$x(\xi)$</u> that satisfies conditions (a) and (b) will give an approximation of the first and second derivatives with second order accuracy, since the "extra truncation errors" due to the nonuniformity of the grid <u>are of second order in</u> $\Delta\xi$. This useful result is due to the fact that although the truncation errors near the boundary may be of first order with respect to the intervals Δx_i, they are very small, so that the overall truncation error remains small.

The form of equations (B.10) and (B.11) suggests the convenience of choosing a function $x = P_n(\xi)$ where P_n is a polynomial of degree greater than one, and in particular the advantage of the choice of the simple function (see Figure 2.4.1)

$$x = \xi^2 \tag{B.12}$$

which has the following attractive properties:

(i) $\quad \max\limits_{0 \leq x \leq 1} \dfrac{dx}{d\xi} = 2 \quad at \quad x = 1$ 　　　　(B.13)

This implies that near x = 1, $\Delta x \simeq \dfrac{2}{N}$, where N is the number of

intervals $N = \dfrac{1}{\Delta \xi}$. This shows that at worst the stretched coor-

dinate gives half the resolution of the uniform grid, which is not

bad at all.

(ii) The first interior point at the boundary $x = 0$ will be such

that

$$\Delta x_1 = (\Delta \xi)^2 = \dfrac{1}{N^2}$$ 　　　　(B.14)

Then the resolution near the boundary layer increases with N^2 and

not with N as the uniform grid

(iii) $\quad \dfrac{d^2 x}{d\xi^2} = 2 \quad ; \quad \dfrac{d^3 x}{d\xi^3} = 0 \quad ; \quad \cdots$ 　　　　(B.15)

Equations (B.10) and (B.11) reduce to

$$\dfrac{f_{i+1} - f_{i-1}}{2\Delta \xi \left(\frac{dx}{d\xi}\right)_i} = f'_i + f''_i (\Delta \xi)^2 + f'''_i \dfrac{2}{3} (\Delta \xi)^2 \xi^2 + O(\Delta \xi)^3$$ 　　　　(B.16)

$$\dfrac{\dfrac{f_{i+1} - f_i}{\left(\frac{dx}{d\xi}\right)_{i+\frac{1}{2}}} - \dfrac{f_i - f_{i-1}}{\left(\frac{dx}{d\xi}\right)_{i-\frac{1}{2}}}}{(\Delta \xi)^2 \left(\frac{dx}{d\xi}\right)_i} = f''_i + f'''_i \dfrac{2}{3} (\Delta \xi)^2 + f^{IV}_i \dfrac{(\Delta \xi)^2}{3} \xi^2 + O(\Delta \xi)^3$$ 　　　　(B.17)

and we see that the "extra truncation error" <u>is independent of x</u>

(except for the variations of the derivatives of f).

When a boundary layer is expected both at x = 0 and at

x = 1, a convenient stretched coordinate is defined by the symmetric

function

$$\chi = \sin^2\left(\frac{\pi}{2}\xi\right) \tag{B.18}$$

with

$$\frac{d\chi}{d\xi} = \pi\sqrt{\chi(1-\chi)} \tag{B.19}$$

It behaves like $\chi = \left(\frac{\pi}{2}\xi\right)^2$ near x = 0, like $\chi = \left\{1-\left[\frac{\pi}{2}(1-\xi)\right]^2\right\}$ near x = 1, and

is rather linear in the interior (see Figure 2.4.2). At the bound-

aries, the first interior point is at a distance

$$\Delta\chi \simeq \frac{\pi^2}{4N^2} \tag{B.20}$$

and at the center point, x = 0.5,

$$\Delta\chi \simeq \frac{\pi}{2N}$$

Both types of stretched coordinates have been successfully

used in two-dimensional numerical models of the atmosphere of Venus.

Finally we compare our results with those obtained by Sund-

qvist and Veronis (1970), who solved numerically the following dif-

ferential equation proposed by Stommel (1948) for the wind-driven

circulation in a homogeneous ocean:

$$\varepsilon \left(\psi'' - \psi \right) + \psi' = -\sin x \qquad \text{for } \varepsilon = 0.05$$

$$\psi = 0 \quad \text{at} \quad x = 0, \pi \tag{B.21}$$

which has a boundary layer at x = 0. Sundqvist and Veronis set

$$\Delta X_{i+\frac{1}{2}} - \Delta X_{i-\frac{1}{2}} = \frac{\alpha}{\pi} \left(\Delta X_{i-\frac{1}{2}} \right)^2 , \qquad \alpha = 2 \tag{B.22}$$

The exact solution of (B.21) is also included in their paper.

Figure (B.2) compares the percentage errors introduced by the Sundqvist-Veronis method with those introduced by using the stretched coordinate $X = \xi^2$. Note that not only are the latter smaller, but that there is no tendency for the relative errors to grow as $X \to 0$, even though the function itself tends to zero.

If we compare (B.22) with (B.9) and (B.7) we see that the choice (B.22) corresponds approximately to the use of a stretched coordinate defined by the differential equation

$$\frac{d^2 x}{d\xi^2} = \frac{\alpha}{\pi} \left(\frac{dx}{d\xi} \right)^2 \tag{B.23}$$

which has the solution

$$\xi = e^{-\frac{\alpha}{\pi} x} \tag{B.24}$$

Then the grid spacing is given by

$$\Delta x \approx \frac{\pi}{\alpha} \frac{(1 - e^{-\alpha})}{N} \qquad \text{near } x = 0 \tag{B.25}$$
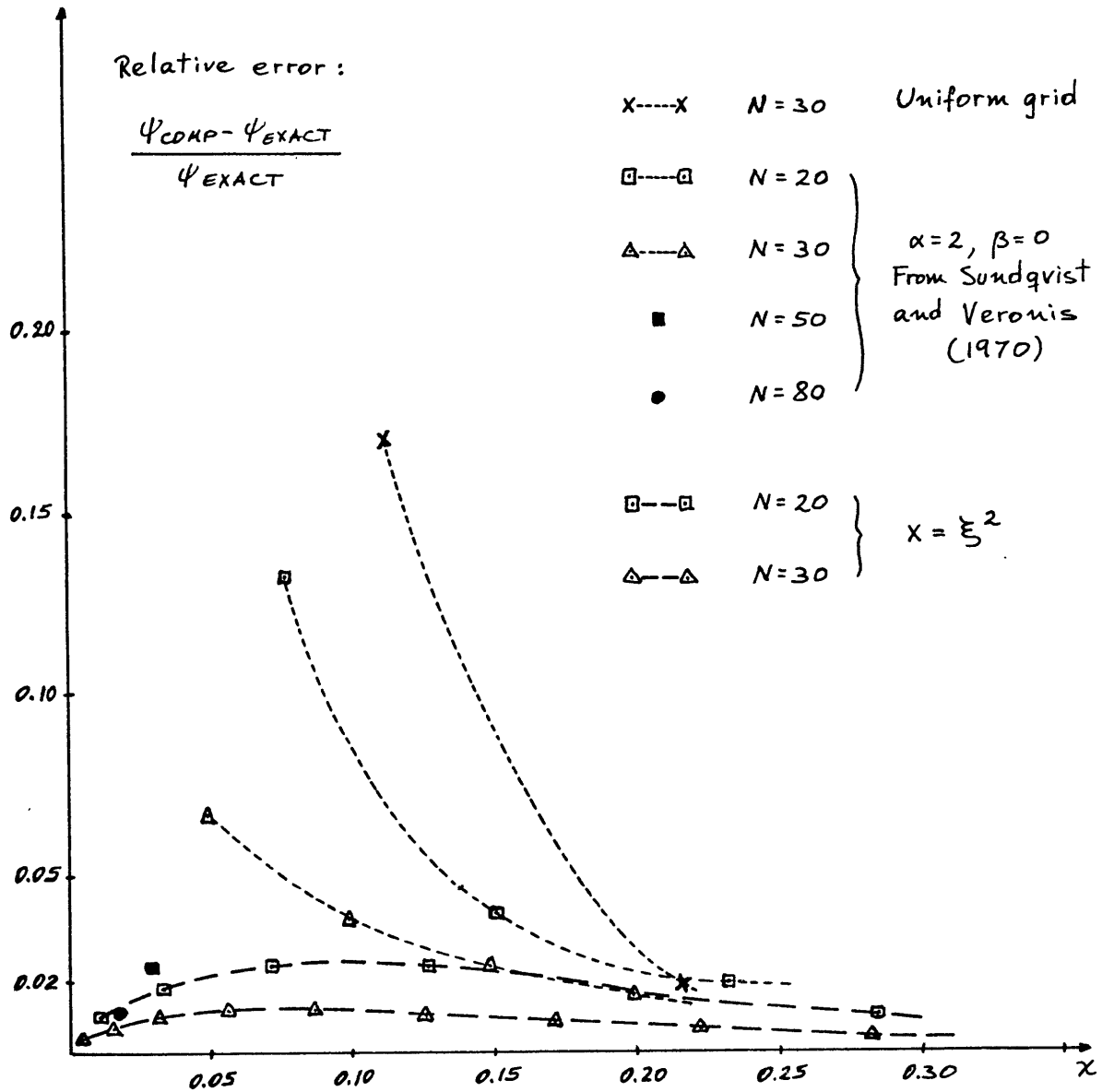
Figure B.2: Comparison of the results obtained by Sundqvist and
Veronis and by using the stretched coordinate $x = \xi^2$.

and

$$\Delta x \approx \frac{\pi}{\alpha} \frac{(1-e^{-\alpha})}{e^{-\alpha}} \qquad near \quad x = \pi \qquad\qquad (B.26)$$

This is obviously not a good choice of $x(\xi)$ because as Sundqvist and Veronis pointed out, to obtain a good resolution near the origin , α should be large, and that would spoil the computations near $x = \pi$.

Beardsley (1971) used the stretched coordinate $x = \sqrt{\xi}$ to solve a problem with a boundary layer near x = 1. Since $\frac{dx}{d\xi}$, $\frac{d^2x}{d\xi^2}$, ... $\rightarrow \infty$ as $x \rightarrow 0$, an inspection of equations (B.10) and (B.11) shows clearly why the truncation errors that he obtained were very large near x = 0. Near x = 1 this stretched coordinate gives $\Delta x \approx \frac{1}{2N}$, so that it only increases by 2 the resolution of a regular grid!

Another advantage of the method proposed here is that the actual spacing of the grid points is obtained immediately, once N is given,whereas the method proposed by Sundqvist and Veronis requires the solution of a rather cumbersome equation for Δx_i .

APPENDIX C

Estimation of the Magnitude of π' at the Top

in the Non-rotating Quasi-Boussinesq Model

From the meridional momentum equation (3.2.7) and from the
numerical values of the terms in the vorticity equation near the top
of the atmosphere, we see that in the region where π' at the top
may be largest, near the antisolar point,

$$\frac{c_p \theta_a}{a} \frac{\partial \pi'}{\partial \alpha} \lesssim \frac{v}{a} \frac{\partial v}{\partial \alpha}$$

Hence the magnitude of π' at the top will be

$$[\pi'_{TOP}] \lesssim \frac{[v]^2}{c_p \theta_a} = \frac{[v]^2}{g D}$$

We take the worst value of v

$$[v] \simeq 3 \times 10^3 \ cm/sec$$
$$g = 0.85 \times 10^3 \ cm/sec$$
$$D = 7.3 \times 10^6 \ cm$$
$$\therefore \ [\pi'_{TOP}] \lesssim 1.4 \times 10^{-3}$$

At the top

$$T_{TOP} = T_{a_{TOP}} + \pi_{a_{TOP}} \theta'_{TOP} + \theta_a \pi'_{TOP}$$

where

$$\pi_{a_{TOP}} = 0.274$$
$$\theta_a = 730 \ °K$$
$$[\theta'_{TOP}] \simeq 20 \ °K$$

Then

$$[\pi_{a_{TOP}} \, \theta'_{TOP}] \simeq 5.5 \, °K$$

and

$$[\pi'_{TOP} \, \theta_a] \lesssim 1.1 \, °K$$

Therefore in the computation of the temperatures, π'_{TOP} can be assumed to be zero without producing significant errors.

J	Z	S	HEIGHT	PI	P*10**-6	T	TAUS	TAUT	RHO*100	TFLUX*10**-5
1	-0.004	0.0	-0.193	1.003	102.505	0.0	0.0	0.0	0.0	
	0.0	0.095	0.0	1.000	101.300	729.986	55.03?	221.977	7.304	0.401
2	0.004	0.189	0.193	0.997	100.106	0.0	0.0	0.0	7.237	
	0.015	0.376	0.770	0.989	96.606	722.286	52.474	211.660	7.040	0.787
3	0.032	0.557	1.722	0.976	91.039	0.0	0.0	0.0	6.722	
	0.057	0.730	3.035	0.958	83.771	699.632	45.480	183.449	6.302	0.815
4	0.089	0.892	4.691	0.936	75.261	0.0	0.0	0.0	5.799	
	0.126	1.042	6.664	0.909	66.010	663.343	35.801	144.410	5.237	0.840
5	0.168	1.176	8.927	0.878	56.517	0.0	0.0	0.0	4.643	
	0.216	1.293	11.446	0.843	47.233	615.525	25.570	103.139	4.039	0.878
6	0.268	1.391	14.185	0.806	38.533	0.0	0.0	0.0	3.448	
	0.323	1.469	17.103	0.766	30.687	558.959	16.553	66.771	2.889	0.908
7	0.380	1.525	20.158	0.724	23.864	0.0	0.0	0.0	2.377	
	0.440	1.559	23.306	0.681	18.131	496.933	9.712	39.173	1.920	0.947
8	0.500	1.571	26.500	0.637	13.469	0.0	0.0	0.0	1.525	
	0.560	1.559	29.694	0.593	9.797	433.050	5.170	20.854	1.191	1.003
9	0.620	1.525	32.842	0.550	6.990	0.0	0.0	0.0	0.916	
	0.677	1.469	35.897	0.508	4.906	371.023	2.505	10.104	0.696	1.075
10	0.732	1.391	38.815	0.468	3.401	0.0	0.0	0.0	0.524	
	0.784	1.293	41.554	0.431	2.341	314.457	1.107	4.465	0.392	1.163
11	0.832	1.176	44.073	0.396	1.611	0.0	0.0	0.0	0.293	
	0.874	1.042	46.335	0.365	1.119	266.639	0.441	1.780	0.221	1.273
12	0.911	0.892	48.309	0.338	0.793	0.0	0.0	0.0	0.169	
	0.943	0.730	49.965	0.316	0.582	230.350	0.148	0.599	0.133	1.418
13	0.968	0.557	51.278	0.298	0.447	0.0	0.0	0.0	0.108	
	0.985	0.376	52.230	0.285	0.366	207.697	0.031	0.125	0.093	1.542
14	0.996	0.189	52.807	0.277	0.323	0.0	0.0	0.0	0.084	
	1.000	0.095	53.000	0.274	0.309	199.996	0.0	0.0	0.081	1.586
15	1.004	0.0	53.193	0.271	0.296	0.0	0.0	0.0	0.0	
	1.015	0.0	53.770	0.0	0.0	0.0	0.0	0.0	0.0	0.0

APPENDIX D

VERTICAL STRUCTURE OF THE

ADIABATICALLY STRATIFIED ATMOSPHERE

REFERENCES

Arakawa, A., 1966: Computational design for long term numerical integration of the equations of fluid motion. Two-dimensional incompressible flow: Part I. J. Comp. Phys. 1, 119-143.

Avduevsky, V.S., M. Ya. Marov, and M.K. Rozhdestvensky, 1970: A tentative model of the Venus atmosphere based on the measurements of Veneras 5 and 6. J. Atmos. Sci. 27, 561-568.

Avduevsky, V.S., M. Ya. Marov, M.K. Rozhdestvensky, N.F. Borodin, and V.V. Kerzhanovich, 1971: Soft landing of Venera 7 on the Venus surface and preliminary results of our investigations of the Venus atmosphere. J. Atmos. Sci. 28, 263-269.

Barath, F.T. (ed), 1964: Symposium on radar and radiometric observations of Venus during the 1962 conjunction. Astron. J. 69, 1.

Barcilon, V. and G. Veronis, 1965: Thermal convection generated by differential heating along a horizontal surface. M.I.T. unpublished manuscript, 22 pages.

Beardsley, R.C., 1971: Integration of the planetary vorticity equation on a parabolic circular grid. J. Comp. Phys. 7, 273-288.

Bohachevsky, I.O. and I.J. Eberstein, 1971: Calculation of the thermodynamic state of a three-dimensional atmosphere. Bellcomm TM-71.

Bohachevsky, I.O. and Yeh, T.T.J., 1969: General circulation of the atmosphere of Venus driven by polar and diurnal variations of surface temperature. Bellcomm TR-69-103-7-2.

Boyer, Ch. and H. Camichel, 1961: Ann. d'Astrophysique 24, 531.

Boyer, Ch. and R.E. Newell, 1967: Ultraviolet photographs and the radar cross-section of Venus in 1966. Astron. J. 72, 679-681 and 779-780.

Bryan, K., 1966: A scheme for numerical integration of the equations of motion on an irregular grid free from nonlinear instability. Mon. Wea. Rev. 9, 39-40.

Charney, J.G. and Y. Ogura, 1960: A numerical model of thermal convection in the atmosphere. Proceedings of the International Symposium on Numerical Weather Prediction in Tokyo, 1960, the Meteorological Society of Japan, pp 431-451.

Crowder, H.J. and C. Dalton, 1971: Errors in the use of non-uniform mesh systems. J. Comp. Phys. 7, 32-45.

Davey, A., 1967: The motion of a fluid due to a moving source of heat at the boundary. J. Fl. Mech. 29, Part I, 137-150.

Deardorff, J.W., 1971: On the magnitude of the subgrid scale eddy coefficient. J. Comp. Phys. 7, 120-133.

Dollfus, A., 1955: Étude visuelle et Photographique de la Planète Vénus a l'Observatoire de Nice. Compt. Rend. Acad. Sci. III, 587-591.

Dollfus, A., 1968: Synthesis on the ultra-violet survey of clouds in Venus' atmosphere. The Atmospheres of Venus and Mars. J.C. Brandt and M.B. McElroy editors, Gordon and Breach, New York.

Fultz, D., et al, 1959: Studies of thermal convection in a rotating cylinder with some implications for large-scale atmospheric motions. Meteor. Monogr. 4, 36-39.

Gierasch, P.J. and R.M. Goody, 1970: Models of the Venus clouds. J. Atmos. Sci. 27, 224-245.

Gierasch, P.J., 1970: The four-day rotation in the stratosphere of Venus: A study of radiative driving. Icarus 13, 25-33.

Gierasch, P.J., R.M. Goody and P. Stone, 1970: The energy balance of planetary atmospheres. Geoph. Fl. Dynamics 1, 1-18.

Goody, R.M., 1964: Atmospheric Radiation. Oxford University Press, London. 436 pages.

Goody, R.M., 1969: Motions of planetary atmospheres. Annual Review of Astronomy and Astrophysics 7, 303-351.

Goody, R.M. and A.R. Robinson, 1966: A discussion of the deep circulation of the atmosphere of Venus. Astrophys. Journal 146, 339-353.

Hess, S.L., 1968: The hydrodynamics of Mars and Venus. The Atmospheres of Venus and Mars. J.C. Brandt and M.B. McElroy editors, Gordon and Breach, New York.

Hunten, D.M. and R.M. Goody, 1969: Venus: the next phase of planetary exploration. Science 165, 1317-1323.

Leovy, C.B., 1968: Thermal convection in the atmospheric boundary layer. The RAND Corporation, RM5432-1-NSF.

Leovy, C.B. and Y. Mintz, 1969: Numerical simulation of the atmospheric circulation and climate of Mars. J. of Atmos. Sci. 26, 1167-1190.

Lilly, D.K., 1964: Numerical solutions for the shape-preserving two-dimensional thermal convection element. J. Atms. Sci. 21, 83-98.

Lilly, D.K., 1965: On the computational stability of numerical solutions of time-dependent nonlinear geophysical fluid dynamics problems. Mon. Wea. Rev. 93, 11-26.

Lorenz, E.N., 1955: Available potential energy and the maintenance of the general circulation. Tellus 7, 157-167.

Lorenz, E.N., 1960: Maximum simplification of the dynamic equations. Tellus 12, 243-254.

Malkus, W.V.R., 1970: Hadley-Halley circulation on Venus. J. Atm. Sci. 27, 529-535.

Mintz, Y., 1961: Temperature and circulation of the Venus atmosphere. Planet. Sp. Sci. 5, 141-152.

Morrison, D., 1969: Venus: absence of a phase effect at a 2-centimeter wavelength. Science 163, 815-816.

Murray, B.C., R.L. Wildey and J.A. Westphal, 1963: Infrared photometric mapping of Venus through the 8 to 14 micron atmospheric window. J. Geophys. Res. 68, 4813-4818.

Ogura, Y. and N.A. Phillips, 1962: Scale analysis of deep and shallow convection in the atmosphere. J. Atm. Sci. 19, 173-179.

Öpik, E.J., 1961: The aeolosphere and atmosphere of Venus. J. Geophys. Res. 66, 2807-2819.

Orszag, S.A., 1970: Accuracy of numerical simulation of incompressible fluids. NCAR manuscript No. 70-73.

Pearson, C.E., 1965: A computational method for viscous flow problems. J. Fl. Mech. 21, 611-622.

Phillips, N.A., 1959: An example of non-linear computational instability, pp 501-504 in The Atmosphere and the Sea in Motion, New York: Rockefeller Institute Press.

Phillips, N.A., 1966: The equations of motion for a shallow rotating atmosphere and the "traditional approximation". J. of Atm. Sci. 23, 626-628.

Piacsek, S.A. and G.P. Williams, 1970: Conservation properties of convection difference schemes. J. Comp. Phys. 6, 120-133.

Pollack, J.B. and C. Sagan, 1965: Polarization of thermal emission from Venus. The Astrophys. Journal 141, 1161-1183.

Roberts, J., 1963: Radio emission from the planets. Planet. Sp. Sci. 11, 221-259.

Sagan, C., 1962: Structure of the lower atmosphere of Venus. Icarus 1, 151-169.

Schubert, G., 1969: High velocities induced in a fluid by a traveling thermal source. J. Atm. Sci. 26, 767-770.

Schubert, G. and J.A. Whitehead, 1969: Moving flame experiments with liquid mercury: possible implications for the atmosphere of Venus. Science 163, 71-72.

Schubert, G. and R.E. Young, 1971: The four-day circulation driven by periodic thermal forcing. J. Atm. Sci. 27, 523-528.

Schubert, G., R.E. Young and J. Hinch, 1971: Prograde and retrograde motion in a fluid layer: consequences for thermal diffusion in the Venus atmosphere. J. Geophys. Res. 76, 2126-2130.

Smagorinsky, J.W., 1963: General circulation experiments with the primitive equations. I: The basic experiment. Mon. Wea. Rev. 91, 99-164.

Smagorinsky, J.W., S. Manabe and J.L. Holloway, 1965: Numerical results from a nine-level general circulation model of the atmosphere. Mon. Wea. Rev. 93, 727-798.

Smith, B.A., 1967: Rotation of Venus: continuing contradictions. Science 15, 114-116.

Somerville, R.C.J., 1966: A non-linear spectral model of convection in a fluid unevenly heated from below. Ph. D. Thesis, New York University.

Spiegel, E.A. and G. Veronis, 1960: On the Boussinesq approximation for a compressible fluid. Astrophys. J. 131, 442-447.

Stern, M.E., 1959: The motion of a fluid due to a moving source of heat at the boundary. J. Fl. Mech. 29, 137-150.

Stommel, H., 1948: The westward intensification of wind-driven
        ocean currents. Trans. Am. Geoph. Union 29, 202-206.

Stommel, H., 1962: On the smallness of sinking regions in the ocean.
        Proc. Nat. Acad. Sci. 48, 766-772.

Sundqvist, H. and G. Veronis, 1970: A simple finite-difference
        grid with non-constant intervals. Tellus 22, 26-31.

Taylor, G.I., 1923: Stability of a viscous liquid contained be-
        tween two rotating cylinders. Proc. Roy. Soc., A132, 499-
        523.

Thaddeus, P., 1968: The dry massive model of the atmosphere of
        Venus and the microwave phase effect. The Atmospheres
        of Venus and Mars. J.C. Brandt and M.B. McElroy editors,
        Gordon and Breach, New York.

Thompson, R., 1970: Venus' general circulation is a merry-go-round.
        J. Atm. Sci. 27, 1107-1116.

Williams, G.P., 1967: Thermal convection in a rotating fluid annulus:
        Part I. The basic axisymmetric flow. J. Atm. Sci. 24,
        144-161.

BIOGRAPHICAL SKETCH

I was born on October 1st, 1942 in Buenos Aires, Argentina. I attended the Universidad Nacional de Buenos Aires from 1960 to 1965, where I received the degree "Licenciatura en Ciencias Meteorológicas". At the university I met Alberto M. Rivas, and we got married in 1965. In January 1967 we came to the United States and I began studying at the Massachusetts Institute of Technology. On January 7, 1970 our son Jorge Rodrigo was born.